Dissertation

submitted to the

Combined Faculty of Natural Sciences and Mathematics

of Heidelberg University, Germany

for the degree of

Doctor of Natural Sciences

Put forward by

Julian Gunnar Josef Stark

born in: Nürtingen

Oral examination: 29.07.2020

An Ultralow-Noise Superconducting Radio-Frequency Ion Trap for Frequency Metrology with Highly Charged Ions

Referees: **Priv. Doz. Dr. José R. Crespo López-Urrutia**

Priv. Doz. Dr. Wolfgang Quint

Eine ultra-rauscharme, supraleitende Hochfrequenz-Ionenfalle für Frequenzmetrologie mit hochgeladenen Ionen

Hochgeladene Ionen sind aussichtsreiche Kandidaten für Frequenzstandards der nächsten Generation, da sie eine stark unterdrückte Sensitivität für externe Störungen aufweisen, und wurden zudem vorgeschlagen, Physik jenseits des Standardmodells der Teilchenphysik zu testen. Diese Anwendungen erfordern Spektroskopie hochgeladener Ionen mit der Genauigkeit moderner Frequenzstandards basierend auf gespeicherten, einfach geladenen Ionen. Um die vorherrschenden Limitierungen durch bewegungsbedingte Frequenzverschiebungen zu überwinden, ist eine effektive Unterdrückung der fallenspezifischen Heizraten unabdingbar. Zu diesem Zweck wurde im Rahmen dieser Arbeit ein neues kryogenes Paulfallen-Experiment, CryPTEx-II, entwickelt und in Betrieb genommen. Es besteht aus einer neuartigen, supraleitenden Paulfalle, die als einzigartige Kombination von Hochfrequenz-Resonator und Ionenfalle realisiert ist, und einer vibrationsarmen, kryogenen Zuleitung, welche die Fallenregion auf Temperaturen von 4.15 K abkühlt und von externen Vibrationen entkoppelt. Der Resonator weist eine Quadrupolresonanz des elektrischen Feldes bei 34.52 MHz mit einer Güte von $\sim 2.3 \times 10^5$ auf. Diese sollte die stabile Speicherung von Ionen in ultra-rauscharmen Hochfrequenzfeldern bei drastisch unterdrückten Heizraten der Bewegung ermöglichen. Die im Rahmen dieser Arbeit durchgeführte Inbetriebnahme beinhaltet die Verwendung des Resonators als Quadrupol-Massenfilter zur Fokussierung hochgeladener Ionen durch diesen hindurch und die ersten Experimente mit gespeicherten, Laser-gekühlten $^9Be^+$-Ionen. Dies beweist die volle Funktionalität dieser einzigartigen Apparatur, welche zukünftig Anwendung bei Hochpräzisionsexperimenten mit hochgeladenen Ionen finden wird.

An ultralow-noise superconducting radio-frequency ion trap for frequency metrology with highly charged ions

Highly charged ions (HCIs) are excellent candidates for next-generation frequency standards, as they feature a much reduced susceptibility to external perturbations, and are proposed to stringently test physics beyond the Standard Model of particle physics. These applications require spectroscopy of HCIs with an accuracy on the level of state-of-the-art trapped-ion frequency standards. In order to overcome the current limitations due to motional frequency shifts, an efficient suppression of trap-induced heating rates is essential. To that end, a new cryogenic Paul trap experiment, CryPTEx-II, was developed and commissioned within this work. It consists of a novel superconducting ion trap uniquely combining a radio-frequency (rf) cavity and a Paul trap, and a low-vibration cryogenic supply to cool the trap to temperatures of 4.15 K while decoupling external vibrations. The cavity features an electric quadrupole mode at 34.52 MHz with a quality factor of $\sim 2.3 \times 10^5$, which allows for stable confinement of ions in ultralow-noise rf potentials and is expected to result in strongly suppressed motional heating rates. Commissioning experiments comprised the operation of the cavity as a quadrupole mass filter to focus HCIs through the cavity as well as the first trapping and laser cooling of $^9Be^+$ ions. These constitute the successful proof-of-principle operation of this unique apparatus, which will be used for high-precision experiments with HCIs in the future.

Contents

List of Figures

List of Tables

Acronyms

ac	alternating current
AOM	acousto-optic modulator
BBO	beta barium borate
BCS	Bardeen–Cooper–Schrieffer
CAD	computer-aided design
CryPTEx	cryogenic Paul trap experiment
dc	direct current
EBIT	electron beam ion trap
EDM	electrical discharge machining
em	electromagnetic
EMCCD	electron multiplying charge-coupled device
EP	electropolishing
EuXFEL	European X-Ray Free-Electron Laser
FEM	finite element method
HCI	highly charged ion
MCP	microchannel plate
MP	multipacting
MPIK	Max-Planck-Institut für Kernphysik
OFHC	oxygen-free high thermal conductivity
PEEK	polyether ether ketone
PSD	position-sensitive detector
PTB	Physikalisch-Technische Bundesanstalt
PTFE	polytetrafluoroethylene

QED	quantum electrodynamics
QLS	quantum logic spectroscopy
rf	radio-frequency
RRR	residual-resistance ratio
SM	Standard Model of particle physics
SNR	signal-to-noise ratio
TMP	turbomolecular pump
TOF	time-of-flight
TTU	thermal transfer unit
UHV	ultra high vacuum
UV	ultraviolet
VUV	vacuum ultraviolet
XHV	extreme high vacuum
XUV	extreme ultraviolet

1

Introduction

Our understanding of fundamental physics has tremendously grown over the last 200 years. However, there is still a number of open questions representing a great challenge for modern physics. Among them are the unification of the three fundamental interactions described within the Standard Model of particle physics (SM) with gravity. In addition, the composition of our universe is not completely understood, as studies of the cosmic microwave background suggest that only a minor fraction of its total content can be related to normal matter [Ade+14]. The large majority of the universe seems to be made up of dark matter and dark energy. While the former has found experimental support, e.g. observations of gravitational lensing [Aub+93; Alc+93] or dynamics of spiral galaxies [FG79], the latter is proposed as a possible explanation for the accelerated expansion of the universe [PR03]. However, neither dark matter nor dark energy are understood regarding their nature and interaction with SM particles. Furthermore, the visible fraction of the universe is made up almost exclusively of baryonic matter and contains basically no antimatter [DK03]. This great surplus of matter over antimatter remains to be explained.

There are two complementary approaches to searches for new physics, which may contribute answers to these questions. At high energy scales, astronomical observations or experiments based on particle accelerators are used. In contrast, the excellent control of systematic shifts in small-scale, i.e. table-top, laboratory experiments allows to stringently test SM predictions with extremely high precision at low energies. Here, an important technique has been and still is spectroscopy, especially for studies in atomic physics. Starting with Bunsen and Kirchhoff in 1861, who used a prism to analyze the

spectra of different chemical elements [KB61], spectroscopy was used to improve our understanding of atomic and fundamental physics ever since. The invention of the laser as a monochromatic light source in 1960 [Mai60] increased the achievable spectroscopic precision. The subsequent application of laser cooling to atoms and ions, e.g. [Neu+78; WI79], allowed to reduce the thermal velocity spread of ensembles of atomic systems and thereby the Doppler broadening of the observed electronic transitions. In combination with the development of ion traps by Dehmelt [Deh90] and Paul [PS53], this provides the basis for modern high-precision experiments with long interrogation times under well-controlled conditions.

The two most common means to confine ions are Paul traps and Penning traps. While Penning traps restrict the motion of ions using static magnetic and electric fields, Paul traps employ a superposition of radio-frequency (rf) and static electric potentials. The focus of the following description is on Paul traps, since these allow to confine ions in a zero-field environment, which makes them especially suited for high-precision laser spectroscopy or frequency metrology [Gil05; Lud+15]. The exceptional control of systematic uncertainties in these traps enabled the highest precision measurements with single ions. Examples for the low systematic uncertainties that have been demonstrated with single-ion frequency standards are the Yb^+ clock at Physikalisch-Technische Bundesanstalt (PTB) with a fractional frequency uncertainty of $\Delta\nu/\nu = 3.2 \times 10^{-18}$ [Hun+16] and the Al^+ clock at National Institute of Standards and Technology (NIST) with 9.5×10^{-19} [Bre+19]. Recently, even multi-ion traps were developed which reported on a control of trap-induced frequency shifts below a relative uncertainty of 10^{-19} [Kel+19]. This makes trapped-ion frequency standards extremely sensitive probes to study fundamental physics, such as searches for a possible variation of fundamental constants [Ros+08; Hun+14] or tests of local Lorentz invariance [Pru+15; Meg+19; San+19].

The systematic uncertainty of a frequency standard corresponds to the residual lack of knowledge about systematic effects on the frequency determination. The magnitude of these perturbations depends on the atomic properties of the probed system and the involved electronic states [Lud+15]. In this respect, highly charged ions (HCIs) are promising candidates to reduce systematic frequency shifts, as was originally pointed out by [Sch07]. Due to their small size and the strong internal fields, HCIs are rather insensitive to many external perturbations, which typically limit state-of-the-art frequency standards [Koz+18]. Thus, HCIs were proposed as candidates for next-generation frequency standards with a potential fractional uncertainty on the level of 10^{-19} and below, e.g. [Ber+12a; DDF12a]. In addition, HCIs feature dipole-forbidden transitions with an enhanced sensitivity to effects beyond the SM, such as a possible variation of fundamental constants [Sch07; Ber+11; Ber+12b; DDF12c; Koz+18]. The unique properties of HCIs as well as their capability as probes for fundamental physics and next-generation frequency standards make them attractive species to study in experiment (see Sec. 1.1).

One of the largest contributions to the systematic uncertainty of trapped-ion frequency standards are motional shifts [Hun+16; Bre+19]. These can be caused by trap-induced heating of the ion motion, e.g. by electric-field noise, as well as mechanical vibration of the trap setup. In order to overcome the current limitations, a new cryo-

genic Paul trap experiment, CryPTEx-II, was developed in the framework of this thesis. It features a low-vibration cryogenic supply which provides mechanically ultra-stable trapping conditions by decoupling external vibrations from the trap region. Most importantly, the novel ion trap is realized by a unique combination of a superconducting rf cavity and a Paul trap. Confinement of ions inside the ultra-stable rf potentials should strongly reduce motional frequency shifts due to suppressed heating of trapped ions by rf noise.

This is essential for the planned experiments with HCIs. Due to their increased electric charge, they feature an enhanced sensitivity to electric-field noise compared to singly charged ions. In this respect, the new ion trap experiment represents a sophisticated approach to improve the typical trapping conditions of modern Paul trap experiments, which could contribute to the realization of frequency standards based on HCIs as well as to unlock their full potential for tests of fundamental physics. A comparison with conventional Paul traps is given Sec. 1.2 together with a brief overview of the field of rf cavities.

1.1 The physics and applications of highly charged ions

Over the past decade there has been a growing interest in HCIs for applications in frequency metrology and fundamental physics [QV14; Koz+18]. The reasons are partly related to the extraordinary inherent properties of HCIs. Additionally, they offer a whole new range of systems to study, as each element of the periodic table can be prepared in a variety of charge states. Two prominent applications of HCIs will be discussed in the following. Here, the main focus is on optical transitions, for which the current experimental state of the art is discussed.

It has to be noted that only a minor fraction of the available atomic systems can be studied with high-precision laser spectroscopy, since many of the methods applied in frequency metrology are refined for the microwave and optical range. For HCIs, the number of transition in this region is limited due to the strong scaling of the electronic gross structure with the nuclear charge Z, e.g. $E \propto Z^2/n^2$ for hydrogen-like ions, where n is the principal quantum number. Thus, electronic dipole transitions are typically shifted to the x-ray range. Nevertheless, there are different types of optical transitions in HCIs, which are dipole forbidden. First, fine-structure and hyperfine-structure transitions scale strongly with the nuclear charge, $\Delta E \propto Z^3$ and Z^4 for hydrogen-like ions, respectively [Ber+12a], and are shifted into the optical range already at medium charge states ($q \approx 10\,e$) [Leo18]. Additionally, transitions between different electronic configurations at so-called level crossings [BDF10; Bek+19] are found to be in the optical range and strongly dipole forbidden. These level crossings occur due to the fundamentally different ordering of electronic orbitals for neutral systems (Madelung ordering) and hydrogen-like ions (Coulomb ordering). Thus, at some intermediate charge state the different electronic levels are close in energy and exhibit energy differences in the optical range.

1.1.1 State-of-the-art optical spectroscopy

For many years, the achievable precision with HCI spectroscopy was limited by the extreme conditions in which they are produced. Due to the high nuclear charge, energies up to 100 keV are required to remove bound electrons and prepare the ion in the required charge state. Large cross sections for charge-exchange reactions with neutral gas require extreme high vacuum (XHV) conditions to maintain high charge states. Finally, in order to reach long interrogation times, a mechanism for confinement needs to be provided. Over the past decades, various devices were employed to study HCIs, such as electron beam ion traps (EBIT) and sources (EBIS), electron cyclotron resonance ion sources (ECRIS), plasma and fusion devices, Penning traps and accelerators [BS03].

Until recently, the most precise optical spectroscopy of HCIs was performed using a hot plasma confined inside an EBIT. These devices employ a mono-energetic beam of electrons accelerated to high kinetic energies to produce multiply charged ions by sequential impact ionization of gas atoms. The ions are radially bound by the negative space charge of the electron beam and axially confined inside the electrostatic trapping potential of surrounding electrodes. However, space-charge effects, trapping-field inhomogeneities, and voltage noise have limited the ion temperatures to $T > 10^5\,\mathrm{K}$ [Koz+18]. The corresponding Doppler broadening on the order of 100 GHz limited the spectral resolution typically achieved to the ppm level [Dra+03; Sor+07; Mäc+11].

Recently, this was improved by high-precision laser spectroscopy of an HCI inside a Penning trap. Here, the laser-induced electronic excitation of a single $^{40}Ar^{13+}$ ion, resistively cooled to 1 K, was detected through interrogation of its spin state. This allowed to measure the forbidden $2p\,^2P_{1/2} \rightarrow {}^2P_{3/2}$ transition at 441 nm with a precision of $\Delta\nu/\nu \simeq 9.4 \times 10^{-9}$ [Egl+19]. Other Penning trap experiments aiming at optical spectroscopy of trapped HCIs employ the laser-microwave double resonance technique [Vog+19; Qui+08] to simultaneously determine electronic and nuclear g factors. In addition, mass measurements in Penning traps recently allowed for the identification of a long-lived metastable transition in highly charged rhenium ions [Sch+20]. Despite the comparably large uncertainty of 2 eV, this method can be used to discover and identify potential clock transitions in HCIs.

Despite this major improvement in spectral resolution, the lack of methods for cooling and state preparation still hindered spectroscopy of HCIs on the level of optical frequency standards. For both, a fast cycling transition in the laser-accessible range is required, which cannot be found in HCIs [Koz+18]. Therefore, sympathetic cooling is employed to reduce the HCI temperature by the strong Coulomb interaction with co-trapped laser cooled ions. This was for the first time implemented inside a Penning trap [Gru+01]. Subsequently, the concept was adopted to Paul traps and demonstrated using $^{40}Ar^{13+}$ ions implanted into a Coulomb crystal of Doppler cooled $^9Be^+$ ions [Sch+15a]. The next major step towards the application of state-of-the-art spectroscopy schemes was the preparation of a two-ion crystal consisting of HCI and $^9Be^+$ ion and the application of resolved sideband cooling. Recently, this enabled the preparation of an $^{40}Ar^{13+}$ ion in the quantum mechanical ground state of its motion [Mic20; Leo+19]. This paved the way for the application of quantum logic spectroscopy (QLS) to HCIs. Using the

strong motional coupling of the co-trapped ions, the electronic excitation of the HCI is transferred to the cooling ion and there efficiently detected. It was for the first time demonstrated using the forbidden optical transition in $^{40}Ar^{13+}$ at 441 nm [Mic+20]. The reported statistical uncertainty of $\Delta\nu/\nu \simeq 10^{-15}$ opens up the potential of HCIs for high-precision experiments.

1.1.2 Tests of fundamental physics

Experiments with HCIs allow to test the understanding of physics under extreme conditions, where the effects of quantum electrodynamics (QED), special relativity, and nuclear physics are greatly enhanced compared to neutral or singly charged systems [Gil01; QV14; Koz+18]. This is related to their electronic structures. Compared to neutral atoms, the number of electrons bound to the nucleus is reduced in HCIs of the same element. Accordingly, the valence electrons experience a reduced screening of the nuclear charge and are therefore more strongly bound to the nucleus. In addition, the spatial extent of the electronic wavefunction is scaled down. Thus, the overlap of electronic and nuclear wavefunction is increased, which enhances the nuclear contributions to the electronic energy levels [Kla+94; Cre+96; Ort+06]. Furthermore, as the remaining electrons are bound closely to the nucleus, they are part of highly relativistic systems and feature scaled-up relativistic and QED effects [Ind19].

A detailed comparison of experiments with advanced atomic structure calculations allows to refine the understanding of the underlying interactions. Besides the comparably large magnitude of the effects, HCIs are especially appealing for such studies as they feature a reduced number of bound electrons, which makes them easier to calculate with high accuracy. Additionally, HCIs feature the possibility to study the scaling laws of these effects as a function of the nuclear charge with identical number of electrons, or by varying the number of electrons for the same nucleus. Therefore, HCIs are suitable systems to benchmark the understanding of electron correlations, electron-nucleus interactions, special relativity, and QED. In the following, two proposed applications of HCIs for tests of fundamental physics will be discussed in more detail.

Isotope shift spectroscopy

An interesting avenue in the search for new physics uses isotope shift spectroscopy, see e.g. [Geb+15], in combination with a King plot analysis [Kin63] to probe nuclear physics. Here, the frequency difference of two electronic transitions in the same atomic system is compared for different combinations of isotopes. This method can be used to constrain new physics, e.g. probe 5^{th} force theories, which predict a new bosonic mediator coupling electrons to neutrons [Ber+18; Koz+18]. Such an additional force would show up as a non-linearity in the King plot and can thus be constrained by isotope shift measurements using at least three different isotopes. However, it has to be noted that non-linearities are also expected within the SM and can be caused by next-to-leading order contributions to the isotope shift [PCE16].

For these studies, HCIs are appealing, since they offer a large amount of systems to choose from, which increases the number of available electronic transitions for identical nuclei. Additionally, the expected non-linearities within the SM can be calculated to higher precision for HCIs compared to neutral systems.

Time variation of fundamental constants

Another example for tests of new physics using HCIs is to probe a possible temporal variation of fundamental constants [Ber+11; Koz+18]. This allows to test and constrain certain extensions of the SM, which either allow for or directly suggest a variation of fundamental constants, see e.g. [Wet03; DSW08]. In addition, certain models of scalar dark matter predict a coupling to the electronic energy levels in atomic systems [DP14], which causes a shift of transition frequencies and could be interpreted as a change of the fine-structure constant. The corresponding research is performed using a wide range of systems, among others a natural nuclear reactor or astrophysical studies [Uza11]. Here, only the laboratory limits based on atomic clock comparisons will be covered.

The basic idea is that the transition frequency between two electronic energy levels in an atom depends on the exact value of the fine-structure constant α. In addition, the energy difference between two hyperfine levels depends on the electron-to-proton mass ratio $\mu = m_\mathrm{e}/m_\mathrm{p}$ as well as the nuclear g factor. Thus, the frequency comparison of two optical or microwave clocks can be used to constrain a possible variation of the corresponding fundamental constants, which would be detectable as a temporal change of the measured frequency ratio $r = \nu_1/\nu_2$. The best constraint on a possible α variation obtained by a single optical clock comparison is given by $\dot{\alpha}/\alpha = -1.6(2.3) \times 10^{-17}\,\mathrm{yr}^{-1}$ [Ros+08]. In combination with the results from various comparisons of optical and microwave clocks as well as dysprosium measurements, the present day limits for the variation of α and μ are given by [Lee+13; Hun+14; God+14]

$$\begin{aligned} \frac{\dot{\alpha}}{\alpha} &= -2.0(2.0) \times 10^{-17}\,\mathrm{yr}^{-1} \quad , \\ \frac{\dot{\mu}}{\mu} &= 0.2(1.1) \times 10^{-16}\,\mathrm{yr}^{-1} \quad . \end{aligned} \tag{1.1}$$

The sensitivity of a specific electronic transition to a possible variation of the fine-structure constant can be predicted using atomic structure calculations of the transition energies for changing values of α. It is typically expressed by the parameter K, which relates a change of α to a change of transition frequency [DFM03; Koz+18]:

$$\frac{\delta\nu}{\nu_0} = K\,\frac{\delta\alpha}{\alpha_0} \quad \rightarrow \quad \frac{\delta r}{r_0} = |K_1 - K_2|\,\frac{\delta\alpha}{\alpha_0} \quad . \tag{1.2}$$

The K factor of most atomic clocks which are currently in operation or development is below 1, except for the Hg^+ clock and the Yb^+ octupole transition, which reach sensitivities of -3 and -6, respectively [Koz+18].

Larger sensitivities can be found in HCIs. Over the last years, several systems were predicted to be very sensitive to a potential α variation [Sch07; Ber+11; Ber+12b;

DDF12c; Koz+18]. Especially optical transitions at level crossings are predicted to feature K parameters which are up to two orders of magnitude larger compared to singly charged or neutral systems. This is related to the enhanced relativistic effects, the high ionization threshold as well as the large proton number of HCIs [BDF10; Koz+18].

In addition, since hyperfine transitions are shifted to the optical range in HCIs, they become potentially available for high-precision laser spectroscopy. This allows for sensitive tests of a variation of nuclear g factors or μ using HCIs. An overview of the proposed systems and their applications in fundamental studies can be found in [Koz+18].

1.1.3 Frequency standards based on highly charged ions

In order to unlock the potential of HCIs for the aforementioned studies of fundamental physics, a frequency standard based on HCIs needs to be set up. In principle, they are well-suited to reach lower systematic uncertainties compared to state-of-the-art single-ion clocks, due to their advantageous atomic properties [Sch07; Koz+18]. In particular, the small size of the electronic wavefunction yields a suppressed polarizability of the ions, which scales with Z^{-4} [Ber+12a]. As a result, many of the field-induced shifts are suppressed, e.g. the electric quadrupole shift (Z^{-2}) and the second-order Stark shift (Z^{-4}) [Ber+12a]. The stated scalings with the nuclear charge Z apply strictly only for hydrogen-like ions and become more complicated for many-electron systems, where the screening of the nuclear charge has to be taken into account. However, also in this case many of the systematic shifts are greatly suppressed and additionally accompanied by reduced uncertainties [Koz+18]. Thus, several HCIs were proposed as promising candidates for next-generation frequency standards with predicted fractional uncertainties at the level of 10^{-19} and below, e.g. [Sch07; Ber+12a; DDF12a; DDF12b; YTD14]. A detailed evaluation of different clock candidates is provided in [Koz+18].

Although the individual contributions to the total systematic uncertainty of an optical clock depend on the details of the atomic systems, two effects are expected to be dominant for HCIs [Koz+18; Mic20]. First, the linear Zeeman shift of the involved electronic energy levels is rather insensitive to the nuclear charge, and thus not suppressed compared to singly charged or neutral systems. However, it can be removed by averaging over different Zeeman components of the probed transition. Second, motional shifts are expected to be more pronounced in highly charged systems. This requires a careful calibration and minimization of the corresponding sources, e.g. excess micromotion, and suppressed motional heating rates inside the trap [Koz+18]. The latter causes an increased motional shift over the interrogation time as well as an increased shift uncertainty and can thus limit the systematic uncertainty. This will be discussed in Sec. 1.1.4.

Besides the use of HCIs as optical frequency standards, they offer the prospect to expand frequency metrology to higher transition frequencies. This would allow to improve the fractional statistical uncertainty, which is typically limited by quantum projection

noise and scales as [Lud+15; Koz+18]

$$\sigma \propto \frac{1}{\nu_0 \sqrt{N \tau t}} \quad , \tag{1.3}$$

where N denotes the number of references, τ is the probe time, t is the averaging time and ν_0 is the probed transition frequency. Thus, a long probe time and a high transition frequency are needed in order to limit the averaging time required to reach a given statistical uncertainty. Typically, the probe time is limited either by the excited state lifetime or the coherence time of the interrogating laser. Thus, it is desirable to increase the transition frequency and develop a frequency standard based on a transition in the vacuum ultraviolet (VUV), extreme ultraviolet (XUV), or even in the x-ray range.

This is difficult to realize with neutral or singly charged systems, since the irradiation with high-energy photons might result in ionization or couple the involved electronic states to the continuum and thereby broaden the transition. These limitations can be overcome using HCIs, which feature strongly bound valence electrons due to their increased nuclear charge. In addition, they offer dipole-forbidden transitions in the VUV and XUV regions, which feature sufficiently long lifetimes to be used as future frequency standards [Koz+18; Sch+20]. However, in order to benefit from higher transition frequencies, the systematic uncertainties need to be reduced to a similar level as the improved statistical ones. In addition, the developed methods for frequency metrology in the optical regime need to be transferred to higher frequencies. This can be achieved using XUV frequency combs based on high harmonic generation [Goh+05; Jon+05], which allows to transfer the temporal coherence and comb structure of an optical frequency comb to the XUV. One of these devices has been set up and commissioned at Max-Planck-Institut für Kernphysik (MPIK) [Nau+17; Nau20; Oel21]. Besides the use for frequency-metrology, the combination with the presented ion trap experiment in the near future will allow for direct frequency comb spectroscopy of cold HCIs in the XUV range.

1.1.4 Motional shifts of trapped ions

One of the largest contributions to the systematic uncertainty of modern frequency standards based on trapped ions are motional shifts [Hun+16; Bre+19], which are also expected to be relevant for HCIs. The presented ion trap experiment aims to reduce these trap-induced frequency shifts by production of ultra-stable rf potentials, as discussed in Sec. 1.2. In the following, the different contributions to motional shifts are discussed.

The first order Doppler shift arises from the relative movement of the ion in the direction of the interrogating laser and ideally averages to zero for its motion inside the harmonic trapping potential. However, thermal effects and patch potentials at the trap electrodes can lead to a drift of the mean ion position relative to the probe laser over the course of the measurement. This was measured to yield a fractional shift on the order of 5×10^{-17} [Bre+19], which corresponds to a mean drift velocity on the order of $10\,\mathrm{nm\,s^{-1}}$. It can be compensated by using counterpropagating probe beams or stabilizing the interrogation laser to the trap. For cryogenic environments, the thermal

expansion of the trap is greatly reduced, which should suppress the movement of the ion trap itself.

The second order Doppler shift gives rise to a relativistic time dilation due to the residual motion of the ion with respect to the spectroscopy laser. This amounts to a fractional shift of 1×10^{-18} for a velocity of $0.42\,\mathrm{ms}^{-1}$ [Kel15]. In order to account for this effect, a precise knowledge of the ion motional state over the course of the measurement is required. The two contributions to this shift are the thermal ion motion inside the harmonic pseudopotential of the trap and the micromotion, which is driven by the confining rf potential. The latter comprises contributions from the intrinsic micromotion which is naturally present in Paul traps and depends on the spatial extent of the wavefunction of the ion. Another contribution results from excess micromotion which is caused by residual rf fields at the potential minimum of the trap. The corresponding motional shift needs to be carefully evaluated and minimized, e.g. using the methods described in [Ber+98; Kel+15].

The thermal ion motion can be minimized by preparing the ion in the quantum mechanical ground state of its motion using appropriate cooling schemes. However, the ion is still susceptible to external electric-field noise, which couples to the ion motion and induces heating. The precise determination of the motional state of the ion with low uncertainty thus demands low motional heating rates over the course of the measurement. The estimated heating rate for an ion with charge q and mass m scales with q^2/m [Bro+15] and is thus potentially enhanced for HCIs compared to singly charged ions. This becomes even more important for few-ion crystals consisting of an HCI and a laser-cooled ion, which is used for QLS of HCIs [Mic+20; Mic20]. The reported heating rates for a two-ion crystal consisting of one $^{40}Ar^{13+}$ ion and one $^{9}Be^{+}$ ion [Mic20] are more than one order of magnitude larger compared to the measured values without HCI [Leo+19]. This renders the suppression of motional heating rates indispensable for high-precision experiments with HCIs.

1.2 Superconducting radio-frequency cavities

The new ion trap developed within this thesis is designed to provide ultra-stable rf trapping conditions with suppressed motional heating rates. It represents a unique combination of a superconducting rf cavity and a linear Paul trap, where the ions are confined by the standing electromagnetic (em) fields of the resonant mode. The following section gives a brief overview of the field of rf cavities and compares the new apparatus to conventional Paul trap experiments.

An rf cavity describes a largely closed metal structure, which supports various resonant modes of the enclosed em fields. Several types of rf cavities are elementary constituents of many modern particle accelerators, where they are used to accelerate a wide range of charged particles. They exhibit typical resonance frequencies in the range from 50 MHz to 4000 MHz and were historically made of copper [Pad17]. However, due to the quadratic increase of ohmic losses with the intra-cavity voltages, normal-conducting cavities suffer from heat-up, vacuum degradation and thermal expansion at high em

energies. With the demand for higher fields, normal-conducting cavities thus became uneconomical and superconducting cavities developed into the technology of choice.

Since the first development of superconducting cavities in the 1960s [TV70], they have found wide-spread application over the last decades at particle accelerators for high-energy physics, nuclear physics, light sources, neutron sources and proton accelerators [Pad17]. The largest deployment of superconducting rf technology today is the European X-Ray Free-Electron Laser (EuXFEL) [Abe+06] located at Deutsches Elektronen-Synchrotron (DESY) in Hamburg, Germany. It comprises 800 superconducting cavities, which were qualified with a maximum gradient of $30\,\mathrm{MVm}^{-1}$ at 1.3 GHz frequency, providing beam energies of up to 17.5 GeV [Res+17]. The largest future application under consideration at the moment is the International Linear Collider (ILC) in Japan. It is an electron-positron collider based on 16000 superconducting cavities, which should provide up to 500 GeV beam energy [Ado+13].

Although the high beam energies are very different from the kinetic energies of ions confined inside Paul traps, which typically employ trapping potential depths $< 1\,\mathrm{eV}$, the extremely high quality factors of $Q > 10^{10}$ routinely achieved with superconducting rf cavities make them attractive instruments for the application at low-energy ion traps. This is related to the superior properties of the rf fields inside a high-Q cavity. As the quality factor corresponds to the ratio of the stored em energy to the dissipated power per rf period, many cycles of the rf supply are stored inside the cavity which yields an increased amplitude and phase stability. In addition, the quality factor defines the frequency bandwidth $\Delta\omega$ of the resonant mode, $\Delta\omega \propto Q^{-1}$. Thus a high quality factor increases the stability of the rf potentials and efficiently suppresses external rf noise.

At conventional Paul trap experiments, the rf potentials for the radial confinement of ions are usually produced by an external rf resonator. The most common types are quarter wave or helical resonators, which feature typical resonance frequencies between 1 kHz and 100 MHz [Siv+12]. Values reported for the loaded quality factor, i.e. the quality factor of resonator connected to ion trap, are on the order of $Q \simeq 10^3$ [Joh+16; Bra+16; Siv+12]. At these quality factors, the insufficient filtering of the rf drive noise at the trap electrodes can limit the achievable motional heating rates, as was reported in [Leo+19].

This is improved substantially by the novel superconducting ion trap developed in this thesis. Integrating the trap electrodes into the cavity allows to suppress rf losses and accordingly enhance the quality factor. Confining the ions inside the ultra-stable standing em fields of the high-Q cavity is expected to provide drastically reduced motional heating rates compared to state-of-the-art Paul traps. This will allow to maintain small ion temperatures even for the extended interrogation times required for high-precision spectroscopy, which is crucial for the planned experiments with HCIs.

1.3 Thesis outline

This thesis reports on the development and construction of the new cryogenic Paul trap experiment CryPTEx-II located at MPIK. The performed commissioning experiments

include the first trapped ions and represent the proof-of-principle operation of the novel resonator ion trap combination.

In the next chapter, Chapter 2, the theoretical background for the presented work is provided. This includes a discussion of the general aspects of ion confinement inside rf ion traps, as well as the intended cooling methods. In addition, the main characteristics of rf cavities are covered together with the basics of rf superconductivity.

In Chapter 3, an overview of the complete experimental setup is provided, including the employed laser systems as well as atom and ion sources. The main focus is on the development and performance characterization of the low-vibration cryogenic supply and cryogenic setup of the ion trap.

Subsequently, in Chapter 4, the superconducting cavity constituting the main part of the new experiment is presented. The final design was developed using various simulations of the trapping potentials, the em eigenmodes of the resonant structure, as well as the injection performance of HCIs. These are presented together with a feasibility study for the application of image current detection techniques.

The commissioning of CryPTEx-II is presented in Chapter 5. This includes a detailed performance characterization of the superconducting cavity based on the rf properties of its electric quadrupole mode. The confinement of ions inside the cavity operated as a quadrupole mass filter is investigated by measuring the transmission of HCIs. In addition, the first experiments with trapped and laser-cooled $^{9}Be^{+}$ ions are discussed, which completes the commissioning of the superconducting cavity and the Paul trap experiment developed in this thesis.

The work closes with a summary and an outlook in Chapter 6, where possible modifications of the experimental setup as well as ideas for future measurements are discussed.

2

Theoretical Background

The ion trap developed and commissioned within the framework of this thesis represents a combination of a linear Paul trap and a radio-frequency (rf) cavity. Accordingly, this chapter covers physics from both fields and is divided into two parts. The first half (Sec. 2.1 and Sec. 2.2) starts with a description of the motion of a single ion confined in a Paul trap, followed by a discussion of the influences from imperfect trapping potentials (Sec. 2.1). Subsequently, an overview of the experimental techniques to cool trapped ions by interaction with laser light is given in Sec. 2.2. The second half of this chapter (Sec. 2.3 and Sec. 2.4) covers the basics and main characteristics of rf cavities and rf superconductivity. This includes a discussion of the experimental techniques for cavity characterization employed within this thesis (Sec. 2.3). The chapter closes with an introduction to the rf properties of superconductors (Sec. 2.4).

2.1 The linear radio-frequency ion trap

A linear rf ion trap, also called Paul trap, is the key element of the experimental apparatus presented in the thesis. Here, a brief summary of the underlying working principle, based on [Gho95] and [Win+98a], will be given. In addition, deviations from the ideal Paul trap and their influence on the ion motion are discussed.

2.1.1 Ion motion in the trap

Three-dimensional harmonic confinement of charged particles requires an electric potential of the general form

$$\Phi(x, y, z) = \alpha x^2 + \beta y^2 + \gamma z^2 \quad . \tag{2.1}$$

Following from the Laplace equation, $\Delta\Phi = 0$, the coefficients have to obey the relation $\alpha + \beta + \gamma = 0$. This results in a repulsive force in at least one direction. Therefore, it is not possible to realize a three-dimensional potential minimum using exclusively static electric potentials. This is also known as Earnshaw's theorem [Ear48].

In order to circumvent this repulsive contribution, a Paul trap employs a combination of rf and static electric fields. Thereby, a time-dependent quadrupole potential confines the ions along two directions. A static potential well is added along the third direction to restrict the ion motion along the central axis of the quadrupole.

In the simplest form, a linear Paul trap consists of four hyperbolic trap electrodes, as sketched in Fig. 2.1. These are used to produce the quadrupole potential for the radial confinement of ions along (x, y). Close to its minimum, it can be approximated by a harmonic potential:

$$\Phi_{\mathrm{QP}}(x, y, t) = \Phi_0(t)\frac{x^2 - y^2}{r_0^2} \quad , \tag{2.2}$$

where r_0 describes the distance from the trap electrodes to the symmetry axis. The quadrupole amplitude $\Phi_0(t)$ depends on the voltage amplitude V_{rf} and the frequency Ω of the rf trap drive,

$$\Phi_0(t) = V_{\mathrm{rf}} \cos(\Omega t) + U_{\mathrm{dc}}^r \quad . \tag{2.3}$$

Additionally, a static voltage U_{dc}^r is added in some cases to introduce a controlled anisotropy and lift the degeneracy of the radial motional frequencies (see Eq. (2.9)).

For the confinement along the trap axis (z), a static potential U_{dc}^z is applied to the outer electrode segments on both sides of the trap center separated by the distance $2z_0$ (see Fig. 2.1). Around its minimum, the resulting potential can be approximated by

$$\Phi_{\mathrm{dc}}(x, y, z) = \frac{\kappa U_{\mathrm{dc}}^z}{2z_0^2}\left(2z^2 - x^2 - y^2\right) \quad . \tag{2.4}$$

Here, the geometric factor $\kappa < 1$ corresponds to the fraction of the applied direct current (dc) voltage, U_{dc}^z, that is converted to the harmonic potential along the trap axis. It is determined by simulations (see Sec. 4.5.1).

The total trapping potential is given by the sum of the axial (Eq. (2.4)) and radial (Eq. (2.2)) contributions. The equations of motion for an ion of mass m and charge q moving through this potential are given by the so-called Mathieu equations:

$$\frac{\mathrm{d}^2}{\mathrm{d}t^2}u + \frac{\Omega^2}{4}\left(a_u - 2q_u\cos(\Omega t)\right)u = 0 \quad \text{with} \quad u = x,\, y,\, z \quad , \tag{2.5}$$

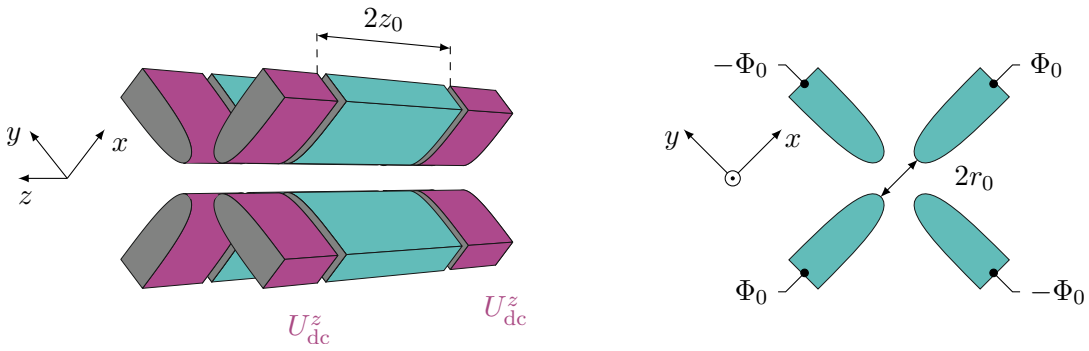

Figure 2.1: Schematic drawing of a linear Paul trap geometry with hyperbolic trap electrodes. The four quadrupole electrodes are segmented into three parts. All segments are supplied with the quadrupole potential $\pm\Phi_0(t)$ to radially confine ions. This can be seen on the right side, where the potentials of the center segments (cyan) are indicated in a section view through the trap center. Axial ion confinement is provided by the outer segments (magenta), additionally supplied with an electrostatic potential U^z_{dc}.

where the dimensionless transformation parameters a_u and q_u are introduced:

$$a_{x,y} = \pm\frac{4q}{m\Omega^2}\left(\frac{2U^r_{\mathrm{dc}}}{r_0^2} \mp \frac{\kappa U^z_{\mathrm{dc}}}{z_0^2}\right) \quad , \qquad q_{x,y} = \mp\frac{4qV_{\mathrm{rf}}}{mr_0^2\Omega^2} \quad ,$$
$$a_z = \frac{8q\kappa U^z_{\mathrm{dc}}}{mz_0^2\Omega^2} \qquad \text{and} \qquad q_z = 0 \quad . \tag{2.6}$$

Solutions to equation Eq. (2.5) can be divided into stable and unstable trajectories. The former describe an ion motion which is restricted to a finite volume around the potential minimum of the ion trap.

In axial direction, stable solutions require $a_z > 0$ as well as the kinetic energy of the particle to be smaller than the depth of the axial trapping potential. In radial direction, the stability of the ion motion depends only on the parameters $a_{x,y}$ and $q_{x,y}$. The stability diagram for the motion of a single ion inside a linear Paul trap is shown in Fig. 2.2. While different regions in the (a_u, q_u) parameter space allow for stable confinement in both radial directions, most Paul traps are operated in the stability region closest to the origin $(a_u, q_u = 0)$ for practical reasons. This is also the case for the ion trap described in this thesis, with typical stability parameters in the range $|a_u| \ll |q_u| < 0.4$.

For such small stability parameters, the so-called adiabatic approximation can be applied, which yields simple solutions to Eq. (2.5), given by

$$u(t) = u_1\cos(\omega_u t)\left(1 + \frac{q_u}{2}\cos(\Omega t)\right) \quad \text{with} \quad \omega_u = \frac{\Omega}{2}\sqrt{a_u + \frac{q_u^2}{2}} \quad . \tag{2.7}$$

The ion motion separates into two harmonic oscillations, the slow secular motion at frequency ω_u and amplitude u_1 around the potential minimum and the fast micromotion

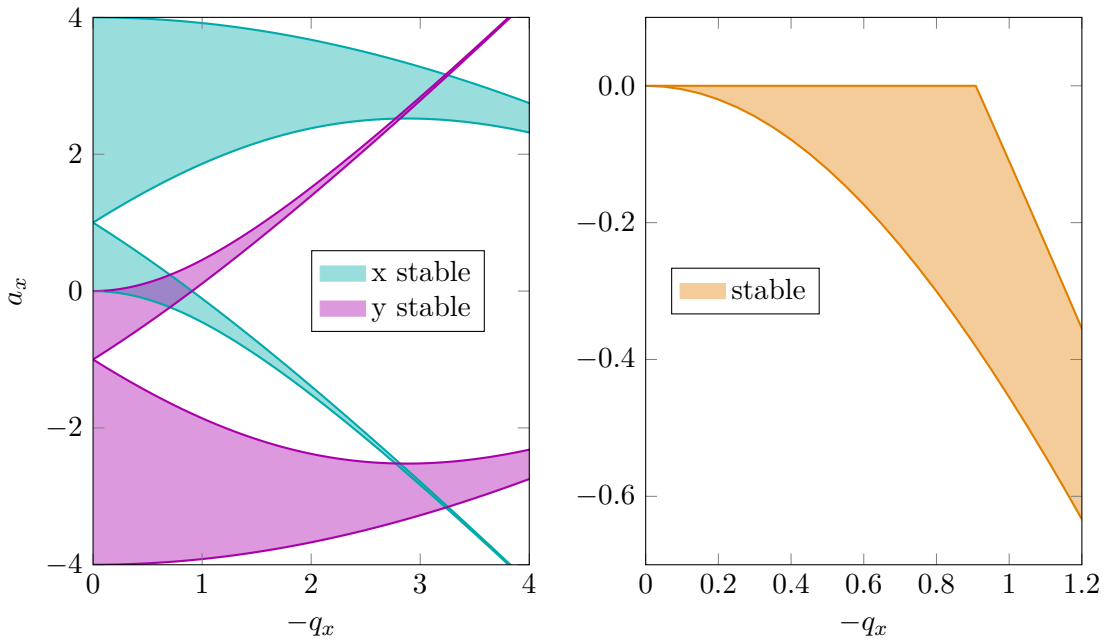

Figure 2.2: Stability diagram for the radial motion of a single ion as a function of the parameters a_x and q_x defined in Eq. (2.6). **Left:** The regions of stability for a quadrupole mass filter, i.e. $U^z_{\mathrm{dc}} = 0$ and $a_x = -a_y$, are shown separately for the motion in x (cyan) and y (magenta) direction. **Right:** The region of stability in both radial directions closest to the origin is shown for a linear Paul trap with $U^r_{\mathrm{dc}} = 0$ and $a_x = a_y$ for the case of $a_z > 0$, which allows for axial confinement of the ion.

at the trap drive frequency Ω. The latter describes a driven motion for which two contributions need to be distinguished.

The main source of micromotion is the so-called intrinsic micromotion, which is described by Eq. (2.7). It is a fundamental property of Paul traps. Compared to the secular motion, its amplitude is reduced by a factor of $q_u/2$ and, therefore, vanishes along the trap axis. Due to its scaling with the secular motion amplitude u_1, it is strongly suppressed around the rf node and can be reduced by cooling, which reduces u_1, but never vanishes completely.

Further contributions to micromotion are called excess micromotion. In contrast to intrinsic micromotion, which exists only for the radial modes, it also can affect the axial direction. A detailed description of the different sources of excess micromotion and methods to minimize its effect are given in [Ber+98; Kel+15]. In general, this motion is driven by residual rf electric fields at the potential minimum, which are caused by imperfect trapping potentials.

Radial rf fields at the potential minimum can be caused by static electric offset potentials on the trap electrodes displacing the ion from the rf node or by phase shifts of

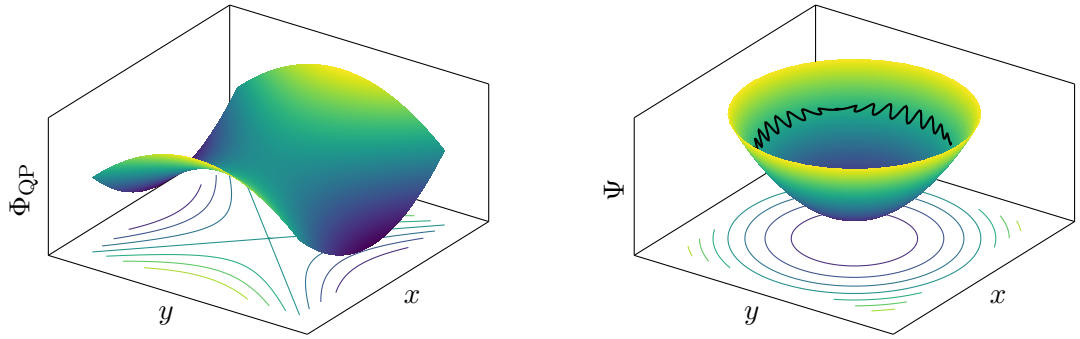

Figure 2.3: Schematic drawing of the radial trapping potential of a linear Paul trap. **Left:** The static quadrupole potential Φ_{QP} restricts the ion motion only along one direction. **Right:** For radial stability parameters satisfying $|a_u| \ll |q_r| < 0.4$, the ion is radially confined by the time-averaged harmonic pseudopotential Ψ. Its motion along x and y is composed of the slow secular motion at frequency ω_u and the fast micromotion at frequency Ω (see Eq. (2.7)). One possible trajectory is sketched for $\Omega/\omega_u = 34$ (black line).

the rf voltages on opposite electrodes. Additionally, imperfections in the trap electrode alignment can result in a driven motion along the trap axis [Leo+19]. Typically, several sources of excess micromotion are present at the same time. Since the size of its effect depends on the position of the ion, it can be minimized by adjusting the position of the static potential minimum with respect to the rf node.

In adiabatic approximation, the ion motion averaged over one cycle of the rf drive is given by three independent harmonic oscillators with secular frequencies ω_u. The trapping potential is then effectively described by a static pseudopotential:

$$\Psi(x,y,z) = \frac{m}{2q}\left(\omega_x^2 x^2 + \omega_y^2 y^2 + \omega_z^2 z^2\right) \quad , \tag{2.8}$$

which is shown on the right side of Fig. 2.3. The secular frequencies from equation Eq. (2.7) are given by

$$\begin{aligned} \omega_{x,y} &= \sqrt{\frac{2q^2V_{\mathrm{rf}}^2}{m^2r_0^4\Omega^2} - \frac{1}{2}\omega_z^2 \pm \frac{2qU_{\mathrm{dc}}^r}{mr_0^2}} \quad , \\ \omega_z &= \sqrt{\frac{2q\kappa U_{\mathrm{dc}}^z}{mz_0^2}} \quad . \end{aligned} \tag{2.9}$$

For the Paul trap described in this thesis, no electrostatic contribution is added to the quadrupole potential, $U_{\mathrm{dc}}^r = 0$, and the pseudopotential is cylindrically symmetric with $\omega_x = \omega_y$. However, for small deviations from the ideal electrode geometry this degeneracy is cancelled again and the eigenfrequencies follow the hierarchy $\omega_z < \omega_x \simeq \omega_y$.

According to Eq. (2.6), the stability parameters a_u and q_u depend on the charge-to-mass ratio q/m of the ion. Due to the extended stability region (see Fig. 2.2), it

is possible to confine different ion species with similar q/m simultaneously in the same trapping potential. This will be used in the presented experiment to sympathetically cool highly charged ions (HCIs) by Coulomb interaction with co-trapped, directly laser-cooled $^9Be^+$ ions [Sch17] (see Sec. 2.2.3). Since the pseudopotential strongly depends on q and m, the ions will arrange themselves such that the ion species with higher q/m is positioned closer to the trap axis, thereby minimizing the total energy.

2.1.2 The real Paul trap

Deviations from the ideal Paul trap potentials described in Sec. 2.1.1 can be caused by non-ideal trap electrode geometries as well as manufacturing tolerances. Here, the possible effect of these imperfections on the motion of a trapped ion is discussed.

Axial confinement

Axial confinement of ions is achieved by endcap electrodes supplied with an electrostatic potential U_{dc}^z (see Fig. 2.1). The corresponding potential along the trap axis can be expanded around its minimum in a power series including higher order corrections to the harmonic confinement:

$$\Phi(z) = U_{\mathrm{dc}}^z \left(C_0 + C_2 z^2 + C_4 z^4 + C_6 z^6 + \dots \right) \quad . \tag{2.10}$$

The harmonic approximation of Eq. (2.4) is recovered for $C_2 = \kappa / z_0^2$. Accounting for the anharmonic contributions from Eq. (2.10), the resulting equation of motion is given by a nonlinear differential equation, a so-called Duffing equation [Moo87]:

$$\ddot{z} = -\frac{q}{m}\frac{\partial \Phi(z)}{\partial z} = -\frac{2qC_2U_{\mathrm{dc}}^z}{m}\left(z + \frac{2C_4}{C_2} z^3 + \frac{3C_6}{C_2} z^5 + \dots \right) \quad . \tag{2.11}$$

In the presence of non-vanishing anharmonicities C_4 and C_6, the eigenfrequency of the ion depends on its position along the trap axis and, therefore, also on its energy [Ulm11]. Including the first two perturbation orders, the dependency of the axial eigenfrequency ω_z on the axial energy, $E_z = m\omega_z^2 z^2/2$, is given by [Ulm11]:

$$\frac{\Delta\omega_z}{\omega_z} = \frac{3}{4}\left(\frac{C_4}{C_2^2} + \frac{5}{4}\frac{C_6}{C_2^3}\frac{E_z}{qU_{\mathrm{dc}}^z} \right) \frac{E_z}{qU_{\mathrm{dc}}^z} \quad . \tag{2.12}$$

Using an electrode geometry as shown in Fig. 2.1 with one set of dc electrodes at each side of the trap, it is possible to simultaneously reduce C_4 and C_6 to zero by optimizing the electrode geometries and distances. However, taking manufacturing tolerances into account, additional correction electrodes are required to compensate these anharmonic contributions. Additionally, the trap can be designed orthogonal by choosing adequate electrode geometries [Ulm11]. In this case, the voltage applied to the correction electrodes does not change the axial eigenfrequency.

The suppression of anharmonic contributions to the trapping potential is crucial for efficient coupling to the motion of the ion. It becomes especially relevant for the application of image current detection techniques [WD75] to measure the motional frequencies

of the ion in the trap. The feasibility to implement these techniques at the presented Paul trap experiment is discussed in Sec. 4.6. In order to minimize the anharmonicities of the electrode design and determine possible frequency shifts, simulations of the axial potential were performed (see Sec. 4.5.1).

Radial confinement

The quadrupole potential for the radial confinement of ions can be created by hyperbolic trap electrodes as shown in Fig. 2.1. This geometry is the natural choice, since the electrode surface follows the equipotential lines of the quadrupole. However, in order to allow for larger optical access to the trap center, the hyperbolic electrode geometry is usually modified. This deviation from the ideal geometry introduces higher-order contributions to the radial potential, which can be expanded as a multipole series [Den+15; Ped+10]:

$$\Phi_{\mathrm{QP}}(x, y, t) = A_0 + \sum_{n=1} A_n \phi_n \quad , \tag{2.13}$$

where ϕ_n represents a multipole with n poles. For symmetry reasons and including boundary conditions, only terms with $n = 2(2m + 1)$ and $m \in \{0, 1, 2, \dots\}$ contribute to this expansion [Den+15]. The first term, A_0, corresponds to the offset potential while the quadrupole contribution is given by the second term, A_2. The third term, A_6, represents the leading order anharmonicity and should be minimized in order for Φ_{QP} to resemble an ideal quadrupole potential.

The relative amplitude of the anharmonic terms in Eq. (2.13) depends on the distance from the symmetry axis $(x, y) = 0$. For example, the contribution from A_6 needs to be considered for radially extended ion crystals, while it is usually small for ion strings or small ion crystals close to the trap axis [Ped+10].

In case of circular trap electrodes, it has been shown that the leading-order anharmonicity A_6 vanishes for $r_e/r_0 = 1.14511$, where r_e describes the electrode radius [Reu+96]. For the blade electrode geometry developed in this thesis (see Sec. 4.2) with $r_e/r_0 = 0.51$, this was discarded to further increase optical access to the trap center. In order to exclude higher order contributions to the radial trapping potentials, the electrode geometries were optimized using simulations (see Sec. 4.5.1).

2.2 Atom-light interaction and manipulation of the ion motion

Confinement of ions as described in Sec. 2.1 typically allows to trap ions with energies of up to 10 % of the potential depth [Lei+03]. This corresponds to kinetic energies on the order of 1 eV or an ion temperature of 10^4 K. In order to reduce the kinetic energy, laser cooling is applied. Initial cooling after loading of ions into the trap is usually realized by Doppler cooling, which is then followed by more advanced cooling methods, e.g. sideband cooling. The ultimate goal is to cool the ion to the ground state of its secular motion.

Here, a brief description of the different cooling methods implemented in this thesis and intended for the presented experiment will be given.

2.2.1 Doppler cooling

Doppler cooling describes the cooling of atoms or ions by interaction with a directed light field, e.g. a laser. It is based on the momentum transfer caused during absorption and emission of single photons. Due to momentum conservation, each absorbed photon changes the ion momentum by one photon recoil in the propagation direction of the light field. The subsequent de-excitation by spontaneous emission and the corresponding momentum transfer is isotropic. Thus, the net recoil averaged over many emission processes is zero. This leads to a directed momentum transfer averaged over many absorption-emission cycles. Since the force exerted onto the ion by the laser depends on the ion velocity due to the Doppler effect, this can be used for cooling.

For neutral atoms, cooling of all motional degrees of freedom typically requires two counterpropagating laser beams along three spatial directions. This is different in ion traps, since the ion is bound to the confining trapping potential. Thus, it is sufficient to use a single laser beam to cool all motional modes to the Doppler limit, provided that the laser couples to all modes. At the presented experiment, the cooling laser enters the trap in the horizontal plane with an angle of 30° to the trap axis. This guarantees coupling to axial and radial degrees of freedom. Since the blade electrodes are tilted by 45° with respect to the horizontal plane (see Fig. 2.1), both radial modes along $\hat{x}$ and $\hat{y}$ are coupled to the cooling laser. The following discussion of Doppler cooling inside an rf ion trap is based on [Lei+03] and references therein.

In a simplified approach, the influence of micromotion is neglected and the ion motion inside the time-independent pseudopotential is treated non-relativistically. It is composed of three uncoupled harmonic oscillators, described by the secular frequencies $(\omega_x, \omega_y, \omega_z)$ (see Eq. (2.9)). If these eigenfrequencies are smaller than the linewidth Γ of the cooling transition, $\omega_u \ll \Gamma$, the ion velocity is approximately constant during one absorption and emission cycle. This is the case for the experiments described in this thesis using $^9Be^+$ ions, as the cooling transition with a wavelength of $\lambda \simeq 313\,\mathrm{nm}$ has a linewidth of $\Gamma/2\pi = 17.97\,\mathrm{MHz}$ [Kra+19]. This is larger than the typical axial and radial secular frequencies around 1 MHz. Therefore, the ion can be treated as a quasi-free particle and the interaction with the cooling light can be modeled as a continuous force that depends on the velocity of the ion.

The following description is reduced to one spatial dimension, where the photons are propagating either parallel or anti-parallel to the ion. Additionally, the ion is treated as an electronic two-level system with energy splitting $\Delta E = \hbar\omega_e$. The light wave with frequency ω_l is detuned with respect to the resonance frequency of the ion at rest by $\Delta = \omega_\mathrm{l} - \omega_e$. Due to the ion motion with velocity $\vec{v}$, the photon energy in the rest frame of the ion is shifted according to the Doppler effect. The effective detuning is given by

$$\delta_\mathrm{eff} = \Delta - \vec{k} \cdot \vec{v} \quad , \tag{2.14}$$

where $\vec{k}$ describes the wave vector of the light field. The photon scattering rate depends on the probability to populate the excited state, ρ_{ee}, and the excited state lifetime, Γ^{-1}. Averaged over many absorption and emission cycles, the force of the light field onto the ion is given by

$$\left(\frac{\mathrm{d}p}{\mathrm{d}t}\right)_a \simeq F_a = \hbar k \Gamma \rho_{\mathrm{ee}} \quad , \tag{2.15}$$

with the reduced Planck constant $\hbar = h/2\pi$. The probability to populate the excited state,

$$\rho_{\mathrm{ee}} = \frac{s/2}{1 + s + (2\delta_{\mathrm{eff}}/\Gamma)^2} \quad , \tag{2.16}$$

depends on the saturation parameter of the transition:

$$s = 2\frac{\Omega_{\mathrm{r}}^2}{\Gamma^2} = \frac{I}{I_s} \quad , \tag{2.17}$$

where Ω_{r} denotes the on-resonance Rabi frequency. It can also be expressed by the ratio of laser intensity I to saturation intensity I_s of the electronic transition. For an electronic two-level system connected by an electronic dipole transition, the saturation intensity is given by $I_s = \pi h c \Gamma / 3\lambda^3$ [Foo05].

For small velocities ($|\vec{k}\vec{v}| \ll \Gamma$), the force onto the ion can be linearized in v:

$$F_a \simeq F_0(1 + \beta v) \quad . \tag{2.18}$$

The velocity-independent term,

$$F_0 = \hbar k \Gamma \frac{s/2}{1 + s + (2\Delta/\Gamma)^2} \quad , \tag{2.19}$$

does not contribute to cooling and represents the averaged radiation pressure displacing the ion from the trap center. The second term features the friction coefficient

$$\beta = \frac{8k\Delta/\Gamma^2}{1 + s + (2\Delta/\Gamma)^2} \quad , \tag{2.20}$$

which causes damping of the ion motion in case of a red-detuned light field, $\Delta < 0$. Neglecting the statistical nature of absorption and emission processes, this would allow to cool the ion to zero energy. However, the ion constantly scatters photons even at $v = 0$ which causes momentum kicks of $\hbar k$. Although the emission is isotropic and the corresponding recoil is distributed symmetrically, $\langle \vec{p} \rangle = 0$, the randomness of the process causes diffusion, $\langle p^2 \rangle \neq 0$. Additional diffusion originates from the discreteness of the absorption processes occurring at random times. This leads to a random walk in momentum space similar to Brownian motion, and can be identified with a heating rate.

In thermal equilibrium, the minimum achievable ion temperature for small intensities ($s \ll 1$) is reached for $\Delta = -\Gamma\sqrt{1+s}/2$ and is given by

$$T_\mathrm{D} = \frac{\hbar\Gamma\sqrt{1+s}}{4k_\mathrm{B}}(1+\zeta) \quad , \tag{2.21}$$

where k_B describes the Boltzmann constant. The parameter ζ accounts for the different directionality of absorption and emission and equals to $\zeta = 2/5$ for electronic dipole transitions [Ste86]. In case of $^9\mathrm{Be}^+$ the Doppler limit is $T_\mathrm{D} = 302\,\mu\mathrm{K}$.

So far, the influence of micromotion on the cooling process was completely neglected. However, for trap drive frequencies $\Omega \gtrapprox \Gamma$, the electronic excitation spectrum of the ion shows additional sidebands due to micromotion. This is the case for the ion trap developed in this thesis, where a trap drive frequency of $\Omega/2\pi \simeq 34.52\,\mathrm{MHz}$ is used. Taking micromotion into account, the excitation spectrum of the ion features a strong carrier transition at the Doppler cooling wavelength, and additional sidebands at frequencies $n\Omega \pm \omega_u$ with $n \in \mathbb{Z}$. All sidebands at $n\Omega + \omega_u$ lead to heating even though the laser might be red-detuned from the cooling transition. This additional heating might prevent cooling all the way to the Doppler limit stated in Eq. (2.21). However, since the sideband coupling strength can be reduced by micromotion compensation, the minimum temperature T_D still represents a good estimate for a well-compensated trap [Lei+03].

The total energy of the ion inside the harmonic pseudopotential of the Paul trap is composed of equal amounts of potential and kinetic energy, according to the virial theorem. Thus, the energy per degree of freedom amounts to $E_i = 2 \times k_\mathrm{B}T_i/2$. The corresponding mean phonon number $\langle n_i \rangle$ of the motional mode ω_i is given by [WI79]

$$E_i = k_\mathrm{B}T_i = \hbar\omega_i\left(\langle n_i\rangle + 1/2\right) \quad . \tag{2.22}$$

In case of $^9\mathrm{Be}^+$, cooling all modes to the Doppler limit results in $\langle n_i \rangle \simeq 6.3\,\mathrm{MHz}/\nu_i$. Accounting for power broadening of the cooling transition ($s > 0$) and typical secular frequencies on the order of 1 MHz, it is not possible to reach $\langle n_i \rangle < 1$ using Doppler cooling. Therefore, sideband cooling will be employed at the presented experiment to cool the ions to the motional ground state.

2.2.2 Resolved sideband cooling

Resolved sideband cooling represents a method to cool trapped ions far below the Doppler limit and allows to prepare them in the quantum mechanical ground state of their motion. Here, a brief summary of the main aspects will be given, following the description in [Win+98a; Lei+03].

The motion of an ion confined inside a Paul trap can be approximated by three uncoupled harmonic oscillators. The spacing of the equidistant energy levels, $E_n = \hbar\omega_i(n_i + 1/2)$, is given by the secular frequencies ω_i. Besides these external eigenstates, the ion has an internal electronic structure which is again approximated by a two-level system with energy splitting $\hbar\omega_e$. The total energy level structure of a confined ion inside the Paul trap consists of the motional states which are superimposed with the

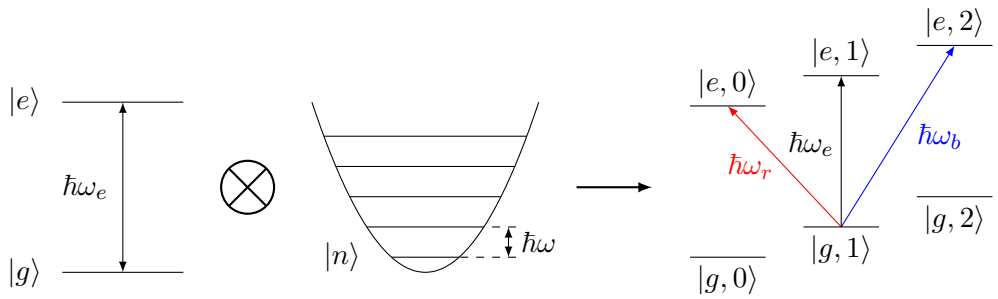

Figure 2.4: Schematic drawing of the coupled energy levels of an atomic two-level system bound to a one-dimensional harmonic potential (not to scale). The combined energy levels are given by the product state of the electronic states ($|g\rangle, |e\rangle$) and the motional state $|n\rangle$ with phonon number n. Here, the case of resolved motional sidebands is depicted, which requires a small electronic transition linewidth ($\Gamma \ll \omega$). Transitions between the electronic ground state $|g, n\rangle$ and excited state $|e, n + \Delta n\rangle$ are called red sidebands ($\Delta n < 0$, $\omega_r = \omega_e + \omega\Delta n$), blue sidebands ($\Delta n > 0$, $\omega_b = \omega_e + \omega\Delta n$) or carrier transitions ($\Delta n = 0$, ω_e).

internal structure, as shown in Fig. 2.4. The following description of resolved sideband cooling is reduced to one motional mode ω, if not stated differently.

Three different types of transitions of the coupled system can be driven using a light field. Transitions between energy levels with equal motional quantum number n are called carrier transitions. Additionally, so-called sidebands allow to reduce (red) or increase (blue) the motional quantum number of the ion. The coupling strength of a transition between two motional levels $|n\rangle$ and $|n + m\rangle$ can be expressed as

$$\Omega_{n,n+m} = \Omega e^{-\eta^2/2}\, \eta^{|m|} \sqrt{\frac{n_<!}{n_>!}}\, L_{n_<}^{|m|}\left(\eta^2\right) \quad , \tag{2.23}$$

where the Rabi frequency of the carrier transition is given by Ω. Here, $n_{\lessgtr}$ denote the lesser and greater number of n and $n+m$, respectively, and L is the generalized Laguerre polynomial. The coupling strength of the sideband transitions depends on the Lamb-Dicke parameter, $\eta = kz_0$. It defines the ratio of the spatial extent of the motional ground state wavefunction, $z_0 = \sqrt{\hbar/(2m\omega)}$, to the wavelength of the transition, $\lambda = 2\pi/k$.

If the extension of the motional wavefunction $|\Psi_\mathrm{m}\rangle$ is much smaller than $1/k$, the Lamb-Dicke criterion is satisfied: $\sqrt{\langle\Psi_\mathrm{m}|kz|\Psi_\mathrm{m}\rangle} \ll 1$. In the Lamb-Dicke regime, the ion experiences a uniform electric field from the interacting radiation and $\eta \ll 1$ holds. Therefore, all transitions changing the motional quantum number by more than one are strongly suppressed. This allows for efficient cooling to the motional ground state, since the recoil by scattered photons does not change the motional state of the ion and is absorbed by the trap. Driving the first-order red sideband transition incrementally reduces the motional quantum number n and thereby cools the ion.

In case of large Lamb-Dicke parameters $\eta \leq 1$, the coupling strength of the sideband transitions becomes comparable to the carrier and higher order sidebands need to be considered. Accordingly, spontaneous emission on motional sidebands is no longer suppressed. Therefore, ground state cooling in this case requires the application of higher order sidebands to counteract motional recoil heating [Yu+18].

As a pre-requisite for the cooling scheme described above, the motional sidebands of the cooling transition need to be resolved, which allows to address distinct sideband transitions individually. This requires the linewidth of the driving radiation as well as the linewidth of the atomic transition to be much smaller than the secular frequency. Since $^9Be^+$ does not offer such a transition, stimulated Raman transitions between the ground state hyperfine levels separated by 1250 MHz can be used for resolved sideband cooling [Win+03].

The Lamb-Dicke parameters for the three motional modes are given by [Leo18]

$$\eta_i = \sum_i \Delta\vec{k} \cdot \hat{x_i}\, z_{0,i} \quad \text{with } i \in \{x, y, z\} \quad . \tag{2.24}$$

Here, $z_{0,i}$ denotes the wavepacket extension in the ground state of mode ω_i and the difference of the two Raman beam wavevectors is given by $\Delta\vec{k} = \vec{k}_1 - \vec{k}_2$. The small mass of beryllium results in large Lamb-Dicke parameters, e.g. $\eta \simeq 0.62\sqrt{2\pi\text{MHz}/\omega_i}$ in case of parallel Raman beams, $\Delta\vec{k} \cdot \hat{x_i} = k_1 - k_2$. Therefore, high secular frequencies on the order of 1 MHz are required for sideband cooling to the motional ground state.

2.2.3 Sympathetic cooling

Efficient Doppler cooling (see Sec. 2.2.1) requires a short-lived excited state ($\Gamma^{-1} \simeq 10\,\text{ns}$) which exhibits a transition in the laser-accessible wavelength range. Additionally, in order to simplify the cooling scheme, a simple electronic level structure with a closed or quasi-closed transition, e.g. involving an additional repumping laser, is needed. Since HCIs generally lack such transitions [Koz+18], sympathetic cooling is employed. To this end, HCIs are confined together with a second ion species, which can be directly laser-cooled, inside the same trapping potential. Due to the strong Coulomb interaction between the two species, the ions share common modes of motion. This allows to cool the HCI by performing laser-cooling on the co-trapped cooling ions.

The crucial parameter for sympathetic cooling inside a Paul trap is the charge-to-mass ratio q/m of the involved ions. It defines the position inside the stability diagram (see Fig. 2.2) and, therefore, determines the range of HCIs that can be trapped together with the cooling ion. At the presented experiment, the use of $^9Be^+$ as the cooling ion allows to sympathetically cool a broad range of HCIs inside a Paul trap [Sch17].

2.3 Radio-frequency cavities

This section gives an overview of the basic characteristics of rf cavities. Starting with a description of the electrodynamic properties, the relevant figures of merit are introduced

in Sec. 2.3.1 based on [PHK98]. Subsequently, using a lumped element model of rf cavities (Sec. 2.3.2), the main experimental techniques for characterization (Sec. 2.3.3) and impedance matching (Sec. 2.3.4) employed during this thesis are discussed.

2.3.1 Radio-frequency cavity fundamentals

In general, rf cavities are resonant structures made of electrically conducting material enclosing an inner volume. The electromagnetic (em) fields inside the cavity are derived from the wave equation [Jac07],

$$\left(\Delta - \frac{1}{c^2}\frac{\partial^2}{\partial t^2}\right)\begin{pmatrix}\vec{E}\\ \vec{H}\end{pmatrix} = 0 \quad , \tag{2.25}$$

where $\vec{E}$ and $\vec{H}$ denote the electric and magnetic field, respectively, and the speed of light is given by c. At physical boundaries and interfaces between different materials, solutions to Eq. (2.25) are subject to boundary conditions [Jac07]:

$$\begin{aligned} \vec{n}_1 \times (\vec{D}_2 - \vec{D}_1) = 0 \quad , \qquad & \vec{n}_1 \cdot (\vec{D}_2 - \vec{D}_1) = \rho \quad , \\ \vec{n}_1 \cdot (\vec{H}_2 - \vec{H}_1) = 0 \quad \text{and} \quad & \vec{n}_1 \times (\vec{H}_2 - \vec{H}_1) = \vec{j} \quad . \end{aligned} \tag{2.26}$$

Here, $\vec{n}_i$ is the unit normal to the respective surface, ρ denotes the surface charge density, $\vec{j}$ represents the surface current density and $\vec{D}$ is the electric displacement field. In principle, an rf cavity can sustain an infinite number of resonant modes. For simple geometries, e.g. pillbox cavities, the resonance frequency and the corresponding mode-structure of the em fields can be calculated analytically [Cio15]. For more complex geometries, simulations are required. The resonant modes of the cavity developed in this thesis are determined using finite element method (FEM) simulations, which are presented in Sec. 4.4.1. There, the main focus is on the quadrupole resonant mode which can be used to radially confine ions as described in Sec. 2.1.

When excited with an rf signal close to its resonance, the em energy stored inside the cavity increases steadily until the rf losses are equal to the input power. The energy density u inside the cavity is given by the sum of the electric and magnetic contributions:

$$u = \frac{1}{2}\left(\epsilon\vec{E}^2 + \mu\vec{H}^2\right) \quad , \tag{2.27}$$

where the permeability ϵ and permittivity μ of the material are introduced. The stored energy is transferred periodically between the electric and the magnetic fields of the cavity. The time-averaged total energy U can be expressed as:

$$U = \int_V \frac{1}{2}\mu|\vec{H}|^2 \mathrm{d}^3r = \int_V \frac{1}{2}\epsilon|\vec{E}|^2 \mathrm{d}^3r \quad . \tag{2.28}$$

In order to characterize the losses inside the cavity, the quality factor Q_0 is introduced. It is formally defined as the ratio of the stored em energy to the dissipated power P_d per cycle of the rf field:

$$Q_0 = \frac{\omega_0 U}{P_\mathrm{d}} \quad , \tag{2.29}$$

where ω_0 denotes the resonance frequency of the cavity. The dissipated power is the sum of all individual losses inside the cavity. This includes, for example, resistive losses inside the cavity surface or dielectric losses originating from dissipation inside dielectric materials. The overall quality factor is given by the inverse sum of the individual contributions:

$$P_\mathrm{d} = \sum_n P_{\mathrm{d},n} \quad , \qquad \frac{1}{Q_0} = \sum_n \frac{1}{Q_n} \quad . \tag{2.30}$$

Therefore, all loss mechanisms need to be evaluated carefully and reduced to the same level. For the cavity developed in this thesis, the typical loss mechanisms of rf cavities are discussed in Sec. 4.4.2.

The dissipated power of the cavity depends on the surface resistance R_s, which will be described in Sec. 2.4.2. The resistive losses are given by the surface integral over the cavity walls:

$$P_\mathrm{d} = \frac{1}{2}\int_S R_s |\vec{H}|^2 \mathrm{d}^2 r \quad . \tag{2.31}$$

The quality factor is then given by

$$Q_0 = \frac{\omega_0 \mu \int_V |\vec{H}|^2 \mathrm{d}^3 r}{\int_S R_s |\vec{H}|^2 \mathrm{d}^2 r} \simeq \frac{G}{R_s} \quad , \tag{2.32}$$

and depends on the geometry as well as the material of the cavity. By approximating the surface resistance to be constant, one can separate both contributions to the quality factor. This allows to define the geometry factor G, which is independent of the size and the material of the cavity and depends only on its shape and the em mode. Since the surface resistance characterizes the material-dependent resistive losses, it is one of the most important figures of merit for rf cavities. A detailed discussion of the surface resistance is given in Sec. 2.4.2.

2.3.2 Lumped element circuit

Around an isolated resonance, the properties of an rf cavity can be modelled by a lumped element circuit as shown in Fig. 2.5 [MDP48]. The equivalent LCR parallel circuit consists of an inductance L, a capacitance C and a resistor R_p, which accounts for the resistive losses of inductance (R_L) and capacitance (R_C). When excited with an rf signal, the voltage drop U over R_p is defined by the differential equation [AL05]

$$\ddot{U} + \frac{1}{R_\mathrm{p} C}\dot{U} + \frac{1}{LC}U = 0 \quad . \tag{2.33}$$

This describes a damped harmonic oscillator with damping constant $\gamma = (2R_\mathrm{p}C)^{-1}$, free resonance frequency $\omega_0^2 = (LC)^{-1}$ and damped eigenfrequency $\omega_d^2 = \omega_0^2 - \gamma^2$. Here, only the case of small damping ($\gamma \ll \omega_0$) will be considered, which corresponds to small

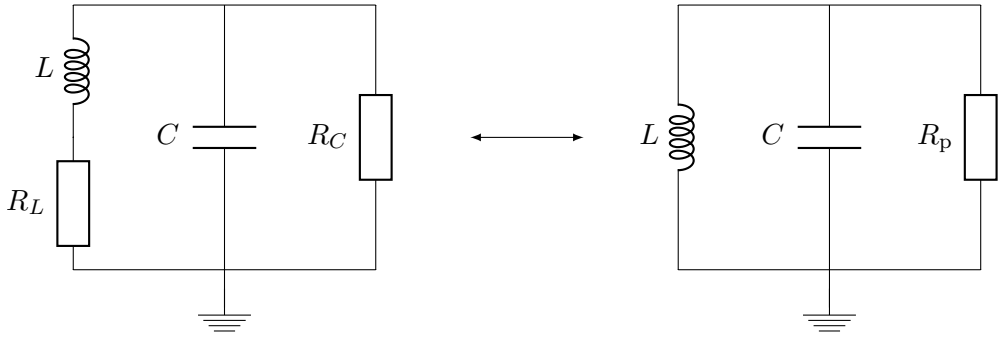

Figure 2.5: Lumped element circuit of an rf cavity around an isolated resonance. **Left:** The real *LCR* parallel circuit is shown, which includes the losses of inductance (R_L) and capacitance (R_C). **Right:** The equivalent *LCR* parallel circuit accounts for the losses by R_p.

resistive losses of the resonant circuit. In this approximation, the quality factor can be expressed as

$$Q_0 = \frac{\omega_0}{2\gamma} = \frac{R_\mathrm{p}}{\omega_0 L} \quad . \tag{2.34}$$

This allows to experimentally determine the quality factor of the resonance by measuring the decay of the stored em energy. Using Eq. (2.34), the total impedance of the equivalent circuit is given by

$$\begin{aligned} Z_\mathrm{cav} &= \left(R_\mathrm{p}^{-1} + (\mathrm{i}\omega L)^{-1} + \mathrm{i}\omega C\right)^{-1} \\ &= R_\mathrm{p}\left(1 + \mathrm{i}Q_0\left(\frac{\omega}{\omega_0} - \frac{\omega_0}{\omega}\right)\right)^{-1} \quad . \end{aligned} \tag{2.35}$$

This basic model of rf cavities will be used in the following to discuss coupling to the cavity as well as impedance matching of the cavity to an external circuit.

2.3.3 Coupling to the cavity

In order to drive the rf cavity, it can be connected to an external electrical circuit using rf couplers, e.g. antennas. The transmitted or reflected power from such so-called ports can be calculated using the scattering matrix formalism [Cas12; Dit00], where the voltage and current at any port i of the cavity are given by:

$$\begin{aligned} U_i &= \sqrt{Z_0}\left(a_i \mathrm{e}^{\mathrm{i}kz} + b_i \mathrm{e}^{-\mathrm{i}kz}\right) \quad , \\ I_i &= \frac{1}{\sqrt{Z_0}}\left(a_i \mathrm{e}^{\mathrm{i}kz} - b_i \mathrm{e}^{-\mathrm{i}kz}\right) \quad . \end{aligned} \tag{2.36}$$

Here, $a_i\sqrt{Z_0}$ and $b_i\sqrt{Z_0}$ denote the voltage amplitude of the incident and reflected wave, respectively. The impedance of the external circuit is denoted with Z_0 and is typically

equal to 50 Ω. The relation between the incident and reflected rf signals at different ports is given by the scattering matrix $\hat{S}$:

$$\vec{b} = \hat{S}\vec{a} \quad \text{with} \quad S_{ij} = \frac{b_i}{a_j} \quad . \tag{2.37}$$

Elements with $i = j$ describe reflection at the corresponding port, whereas entries with $i \neq j$ describe transmission from port j to port i. For a system with N ports, $\hat{S}$ has the dimension $N \times N$. Each port couples to the cavity and introduces losses to the system. At resonance, the dissipated power in port i can be parametrized by $P_{\mathrm{d},i} = \omega_0 U/Q_i$ (see Eq. (2.29)). Including these external losses, the loaded quality factor of the cavity is given by

$$\frac{1}{Q} = \frac{1}{Q_0} + \sum_{n=1}^{N} \frac{1}{Q_n} \quad , \tag{2.38}$$

where the unloaded quality factor Q_0 includes only the internal losses of the cavity as described by Eq. (2.30). Using the scattering matrix formalism, the coupling between two ports at frequency ω can be expressed by

$$S_{ij} = \delta_{ij} - \frac{2\sqrt{Q^2(Q_iQ_j)^{-1}}}{2\mathrm{i}Q\left(\frac{\omega}{\omega_0} - 1\right) + 1} \simeq \delta_{ij} - \frac{2\sqrt{Q^2(Q_iQ_j)^{-1}}}{\mathrm{i}Q\left(\frac{\omega}{\omega_0} - \frac{\omega_0}{\omega}\right) + 1} \quad , \tag{2.39}$$

where δ_{ij} denotes the Kronecker delta and the approximation $(\omega - \omega_0)/\omega_0 \ll 1$ was used. If one port dominates the external losses in Eq. (2.38), the system can be approximated by a single port description. The reflected signal in this case is described by

$$S_{11} = 1 - \frac{2k}{\mathrm{i}Q_0\left(\frac{\omega}{\omega_0} - \frac{\omega_0}{\omega}\right) + k + 1} \quad , \tag{2.40}$$

where the coupling parameter $k = Q_0/Q_1$ was introduced. Its absolute value is given by

$$|S_{11}| = \frac{\sqrt{(k-1)^2 + Q_0^2\left(\frac{\omega}{\omega_0} - \frac{\omega_0}{\omega}\right)^2}}{\sqrt{(k+1)^2 + Q_0^2\left(\frac{\omega}{\omega_0} - \frac{\omega_0}{\omega}\right)^2}} \quad . \tag{2.41}$$

Typical reflection spectra are shown in the left panel of Fig. 2.6 for different coupling parameters k. The reflected power at resonance vanishes for $k = 1$, which corresponds to the case of perfect impedance matching between cavity and external circuit. This can be seen using another derivation of S_{11}, which will be briefly discussed here.

The impedance of the cavity Z_{cav} can be expressed in terms of the incident and reflected wave amplitudes given in Eq. (2.36):

$$Z_{\mathrm{cav}} = \frac{U_1}{I_1} = Z_0 \frac{a_1 + b_1}{a_1 - b_1} \quad . \tag{2.42}$$

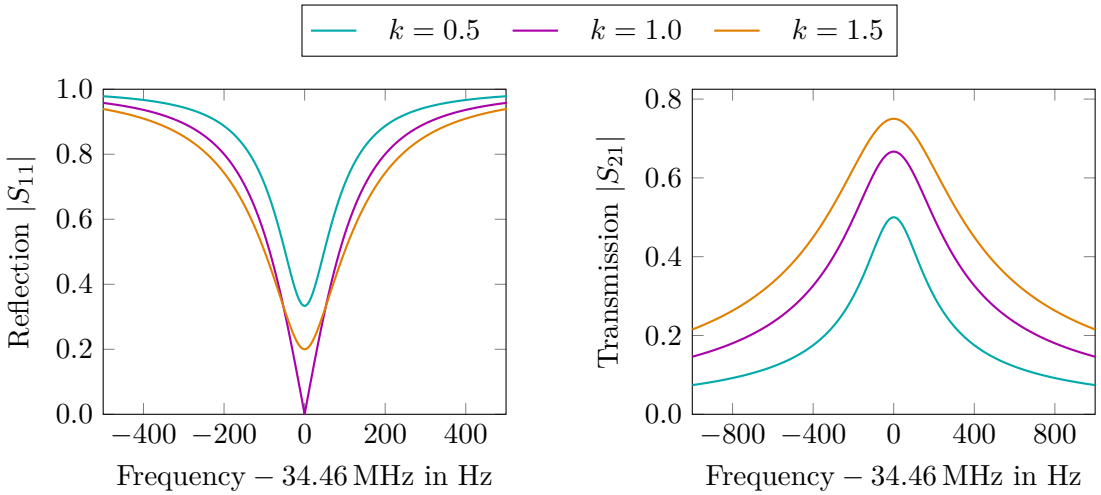

Figure 2.6: Calculated reflection and transmission spectra for a cavity with an unloaded quality factor $Q_0 = 2.3 \times 10^5$ and resonance frequency $\omega_0/2\pi = 34.46\,\mathrm{MHz}$. Different colors represent different coupling constants: $k = 0.5$ (cyan), $k = 1.0$ (magenta) and $k = 1.5$ (orange). **Left:** The reflection $|S_{11}|$ in single port approximation is shown. **Right:** The transmission $|S_{21}|$ is shown for the case of two ports with identical coupling constant.

This yields another expression for the reflected signal:

$$S_{11} = \frac{b_1}{a_1} = \frac{Z_{\mathrm{cav}}/Z_0 - 1}{Z_{\mathrm{cav}}/Z_0 + 1} \quad . \tag{2.43}$$

In the case of an isolated resonance, which is considered here, Z_{cav} is given by Eq. (2.35). Inserting this into Eq. (2.43) yields an expression for $|S_{11}|$ which is identical to Eq. (2.41) for $k = R_{\mathrm{p}}/Z_0$. Thus, $k = 1$ corresponds to equal impedances of the external circuit and the cavity at resonance. The experimental realization of impedance matching employed for the cavity presented in this thesis will be discussed in Sec. 2.3.4.

In the case where several ports are coupled to the cavity, the transmission between port i and port j is given by:

$$|S_{ij}| = \frac{2\sqrt{Q^2\left(Q_i Q_j\right)^{-1}}}{\sqrt{1 + Q^2\left(\frac{\omega}{\omega_0} - \frac{\omega_0}{\omega}\right)^2}} \quad , \quad i \neq j \quad , \tag{2.44}$$

which is shown in the right panel of Fig. 2.6. In contrast to the single port approximation, it is in general not possible to determine the unloaded quality factor Q_0 by measuring the transmission. This is due to the fact that the measurement itself draws some fraction of stored em energy from the cavity and thereby introduces losses to the system. In the case of strong coupling, $Q_{i,j} \geq Q_0$, these losses cannot be neglected and the loaded quality

factor will be significantly smaller than the unloaded one. Only for very weak coupling, $Q_{i,j} \gg Q_0$, the transmission measurement yields a good approximation of the unloaded quality factor. However, the transmitted signal amplitude decreases accordingly (see Fig. 2.6).

The described behaviour of an rf cavity in reflection and transmission is used to characterize the cavity presented in this thesis. This allows to determine its rf properties, in particular its quality factor and resonance frequency, as well as to quantify the coupling strength of the employed rf couplers.

2.3.4 Impedance matching

According to Eq. (2.35), the cavity impedance at resonance is given by R_p, which scales directly with the quality factor, $R_\mathrm{p} \propto Q_0$. Typical values for superconducting rf cavities employed at ion-trap experiments range from MΩ to GΩ, e.g. [Ulm+09]. This is much larger than the impedance of the rf source, which is usually 50 Ω. In order to efficiently drive the cavity and ensure that only a minor fraction of the supplied power is reflected, the impedance of the cavity needs to be matched to the impedance of the source (see Eq. (2.41)).

Impedance matching of a high-Q resonant circuit can be achieved by different methods, e.g. impedance matching networks such as so-called L circuits [Poz12]. The impedance of the cavity developed in this thesis is transformed using an inductive coil, which couples to the magnetic field inside the cavity. By adjusting the coupling strength, the transformed cavity impedance can be matched to the source impedance. This is described in the following, based on [Gri86; Sla46].

Around its resonance frequency, the cavity with inductive coupling can be modeled by a series circuit of the coupling coil with self-inductance L_c and the parallel LCR circuit of the cavity (see Fig. 2.7). The input impedance is given by

$$Z_\mathrm{in} = \mathrm{i}\omega L_\mathrm{c} + R_\mathrm{in}\left(1 + \mathrm{i}Q_0\left(\frac{\omega}{\omega_0} - \frac{\omega_0}{\omega}\right)\right)^{-1} \quad . \tag{2.45}$$

The parallel resistance of the free cavity R_p is transformed by the inductive coupling to R_in, as seen from the external circuit. This can, in general, be much smaller than R_p and depends on the coupling strength. In order to derive an expression for R_in, purely resonant excitation of the cavity will be considered in the following.

For a given current amplitude I_0 of the rf drive, the maximum voltage drop over Z_in is given by

$$U_0 = R_\mathrm{in} I_0 + \mathrm{i}\omega_0 L_\mathrm{c} I_0 \quad . \tag{2.46}$$

Another expression for the voltage U_0 can be obtained by analyzing the voltage drop over the coupling coil. During operation, the coil couples to the oscillating magnetic fields inside the cavity. The temporal change of the enclosed magnetic flux Φ_mag induces a voltage drop over the coil:

$$U_\mathrm{ind} = -\frac{\mathrm{d}\Phi_\mathrm{mag}}{\mathrm{d}t} = \omega_0 B_0 N A_\mathrm{c} \cos(\gamma) \quad . \tag{2.47}$$

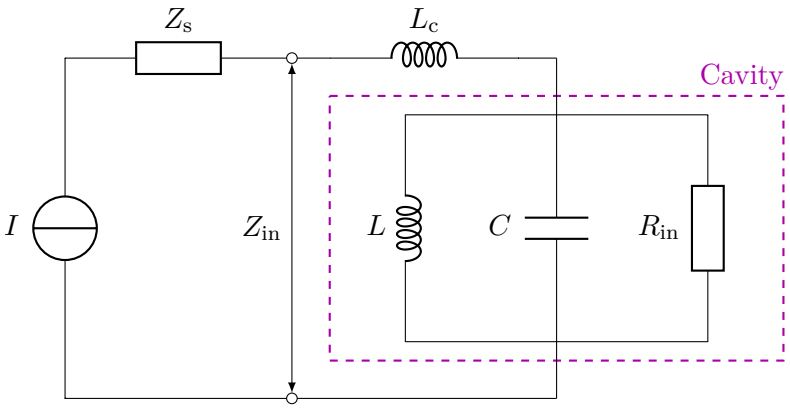

Figure 2.7: Equivalent circuit of an inductively coupled cavity with input impedance Z_in connected to an external current source I with impedance Z_s. The cavity is modeled by an LCR resonant circuit (dashed box). The input resistance R_in of the cavity is transformed by the coupling coil with self-inductance L_c.

It depends on the number of windings N and the area A_c of the coil, the average magnetic field amplitude inside the coil B_0 and the angle $\gamma = \sphericalangle(\vec{B}, \vec{A}_\mathrm{c})$ between magnetic field vector and surface normal.

Additionally, the current causes a voltage drop over the coupling inductance. This yields the total voltage drop over Z_in:

$$U_0 = U_\mathrm{ind} + \mathrm{i}\omega_0 L_\mathrm{c} I_0 \quad . \tag{2.48}$$

This expression has to be identical to the result from Eq. (2.46). Using the relation of dissipated power and quality factor from Eq. (2.29),

$$P_\mathrm{d} = \frac{1}{2} R_\mathrm{in} I_0^2 = \frac{\omega_0 U}{Q_0} \quad , \tag{2.49}$$

one finds the following expression for the transformed real part of the cavity impedance at resonance:

$$R_\mathrm{in} = \frac{1}{2}\omega_0 N^2 A_\mathrm{c}^2 \frac{B_0^2}{U} Q_0 \cos^2\gamma \quad . \tag{2.50}$$

By adjusting the angle between the inductive coil and the magnetic field, the input resistance can be varied between $R_\mathrm{in} = 0$ and the maximum value, which depends on the geometry of the coil and the em fields inside the cavity. The value B_0^2/U is independent of the stored energy inside the cavity and can be determined by simulations. For a given coil geometry, the coupling strength can be tuned by adjusting the angle γ. This can be seen in Fig. 2.8, where the input impedance Z_in is shown as a function of frequency and coil orientation γ.

For impedance matching, the total impedance Z_in needs to match the real impedance of the voltage source Z_s, i.e. $\Re(Z_\mathrm{in}) = Z_\mathrm{s}$ and $\Im(Z_\mathrm{in}) = 0$. This yields two conditions for

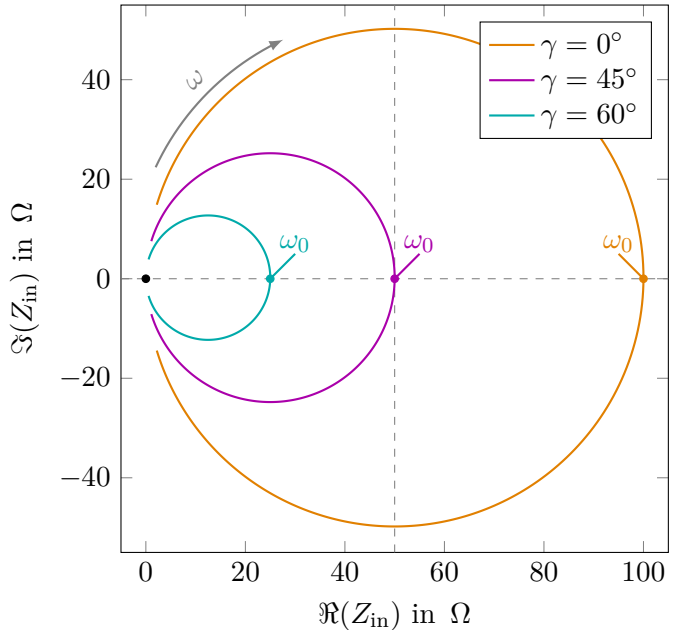

Figure 2.8: Transformed input impedance Z_{in} of a cavity with $Q_0 = 2.3 \times 10^5$ and $R_{\text{in}}/\cos^2\gamma = 100\,\Omega$ as a function of frequency around its resonance $\omega_0/2\pi = 34.46\,\text{MHz}$. Different colors represent different angles γ of the inductive coupling coil. The frequency increases by following the curves clockwise, while the point at $\Re(Z_{\text{in}}) = \Im(Z_{\text{in}}) = 0$ corresponds to $\omega = 0$ and $\omega = \infty$. At resonance, the real part of the cavity impedance $\Re(Z_{\text{in}})$ is maximized, which is shifted from the $\Im(Z_{\text{in}}) = 0$ axis by $\omega_0 L_{\text{c}}$ (not considered here). In this example, impedance matching to a typical source impedance of $50\,\Omega$ (marked by the intersection of the dashed lines) is achieved for $\gamma = 45°$.

impedance matching:

$$\begin{aligned} \omega_{\text{m}} &= \omega_0 \left(1 - \frac{\omega_0 L_{\text{c}}}{2 Q_0 Z_{\text{s}}}\right)^{-1} \quad , \\ R_{\text{in}} &= Z_{\text{s}} \left(1 + \left(\frac{\omega_{\text{m}} L_{\text{c}}}{Z_{\text{s}}}\right)^2\right) \quad , \end{aligned} \tag{2.51}$$

where the approximation $(\omega - \omega_0)/\omega_0 \ll 1$ was employed. Thus, the cavity has to be detuned from the resonance and operated at the impedance-matched frequency ω_{m}. This is usually close to ω_0 as the self-inductance of the coupling coil is small, $\omega_0 L_{\text{c}} < 1\,\Omega$. Furthermore, the transformed resistance of the cavity R_{in} has to be chosen larger than the source impedance Z_{s}.

The described scheme for impedance matching will be employed for the presented rf cavity. Therefore, the inductive coupler was designed based on Eq. (2.50), which defines the coil geometry for impedance matching, depending on the cavity parameters.

2.4 Radio-frequency superconductivity

The rf cavity developed in this thesis is made of niobium, which becomes superconducting below 9.25 K [Fis+05]. In the superconducting state, resistive losses inside the material are drastically reduced which suppresses power dissipation. In principle, this allows to reach quality factors on the order of $Q_0 \simeq 10^{10}$ [Res+17].

This section covers the basic relations and scaling laws that are needed to design and characterize a superconducting cavity. Starting with a phenomenological description, the theoretical foundations of superconductivity are presented in Sec. 2.4.1 based on [Tin96]. Subsequently, the specific features of rf superconductivity will be discussed, following the description in [CAS89; Tin96; Kno97; PHK98; Kle17]. Here, the main focus is on two characteristics of superconductors that are of major interest for the development of rf cavities: the surface resistance (Sec. 2.4.2) and the critical magnetic fields (Sec. 2.4.3).

2.4.1 Introduction to superconductivity

Superconducting materials exhibit a different behaviour compared to normal conductors when cooled below their critical temperature T_c. The two most distinct features are perfect dc conductivity, giving rise to the name, and perfect diamagnetism, also known as the Meissner-Ochsenfeld effect [MO33]. These two properties are well-described by the two London equations [LL35].

The first London equation relates any electric field $\vec{E}$ inside the superconductor to a temporal change of superconducting current density $\vec{j}_s$ [LL35]:

$$\frac{\partial}{\partial t}\vec{j}_s = \frac{\vec{E}}{\mu_0 \lambda_L^2} \quad , \tag{2.52}$$

with the vacuum permeability μ_0. Here, the London penetration depth

$$\lambda_L = \sqrt{\frac{m_s}{\mu_0 n_s q_s^2}} \tag{2.53}$$

is introduced as a phenomenological parameter depending on the charge q_s, mass m_s and density n_s of the superconducting charge carriers. In the dc case, the first London equation, Eq. (2.52), describes charge transport without resistance, since any electric field $\vec{E}$ accelerates the superconducting charge carriers. This is fundamentally different from charge transport in normal conductors as described by Ohm's law [Jac07]:

$$\vec{j}_n = \sigma_n \vec{E} \quad . \tag{2.54}$$

Here, the electric field preserves the normal current density $\vec{j}_n$ and, thereby, also the velocity of the normal charge carriers with conductivity σ_n. In the case of time-dependent currents in superconductors, the electrical resistance is generally larger than zero. This will be discussed in Sec. 2.4.2.

The second London equation is given by [LL35]

$$\vec{\nabla} \times \vec{j}_s = -\frac{\vec{B}}{\mu_0 \lambda_L^2} \quad , \tag{2.55}$$

where $\vec{B}$ describes the magnetic flux density inside the superconductor. According to the Meissner-Ochsenfeld effect, any external magnetic field will be expelled from the superconductor by shielding currents $\vec{j}_s$. However, Eq. (2.55) shows that these shielding currents require the presence of some magnetic field inside the material. This can be seen by inserting the Maxwell equation $\vec{\nabla} \times \vec{B} = \mu_0 \vec{j}_s$ [Jac07] into Eq. (2.55). The magnetic field component B_z parallel to the surface of a superconductor expanding into $x > 0$ is then given by:

$$\frac{\mathrm{d}^2}{\mathrm{d}x^2} B_z(x) = \frac{1}{\lambda_L^2} B_z(x) \quad . \tag{2.56}$$

This describes an exponential decay of the magnetic field and the shielding current inside the superconductor:

$$B_z(x) = B_0 \, \mathrm{e}^{-x/\lambda_L} \quad , \quad j_{s,y}(x) = j_{s,0} \, \mathrm{e}^{-x/\lambda_L} \quad , \tag{2.57}$$

where the characteristic decay length is given by the London penetration depth. However, experimental investigations of rf field penetration in superconductors yield penetration depths λ that are always larger than λ_L. This discrepancy was resolved using a nonlocal description of the second London equation, which accounts for the spatial extent of the superconducting charge carrier wavefunction by introducing the coherence length ξ_0 [PB53]. If the vector potential inside the superconductor decreases considerably over length scales $\lambda \ll \xi_0$, the supercurrent response is weakened, leading to increased penetration depths. Additionally, in order to account for scattering from impurities, which are characterized by the mean free path l, the effective coherence length ξ is introduced [PB53; Tin96]:

$$\frac{1}{\xi} = \frac{1}{l} + \frac{1}{\xi_0} \quad . \tag{2.58}$$

The coherence length ξ_0 can be estimated using an uncertainty principle argument [PB53; Tin96] by taking into account that only electrons within the range of $k_\mathrm{B} T_\mathrm{c}$ from the Fermi energy $E_F = \frac{1}{2} m_e v_\mathrm{F}^2$ can contribute to a process setting in at temperature T_c. This defines the characteristic length scale of the wavefunction:

$$\xi_0 \propto \Delta x \simeq \frac{\hbar}{\Delta p} = \frac{\hbar v_\mathrm{F}}{k_\mathrm{B} T_\mathrm{c}} \quad , \tag{2.59}$$

which is identical to the result obtained within the Bardeen–Cooper–Schrieffer (BCS) theory [BCS57b] up to a numerical factor.

For penetration depths $\lambda \gg \xi_0$ and a mean free path $l \gg \xi_0$, one recovers the result from the London theory: $\lambda = \lambda_L$. In the case of $\lambda \ll \xi_0$, the effective penetration depth

is increased and depends on the mean free path, since the scattering on defects reduces the shielding [PB53]:

$$\lambda \simeq \begin{cases} 0.65(\lambda_L^2 \xi_0)^{1/3} & \text{for } l \gg \xi_0 \\ \lambda_L \sqrt{1 + \dfrac{\xi_0}{l}} & \text{for } l \ll \xi_0 \end{cases} \quad . \tag{2.60}$$

Following these phenomenological models, a microscopic description of classical superconductivity is given within the BCS theory by Bardeen, Cooper and Schrieffer [BCS57a; BCS57b]. It was shown that it is energetically favourable for electrons in superconductors at temperatures below T_c to form a bound state. This was explained by a weak attractive interaction between the electrons caused by electron-phonon interaction. These so-called Cooper pairs consist of two electrons with opposite momentum and spin and are, therefore, bosons. They feature a spatial extent of ξ_0 and are the superconducting charge carriers described in the phenomenological models above.

One of the major predictions from BCS theory is the energy gap $E_g(T) = 2\Delta(T)$ between the bosonic ground state of the Cooper pairs and the energy levels of the unpaired electrons. The energy needed to break a Cooper pair increases from $E_g(T_\mathrm{c}) = 0$ at the critical temperature to the maximum value at zero temperature:

$$E_g(0) = 2\Delta(0) = 3.528 k_\mathrm{B} T_\mathrm{c} \quad , \tag{2.61}$$

which is on the order of a few meV.

For temperatures $0 < T < T_\mathrm{c}$, not all electrons are condensed into Cooper pairs, as some are thermally excited to unpaired electrons. The population of the energy levels is governed by the Boltzmann factor $e^{-\Delta/k_\mathrm{B}T}$. For temperatures $T < T_\mathrm{c}/2$, the Cooper pair density $n_s(T)$ is close to its zero-temperature value $n_s(0)$ and the density of unpaired electrons is given by

$$n_n(T) \simeq 2 n_s(0)\, \mathrm{e}^{-\Delta/k_\mathrm{B}T} \quad \text{with} \quad T < T_\mathrm{c}/2 \quad . \tag{2.62}$$

This will become important for the discussion of rf currents in superconductors in Sec. 2.4.2. There, normal conducting electrons contribute significantly to the total charge transport, which results in a non-zero electrical resistance.

2.4.2 The surface resistance

Unlike in the dc case, the electrical resistance of superconductors does not vanish at finite temperatures for time-dependent fields. This can be understood by the phenomenological two-fluid model of superconductors, which was developed by Gorter and Casimir [GC34] before the BCS theory. It is based on co-existing normal conducting and superconducting charge carriers. For dc currents, the resistivity is zero since the lossless Cooper pairs short out the external field and shield the normal conducting electrons, which do not contribute to the charge transport. This is different in the rf case. Since the Cooper pairs have momentum, they do not adapt instantaneously to time-dependent fields and

the external field is only partially shielded. Hence, the normal-conducting electrons are accelerated and cause power dissipation.

According to the two-fluid model, there are two fluids in superconductors, a superfluid of charge carrier density n_s and a normal fluid with charge carrier density n_n that make up the total charge carrier density:

$$n = n_n + 2n_s \quad . \tag{2.63}$$

The normal and the superconducting current, described by their current densities $\vec{j}_n$ and $\vec{j}_s$, respectively, are assumed to flow in parallel and the total current density $\vec{j}$ is given by the sum, $\vec{j} = \vec{j}_n + \vec{j}_s$.

In case of a harmonically oscillating current with frequency ω, the first linearized London equation (Eq. (2.52)) yields

$$\mathrm{i}\omega\mu_0\lambda_L^2\vec{j}_s = \frac{1}{\sigma_s}\vec{j}_s = \vec{E} \quad , \tag{2.64}$$

where the conductivity of the superfluid σ_s was introduced according to Ohm's law (see Eq. (2.54)). Due to the purely imaginary conductivity, the current is 90° out of phase with the electric field and thus does not dissipate energy.

The normal conducting fluid can be described classically by $\vec{j}_n = n_n e\vec{v}_n$, where $\vec{v}$ is the average velocity of the normal charge carriers. For harmonically oscillating currents $\vec{j}_n$, the normal conductivity can be described using the Drude model [Dru00]:

$$\sigma_n = \left(\frac{n_n e^2\tau}{m_n}\right)\frac{1}{1-\mathrm{i}\omega\tau} \quad . \tag{2.65}$$

Here, τ is the scattering time of the normal charge carriers, which is typically on the order of $\tau \simeq 10^{-12}\,\mathrm{s}$ [Tin96]. Since only frequencies in the rf regime are relevant for this thesis, $\omega\tau \ll 1$ holds true. Using this approximation, the total conductivity of a superconductor is given by

$$\sigma = \sigma_n + \sigma_s = \frac{n_n e^2\tau}{m_n} - \mathrm{i}\frac{1}{\omega\mu_0\lambda_L^2} \quad . \tag{2.66}$$

This can be used to calculate the superconducting surface impedance, which characterizes the resistive losses in rf cavities (see Sec. 2.3.1). In general, it is defined as the ratio of the tangential electric and magnetic field at the surface of an electrically conducting material [Pip47; Ker99]:

$$Z_s = R_s + \mathrm{i}X_s = (1+\mathrm{i})\sqrt{\frac{\mu_0\omega}{2\sigma}} \quad . \tag{2.67}$$

At temperatures below T_c, for which $\sigma_n \ll |\sigma_s|$ holds, the surface impedance of a superconductor within the two-fluid model is given by

$$Z_s = R_s + \mathrm{i}X_s = \frac{1}{2}\omega^2\mu_0^2\lambda_L^3\sigma_n + \mathrm{i}\omega\mu_0\lambda_L \quad . \tag{2.68}$$

The surface resistance R_s increases proportional to the normal conductivity σ_n, since it determines the fraction of the total current that is carried by normal conductors. Due to the quadratic scaling with frequency, $R_s \propto \omega^2$, resistive losses are suppressed in low-frequency cavities.

The main difference between the two-fluid model result and the complete description within the BCS theory is the temperature dependence of R_s. Due to the energy gap, the amount of normal conducting electrons and thus also the normal conductivity will decay exponentially towards lower temperatures (see Eq. (2.62)). At low temperatures, $T < T_c/2$, and frequencies $\omega < \Delta/\hbar$, the BCS result for the surface resistance is given by [Gur12]

$$R_{s,\mathrm{BCS}} \simeq \mu_0^2 \omega^2 \lambda^3 \sigma_n \frac{\Delta}{k_\mathrm{B} T} \ln\left(\frac{2.246 k_\mathrm{B} T}{\hbar\omega}\right) \mathrm{e}^{-\Delta/k_\mathrm{B}T} \quad . \tag{2.69}$$

It is important to note that the surface resistance depends on the purity of the material. This is related to the mean free path of the electrons which enters in the calculation of the effective penetration depth λ (see Eq. (2.60)).

For niobium cavities operated at 1.3 GHz, typical values for $R_{s,\mathrm{BCS}}$ amount to 800 nΩ at 4.2 K, which decreases to 15 nΩ at 2 K [Aun+00]. In contrast to the BCS description, which predicts a vanishing surface resistance for small temperatures $T \gtrsim 0$, experiments show a finite, temperature-independent contribution R_res, called residual resistance:

$$R_s(T) = R_{s,\mathrm{BCS}}(T) + R_\mathrm{res} \quad . \tag{2.70}$$

Several contributions to the residual resistance are distinguished in literature, e.g. absorbed gases, microscopic particles on the cavity surface, material impurities or trapped magnetic flux [Kno97; Cio15]. For niobium cavities, values of the residual resistance down to a few nΩ have been reported [Aun+00].

As discussed in Sec. 2.3.1, the quality factor of rf cavities depends on the surface resistance of the cavity material. Therefore, the discussed dependence of R_s on temperature and material properties was considered for the design and material selection of the cavity presented in this thesis.

2.4.3 Critical magnetic fields

According to the Meissner-Ochsenfeld effect [MO33], superconductors expel any external dc magnetic field H_ext once they are cooled below their critical temperature. The expulsion of magnetic flux increases the free energy of the superconductor by $\mu_0 H_\mathrm{ext}^2/2$ per unit volume. This needs to be smaller than the energy gained by forming Cooper pairs for the superconducting phase to be energetically favourable. For increasing magnetic field strength, the free energy of the superconductor is raised and finally reaches the value of the normal conductor. The resulting breakdown of the superconducting phase defines a thermodynamic critical field $H_{c,\mathrm{th}}(T)$ by the difference in free energy density $f(T,H)$ between the normal (f_n) and the superconducting (f_s) state [Tin96]:

$$\frac{1}{2}\mu_0 H_{c,\mathrm{th}}^2(T) = f_n(T,0) - f_s(T,0) \quad . \tag{2.71}$$

At the interface between a superconductor and a normal conductor, the magnetic field strength decreases over the length scale λ, while the superconducting charge density changes over ξ (see Sec. 2.4.1). Therefore, the ratio $\kappa = \lambda/\xi$ determines weather it is favourable for a superconducting phase to form in the presence of an external magnetic field. This allows to distinguish two classes of superconductors, which exhibit different behaviour in magnetic fields.

In the case of type I superconductors, defined by $\kappa < 1/\sqrt{2}$, any external magnetic field is expelled up to a temperature-dependent critical magnetic field strength H_c, which is identical to the thermodynamic critical field $H_\mathrm{c,th}(T)$ defined by Eq. (2.71). The temperature dependence of the critical magnetic field is well-described by the empirical relation [Tin96]

$$H_\mathrm{c}(T) = H_\mathrm{c}(0)\left(1 - \left(\frac{T}{T_\mathrm{c}}\right)^2\right) \quad . \tag{2.72}$$

Type II superconductors, such as niobium, are characterized by $\kappa > 1/\sqrt{2}$. They feature two critical magnetic fields, $H_\mathrm{c1} < H_\mathrm{c,th}(T) < H_\mathrm{c2}$. For external magnetic fields below H_c1, the superconductor is in a perfect Meissner phase and the external magnetic field is completely expelled. For higher field strengths $H_\mathrm{c1} < H_\mathrm{ext} < H_\mathrm{c2}$, the superconductor is in the so-called Shubnikov phase. The external magnetic field is only partially expelled and enters the bulk material in the form of flux vortices. Each vortex carries a single flux quantum $\phi_0 = hc/2e$ and features a normal-conducting core. For increasing magnetic field strength, the density of the flux tubes increases until the sample becomes normal conducting above the critical field H_c2.

In case of rf magnetic fields, the situation is different. It was found that the formation of a normal conducting region inside a superconductor takes a finite amount of time, once the critical field strength is exceeded, $H_\mathrm{ext} > H_\mathrm{c,c1}$. This time span on the order of microseconds [Fli65] is much longer than the typical rf period. Therefore, theory predicts that the Meissner phase persists up to a superheating field, $H_\mathrm{sh} > H_\mathrm{c,c1}$ [MS67].

The critical magnetic fields of a superconductor affect its rf losses (see Sec. 4.4.2). Among all elemental superconductors, niobium features the highest critical magnetic field H_sh and is thus commonly used for the fabrication of superconducting rf cavities [Pad01].

3

The Cryogenic Paul Trap Experiment CryPTEx-II

The cryogenic Paul trap experiment CryPTEx-II aims to perform high-precision laser spectroscopy of cold, highly charged ions (HCIs). The main parts of the experiment, a novel superconducting radio-frequency (rf) ion trap as well as a cryogenic supply and trap environment, were developed and commissioned during this thesis. An overview of the complete experimental setup is shown in Fig. 3.1. It comprises an electron beam ion trap (EBIT) [Mic+18; Küh21] as a universal source for HCIs, which is connected to the rf ion trap using a low-energy transfer beamline [Ros19; Mic20; Küh21]. The apparatus is located at the Max-Planck-Institut für Kernphysik (MPIK) in Heidelberg.

For laser spectroscopy of HCIs, different laser sources are available for this setup. A tunable Ti:Sapphire based spectroscopy laser [Leo+16] allows to address a wide range of optical transitions in HCIs. Additionally, the spectroscopy wavelength range can be extended to the extreme ultraviolet (XUV) region. For this, an XUV frequency comb [Nau+17; Nau20; Oel21] was developed at MPIK, which is shown in its future position in Fig. 3.1. It is based on high-harmonic generation inside an enhancement cavity. The combination of both experiments will allow for direct frequency comb spectroscopy of cold HCIs in the XUV region.

The experimental procedure for the preparation of cold HCIs inside the Paul trap starts with their production inside the EBIT using electron impact ionization. After a breeding time of about 100 ms inside the trap, the ions are ejected in bunches into the beamline with typical kinetic energies around $695\,\mathrm{eV} \times q$. During transfer, the ion bunch

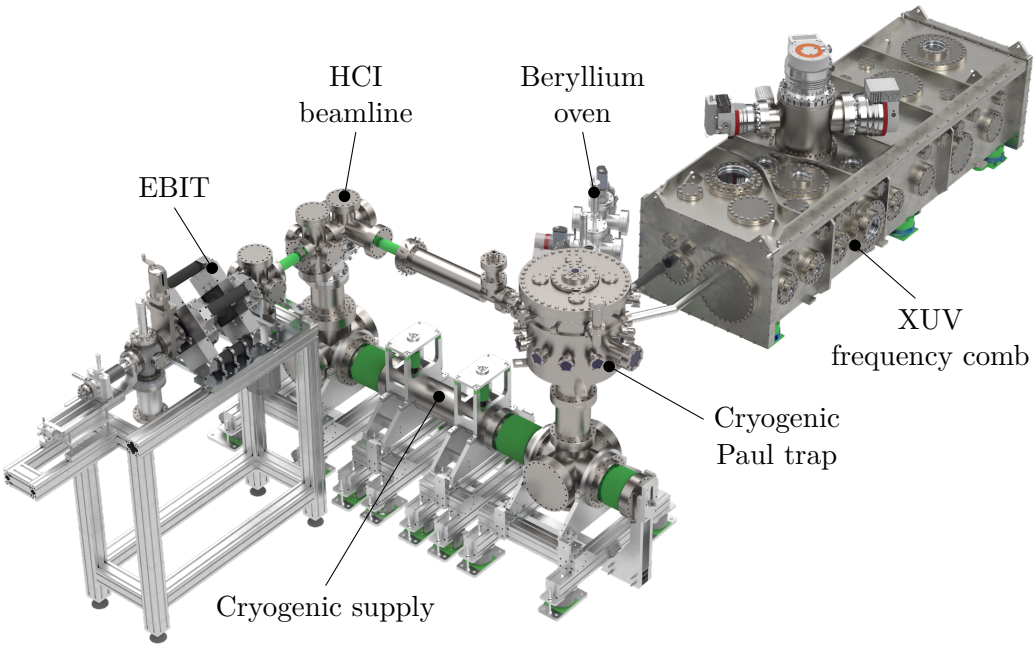

Figure 3.1: Overview of the complete experimental setup of CryPTEx-II at MPIK. It consists of a cryogenic supply and ion trap, an atomic beryllium oven, an EBIT, and an HCI transfer beamline. The XUV frequency comb intended for direct frequency comb spectroscopy of HCIs is shown at its future position.

separates according to the charge-to-mass ratio q/m of its constituents. This allows to isolate the HCI species of interest using kicker electrodes, which grants transmission to a certain time-of-flight (TOF) window. Additionally, the kinetic energy of the ions is reduced to below $130\,\mathrm{eV} \times q$ using pulsed drift tubes before entering the Paul trap. Here, the HCIs are retrapped (see Sec. 4.5.2) and sympathetically cooled by laser-cooled $^9\mathrm{Be}^+$ ions.

In order to allow for long interrogation times on the order of minutes, experiments with HCIs crucially depend on extreme high vacuum (XHV) conditions to suppress charge-exchange reactions with residual background gas. This is achieved by integrating the ion trap into a cryogenic environment, for which pressure levels below $10^{-14}\,\mathrm{mbar}$ are typically reached [Sch+12; Pag+18].

The ion trap and cryogenic setup developed in this thesis is the successor experiment of cryogenic Paul trap experiment (CryPTEx) [Sch+12] at MPIK, and is thus named CryPTEx-II. Its center piece, the novel superconducting rf ion trap, is described in detail in Chapter 4. The associated cryogenic setup consists of a low-vibration cryogenic supply and the cryogenic trap chamber. The former was developed in collaboration with the Physikalisch-Technische Bundesanstalt (PTB) in Braunschweig, where the twin setup is located, and is described in [Mic+19]. The PTB setup, CryPTEx-PTB [Leo+19],

features a blade-style ion trap and is designed for quantum logic spectroscopy (QLS) of HCIs cooled to their motional ground state [Mic+20].

The following description of the experimental setup of CryPTEx-II focuses on the cryogenic parts of the apparatus. First, the cryogenic setup as well as the general concept to isolate vibrations from the trap region are presented in Sec. 3.1. This includes an estimation of the thermal budget as well as the performance characterization of the cryogenic supply. Subsequently, the experimental cold stage holding the ion trap is covered together with the cryogenic trap environment in Sec. 3.2. In Sec. 3.3, a description of the atomic beryllium source, as well as a brief overview of the laser systems used for photoionization of beryllium and laser cooling of $^9Be^+$ are provided. The chapter closes with a brief description of the HCI source as well as the low-energy transfer beamline (Sec. 3.5).

3.1 The cryogenic setup

The design requirements for a cryogenic ion trap setup for applications in high-precision laser spectroscopy are diverse. Stable positioning of the ions inside the trap requires high mechanical stability of the cryogenic setup. This should suppress any differential movement between optical table and ion trap and ensure reproducible positioning of the trap after thermal cycling. In addition, external vibrations need to be decoupled from the trap to avoid motional heating of the trapped ions. Finally, long-term measurements demand reliable operation with low maintenance over months. Based on these main design criteria, a low-vibration cryostat was developed, which is shown in Fig. 3.2.

It is based on a closed-cycle pulse-tube cryocooler[1], which is connected to the cryogenic Paul trap via the thermal transfer unit (TTU). The cryogenic setup consists of two nested temperature stages with nominal temperatures of 4 K (second stage) and 40 K (first stage), which are mounted inside a vacuum chamber. The outer temperature stage shields the inner stage from room temperature thermal radiation and serves as a thermal anchor for heat conduction through mechanical or electrical connections. The following description of the cryogenic supply and the measures taken for vibrational decoupling is partly based on [Mic+19], wherein the PTB setup is described.

3.1.1 Design

The low-vibration cryogenic supply can be divided into three segments, which are indicated in the CAD model shown in Fig. 3.2. The individual components of the apparatus are described in the following.

Thermal transfer unit

The two temperature stages of the pulse-tube cryocooler are connected to the ones of the Paul trap via the TTU, which is shown in Fig. 3.2. It has a total length of over

[1] model RP-082 from Sumitomo Heavy Industries

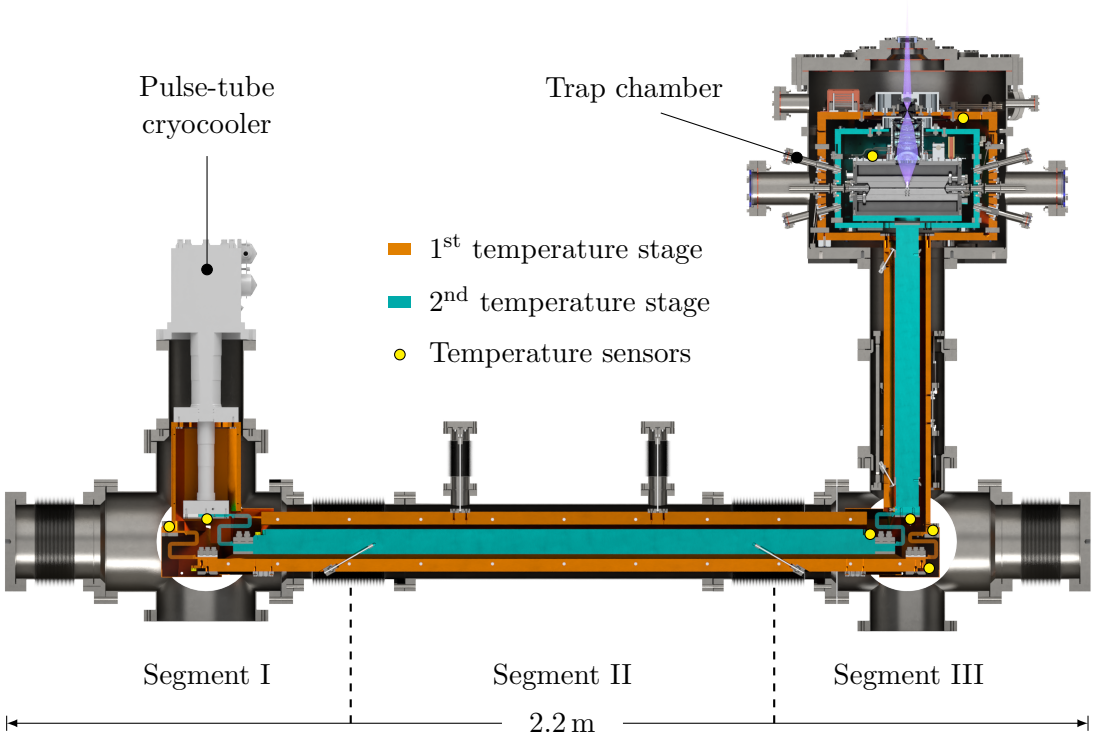

Figure 3.2: Section view of the CAD model of the low-vibration cryogenic supply and Paul trap. The cryogenic setup consists of two nested temperature stages at nominal temperatures of 4 K (cyan) and 40 K (orange). In order to monitor the temperature distribution of the two stages, eight temperature sensors are installed at the indicated positions (yellow circles).

2.2 m. In order to ensure efficient cooling of the ion trap, the thermal resistances of the TTU elements as well as the external heat load onto both temperature stages need to be carefully evaluated. This is discussed in detail in Sec. 3.1.3.

All parts of the TTU are made of high-purity oxygen-free high thermal conductivity (OFHC) copper (99.995 – 99.999 %), which features a high thermal conductivity at cryogenic temperatures. This is enhanced by vacuum annealing, which partially recrystallizes the copper and, thereby, increases its residual-resistance ratio (RRR). For the brazed parts of segment I and III of the TTU, the annealing was done simultaneously with the vacuum brazing at 850 °C. The parts of segment II as well as the second stage rod of segment III were vacuum annealed at 650 °C.

In order to reduce the heat load by thermal conduction, mounting of the TTU to the vacuum chamber as well as the second stage inside the first stage is realized using stainless-steel spokes of 2 mm diameter. This yields a good thermal insulation between the temperature stages due to the low thermal conductivity of the material, while its high

mechanical strength ensures a stiff mounting. The spokes are made of standard bicycle spokes, which are point-welded into fitting bores drilled along the axis of an Allen-setscrew. Each screw is equipped with a nut on the thread, which allows to precisely balance the tension on the different spokes and adjust the position of the cryogenic elements.

In segment I, the two temperature stages of the cryocooler are connected to the TTU. At the first temperature stage, a hollow octagon consisting of eight 220 mm long and 8 mm thick copper bars (99.999 %) with trapezoidal cross section is directly mounted to the pulse tube. The bars are vacuum brazed together to increase the effective cross section contributing to heat transport. It encloses the second stage of the cryocooler. Both are connected to the next segment of the TTU using flexible copper links (see Fig. 3.3).

The first temperature stage of segment II consists of a hollow octagon with a length of 1470 mm. Eight copper bars (99.995 %) of trapezoidal cross section and 25 mm thickness are bolted together. It is suspended from the room temperature chamber by two spokes connected to stainless-steel insets on top of stage one. The enclosed second temperature stage rod made of 99.999 % copper has a diameter of 50 mm and a length of 1340 mm. It is mounted to the first stage using six counteracting spokes, three at each end. The connection to segment III is realized by the second set of flexible links.

In segment III, the room temperature frame of the TTU is resting on the DN160CF vacuum tube connecting the six-way cross to the ion trap chamber. The first temperature stage is mounted into the frame using twelve counteracting stainless-steel spokes. It consists of twelve 10 mm thick trapezoidal copper bars (99.999 %) of 591 mm length, which are vacuum brazed together to form a hollow dodecagon. They enclose the second temperature stage rod of 576 mm length and 50 mm diameter, which is made of 99.999 % copper. The rod is vacuum brazed into a copper socket of equal purity, which allows to connect the flexible links to its lower end. It is mounted to the first stage using six counteracting spokes, three at each end.

The upper end of both temperature stages in segment III is directly connected to the cryogenic shields of the ion trap chamber. Inside the trap chamber, mounting of the first stage to the vacuum chamber and the second stage inside the first stage is realized by two sets of twelve counteracting spokes. This is described in more detail in Sec. 3.2.1.

Connections between the different segments of the TTU are established using flexible copper links, which are located in each of the two six-way crosses of the vacuum chamber (see Fig. 3.2). Pictures of the links are shown in Fig. 3.3. Both sides of Segment II are equipped with three links at each temperature stage. The links are machined from a solid block of high-purity copper (99.999 %) using wire electrical discharge machining (EDM). They consist each of 10 layers of 0.4 mm thickness and have a width of 14 mm and 25.4 mm at the second and first temperature stage, respectively. This design exploits the high flexibility of the individual thin layers and at the same time avoids thermal resistances between the layers at the contact points to the TTU. Additionally, the links are vacuum annealed to increase their RRR and soften them. All three 4 K links in each six-way cross are one-sidedly vacuum brazed into a copper socket and, thereby, annealed

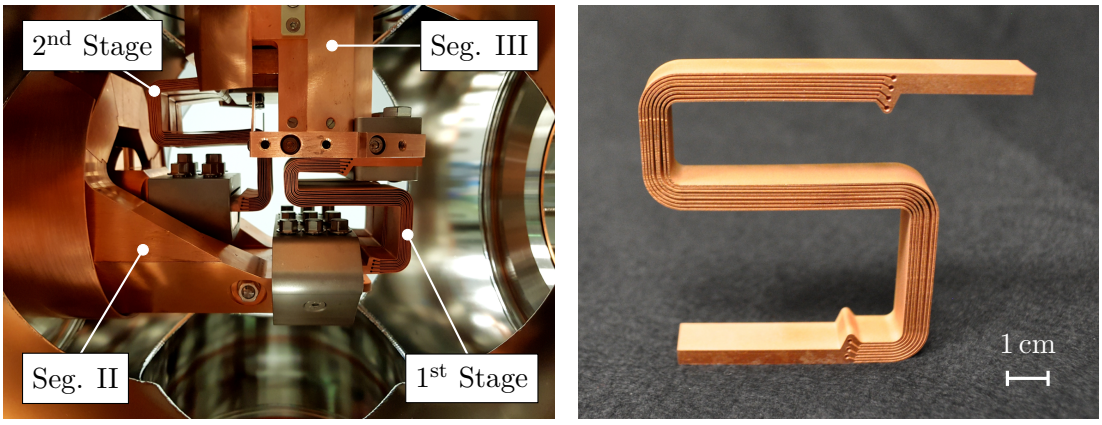

Figure 3.3: **Left:** Picture of the flexible links installed in the six-way cross below the Paul trap with the 40 K heat shields removed. **Right:** Close-up view of one flexible link to be installed at the 4 K stage of the pulse tube.

at 850 °C. The 40 K links are mounted individually to the cryogenic stages and were vacuum annealed at 650 °C.

One major difference to the low-vibration cryogenic supply at PTB are the flexible links. Instead of massive copper parts, they employ flexible links[2] made of high-purity copper-braid (> 99.995 %), which is clamped into copper sockets and annealed at 550 °C. This has the advantage of an increased flexibility for vibrations orthogonal to the S-shape of the design presented here. However, as the links represent the thermal bottleneck of the setup, the increased cross-section of the 4 K links developed in this thesis results in a lower final temperature of the trap (see Sec. 3.1.4). Eventually a trade-off has to be made between trap temperature and vibrations once they are measured and turn out to pose a limitation for experiments.

In order to shield the flexible links from room temperature thermal radiation, heat shields are employed in both six-way crosses. These shields consist of 1 mm thick copper sheets of 99.95 % purity. Care is taken to ensure vibration decoupling on the cryogenic stages by mounting the shields such that the different segments of the TTU are not connected to each other.

For monitoring the temperature distribution along the TTU, eight calibrated temperature sensors are mounted in various locations, which are indicated in Fig. 3.2. Two different types of sensors are used. Cernox sensors[3] are employed close to the cryocooler, since they can be operated in the residual magnetic field generated by the EBIT. Additionally, silicon diodes[4] are used to measure the trap temperatures and the second stage temperatures in segment II and III. The sensors are all mounted inside their respective temperature stage enclosures, except for the two silicon diodes at the second tempera-

[2] model UltraFlex from Technology Applications, Inc.
[3] model CX-1050-CU-HT-1.4L and 4L from Lake Shore Cryotronics, Inc
[4] model DT-670-SD-1.4L from Lake Shore Cryotronics, Inc

ture stage of segment II and III, due to spatial constraints. They are exposed to thermal radiation from stage one, which affects the temperature measurement (see Sec. 3.1.4).

Vacuum system

The three segments of the vacuum chamber are divided by edge-welded bellows (see Fig. 3.2 and Fig. 3.4). The pulse-tube cryocooler is mounted to the top of segment I and connected to the first six-way cross using a DN160CF vacuum tube. Connection to the six-way cross of segment III via the horizontal tube of segment II is provided using two DN160CF edge-welded bellows. Two additional DN160CF edge-welded bellows are mounted to the outer flanges of the two six-way crosses, in order to balance the atmospheric pressure. Segment III is directly connected to the vacuum chamber of the ion trap using a DN160CF vacuum tube. All parts of the vacuum system of Paul trap and cryogenic supply are made of non-magnetic stainless steel. The vacuum chambers are electropolished on the inside to suppress radiative heating of the cryogenic stages (see Sec. 3.1.3). This additionally reduces outgassing of the material.

3.1.2 Isolation of vibrations

In order to provide mechanically ultra-stable trapping conditions, external vibrations need to be decoupled from the trap environment. The main sources of vibration are scroll pumps (25 Hz), turbomolecular pumps (TMPs) (1350 Hz and 1010 Hz), as well as typical laboratory noise sources like air conditioning, fans, water-cooling systems and external vibrations transmitted via the laboratory floor. Additionally, the pulse-tube cryocooler and its helium compressor introduce acoustic noise to the system. Therein, a rotary valve separates the regions of high and low pressure and expands helium into the cold head with a repetition rate of 1.7 Hz. Since the rotary valve is rigidly mounted to the cold head, vibrations are introduced to the cryogenic stages and the vacuum chamber. All these acoustic noise sources can induce mechanical vibrations to the trap region, which are either transmitted via direct mechanical contact or through ambient air. The experimental setup designed to decouple these vibrations from the trap region is shown in Fig. 3.4, with the vibration decoupling elements highlighted in green.

The experiment is set up in two neighbouring laboratories. Thereby, the trap region is acoustically decoupled from the noisy equipment, like TMPs or the cold head, using a noise-insulating wall. The helium compressor is placed outside the two laboratories and connected to the cold head using 20 m long hoses. The scroll pumps providing the pre-vacuum for the TMPs are also located outside of both laboratories on a separate platform and connected using flexible hoses made of PVC. All TMPs of the apparatus, which are in operation during measurements, are mounted to the six-way cross below the pulse-tube and, therefore, furthest away from the trap chamber.

In addition, different measures are taken to reduce mechanical vibrations on the vacuum chamber. Vibrations induced to the six-way cross on the left side of Fig. 3.4 are decoupled from the trap chamber using edge-welded CF160 bellows with 40 diaphragm pairs, which connect the left six-way cross to the right one via the horizontal tube.

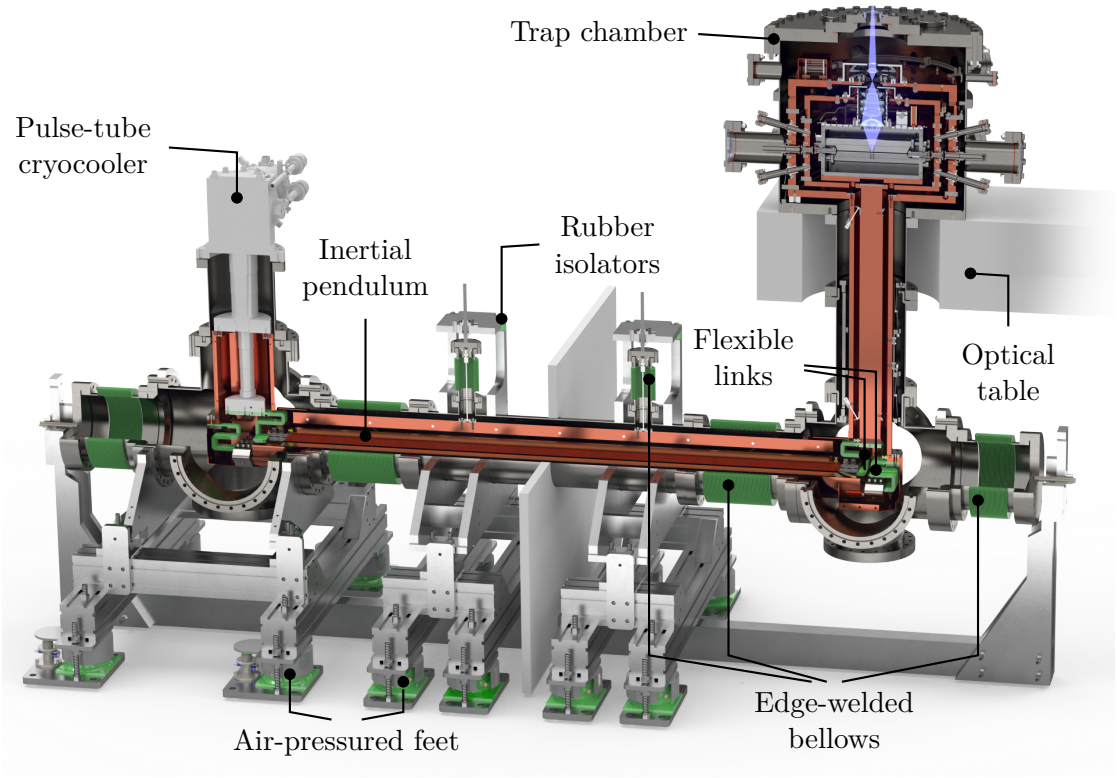

Figure 3.4: Section view of the CAD model of the low-vibration cryogenic supply and ion trap. The apparatus extends over two rooms, which are separated by a noise-insulating wall (indicated in grey). The elements used for vibration decoupling on the vacuum chamber or at the cryogenic stages are shown in green. The ion trap chamber is mounted onto a floating optical table.

The second cross on the right side of the horizontal tube is rigidly connected to the trap chamber, which is mounted onto an optical table. In order to decouple external mechanical vibrations, air-pressured feet[5] are employed to connect the left six-way cross, the horizontal tube, as well as the optical table to the laboratory floor.

Additionally, vibrations can be transmitted to the trap chamber via the HCI beamline and the atomic beryllium source (see Fig. 3.1). The former is one-sidedly mounted to the trap chamber and decoupled from EBIT and vacuum pumps using a DN40CF edge-welded bellow with 46 diaphragm pairs. The beryllium oven is mounted onto the optical table of the ion trap using rubber feet. Connection to the trap chamber is provided by a DN16CF edge-welded bellow with 40 diaphragm pairs.

[5] model FAEBI from Bilz

Table 3.1: Estimated total heat load onto the two temperature stages of the cryogenic setup. This includes the ion trap environment, which is described in Sec. 3.2.1.

	1^{st} stage (W)	2^{nd} stage (W)
Thermal radiation	15.67	0.027
Conduction through spokes	1.57	0.080
Electrical connections	0.12	0.002
Total heat load	17.36	0.109

On the cryogenic stages, vibrations are decoupled using the horizontal pendulum and flexible copper links, which connect neighbouring segments of the TTU (see Sec. 3.1.1). The horizontal pendulum has a total mass of approximately 120 kg. It is suspended by two stainless steel spokes and represents an inertial pendulum acting as a low-pass filter for mechanical vibrations on the cryogenic stages. The spokes are mounted onto a DN40CF flange, which is fixed to a frame mounted onto the horizontal tube. To decouple vibrations transmitted via the vacuum chamber, the flanges supporting the spokes are connected to the horizontal tube using DN40CF edge-welded bellows. Additionally, the flange support is mounted on four rubber rings.

3.1.3 Thermal budget and cryogenic engineering

The cryogenic supply is based on a two-stage pulse-tube cryocooler, which provides steady-state temperatures of 45 K at the first stage and 4.2 K at the second stage at thermal loads of 40 W and 1 W, respectively [SHI19]. Higher thermal loads increase the achievable temperatures. Due to the limited cooling power at the second stage, all thermal heat loads need to be identified and minimized in order to ensure a trap temperature below 5 K. This is crucial in order to ensure a low background pressure inside the trap, which suppresses charge-exchange reactions of HCIs with neutral gas and thus allows for long storage times. The estimated total heat load onto the two temperature stages is listed in Tab. 3.1. A detailed compilation of the individual contributions and the underlying basics of cryogenic engineering is given in this section.

Blackbody radiation

Heating of the cryogenic stages by thermal radiation emitted by a surface at higher temperature, e.g. the vacuum chamber, can easily dominate the total heat load of a cryogenic system. The radiation power $\dot{Q}_{\text{rad}}$ emitted by a surface with area A at temperature T is given by the Stefan-Boltzmann law [Eki06],

$$\dot{Q}_{\text{rad}} = \epsilon_{\text{s}} \sigma_B A T^4 \quad , \tag{3.1}$$

where σ_B denotes the Stefan-Boltzmann constant and ϵ_{s} is the emissivity of the surface. Due to the strong scaling with temperature, the cryogenic setup consists of two nested

temperature stages, where the first stage at 40 K acts as a heat shield for the second stage at 4 K. This suppresses the radiative heat load onto the second stage by a factor of $(300/40)^4 > 3100$.

Additionally, the heat load onto both temperature stages is reduced by optimizing the emissivity ϵ_s, which depends on the material, but also on the surface finish and cleanliness. Most well-polished metallic surfaces exhibit small emissivities ($\epsilon_s < 0.05$), which are are well below that of non-metallic materials [Par14]. Therefore, all vacuum chambers made of stainless steel are electropolished. The heat shields and the cryogenic stages are made of annealed copper with a clean surface. In order to prevent the formation of oxide layers, which results in an increased surface emissivity, the copper parts of the trap chamber are additionally plated with 0.5 µm gold (see Fig. A.4). An intermediate layer of 10 µm silver is applied to prevent the diffusion of gold atoms into the copper surface. The pendulum shield of the cryogenic supply is mostly covered in aluminium foil, which preserves a low emissivity even after many ventings of the system.

The radiative heat load onto the two temperature stages can be estimated using the Stefan-Boltzmann law for diffuse reflection between long concentric cylinders [Eki06]:

$$\dot{Q}_{\mathrm{rad}} = \frac{A_1 \sigma_B \left(T_2^4 - T_1^4\right)}{\frac{1}{\epsilon_{s,1}} + \frac{A_1}{A_2}\left(\frac{1}{\epsilon_{s,2}} - 1\right)} \quad . \tag{3.2}$$

This describes the radiative heat transfer from the outer surface A_2 at temperature T_2 to the inner surface A_1 at temperature T_1. For specular reflection, $A_1 = A_2$ holds true [Eki06], which leads to minor modifications of the results obtained for diffuse reflection. The heat load onto both temperature stages is estimated by averaging both results, which yields 15.67 W and 0.002 W for the first and second stage, respectively. Here, the emissivity for the electropolished stainless steel vacuum chamber as well as for the copper parts is estimated to be 0.05.

The cryogenic shields around the ion trap exhibit openings to provide optical access to the trap center for lasers, the imaging of trapped ions and the injection of HCIs or beryllium atoms (see Sec. 3.2.1). These access ports allow thermal radiation from room temperature to heat the second temperature stage. The exposure of the second stage is restricted by tubes mounted to the horizontal ports of both heat shields and an aperture mounted at the opening for the imaging system in the first stage. The associated radiative heat load can be estimated by approximating the geometry with two parallel plates [Eki06]:

$$\dot{Q}_{\mathrm{rad}} = \frac{A \sigma_B \left(T_2^4 - T_1^4\right)}{\frac{1}{\epsilon_{s,1}} + \frac{1}{\epsilon_{s,2}} - 1} \quad , \tag{3.3}$$

where A is the area of the smaller surface, i.e. the exposed surface of the second temperature stage. This yields an estimated heat load onto the second temperature stage by room temperature thermal radiation of 0.025 W. The emissivity of the view ports attached to the horizontal access ports around the trap was assumed to be equal to the one of glass, $\epsilon_s = 0.9$ [Eki06].

Table 3.2: Estimated thermal resistances of the copper elements of the TTU at their nominal temperatures, i.e. 4 K (second stage) or 40 K (first stage). The thermal conductivities $\lambda_{\mathrm{th}}(T)$ are taken from [Joh61; SDR92]. An RRR of about 1000 is assumed for the copper parts with purities between $(99.995-99.999)\,\%$. The elements of each stage are listed from segment I to segment III (see Fig. 3.2).

Stage	Element	$\lambda_{\mathrm{th}}\,(\mathrm{Wcm^{-1}K^{-1}})$	$R_{\mathrm{th}}\,(\mathrm{KW^{-1}})$
1^{st}	1^{st} vertical shield	20	0.04
1^{st}	1^{st} flexible link	20	0.29
1^{st}	Pendulum shield	20	0.11
1^{st}	2^{nd} flexible link	20	0.21
1^{st}	2^{nd} vertical shield	20	0.12
2^{nd}	1^{st} flexible link	70	0.16
2^{nd}	Pendulum rod	70	0.10
2^{nd}	2^{nd} flexible link	70	0.15
2^{nd}	Vertical rod	70	0.04

Thermal conduction

In order to ensure a low trap temperature, all thermal connections of the trap region to the respective temperature stages of the pulse-tube cryocooler need to provide efficient heat transport. This is ensured by a low thermal resistance. In general, the thermal resistance R_{th} of a material with thermal conductivity $\lambda_{\mathrm{th}}(T)$ at constant temperature T is given by Fourier's law:

$$R_{\mathrm{th}} = \frac{l}{A\lambda_{\mathrm{th}}(T)} \quad , \tag{3.4}$$

where l and A describe the length and the cross section of the object, respectively. Accordingly, all elements of the TTU are made of high-purity OFHC copper, which has an excellent thermal conductivity (see Tab. 3.2) at cryogenic temperatures. In addition, their geometry was chosen to maximize the ratio of cross section to length. An overview of the estimated thermal resistances for all thermal links at their nominal temperatures is shown in Tab. 3.2.

Besides ensuring efficient cooling of the trap region, the heat load by connections between different temperature stages, e.g. for mechanical mounting or electrical connections, needs to be minimized. The heat flow through a link with length l and cross section A connecting two thermal reservoirs at constant temperatures T_2 and T_1 is given by [Eki06]

$$\dot{Q}_{\mathrm{cond}} = \frac{A}{l}\int_{T_1}^{T_2}\lambda_{\mathrm{th}}(T)\mathrm{d}T = \frac{A}{l}\left(\int_{4\,\mathrm{K}}^{T_2}\lambda_{\mathrm{th}}(T)\mathrm{d}T - \int_{4\,\mathrm{K}}^{T_1}\lambda_{\mathrm{th}}(T)\mathrm{d}T\right) \quad . \tag{3.5}$$

The mechanical mounting of the two nested temperature stages inside the vacuum chamber is provided by sets of counteracting spokes made of stainless steel. The low thermal

Table 3.3: Estimated heat conduction through stainless-steel spokes connecting different temperature stages. The thermal conductivity integral values from Eq. (3.5) are taken from [Eki06]. All spokes have a diameter of 2 mm.

Element	T_2 (K)	T_1 (K)	# Spokes	Length (mm)	Heat input (W)
Horizontal shield	300	40	2	150	0.12
Vertical shield	300	40	12	120	0.94
Trap shield	300	40	12	220	0.51
Horizontal rod	40	4	6	97	0.02
Vertical rod	40	4	6	43	0.04
Trap chamber	40	4	12	169	0.02

conductivity of the material ensures a low heat flow, which is further reduced by choosing long and thin spoke geometries. The calculated heat load onto both temperature stages by thermal conduction through spokes is listed in Tab. 3.3.

Electrical connections

The electrical connections of the experiment directly connect the cryogenic stages to the room temperature vacuum feedthrough. Thus, they can represent a significant heat load onto both temperature stages. This effect can be minimized in different ways.

For all applications, which do not draw significant electrical current from the power supply (< 1 mA), resistive wires with an electrical resistance of a few ohm and a small thermal conductivity are used. This is the case for all quasi-static applications, such as temperature sensors, electrostatic lenses, as well as direct current (dc) electrodes and mirror electrodes of the ion trap. They are connected by 203 µm thick phosphor-bronze wires with a 19 µm polyimide insulation[6].

The alternating current (ac) electrical connections to the cold stage are provided by three resistive semi-rigid coaxial cables[7]. They are made of beryllium-copper with polytetrafluoroethylene (PTFE) dielectric and feature a low thermal conductivity and at the same time low attenuation of rf signals. The coaxial cables are connected to the rf couplers of the cavity (see Sec. 4.2.5).

In addition, all cables are thermally anchored at each temperature stage before being connected to the trap. The cable length between the temperature stages is maximized in order to reduce heat conduction along the connection. The cryogenic wires as well as the coaxial cables span a length of more than 0.8 m between two thermalization points. For thermalization of the cryogenic wires inside the trap chamber, they are tightly wrapped around a solid piece of copper, providing a contact length of a few centimeters, and glued in position with a two-component thermally conductive epoxy[8]. The wires of

[6] model QT-32 from Lake Shore Cryotronics, Inc
[7] model SC-219/50-SB-B from COAX CO., LTD.
[8] Stycast 2850 FT with CAT9 from Henkel

Table 3.4: Estimated heat load onto the two temperature stages by thermal conduction through electrical connections. The thermal conductivities $\lambda_{\mathrm{th}}(T)$ for phosphor-bronze [TCD10], polyimide [MLR02], PTFE and beryllium-copper [Joh61] are taken from literature.

	1^{st} stage (W)	2^{nd} stage (W)
Conduction through ac wires	0.11	0.002
Conduction through dc wires	0.01	< 0.001

the temperature sensors of the cryogenic supply are thermally anchored using vacuum-compatible Kapton tape. The coaxial cables are thermalized by directly mounting them onto a solid piece of OFHC copper which is then thermally connected to the respective temperature stage. The estimated heat loads by thermal conduction through electrical connections is listed in Tab. 3.4.

Mechanical connections

Mechanical connections between two elements of the TTU can constitute a major contribution to its total thermal resistance. This effect depends crucially on the force applied onto the pressed contact. Since different materials are involved, it is important to match the thermal expansion coefficient to ensure that the applied force stays constant during cooldown. Furthermore, in order to maximize the surface area contributing to thermal transport across the link, a cryogenic vacuum grease[9] is applied to compensate for the surface roughness of the linked materials. As the thermal conductance of the grease is much smaller than that of the metal, only a very thin and uniform layer is applied to the surface.

3.1.4 Performance characterization of the low-vibration cryostat

The characterization of the cryogenic supply is mainly focused on the temperature distribution of the cryogenic system and the final trap temperatures. Additionally, the vacuum system and the achieved pressure as a crucial parameter for experiments with HCIs are discussed.

The apparatus was set up in the scope of this thesis and partly within [Spi18]. For the commissioning experiments presented in this thesis, it was constructed on the first floor of the experimental hall at MPIK. Here, vibrations from the building and the neighbouring laboratories are more pronounced compared to its final position inside a ground floor laser laboratory. Therefore, no vibration measurements were performed. However, due to the similar design, the results from the CryPTEx-PTB experiment [Mic+19] should be directly comparable. There, the differential vibrations of the 4 K trap region with respect to the optical table were measured using an interferometric setup.

[9] Apiezon N grease from APIEZON

One interferometer arm was directly connected to the trap region, while the reference arm was mounted to the optical table. The measurements show vibration amplitudes below 20 nm in the horizontal plane for frequencies between 1 Hz and 100 Hz, while no vibration peaks were detected at higher frequencies. This corresponds to a suppression of the cryocooler vibrations by three orders of magnitude.

Temperatures

The temperatures of the cryogenic setup are continuously logged using eight temperatures sensors, four on each temperature stage. The positions of the sensors are indicated in Fig. 3.2. A typical measurement of the temperature evolution during cooldown can be seen in Fig. 3.5.

Steady-state temperatures are reached after 9 d and 7 d for the first and second temperature stage, respectively. The quick drop of the second stage temperatures about 2.7 d after start of the cooldown is related to a freeze-out of the phononic and electronic degrees of freedom in the copper parts. This results in a reduced specific heat capacity and an increased thermal conductivity below 40 K [Mic+19]. Due to the increased heat load on the pulse tube, this effect is accompanied by an increase of the first stage temperatures.

After this sudden temperature drop, the second stage temperatures show a slight increase about 2.8 d after start of the cooldown, before they approach their steady-state values. Since this subtle effect was not observed before the installation of the superconducting ion trap, it is suspected to be related to the build-up of the superconducting phase. For the case of zero external magnetic field, this can be described by a second order phase transition and, therefore, does not release latent heat. This is different in an external magnetic field, since the phase transition is of first order. However, for the magnetic fields present in the lab, the temperature increase of about 0.3 K cannot be explained. Thus, an interplay between the reduced specific heat and the decreasing thermal conductivity of niobium below its critical temperature could be responsible for the observed effect.

A final second stage temperature of 4.15 K at the position of the ion trap is reached. This compares well to the 4.60 K reported for the PTB setup [Mic+19]. As the final trap temperature is far below the critical temperature of niobium, $T_c = 9.25\,\mathrm{K}$ [Fis+05], superconducting operation of the ion trap is ensured even for substantial rf power dissipation, see Sec. 5.2.4. The hierarchy of the second stage temperature sensors deviates from the expected behaviour. Ideally, the temperatures along the cryogenic supply should steadily increase from cryocooler to trap chamber. However, the temperatures below the trap and at the horizontal pendulum are above the trap temperature. This might be caused by radiative heating, since the two affected sensors are directly exposed to thermal radiation from 40 K, which is not the case for the other sensors (see Sec. 3.1.1).

The first stage reaches a steady-state temperature of 69.49 K in the trap chamber, which is significantly higher than the 49 K reported for the PTB setup. This is mainly related to the larger thermal resistances of the flexible links, see Tab. 3.2. For their nominal temperatures of 40 K, the thermal resistances of the two links are 50 % and

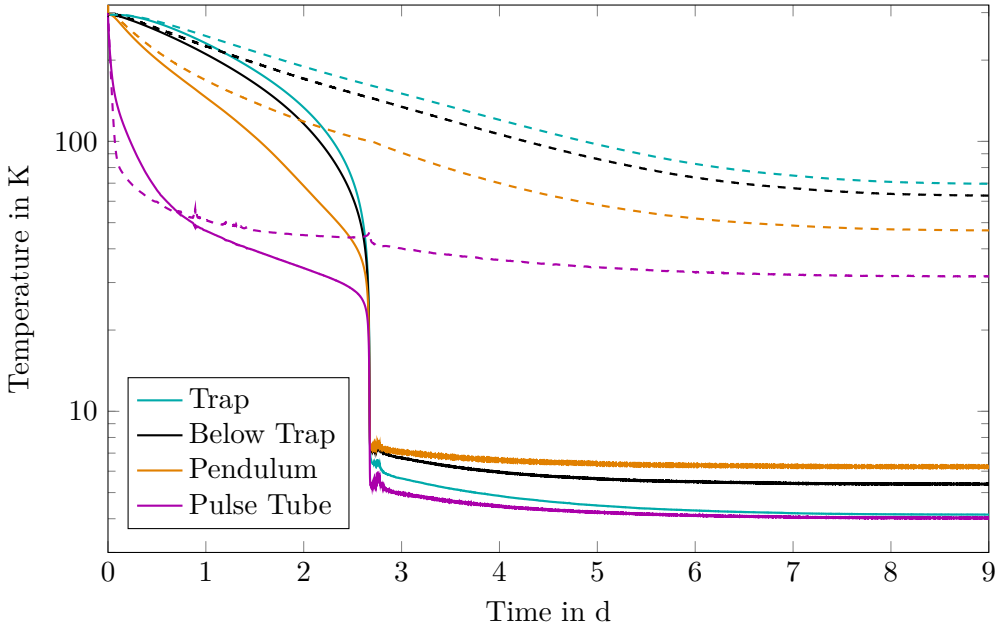

Figure 3.5: Temperature measurements at different positions of the cryogenic supply during cooldown. The dashed (solid) lines represent the temperatures of the first (second) temperature stage. The hierarchy of the second stage temperature sensors is affected by thermal radiation from the first temperature stage. The sensor positions at the TTU are indicated in Fig. 3.2.

90 % larger than for the PTB design. Since the thermal conductivity of copper increases drastically below 50 K, this could be enough to explain the large temperature difference.

Although this is not problematic for the ion trap operation due to the low temperatures reached at the second temperature stage, reducing the thermal resistance of the links could speed up the cooldown. This is much faster for the PTB setup, which reaches steady state after 3 d. Additionally, the vacuum around the cryogenic enclosure could be improved by reducing the first stage trap temperature significantly below 60 K. Thus, the links will be upgraded to larger cross sections in the future.

The final temperatures at the cryocooler can be compared with the capacity map of the pulse tube [SHI19] to get a rough estimate of the total heat load onto the two temperature stages. With final temperatures of 31.59 K and 4.03 K, the heat loads onto the first and second temperature stage are on the level of 25 W and 1 W, respectively. The values are larger than the calculated estimates of 17.37 W and 0.109 W, as given in Tab. 3.1. However, they compare rather well with the values reported for the PTB setup of 22 W and 0.8 W at the first and second stage of the cryocooler, respectively.

Before venting the vacuum chamber in order to perform maintenance work, the temperatures of the cryogenic setup need to be above the dew point. Due to the good thermal insulation of the temperature stages in XHV conditions, the warm up takes about two weeks. By injecting 10^{-2} mbar helium gas into the system, heat convection

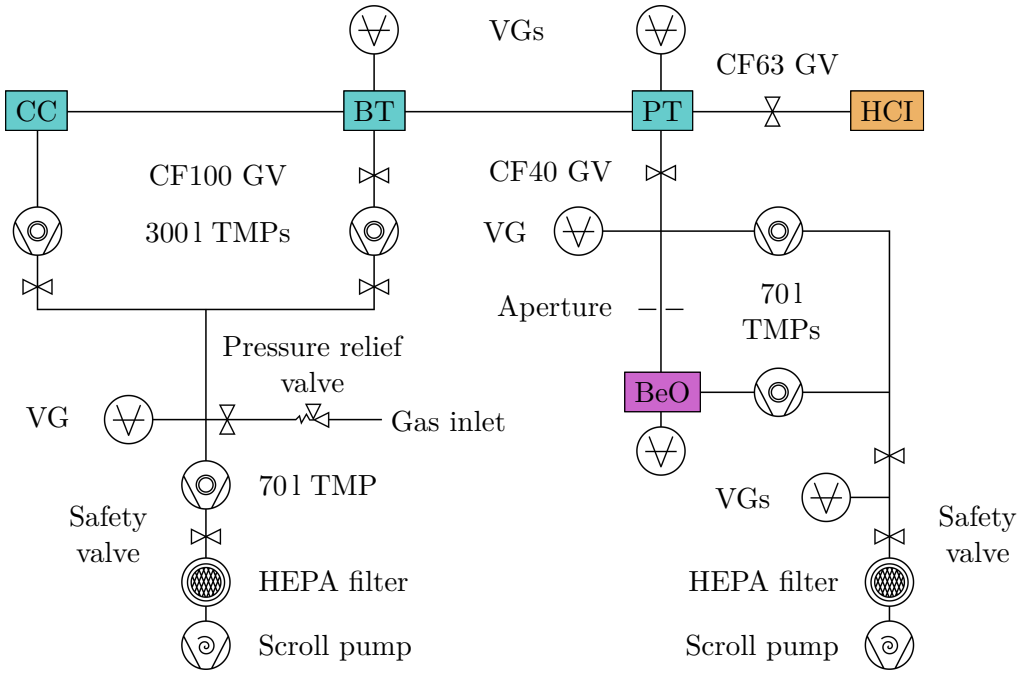

Figure 3.6: Schematic of the vacuum system of CryPTEx-II. It is divided into the vacua of the HCI source and beamline (HCI), the beryllium oven (BeO), and the Paul trap using gate valves (GV). The Paul trap vacuum consists of the trap chamber (PT) and the six-way crosses below the trap (BT) and at the cryo-cooler (CC). The vacuum gauges are denoted with VG. The hand valves in the pre-vacuum system are not labeled.

between the different temperature stages is increased. This leads to reduced warm up times of two to three days until the complete setup has reached room temperature.

Vacuum

The vacuum system of CryPTEx-II is shown in Fig. 3.6. It separates into three distinct vacua of the Paul trap, the beryllium oven (see Sec. 3.3.1) and the HCI source and beamline.

The Paul trap vacuum is pumped using two 300 l TMPs. In order to reduce vibrations during measurements, the one connected to the six-way cross below the trap can be turned off after closing the attached CF100 gate valve. A pre-vacuum below 10^{-4} mbar is provided using a 70 l TMP, which increases the compression rate for molecular hydrogen. This is important, since H_2 represents the main contribution to the residual gas at cryogenic temperatures. All scroll pumps are equipped with a HEPA filter[10] to filter

[10] model SCRINTRPNW25 from Agilent

possible remainders of atomic beryllium. During warmup of the cryogenic stages, the gas inlet can be used to inject a well-defined amount of helium into the system.

The pressure of the main vacuum is measured between the vacuum chamber and the first cryogenic stage using hot filament gauges. They are mounted at the trap chamber and the six-way cross below the Paul trap behind CF40 elbow pieces to reduce radiative heating of the first stage. As described in Sec. 3.1.3, the cryogenic stages are nearly closed and the pumping of the trap volume is only possible through the optical ports. Without cryopumping, a rough estimation yields a pressure inside the cavity housing that is up to two order of magnitude above the measured value between vacuum chamber and the first cryogenic stage. The higher the initial pressure before cooldown, the faster the cryogenic surfaces saturate, resulting in an increased pressure inside the cryogenic enclosure. Thus, the cooldown was only started after the pressure in the Paul trap chamber dropped below 3×10^{-7} mbar.

After cooldown, the constant inflow of residual gas from the room temperature vacuum through optical ports causes a deterioration of the trap pressure over time. Accordingly, other cryogenic Paul traps [Sch17; Leo18] observed declining storage times of trapped Be^+ ions by hydrogenation and trapped HCIs by charge-exchange reactions with residual gas. This effect can be counteracted by regularly performing heat-up cycles, where the cryogenic stages are warmed up to about 20 to 30 K at the second stage by turning off the helium compressor. The desorbed gas is then removed by the TMPs and the lifetimes of trapped ions are increased again after turning on the compressor [Mic+19].

In order to improve the cryopumping around the ion trap, an activated charcoal getter can be installed inside the second stage and outside of the first stage. The charcoal is glued into a copper container using thermally conductive epoxy, which guarantees proper thermalization and functionality as a cryogenic getter. This should increase the lifetime of ions due to the much greater adsorption capacity of the porous charcoal compared to the polished heat shields [Leo18; Mic+19]. However, the getter was not installed during the commissioning experiments presented in this thesis, since it increases the initial pumping time before cooldown significantly. Without charcoal getter, final pressures after cooldown are in the upper 10^{-10} mbar range outside the cryogenic stages.

3.2 The cryogenic trap environment

The main part of the cryogenic setup developed during this thesis is the ion trap environment, which can be seen in Fig. 3.7. It was specifically designed to perform laser spectroscopy of sympathetically cooled HCIs. Two nested cryogenic shields enclose the experimental cold stage at 4 K. Its center piece is the superconducting rf ion trap, which is described in detail in Chapter 4. Mounted on top of the ion trap is the imaging system, which collects the fluorescence photons of trapped ions, see Sec. 3.2.3. Optical access to the trap center for lasers as well as external atom or ion sources is provided by twelve optical ports in the horizontal plane. For the alignment of different light sources to the trap center, a wire-probe alignment system was built, which is described in Sec. 3.2.4. In

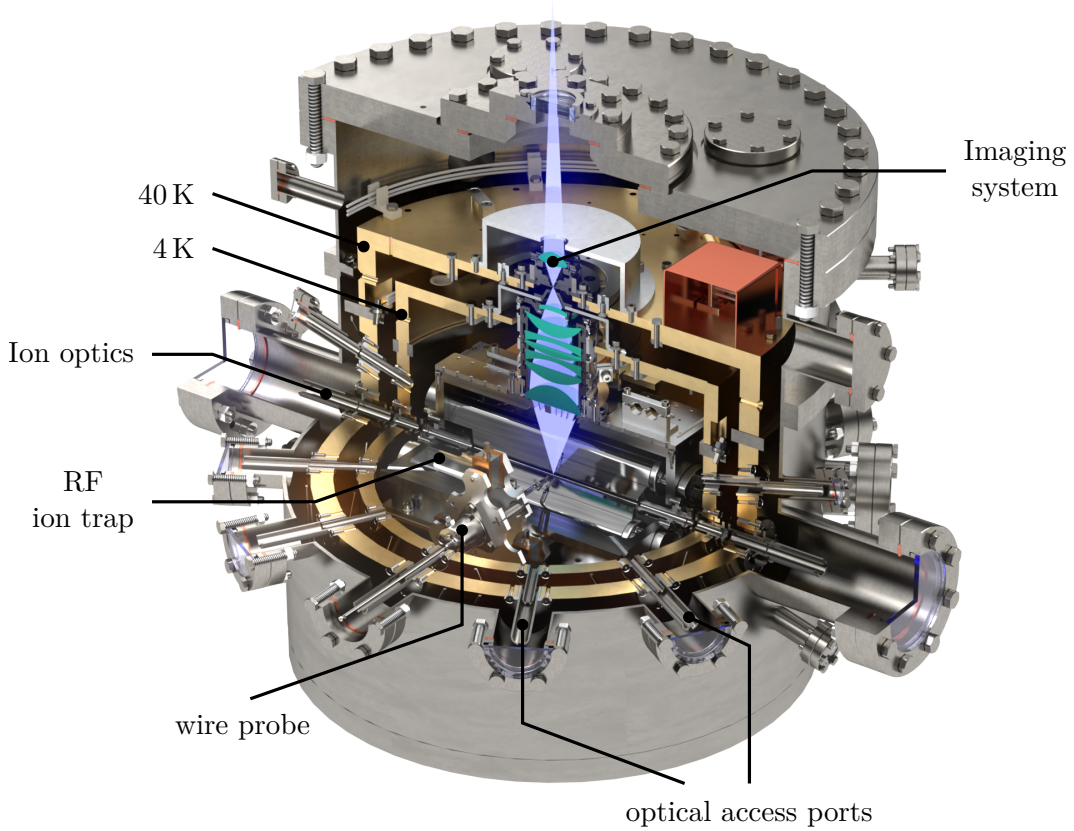

Figure 3.7: CAD model of the trap chamber. The two nested temperature stages enclose the inner trap region at 4 K. It houses the rf ion trap, parts of the imaging system, the wire probe alignment system, and ion optics elements for the injection of HCIs from the EBIT. Not shown is the low-vibration cryogenic supply, which is connected to the lower end of the trap chamber, see Fig. 3.2. Pictures of the two cryogenic shields around the trap region as well as the rf ion trap installed inside the 4 K enclosure of the trap chamber are shown in Fig. A.4 and Fig. A.3, respectively.

addition, the setup contains several ion optics elements, which allow to guide and focus HCIs from the EBIT into the Paul trap.

In the following, an overview of the main design features will be given. This includes the design of the cryogenic shields, which was inspired by the predecessor experiment at MPIK [Sch+12] as well as the CryPTEx-PTB setup [Leo+19].

3.2.1 The experiment cold stage

The two cryogenic shields enclosing the superconducting ion trap are mounted inside the vacuum chamber in a nested configuration. Mounting of the first temperature stage inside the trap chamber and the second stage inside the first stage is realized by two sets of twelve counteracting stainless-steel spokes (see Sec. 3.1.3). The spokes are distributed symmetrically with respect to the trap center. This ensures a high mechanical stability of the mounting and reduces the relative displacement of the trap center with respect to the optical table during cooldown.

The cryogenic shields consist of a cylindrical body, which is closed using two large lids installed above and below the trap center. The shields are made of high-purity OFHC copper ($> 99.99\,\%$) and have a thickness of 17 mm and 12 mm at the first and the second temperature stage, respectively. This ensures proper thermalization and a homogeneous temperature distribution of the shields. Furthermore, since the electrical conductivity of high-purity copper increases dramatically at low temperatures, eddy currents induced inside the copper shields decay only very slowly. Therefore, external ac magnetic field noise is efficiently shielded by the copper enclosure. This was measured at the similar setup of CryPTEx-PTB [Leo+19], for which a suppression of 30 - 40 dB was reported for frequencies between 60 Hz and 1 kHz.

Optical access to the trap center is granted by twelve optical ports in the horizontal plane, one every 30°. The two ports along the trap axis are equipped with two einzel lenses at each side of the ion trap, which are used to guide the injected and transmitted HCIs. One additional port is assigned for the wire probe alignment system. The remaining nine ports are distributed between the lasers for photoionization of beryllium, cooling of $^9Be^+$, and spectroscopy of HCIs as well as the beryllium atomic beam (see Fig. 3.15).

In order to restrict the solid angle of the trap center to the room temperature environment, long and thin stainless steel tubes are mounted to each port. This is needed for two reasons. First, the flux of thermal radiation is reduced which suppresses heating of the cryogenic shields (see Sec. 3.1.3). Second, particle flux from room temperature through optical access ports can drastically reduce the storage times of HCIs in cryogenic Paul traps by collisions and charge-exchange reactions [Sch12; Sch17]. This is suppressed by the tubes mounted to the second temperature shield. With a distance from the trap center of 185 mm and a diameter of 6 mm, the ten optical ports have a total solid angle of $0.07\,\%$ of $4\,\pi$. Additionally, the two electrostatic lenses mounted at a distance of 150 mm to the trap center have a diameter of 5 mm, which adds $0.014\,\%$ of $4\,\pi$. The opening used for the imaging of trapped ions contributes only to radiative heating, since the access to the trap center is blocked by the lens stack. Therefore, $0.084\,\%$ of the solid angle at the center of the trap are exposed to particle flux from room temperature, which improves upon the $2\,\%$ reported for the predecessor experiment CryPTEx [Sch+12] and compares well to the values of the PTB setup [Leo+19].

The experimental cold stage at 4 K has an inner diameter of 269 mm and a height of 180 mm. In its center, the superconducting rf ion trap is mounted on a solid platform made of high-purity OFHC copper ($> 99.99\,\%$), which ensures homogeneous thermal-

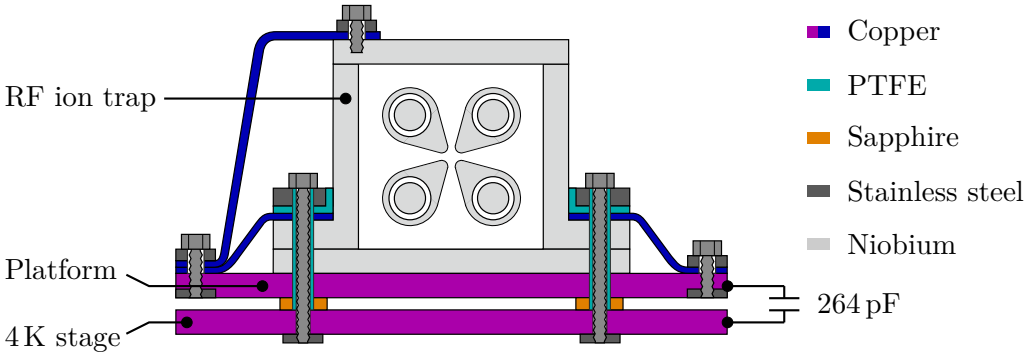

Figure 3.8: Schematic drawing of the copper platform holding the rf ion trap (not to scale). Sapphire crystals (orange) are used to decouple the dc potentials of platform and 4 K stage, while ensuring proper thermalization. For a homogeneous temperature distribution of the trap, the three parts of the cavity housing made of niobium are individually thermalized with the platform using copper links (blue). The rf grounding of the cavity is indicated by the capacitance connecting the platform to the 4 K stage.

ization of the trap. As described in Sec. 4.2, the cavity housing consists of a monolithic body, which is closed by two lids above and below the trap center. In order to thermalize the upper lid as well as the monolithic housing, additional copper parts are mounted around the cavity. This can be seen in Fig. 3.8. The copper platform is mounted to the bottom of the 4 K stage using four sapphire crystals. Each crystal has a height of 5 mm and a cross section of $13 \times 13\,\mathrm{mm}^2$. The high thermal conductivity of sapphire of $230\,\mathrm{W(Km)}^{-1}$ at 4 K [Eki06] ensures proper thermalization with the second temperature stage. Additionally, the crystals isolate the trap from the electrostatic potential of the trap chamber. This is needed in order to bias the trap during the injection and retrapping of HCIs (see Sec. 4.5.2).

Access to the inner trap region can be necessary in case of maintenance work, to adjust the alignment of the individual parts of the imaging system or to change the coupling strength of the inductive rf coupler of the cavity (see Sec. 4.2.5). In order to allow for easy access, the trap chamber has a modular design. The ion-trap environment can be accessed from the top by opening the upper CF400 flange of the trap chamber and removing the two lids of both cryogenic stages. This can be seen in Fig. A.3. In this process, the cryogenic shields remain in position and the alignment of the 4 K region to the optical setup or the HCI beamline remains unchanged. Additionally, the cabling of the ion trap comprising 32 dc wires and 3 coaxial cables, is inserted from the top. They can be easily removed and reinstalled without soldering (see Sec. 3.2.2).

3.2.2 Paul trap electronics

The electrical connections to the cryogenic trap region are provided using 32 dc wires, which supply the dc electrodes of the ion trap, electrostatic lenses, temperature sensors and allow to bias the rf cavity to an elevated ground. Additionally, the rf antennas of the cavity are supplied using three coaxial cables. As described in Sec. 3.1.3, all cables are thermalized at each temperature stage with more than 0.8 m cable length in between to suppress heating of the cryogenic stages by thermal conduction.

In order to allow for easy access to the trap region during maintenance work, the electrical connections are structured in a modular layout. For the electrostatic potentials, the wires are interconnected using cryo-compatible multi-pin connectors[11] between the different temperature stages and on top of the ion trap (see Fig. A.3). The coaxial cables are equipped with SMA plugs[12] on both ends. This allows to completely remove the cabling or the ion trap from the vacuum chamber without any soldering.

The ion trap and the trap platform are dc-wise disconnected from the cryogenic environment by mounting the cavity on sapphire crystals (see Fig. 3.8). In order to decouple the electrostatic potential of the coaxial cables from the trap chamber and the external electronics, floating SMA feedthroughs and dc blocks are used. The latter filter any dc component on signal line or cladding using capacitors. For rf grounding of the trap region, the cavity is capacitively coupled to the 4 K cryogenic shields using twelve capacitors of 22 nF each. This corresponds to a total impedance of 18 mΩ at the resonance frequency of the cavity around 34.52 MHz.

The electrostatic potentials of the dc electrodes are filtered using two-way, single-stage low pass filters, similar to the ones presented in [Leo+19]. A schematic drawing of the 4 K electronic circuit connecting the dc electrodes to the external power supply is shown in Fig. 3.9. The filter boards made of Rogers 4350B are mounted on top of the superconducting cavity at 4 K, which suppresses the Johnson-Nyquist noise [Joh28; Nyq28] of the filter components. Signals towards the trap electrodes are filtered with a cutoff frequency of 30 Hz to increase the stability of the trapping potentials. Accordingly, the rf signals picked up by the dc electrodes are filtered with a cutoff frequency of 30 mHz in order to protect the dc power supply at room temperature. This is necessary due to the high geometric capacitance (15 pF) between the dc and rf electrodes of the cavity (see Sec. 4.2.3), due to which a significant fraction of the rf voltage amplitude is picked up by the dc electrodes. In order to limit the outcoupled fraction of the stored electromagnetic (em) energy inside the cavity, the external circuit is additionally decoupled using 66 MΩ resistors directly at the cavity housing.

The room temperature electronics consist of several 16 bit digital-to-analog converters[13], which supply the dc electrodes of the cavity with individual electrostatic potentials. The rf signals for the cavity are supplied by a signal generator[14]. Due to the high quality factor of the cavity (see Chapter 5) and the resulting enhancement of em fields inside the

[11] model 02-31-036 from CMR Direct
[12] model 235-CON-SMA-V2 from Allectra GmbH
[13] model NI PCI-6703 from National Instruments
[14] model SMB100B from Rohde & Schwarz GmbH & Co. KG

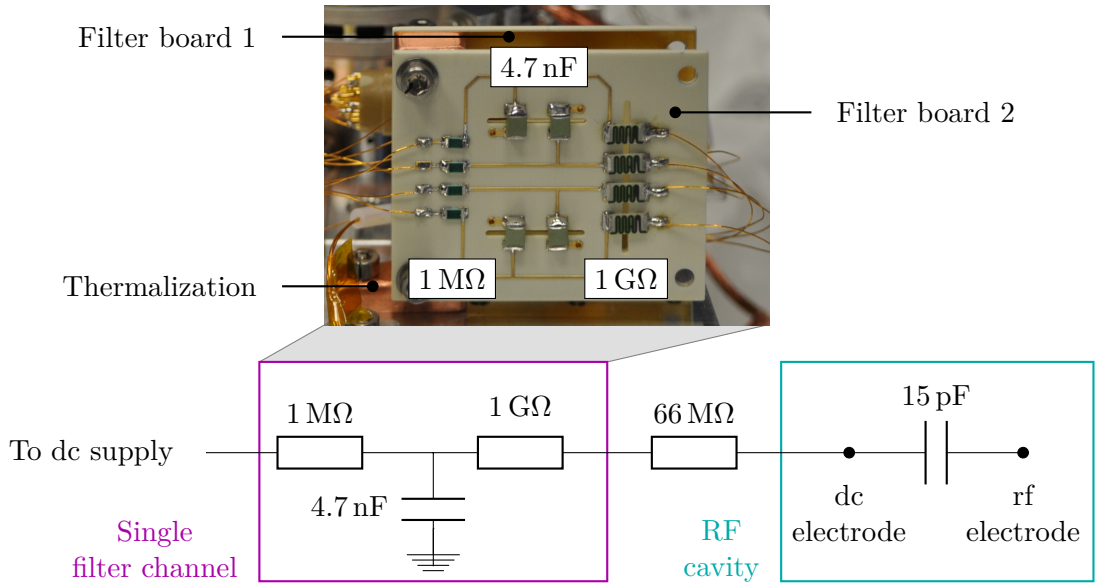

Figure 3.9: Overview of the 4 K electronic circuit connected to the dc electrodes of the ion trap. **Top:** Picture of the cryogenic filter boards mounted on top of the superconducting cavity. Each board contains four channels, which are used to filter the electrostatic potentials of the dc electrodes. **Below:** Schematic drawing of the 4 K electronic circuit connecting a single dc electrode to the external power supply. For details see text.

trap, no additional amplification of the supplied rf potentials is required and the signal generator can be directly connected to the ion trap. However, due to the significant reflected power from the cavity, an rf amplifier[15] is added in between to protect the rf generator.

For the trapping of $^9Be^+$ ions, the cavity is supplied with rf levels between 18 dBm and 21 dBm and dc electrode potentials on the order of 1 V. The elevated platform is set to dc ground. For the retrapping of HCIs, the cavity as well as the dc electrodes can be biased to 130 V to decelerate the injected ions.

3.2.3 The imaging system

The imaging system used to collect fluorescence of trapped ions from the trap center was developed and characterized in [War19] and can be seen in Fig. 3.10. It is designed to yield a maximum collection efficiency at 313 nm to detect and image the fluorescence photons of the cooling transition of $^9Be^+$.

The imaging system consists of eight lenses at the cryogenic stages, which collect the light from the trap center and focus it onto the detection system at room temperature.

[15] model 110LC from RF Power Labs

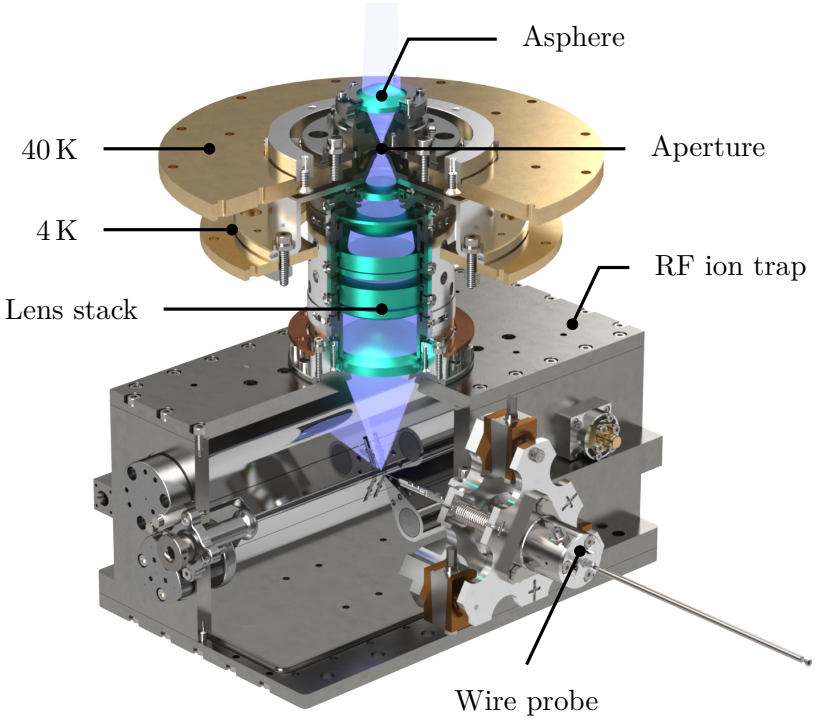

Figure 3.10: CAD model of the cryogenic parts of the imaging system. Fluorescence photons from the trap center are collected by the lens stack on top of the rf ion trap and focused onto a 2 mm aperture in between the two cryogenic stages. The asphere at 40 K refocuses the light onto the detection system at room temperature. A picture of the imaging system mounted to the rf ion trap is shown in Fig. A.2.

Here, the light is equally divided with a beamsplitter and subsequently detected using an electron multiplying charge-coupled device (EMCCD) camera[16], used for crystal diagnostics and imaging, and a photomultiplier tube[17] to investigate ion dynamics. Care must be taken to restrict the solid angle of the trap region to 40 K and room temperature to avoid radiative heating of the 4 K stage. Thus, an intermediate focus between the two cryogenic shields is employed, which allows to introduce an aperture of 2 mm diameter.

The lens stack at 4 K is directly mounted onto the housing of the niobium cavity, which avoids misalignment during cooldown. It is placed at a working distance of 57 mm to the trap center and features a numerical aperture of NA = 0.365. This yields a collection efficiency around 3.45 % at the design wavelength of 313 nm, which corresponds to 2.17 % at the detection system including reflection and absorption losses of the optical elements [War19; War20]. An asphere, positioned inside a movable mount at the 40 K

[16] model iXon Ultra 888 from Andor
[17] model H10682-210 from Hamamatsu

stage behind the intermediate focus, is used to focus the incident light onto the detection system. By adjusting the vertical distance between asphere and intermediate focus, the magnification of the image can be varied between 7.8 and 20.

Each lens is mounted inside a flexible ring holder, which positions the lens by applying a uniform radial pressure. This ensures that the total pressure on the lens stays constant during cooldown and, therefore, avoids damaging of the lens as well as misalignment.

In order to limit chromatic aberrations of the optical setup, different lens materials were used (ultraviolet (UV) fused silica and CaF_2). Thereby, the wavelength range for which photons are efficiently collected is extended and a total collection efficiency of the imaging system above 1.1 % (including absorption and reflection losses of the optical elements) between 300 nm and 440 nm is achieved [War20]. This allows for the application of optical fluorescence spectroscopy on trapped HCIs, e.g. the hyperfine transition of $^{40}Ar^{13+}$ at 441 nm [Mäc+11; Egl+19; Mic+20]. Additionally, even photons at 235 nm originating from the spontaneous decay of the resonantly excited intermediate state during photoionization of beryllium (see Sec. 3.3.2) can be detected to optimize the loading efficiency of $^{9}Be^{+}$ ions.

Since the main parts of the imaging system are located at the cryogenic stages, they have to be aligned before cooldown. For the commissioning experiments described in this thesis, the imaging system was aligned by optimizing the image of the dc electrode tips illuminated with white light. This will be improved in the future using a precise method for alignment, which is described in Sec. 3.2.4.

3.2.4 Wire probe alignment system

During experiments with the cryogenic Paul trap, the alignment of the various lasers, the beryllium oven as well as the imaging system onto the center of the trap is crucial. For this purpose, a cryogenic wire probe was designed in this thesis and in [Bog19], which allows to define a reference point in the center of the trap. It is shown in Fig. 3.11.

The main parts of the wire probe system are located at 4 K and mounted onto a horizontal port of the cavity housing perpendicular to the trap axis (see Fig. 3.10). This avoids misalignment during cooldown. At the tip of the wire probe, a tungsten wire with 50 µm diameter is fixed to a titanium rod. It can be moved axially to position the wire tip in the trap center using a linear drive at room temperature, which is connected to the rod using two interconnected chain links. To prevent thermal bridges between different temperature stages, the links can be disconnected during operation (not shown in Fig. 3.10 or Fig. 3.11).

The titanium rod is suspended using two ball-bearings, which are separated axially by 25 mm. Each bearing consists of three sapphire spheres with 1.5 mm diameter, which are guided using shallow channels inside the bearing and the titanium rod. These channels limit the axial travel range of the probe and, thus, avoid damaging the trap electrodes. Additionally, the tip can be completely retracted into the opening inside the cavity housing to minimize the outcoupled fraction of the em energy stored inside the cavity. In order to maintain the wire orientation and ensure a constant force onto the titanium rod during cooldown, the upper sapphire spheres of both bearings are pressed onto

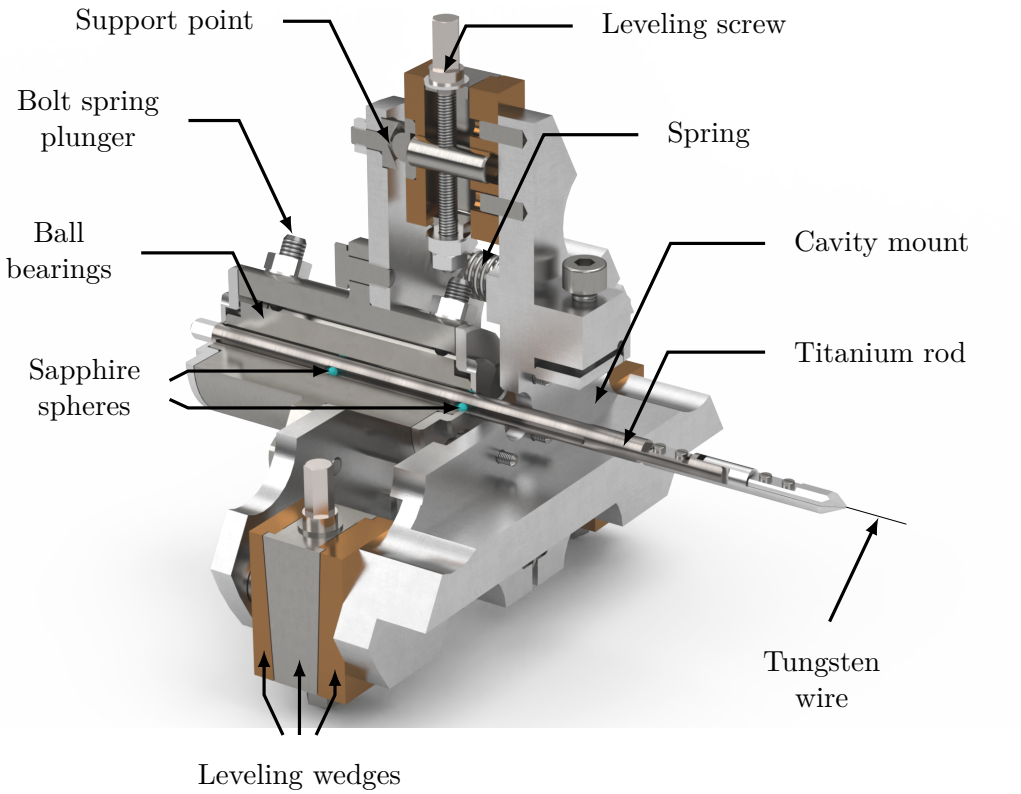

Figure 3.11: Section view of the CAD model of the wire probe alignment system. It is mounted to the cavity housing to define a reproducible reference point in the center of the ion trap (see Fig. 3.10). One support point of the three-point rest, which connects the ball bearings to the cavity mount using leveling wedges, is indicated. The connection of the titanium rod to the linear drive at room temperature is not shown here. For details see text. Modified from [Bog19].

the titanium rod using bolt spring plungers. Both sapphire and titanium exhibit small thermal expansion integrals [Eki06], which guarantees full functionality of the bearings after cooldown. Furthermore, the use of sapphire as a hard material avoids abrasion in the trap region.

In order to allow for precise positioning of the wire tip inside the cavity, the bearings are connected with a three-point rest to the cavity mount, which is fixed to the cavity housing. The orientation as well as the distance to the cavity mount can be adjusted using three high-precision leveling wedges held together by stainless steel springs. The height of each wedge mount can be individually modified using a fine-thread M3 $\times$ 0.25 screw, which defines the position of the central wedge. Due to the small inclination of its opposing surfaces of 6°, a full rotation of the screw changes the angle of the wire

probe by 0.024° and moves the wire tip in the trap center by 40 µm. This should allow to position the wire tip with a precision below 5 µm.

In order to align the cryogenic parts of the imaging system before cooldown, the wire probe is precisely positioned in the geometric center of the cavity. Subsequently, the image of the wire tip illuminated with a 313 nm laser is optimized by adjusting the position of the individual components of the imaging system. After cooldown, the lasers as well as the beryllium oven (see Sec. 3.3.1) are aligned to the trap center by detecting overlap with the wire tip. This method promises to be very robust as well as reproducible and should allow for efficient realignment of all critical components of the experiment after maintenance intervals. Additionally, the wire probe can be used for a wide range of wavelengths and requires only little photon flux to detect overlap with the reference point. This will be used in the near future for the alignment of spectroscopy lasers probing long-lived optical transitions or transitions in the XUV region of trapped HCIs. For the latter, a fluorescing coating can be applied to the wire tip. Since the wire probe was still under construction during commissioning of the trap, it was not installed for the experiments presented in this thesis.

3.3 Production and cooling of $^{9}Be^{+}$ ions

The production and laser cooling of $^{9}Be^{+}$ ions is implemented similarly to the CryPTEx experiment, as described in [Sch17]. First, a thermal beam of beryllium atoms is produced inside an atom oven (Sec. 3.3.1) and directed towards the center of the cryogenic ion trap. Here, it is superimposed with the photoionization laser, which results in partial ionization of the atomic beam via a resonance-enhanced two photon process (Sec. 3.3.2). The produced ions are subsequently confined inside the Paul trap and laser-cooled using the scheme described in Sec. 3.3.3.

3.3.1 Production of an atomic beryllium beam

A thermal beam of neutral beryllium atoms is produced inside an atom oven and subsequently collimated on its way towards the ion trap. The design of the beryllium oven is adapted from [Sch17] and can be seen in Fig. 3.12.

The center piece is an Al_2O_3 crucible with an inner diameter of $d_1 = 1.6$ mm. It is filled with several stripes of 30 µm thick beryllium foil amounting to a total load of approximately 10 mg. The crucible is held in position by a tungsten heating coil, which is surrounded by an Al_2O_3 tube and a heat shield made from tantalum. The latter reflects a fraction of the emitted thermal radiation back onto the oven and thereby suppresses radiative cooling. An additional aluminium housing around the oven is used to avoid contamination of vacuum chamber and TMPs by restricting the beam emittance.

In order to maintain XHV pressures below 10^{-14} mbar inside the cryogenic environment, two apertures ($A_{1,2}$) are used to separate the first and second stage of the differential pumping system from the Paul trap vacuum. Additionally, the skimmer K_1 is used to further reduce the atomic beam width inside the trap. This is necessary since

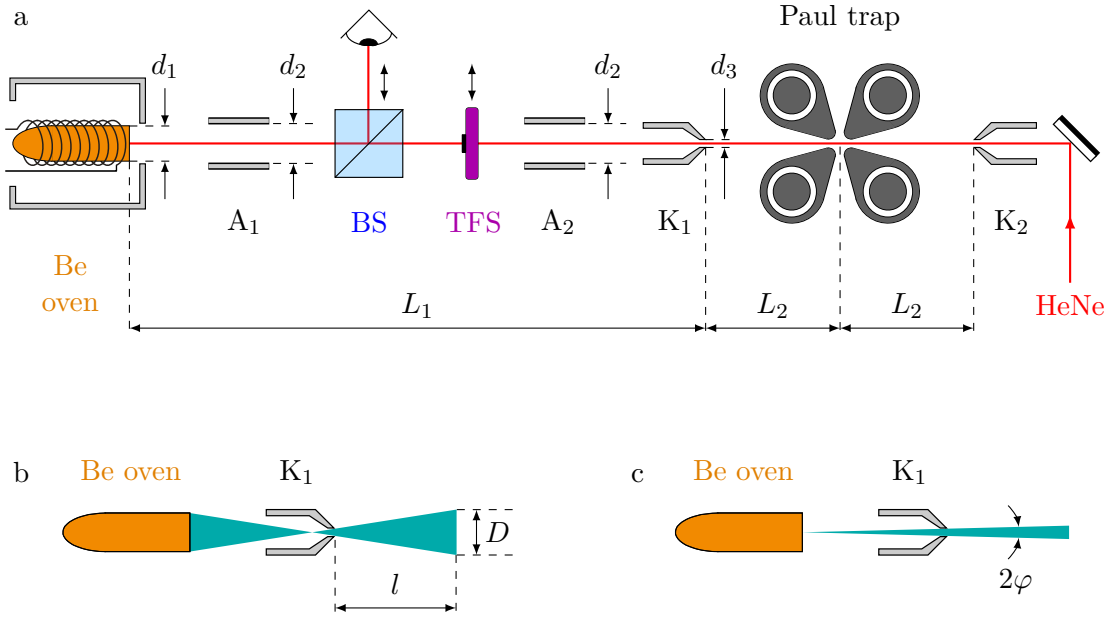

Figure 3.12: Schematic drawing of the beryllium oven. (**a**) The atomic beryllium beam is emitted from the oven and collimated using two 60 mm long apertures A_i of diameter $d_2 = 3\,\text{mm}$. The skimmer K_1 with diameter $d_3 = 800\,\mu\text{m}$ at a distance of $L_1 = 876\,\text{mm}$ from the oven and $L_2 = 58\,\text{mm}$ from the trap center restricts the maximum beam width inside the trap. For diagnostics and alignment, a beamsplitter (BS) and a thin-film sensor (TFS) can be moved into the atom beam. The maximum beam diameter D and collimation angle φ inside the trap are geometrically estimated by treating the oven as an extended source (**b**) or point source (**c**), respectively. For details see text.

already small amounts of deposited beryllium on the trap electrodes can lead to patch potentials and motional heating of the trapped ions (see Sec. 4.1.1).

An upper limit for the beam diameter inside the trap can be estimated by treating the oven as an extended source (see Fig. 3.12(b)). The maximum beam diameter D at distance l behind skimmer K_1 is given by

$$D(l) = d_3 + \frac{l}{L_1}(d_1 + d_3) \quad , \tag{3.6}$$

which results in an atomic beam diameter of about 960 µm throughout the trap region. This avoids deposition of beryllium atoms from the oven onto the trap, as the minimum distance of the quadrupole electrodes amounts to 1.95 mm.

During operation, the oven is typically heated to a temperature of 1250 K. This results in a mean velocity of the Maxwell–Boltzmann distribution for beryllium atoms around $1715\,\text{ms}^{-1}$ [Lau05]. For efficient photoionization of atoms inside the interaction region of superimposed laser and atomic beam, the number of atoms which are addressed

by the laser needs to be maximized. Since the ionization process includes the resonant excitation of an intermediate state (see Sec. 3.3.2), the relative Doppler shift needs to be smaller than the linewidth of the excited state.

Using a relative angle of 90° between atomic beam and photoionization laser reduces the first order Doppler shift to the transversal velocity component of the atoms, which depends on the collimation angle of the atom beam φ. It can be calculated by treating the beryllium oven as a point source (see Fig. 3.12(c)). This is a valid approximation, since both the diameter of the oven d_1 as well as the diameter of the skimmer d_3 are small compared to the distance L_1 between oven and skimmer: $d_1, d_3 \ll L_1$. The full opening angle of the atomic beam is given by

$$2\varphi = 2 \arctan\left(\frac{d_3}{2L_1}\right) \simeq 0.91\,\text{mrad} \quad . \tag{3.7}$$

Since the transversal velocity component scales with $\sin(\varphi) \simeq 5 \times 10^{-4}$, the standard deviation of the first order Doppler shift [Lau05] is on the order of 2 MHz. This is smaller than both the linewidth of the photoionization laser of about 4 MHz [Sch17] as well as the linewidth of the intermediate excited state of beryllium of 87.9 MHz [Kra+19]. Therefore, all atoms in the interaction region are simultaneously addressed by the photoionization laser.

Due to the small diameter of the skimmer K_1, the beryllium oven needs to be precisely aligned with respect to the trap center. This is accomplished using a HeNe alignment laser, as shown in Fig. 3.12(a). First, the HeNe laser is guided through the center of the two skimmers, which are positioned symmetrically around the trap region. Subsequently, the position of the beryllium oven is adjusted using an off-axis port aligner until the HeNe spot is centered inside the Al_2O_3 tube of the oven. This can be visually observed using a retractable beamsplitter.

The emitted flux of beryllium atoms can be measured using a retractable thin-film sensor[18], which is mounted at a distance of 470 mm from the crucible. During commissioning of the oven, a measurement of the emitted flux was performed at a heating current of 13 A in the tungsten filament. The corresponding oven temperature was estimated to 1410 K using an optical pyrometer. This method is typically limited to an accuracy of 100 K [RS95].

The flux measurement yields a total deposited mass of about 20 µg over a period of 1.5 h. This corresponds to an average deposition rate of 2.5×10^{11} beryllium atoms per second. Assuming that the complete detector surface with 8 mm diameter was homogeneously covered with beryllium, a lower limit for the flux inside the trap region is estimated to 7.2×10^8 atoms per second.

This is in agreement with the expected values using the derivation in [Sch17]. For the oven geometry shown in Fig. 3.12, a flux of 1.2×10^8 to 1.1×10^9 atoms per second at the position of the trap is expected at oven temperatures between 1250 K and 1350 K.

[18] model TF-BSH from LewVac Components Limited

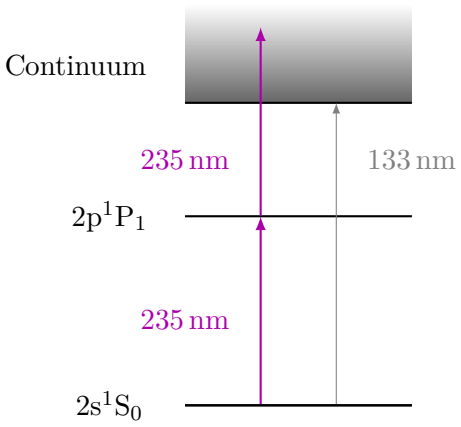

Figure 3.13: Reduced electronic level structure of ^{9}Be in singlet configuration (not to scale). Beryllium is ionized using resonance-enhanced two-photon ionization at 235 nm via an intermediate excited state. For details see text.

3.3.2 Photoionization of beryllium

The reduced electronic level structure of atomic beryllium in singlet configuration is shown in Fig. 3.13. Its ground state, 2s ^{1}S$_0$, has an ionization threshold of 9.32 eV, which corresponds to a wavelength of 133 nm [Kra+19]. As such low wavelengths are technically challenging to generate and handle, a two-step ionization process via a resonantly excited intermediate state is chosen.

The lowest-lying excited state, 2p ^{1}P$_1$, has a lifetime of 1.8 ns, which corresponds to a natural linewidth of 87.9 MHz [Kra+19]. It is connected to the ground state by a dipole-allowed transition at 5.28 eV, which corresponds to a wavelength of 235 nm. The excited state with an ionization threshold of 307 nm can then be ionized by non-resonant absorption of a second 235 nm photon. In order to saturate the first resonant excitation step, the laser is focused to a $1/e^2$ beam diameter of about 250 µm in the center of the trap. Typical laser powers used during the experiments of this thesis are on the order of 1.5 mW. However, reproducible loading of small ion crystals was also performed using smaller laser powers around 80 µW.

The laser system for photoionization is described in [Sch17; Ebe13]. Radiation at 235 nm wavelength is produced in two steps from a commercial diode laser as reported in [Lo+14]. First, light at 940 nm is frequency doubled to 470 nm inside an enhancement cavity using a PPKTP (periodically poled potassium titanyl phosphate) crystal. The subsequent second doubling stage is realized using cavity-enhanced frequency doubling inside a beta barium borate (BBO) crystal. This allows to generate 235 nm radiation with up to 10 mW power.

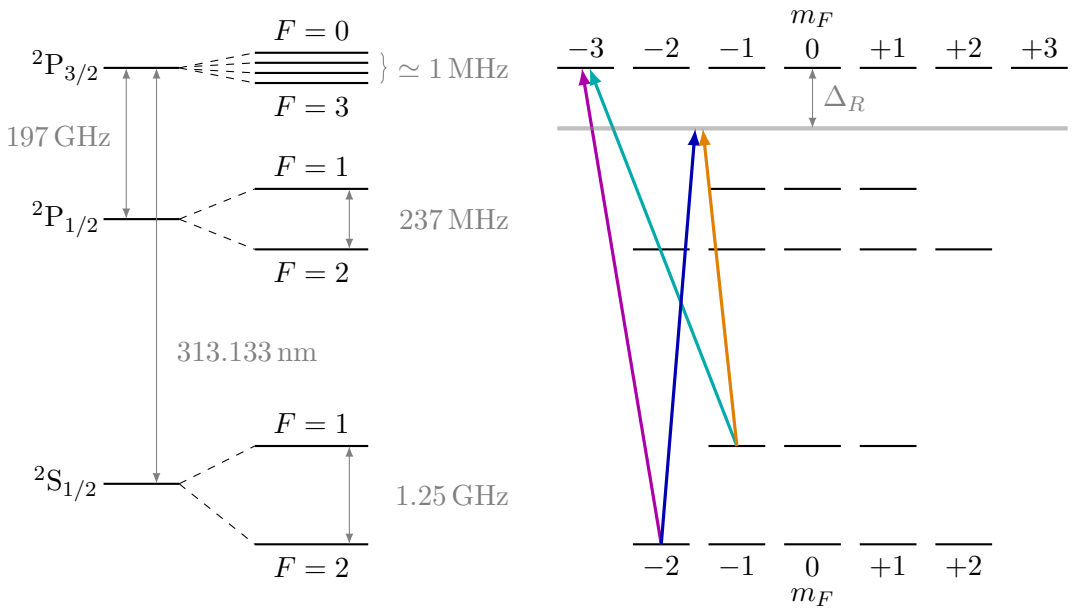

Figure 3.14: Energy level structure of $^9Be^+$ containing the relevant states for laser cooling (not to scale). The hyperfine structure of the excited $^2P_{3/2}$ state ($\simeq 1$ MHz [Mon+95]) is smaller than its natural linewidth and not shown on the right side. The lasers for Doppler cooling (magenta) and repumping (cyan) are shown for the case of σ^- polarization. Additionally, a possible Raman laser configuration for resolved sideband cooling is shown. Both Raman beams (orange and blue) are detuned by Δ_R to the closest resonant excitation. For simplicity, the Zeeman substates with different m_F are drawn energetically degenerate.

3.3.3 Laser cooling of $^9Be^+$

The reduced level structure of singly charged beryllium containing the relevant electronic states for laser cooling is shown in Fig. 3.14. It has an electronic ground state configuration of $[He]2s^1$ and features a single valence electron. Since the closed $1s^2$ shell cannot be excited using optical wavelengths, the ion can be treated here as a quasi one-electron system. Due to the nuclear spin of beryllium, the ground state $^2S_{1/2}$ splits into the two hyperfine levels $F = 1$ and $F = 2$, which are separated by 1.25 GHz [Kra05].

Doppler cooling is performed on the $^2S_{1/2}(F = 2) \rightarrow {}^2P_{3/2}$ transition at 313.133 nm [Kra05]. The excited state has a natural linewidth of $\Gamma/2\pi = 17.97$ MHz [Kra+19] which corresponds to a lifetime of about 8.9 ns. Closed-cycle excitation can be achieved using pure σ^+/σ^- polarization to drive transitions between the Zeeman sublevels $|F, m_F\rangle$ of ground and excited state, $|^2S_{1/2}, 2, \pm 2\rangle$ and $|^2P_{3/2}, 3, \pm 3\rangle$. This is shown in Fig. 3.14 for the case of σ^- polarization. In case of imperfect polarization of the cooling laser, some population of the ground state is transferred to the $^2S_{1/2}(F = 1)$ state. This is

depopulated using a repumper laser, which has the same polarization as the cooling laser and connects the $F = 1$ ground state hyperfine level to the excited state.

Usually, a bias magnetic field is applied to align the quantization axis at the position of the ions with the propagation direction of the cooling laser. However, for the commissioning experiments presented in this thesis, no bias magnetic field was applied and the quantization axis is given by the ambient magnetic field. Therefore, efficient laser cooling requires high intensities of the repumper laser compared to similar experiments [Leo18]. Typical laser intensities amount to 1 mW for the cooling laser and 0.5 mW for the repumper, with $1/e^2$ beam diameters in the trap center of 340 µm and 310 µm, respectively.

After initial Doppler cooling, the ions can be cooled to their motional ground state using resolved sideband cooling, see Sec. 2.2.2. A possible implementation for $^9Be^+$ following [Leo18] is shown in Fig. 3.14. The two hyperfine levels of the ground state are connected by a two-photon Raman transition via a virtual excited state. By choosing this virtual level at about half-way in between the $^2P_{1/2}$ and $^2P_{3/2}$ states, a large common detuning Δ_R of the two Raman beams to the closest resonant excitation is achieved. This reduces the off-resonant scattering rate $\propto 1/\Delta_R^2$ and simultaneously allows for reasonably high Rabi frequencies $\propto 1/\Delta_R$ of the sideband transitions [Win+98a].

The UV laser systems for Doppler cooling are described in [Sch17]. Radiation at 313 nm is produced by non-linear processes from longer wavelength radiation following a two-step method described in [Wil+11]. In a first step, sum frequency generation of two infrared fibre lasers at 1051 nm and 1550 nm inside a PPLN (periodically poled lithium niobate) crystal yields light at 626 nm wavelength. Subsequent cavity-enhanced frequency doubling using a BBO crystal allows to generate 313 nm radiation with up to 300 mW power. A small fraction (10 %) of the 313 nm light is then frequency shifted using an acousto-optic modulator (AOM) setup for the repumper laser.

Due to the large detuning between the Doppler cooling wavelength and the Raman transitions, $\Delta_R \simeq 100$ GHz, an additional laser source at 313 nm is required for sideband cooling. This will be implemented in the future based on a commercial UV laser system[19] producing 313 nm light by frequency quadrupling of a diode laser.

3.4 Optical setup

For the commissioning of CryPTEx-II described in Chapter 5, the experiment was set up on the first floor of the experimental hall at MPIK. The laser systems for photoionization of beryllium and Doppler cooling of $^9Be^+$ are located directly below on the ground floor. They are shared between the two Paul trap experiments, CryPTEx-I & -II. The laser beam guidance to the first floor laboratory will be described in the following. Additionally, the optical setup around the ion trap and the allocation of the optical access ports to the trap center, as can be seen in Fig. 3.15, is covered.

The UV lasers located at the ground floor are guided over a distance of about 8 m to the optical table of CryPTEx-II through free space. Beam delivery using UV fibres

[19] model TA-FHG pro from TOPTICA Photonics AG

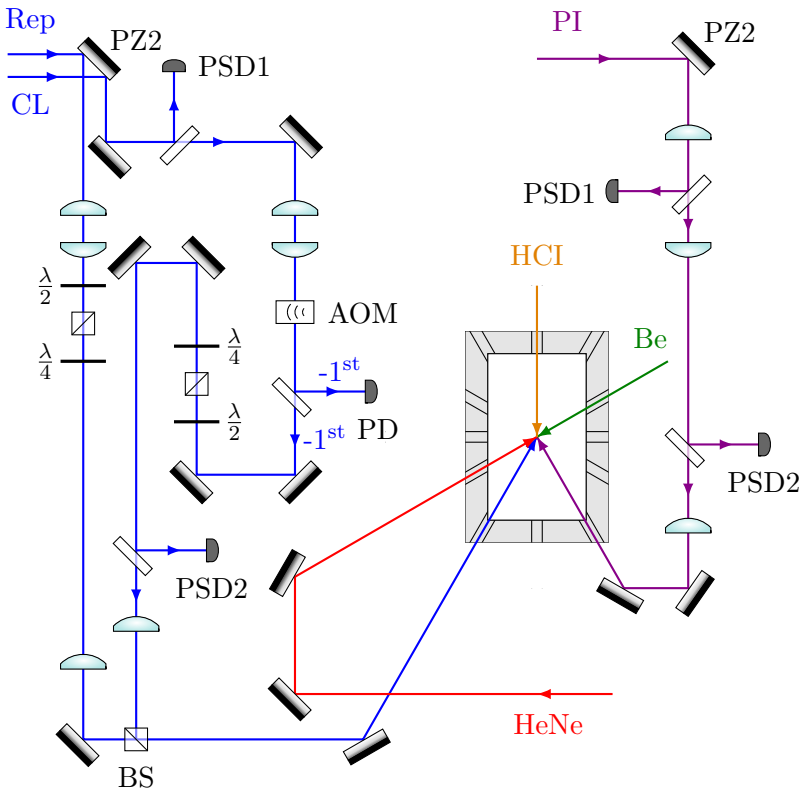

Figure 3.15: Schematic drawing of the optical setup around the ion trap (not to scale). The UV lasers for Doppler cooling (CL, blue), repumping (Rep, blue) and photoionization (PI, magenta) are delivered from the laboratory one story below, where the piezo-driven mirrors (PZ) for the first stage of the pointing stabilization are located (not shown). The intensity of the cooling laser is stabilized using a photodiode (PD). Cooling and repumper laser are overlapped using a non-polarizing beamsplitter (BS). The outlines of the rf ion trap (gray) are indicated to show the allocation of the optical access ports used for the beryllium oven (Be, green), the associated HeNe alignment laser (HeNe, red) and the HCI beamline (HCI, yellow).

was not possible, since stable long-term operation with low transmission losses requires hydrogen loading and successive UV curing of the fibres [Col+14; Mar+17]. However, no manufacturer was able to supply sufficiently long hydrogen-loaded fibers to span the full distance between both optical setups. In order to account for differential vibrations between the two laboratories, the beam pointing is actively stabilized using a commercial stabilization system[20]. It was set up during this thesis and [Bog19].

[20] model compact from MRC Systems GmbH

The stabilization consists of two independent systems which are used to control the beam pointing of cooling and photoionization laser. The repumper laser is guided parallel to the cooling laser and, thereby, passively stabilized. This should be sufficient, since both 313 nm lasers take similar pathways between the two optical setups and should therefore experience comparable perturbations. Each system consists of two piezo-controlled mirrors, which stabilize the beam position at the corresponding position-sensitive detector (PSD). The error signal for stabilization is generated by supplying each PSD with a minor fraction of the laser power (100 µW), which is decoupled from the beams using beam samplers. In order to regulate the beam pointing in two spatial directions, the piezo-driven mirrors are equipped with two piezo actuators each. A first set of piezo-controlled mirrors is mounted in the ground floor laboratory and stabilizes the beam positions at the detectors PSD1 (see Fig. 3.15). These are mounted at a distance of 6.1 m from the piezos, where the lasers enter the optical setup around the ion trap. The second stage is used to stabilize the position of the beam focus inside the trap. Since the PSD cannot be placed close to the trap center, it is mounted in the corresponding virtual point. Thereby, the distance between the PSD (PSD2 in Fig. 3.15) and the associated beam sampler is identical to the distance between beam sampler and trap center.

Along the optical path of the laser beams, the piezo-controlled mirrors of the second stage are mounted in front of the beam samplers supplying the PSD of the first stage, due to spatial constraints. However, the distance between the two components (< 30 cm) is small compared to the total length of the second stage, i.e. the distance between piezo-driven mirror and the PSD, of more than 1 m. Therefore, the interference between both stages should be negligible. Additionally, care was taken to align the beam paths towards PSD1 and PSD2 non-parallel to each other. This increases the number of vibrational modes which can be detected.

The typical performance of the system was measured in [Bog19] using a test setup. Slow perturbations between 1 Hz and 70 Hz are efficiently suppressed to relative amplitudes $< 1/\sqrt{2}$, while higher frequencies lead to larger fluctuations of the beam pointing. This can be improved in the future by reducing the weight of the piezo-driven mirrors. In the current setup, three of the four piezos are equipped with 2 inch mirrors. This is necessary due to the large beam profiles originating from the initial divergence of the laser beams and the long pathway between the two optical tables. Correcting this divergence in the ground floor laboratory allows to reduce the mirror diameter to below 1 inch, which reduces the mirror weight by a factor of four. This should significantly increase the maximum frequency that can be efficiently compensated.

At the optical table around the ion trap (see Fig. 3.15), the laser beams are collimated using telescopes. This allows to reduce the $1/e^2$ beam diameters to typical values of 1.5 mm and 2.1 mm for cooling and repumper laser, respectively, and 2.5 mm for the photoionization laser. The photoionization laser is subsequently focused to the trap center using an anti-reflection coated lens with 500 mm focal length[21], which yields a $1/e^2$ beam diameter of 250 µm at the position of the ions. It enters the ion trap in the

[21] model LA4184-UV from Thorlabs GmbH

horizontal plane under an angle of 90° with respect to the atomic beryllium beam. This is crucial for efficient ionization as it suppresses the first order Doppler shift between thermal atomic beam and 235 nm photons (see Sec. 3.3.1). In order to optimize the ionization efficiency, the overlap between the beryllium beam with a diameter of 960 µm and the photoionization laser needs be maximized. Therefore, the last lens in front of the trap chamber is installed in a two-stage motorized mount[22], which allows to precisely adjust the laser focus position in the center of the trap.

Cooling and repumper laser are separated at the entrance of the optical table. Subsequently, the linear polarization of both beams is cleaned up using a combination of half-wave plate and Glan-Taylor prism, before being converted to circular polarization using a quarter-wave plate. This suppresses unwanted contributions to the laser polarization and yields a high efficiency for the Doppler cooling process (see Sec. 3.3.3). The two circularly polarized beams are overlapped using a non-polarizing 50:50 beamsplitter. They enter the trap in the horizontal plane under an angle of 30° with respect to the trap axis. Thereby, efficient cooling of all three motional modes is ensured (see Sec. 2.2.1). Both beams are lightly focused to the trap center using anti-reflection coated lenses with 1000 mm focal length[23]. This yields $1/e^2$ beam diameters at the position of the trap center of 340 µm and 310 µm for cooling and repumper laser, respectively.

The intensity of the cooling laser is stabilized using a 200 MHz AOM, similar to the method described in [Sch17]. The -1^{st} diffraction order is guided to the experiment, while the 0^{th} diffraction order is blocked. Additionally, some fraction of the -1^{st} order is detected using a photodiode. This signal is used to compensate fast intensity fluctuations of the cooling laser by adjusting the rf power supplied to the AOM and, thereby, the intensity of the detected diffraction order.

3.5 Highly charged ion source and transfer beamline

A Heidelberg compact EBIT [Mic+18] is used as a versatile source of HCIs for the CryPTEx-II experiment. It allows to produce a wide range of HCI species, which can be transported to the cryogenic Paul trap for spectroscopy using a low-energy transfer beamline [Mic20]. The EBIT as well as the beamline were assembled and characterized in [Ros19; Küh21]. A schematic drawing of the experimental setup is shown in Fig. 3.16.

HCIs are produced inside the EBIT using sequential electron impact ionization of a gaseous target. The electrons are emitted from a heated cathode and accelerated towards a set of cylindrical electrodes, also called drift tubes, by the applied potential difference. After passing the trap region, the electrons are dumped on a water-cooled collector. Gas is injected into the trap center by means of a needle valve and ionized by the impacting electrons. In order to reach a high ionization efficiency, a strong magnetic field gradient is used to focus the electron beam down to a diameter on the order of 100 µm in the interaction region. The produced ions are radially trapped by the negative space charge potential of the electron beam and axially confined by the electrostatic potential of

[22] model AGLS25 from Newport Spectra-Physics GmbH
[23] model LA4663-UV from Thorlabs GmbH

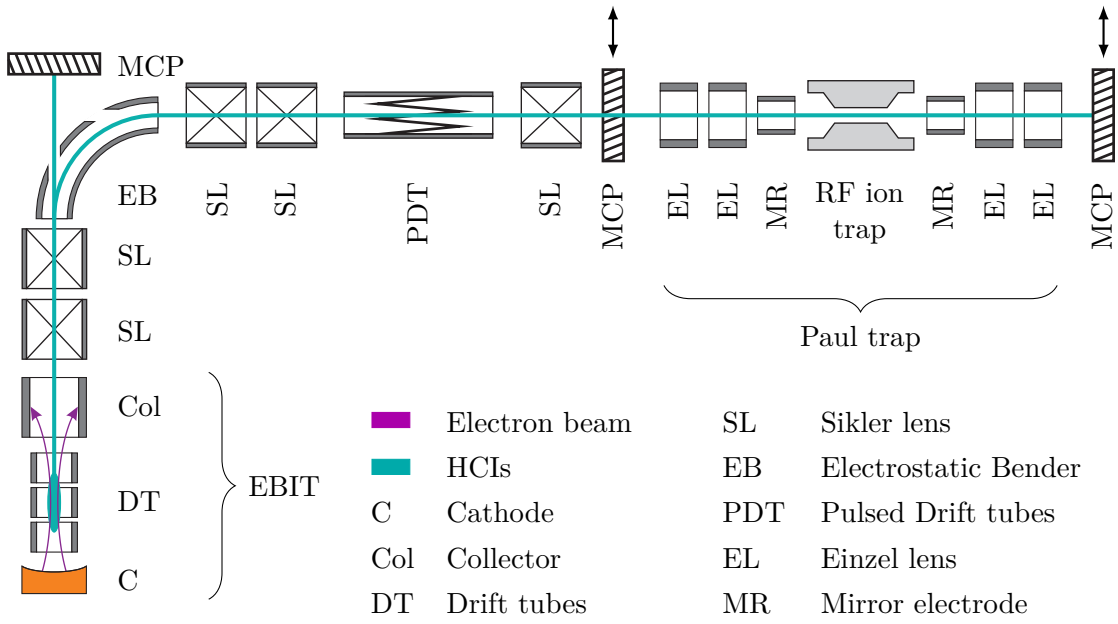

Figure 3.16: Schematic drawing of the HCI source and transfer beamline connected to the cryogenic Paul trap. For details see text.

the trap electrodes. This allows to successively ionize the target up to a maximum charge state, which is reached once the kinetic energy of the electron beam is below the ionization threshold of the target. The highest achievable charge state as well as the charge state distribution depends on the rate coefficients of the competing ionization and recombination processes, see e.g. [Dob19]. Both can be adjusted by tuning the EBIT parameters, e.g. injection pressure, breeding time, as well as electron beam energy and current.

The ions are extracted in bunches through the hollow collector by inverting the trap, i.e. increasing the potential of the central trap electrode above the adjacent ones. After the extraction pulse, which has a typical duration of 200 ns, the charge breeding process starts anew. The extracted ions enter the beamline with typical kinetic energies on the order of 695 eV $\times\, q$, where q denotes the charge state. While being guided towards the Paul trap, several electrostatic lenses, dubbed Sikler lenses [MSM11], allow to focus and steer the ion beam. A 90° electrostatic bender is used to connect the EBIT to the Paul trap. This allows for two-way optical access to the central trapping region of the Paul trap for laser spectroscopy experiments.

During transfer from EBIT to Paul trap, the different constituents of the ion bunch separate according to their charge-to-mass ratio q/m. Neglecting any focusing, which can be q/m-dependent, the TOF of the ions scales according to $t_{\mathrm{TOF}} \propto \sqrt{m/q}$ [Mic20]. This can be used to select the HCI species of interest for the injection into the Paul trap by applying short voltage pulses to one of the electrostatic lenses and, thereby, deflecting undesired ions. In order to allow for efficient retrapping inside the Paul trap (see Sec.

4.5.2), the ions are decelerated using pulsed drift tubes, which leaves them with typical kinetic energies around 130 eV $\times$ q. The serrated electrode structure of the pulsed drift tubes allows in addition for a reduction of the kinetic energy spread and refocusing of the ion bunch, as described in [Sch+15b; Ros19; Mic20].

Three microchannel plate (MCP) detectors are distributed along the beamline for ion beam diagnostics, see Fig. 3.16. The detector behind the electrostatic bender is used for charge-state identification by measuring the TOF of the ions. This allows to optimize the charge breeding inside the EBIT for the desired charge state. A second, retractable detector in front of the Paul trap is equipped with a retarding grid, which allows to determine the kinetic energy and energy spread of the HCIs before they enter the Paul trap. Finally, the MCP behind the Paul trap is used to optimize the beamline parameters for the retrapping process.

4

The Superconducting Radio-Frequency Cavity

The novel superconducting radio-frequency (rf) cavity developed in this thesis constitutes the main part of the cryogenic Paul trap experiment CryPTEx-II, described in Chapter 3. It represents a unique combination of resonator and Paul trap and is designed to confine ions in the low-noise rf potentials of the cavity. This concept promises to yield ultra-stable trapping potentials as well as greatly suppressed motional heating rates of trapped ions.

The following description of the superconducting rf cavity starts with a discussion of the general concept and the basic working principle of the presented resonator ion trap combination (Sec. 4.1). Subsequently, the cavity design is described in Sec. 4.2, followed by a brief summary of the cavity fabrication and material selection (Sec. 4.3). The second part of this chapter contains various simulations, which were performed to evaluate the cavity performance and optimize its geometry. Simulations of the resonant modes and estimates of different cavity loss mechanism are discussed in Sec. 4.4. In addition, Sec. 4.5 provides simulations of the trapping potentials of the Paul trap and the retrapping process of highly charged ions (HCIs). The chapter closes with a brief discussion of the possible application of image current detection techniques to determine the quantum state of ions confined inside the cavity (Sec. 4.6).

4.1 Concept

The cavity developed in this thesis is designed to produce low-noise rf potentials, which allow to confine ions in extremely stable pseudopotentials with suppressed motional heating rates. Thus, the typical sources for motional heating of trapped ions in Paul traps, which are described in Sec. 4.1.1 based on [Bro+15], have to be suppressed. This is achieved using the approach discussed in Sec. 4.1.2, where the basic concept of the superconducting ion trap is described.

4.1.1 Heating rates in radio-frequency ion traps

Trapped ions are susceptible to external electric-field noise, which couples to the ion motion and induces transitions between vibrational states of the confining harmonic potential. This is the case even if the ion is cooled to the quantum-mechanical ground state of its motion. In general, the heating rate of a motional mode ω_i is defined as the temporal change of its mean phonon number, $\frac{\mathrm{d}}{\mathrm{d}t}\langle n_i\rangle$. Here, we will consider the special case of the rate Γ_h at which an ion in the ground state of the harmonic potential is excited to the first excited state. In case of negligible micromotion, this rate can be approximated by [Bro+15]

$$\Gamma_\mathrm{h} \simeq \frac{q^2}{4m\hbar\omega_i} S_E(\omega_i) \quad , \tag{4.1}$$

where q and m describe the charge and mass of the ion and $S_E(\omega)$ denotes the spectral density of the electric field.

In the presence of micromotion, Eq. (4.1) may no longer hold. As discussed in Sec. 2.1, micromotion describes a coherently driven motion. Thus, it does not represent a source of heating by itself. However, for a radial displacement of the ion from the rf node, e.g. due to static offset potentials on the trap electrodes, the time-dependent electric fields from the quadrupole electrodes no longer vanish at the position of the ion. Therefore, any residual voltage noise at the trap electrodes produces fluctuating electric fields at the position of the ion. In case of non-vanishing spectral voltage density $S_V(\Omega \pm \omega_i)$ at the motional sidebands of the trap frequency Ω, this results in heating of the ion motion at secular frequency ω_i. Thus, in order to reduce motional heating of ions, any electric-field noise at the secular frequencies ω_i and the corresponding sidebands $\Omega \pm \omega_i$ of the rf drive needs to be suppressed.

Different sources for electric-field noise in ion traps can be distinguished. The most fundamental ones are blackbody radiation and background electromagnetic (em) fields. The latter can interact either directly with the ion or indirectly by coupling to parts of the experimental apparatus. Another typical noise source in ion trap experiments is technical noise, e.g. from power supplies, which is transmitted to the ion trap via electrical connections. Additional electric-field noise is produced by the thermal motion of electrons in resistive elements of the experiment. The spectral density of this so-called

Johnson-Nyquist noise [Joh28; Nyq28] is given by [Bro+15]

$$S_E^{\mathrm{JN}} = \frac{4k_{\mathrm{B}}TR(\omega,T)}{d_{\mathrm{eff}}^2} \quad . \tag{4.2}$$

Here, k_{B} is the Boltzmann constant, T is the temperature of the resistor with resistance R and d_{eff} is a geometry-dependent characteristic distance. Both, heating by Johnson-Nyquist noise as well as blackbody radiation can efficiently be suppressed by reducing the temperature of the trap and its surrounding.

Furthermore, local variations from the ideal electrode potentials on the microscopic scale result in fluctuating potentials, which can contribute to motional heating of ions. This is sometimes referred to as anomalous heating. Many potential microscopic mechanism have been proposed to cause this noise. Among them are fluctuating patch potentials, adatomic dipoles, and adatomic diffusion. In general, this heating mechanism depends strongly on the electrode-ion distance r_0 and scales with r_0^{-2} to r_0^{-4}, depending on its origin. In addition, heating rate measurements of trapped ions indicate that anomalous heating might be thermally driven and could be suppressed by decreasing the trap temperature [Des+06].

4.1.2 Working principle

In order to suppress motional heating rates, confinement of ions is realized by combining a high-Q resonator with a linear Paul trap to produce ultra-stable rf potentials. The trap electrodes are integral constituents of a resonator structure featuring a quadrupole resonant mode of the electric field. Its resonance frequency ω_0 represents the trap drive frequency Ω of the Paul trap. Ions are confined in a superposition of this quadrupole field and a static electric potential.

As described in Sec. 2.3, an rf resonator can be modelled by an LCR resonant circuit. The realization of a resonant circuit featuring a quadrupole mode of the electric field is shown in Fig. 4.1. For a classical LC circuit, Fig. 4.1(i), the total em energy of the system is transferred periodically between the electric field stored inside the capacitor and the magnetic field of the inductance. The capacitance is formed by the two poles of the resonant circuit, whose geometry defines the structure of the electric field. Modifying this basic geometry allows to pictorially explain the working principle of the cavity presented here. Simplifying the inductance to a single conductor loop, (ii), and subsequently adapting the shape of the capacitor to increase its capacitance, (iii), results in a transformed LC circuit. Revolving this geometry around the indicated axis yields a three-dimension resonant circuit, (v), which is additionally shown in a section view, (iv). It consists of a cylindrical tank surrounding the two poles. In a last step, the number of resonator poles is quadrupled, (vi), which results in a quadrupole mode structure of the electric field around the symmetry axis of the tank. Each quadrupole electrode consists of an inner and an outer electrode, which represent the opposite poles of the resonant circuit. This yields a high capacitance and results in a low resonance frequency of the quadrupole mode, as required for ion confinement (see Sec. 4.2). The relative rf phase of

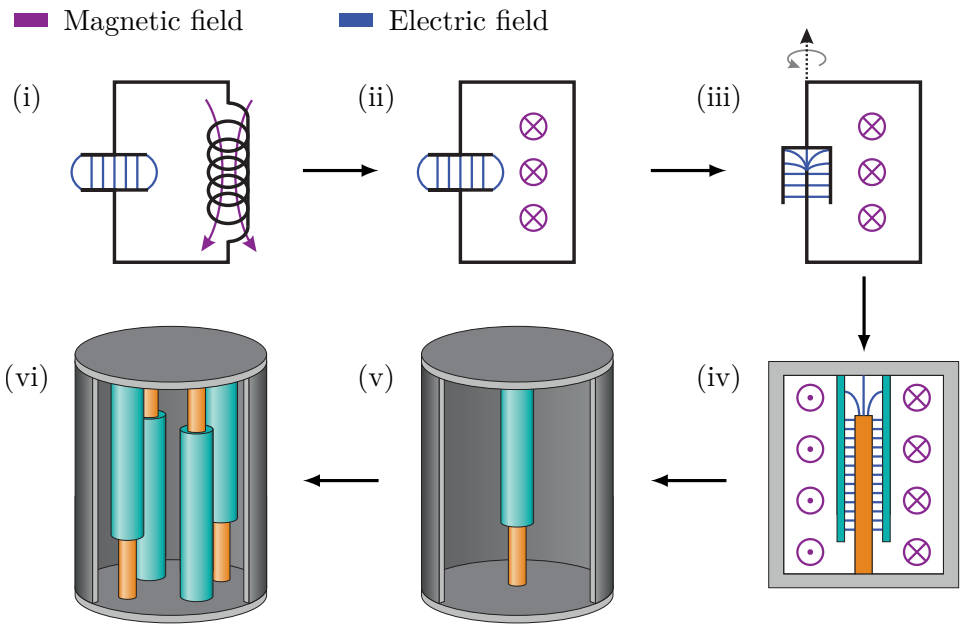

Figure 4.1: Schematic drawing of the realization of an *LCR* resonant circuit for a cavity featuring a quadrupole mode. The resistive losses of the system are represented by the lossy conductors. For details see text.

opposite quadrupole electrodes is exactly defined by geometry, which allows to suppress a typical source for excess micromotion (see Sec. 2.1).

In case of a high quality factor of the quadrupole resonant mode, this concept allows to produce ultra-stable rf potentials. For the cavity presented here, this is achieved by superconducting operation, which suppresses resistive rf losses inside the resonator surface (see Sec. 2.3.1). In general, the quality factor Q is defined as the ratio of the stored em energy U to the dissipated power P_d per rf cycle $1/\omega_0$ (see Sec. 2.3.1):

$$Q = \frac{\omega_0 U}{P_\mathrm{d}} \quad . \tag{4.3}$$

It sets the time scale for the exponential decay of the em energy stored inside the cavity, $\tau = 2Q/\omega_0$. For a high Q value, many cycles of the rf drive will be averaged inside the cavity leading to suppressed amplitude and phase fluctuations of the trapping potentials.

Furthermore, the quality factor defines the bandwidth of the excitation spectrum. An excitation spectrum resembling the one of the rf cavity presented here is shown in Fig. 4.2. In case of a high Q value, the cavity acts as a narrow bandpass filter for the supplied rf signals and features a resonance width of $\Delta\omega = \omega_0/Q$ at 3 dB below the maximum. Any technical noise from the rf drive at frequencies, which are separated by a few linewidths $\Delta\omega$ from the resonance, is strongly suppressed at the trap electrodes. Thus, a high Q value yields ultra-stable rf trapping potentials and accordingly well-defined secular frequencies of the trapped ions, which feature a reduced linewidth.

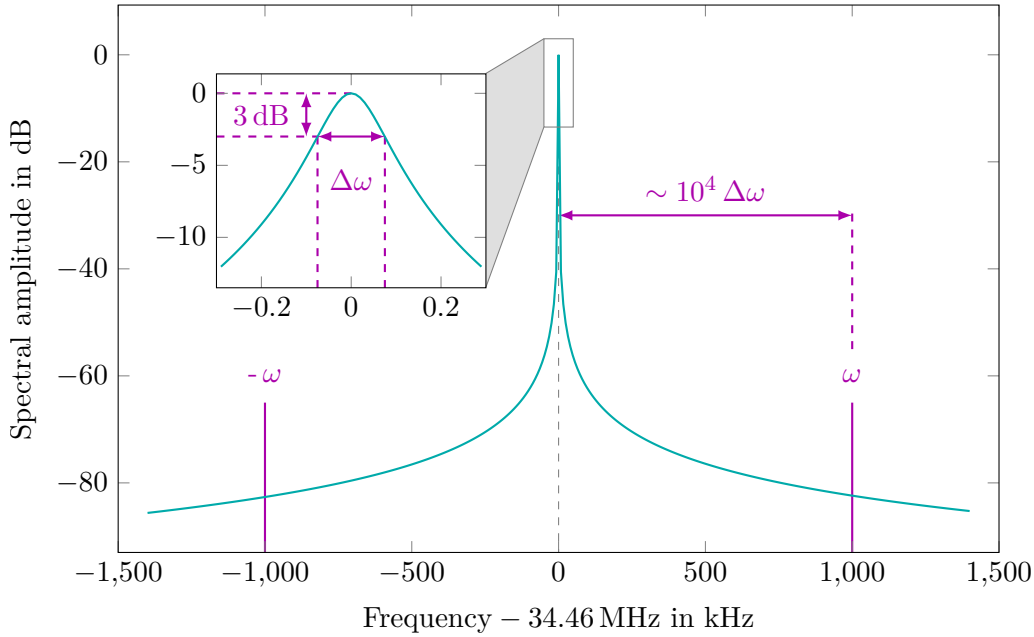

Figure 4.2: Calculated excitation spectrum (cyan) of an rf cavity with quality factor $Q_0 = 2.3 \times 10^5$, resembling the cavity presented in this thesis. The inset shows a detailed view around the resonance at $\omega_0/2\pi = 34.46\,\mathrm{MHz}$, which features a linewidth of $\Delta\omega/2\pi = 150\,\mathrm{Hz}$. The motional sidebands (magenta) of an ion with secular frequency $\omega/2\pi = 1\,\mathrm{MHz}$ are well separated from the carrier excitation at ω_0.

In addition, confinement of ions inside the superconducting cavity is expected to yield suppressed motional heating rates. This includes heating by electric-field noise on the trap electrodes. Technical noise on the quadrupole electrodes is reduced due to the band-pass behaviour of the cavity, which efficiently filters frequency components $S_E(\omega_0 \pm \omega_i)$ at the motional sidebands (see Fig. 4.2). Also, Johnson-Nyquist noise of cavity elements is greatly reduced as the trap is operated at 4 K and completely superconducting. Additionally, the electrostatic potentials of the direct current (dc) electrodes are filtered using low-pass filters, which are also mounted at 4 K to suppress Johnson-Nyquist noise (see Sec. 3.2.2). Furthermore, heating by blackbody radiation is completely rendered negligible due to the cryogenic trap environment.

Other effects of motional heating, referred to as anomalous heating, are greatly reduced due to the macroscopic trap geometry with $r_0 = 1.75\,\mathrm{mm}$, and the cryogenic trap temperatures. Finally, the trap region in the center of the cavity is enclosed by the superconducting walls of the housing. According to the Meissner-Ochsenfeld effect (see Sec. 2.4.3), this should efficiently shield the trapped ions from external alternating current (ac) magnetic field noise.

4.2 Design

The superconducting ion trap presented in this chapter represents a combination of a linear Paul trap and an rf resonator, as described in Sec. 4.1.2. Ions are confined radially in the standing em fields of the cavity similar to a two-dimensional quadrupole mass filter. Axial confinement is achieved by adding dc electrodes to the geometry. These are biased to a static potential and confine the motion of the ions along the symmetry axis of the quadrupole. A CAD model of the cavity is shown in Fig. 4.3.

The cavity is directly mounted onto the 4 K stage of the cryogenic setup described in Chapter 3. It is intended to confine cold HCIs for high-precision laser spectroscopy experiments. The following requirements and specifications were considered for the cavity design:

(i) High mechanical stability and low differential contraction during cooldown to 4 K to avoid misalignment.

(ii) Efficient capturing and preparation of HCIs inside the trap to maximize the measurement time within the experimental cycle, which is limited by the HCI storage time.

(iii) Multiple optical access ports to the trap center for lasers, external atom or ion sources and the imaging system.

For high mechanical stability, (i), the monolithic housing of the cavity supporting the trap electrodes is machined from one piece of niobium. Since the fits for the electrodes were machined in one single run, very tight mechanical tolerances are reached. This guarantees good positioning as well as alignment of the electrodes with respect to each other. Differential contraction as well as distortion during cooldown is suppressed as all electrically conducting parts are made of niobium. Additionally, all insulators used for the positioning of the trap electrodes are made of sapphire, which features advantageous thermal and mechanical properties. Its low thermal contraction compared to niobium [Eki06] and its high mechanical stability suppresses misalignment of the electrodes during cooldown. In addition, the high thermal conductivity of $230\,\mathrm{W(Km)^{-1}}$ at 4 K [Eki06] ensures proper thermalization of the electrodes with the housing. Furthermore, sapphire features small dielectric losses at cryogenic temperatures, which cause only minor rf power dissipation inside the cavity (see Sec. 4.4.2).

The second requirement, (ii), is met by the large trap aperture of $2r_0 = 3.5\,\mathrm{mm}$. This ensures both a high acceptance for the injection of HCIs into the rf quadrupole field of the cavity and allows to store large Coulomb crystals of up to 10^3 ions. The latter is needed to efficiently stop and cool the injected HCIs using the retrapping scheme introduced in [Sch+15b], which is discussed in Sec. 4.5.2.

Optical access to the trap center, (iii), is ensured by twelve ports in the horizontal plane. The two ports along the trap axis are used for the injection and retrapping of HCIs from the electron beam ion trap (EBIT). Additionally, the access port above the trap (not shown in Fig. 4.3) is used for the imaging of trapped ions.

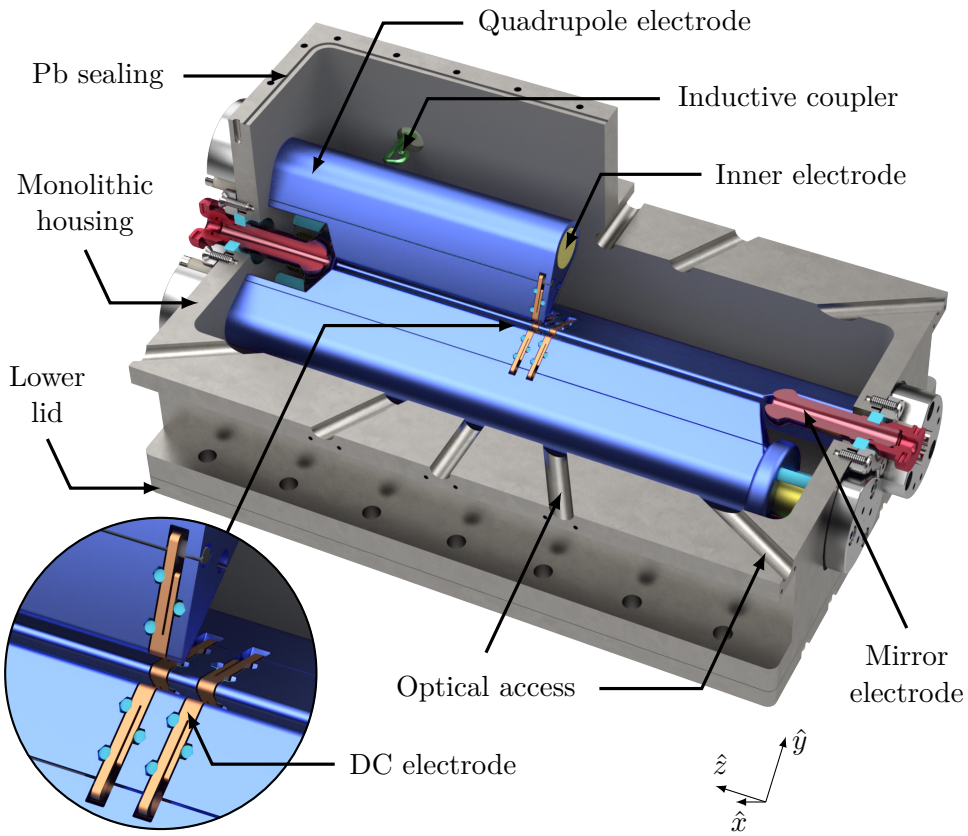

Figure 4.3: Section view of the CAD model of the superconducting rf cavity. A section view through the trap center of the cavity can be seen in Fig. 4.4. Detailed views of the coaxial quadrupole electrodes, the dc electrodes and the rf couplers are shown in Fig. 4.5, Fig. 4.6 and Fig. 4.7, respectively. For details see text.

4.2.1 Cavity tank and optical access

The box-shaped cavity ($220 \times 140 \times 114\,\mathrm{mm}^3$) consists of four parts (see Fig. 4.4). The monolithic body of the housing is used to mount the trap electrodes, the mirror electrodes as well as the rf couplers. It is closed with two large lids above and below the trap center, which are screwed into the wall of the housing. In order to ensure a superconducting electrical connection, the lids are sealed using high-purity (99.99 %) lead wire, which becomes superconducting below 7.2 K [Fis+05]. This is needed since a significant fraction of the rf current inside the cavity walls is passing through the lids (see Sec. 4.4.1).

The upper lid is separated into two parts, where the inner one is used to mount the imaging system. It is structured using a coarse-meshed grid that allows 83.2 % of the incident light from the trap center within a solid angle of $\Omega/4\pi \simeq 0.106$ to be transmitted (see Fig. 4.4). The imaging system mounted to the cavity can be seen in Fig. 3.10. Further optical access to the trap center is provided by twelve ports in the

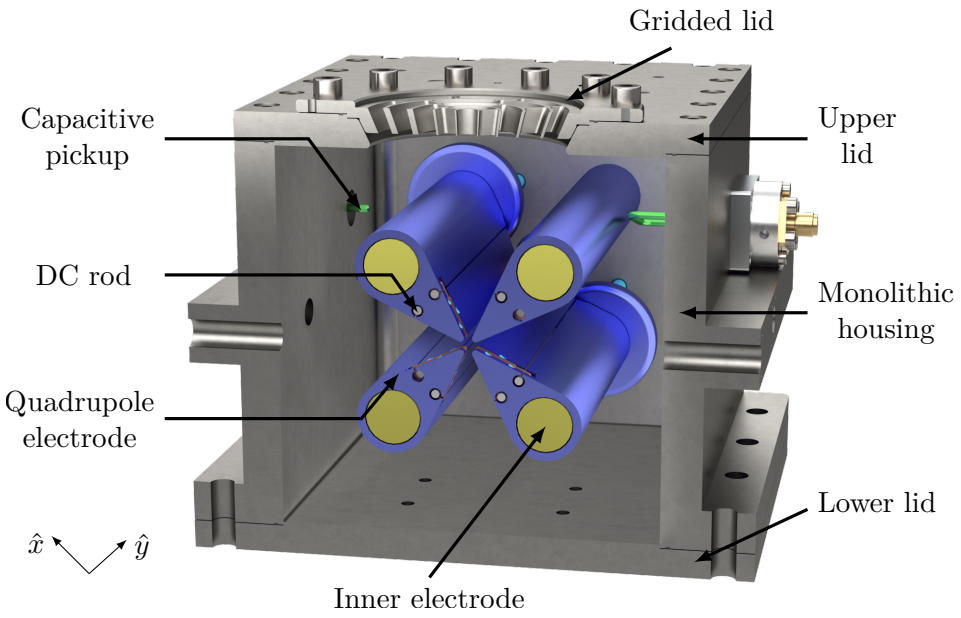

Figure 4.4: Section view of the CAD model of the superconducting rf cavity through the trap center at $z = 0$. For details see text.

horizontal plane, one every 30° (see Fig. 4.3). For all openings inside the cavity housing, the length-to-diameter ratio was maximized to reduce the leakage of em energy from the cavity. In addition, the inner diameters are chosen much smaller than the wavelength of the resonant mode, $\lambda_0 \simeq 8.7\,\mathrm{m}$.

4.2.2 Quadrupole electrodes

A critical design parameter of the cavity is its resonance frequency ω_0, which corresponds to the operating frequency Ω of the ion trap (see Sec. 4.1.2). For stable confinement of ions, it is restricted by the stability condition for the radial motion of an ion inside a linear Paul trap. According to Sec. 2.1.1, the radial stability parameter for the confinement of an ion inside the time-dependent quadrupole potential of the cavity is given by

$$|q_r| = \frac{4qV_{\mathrm{rf}}}{mr_0^2\Omega^2} \quad , \tag{4.4}$$

where q and m denote the charge and mass of the ion, respectively, and V_{rf} is the rf voltage amplitude. As the ion trap is operated inside the first stability region (see Sec. 2.1.1), q_r is limited to values between $0 < |q_r| < 0.908$ for typical stability parameters $|a_r| \ll 1$. However, around the origin $(a_r, q_r) = 0$, the stability region becomes very small. This yields a weak upper bound on the resonance frequency, since the rf amplitude V_{rf} is limited by practical considerations. Additionally, in order to allow for ground state cooling, radial secular frequencies, $\omega_r \simeq \Omega\sqrt{q_r^2/8}$, on the order of 1 MHz are needed (see

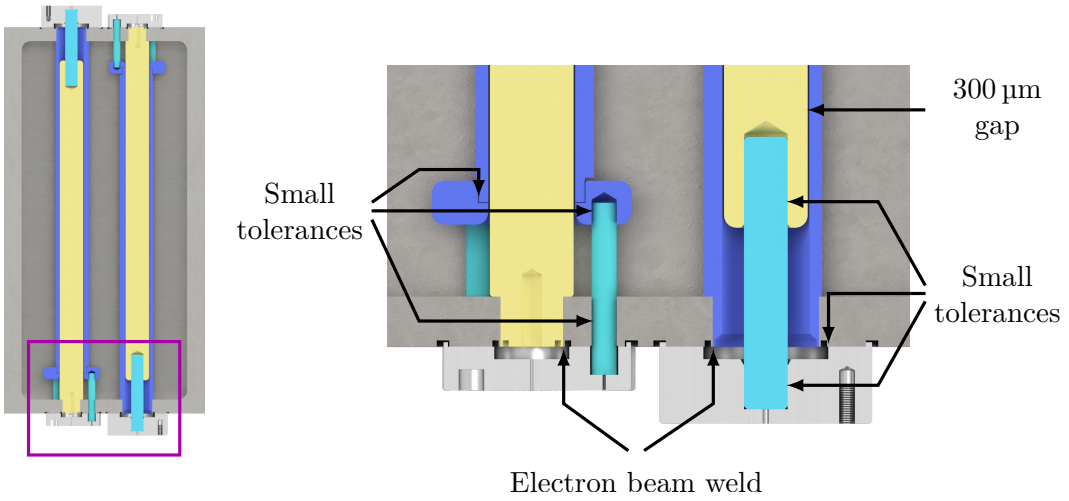

Figure 4.5: Horizontal section view of the CAD model of the rf cavity at the position of the lower coaxial electrodes. A detailed view of the indicated region (magenta) can be seen on the right. The coaxial segments consist of an inner (yellow) and outer (blue) electrode, which are one-sidedly electron-beam welded to the monolithic housing (dark grey) and at the other end fixed in position using sapphire rods (cyan).

Sec. 2.2.2). Inserting the definition of q_r from Eq. (4.4), this corresponds again to an upper limit for the trap frequency Ω and, thus, for the resonance frequency ω_0 of the cavity.

For the trap geometry presented here, resonance frequencies on the order of 200 MHz, for example, would require radial stability parameters around $|q_r| \simeq 0.014$ in order to achieve radial secular frequencies of 1 MHz. According to Eq. (4.4), this corresponds to a voltage amplitude of $V_{\mathrm{rf}} \simeq 6.4\,\mathrm{kV}$. In order to reduce this minimum rf voltage required for sufficiently high secular frequencies, the resonance frequency of the cavity should be restricted to below 100 MHz.

For the presented cavity, a coaxial trap electrode geometry is employed to achieve a small resonance frequency on the level of tens of MHz. This is shown in Fig. 4.4 and Fig. 4.5. Each quadrupole electrode consists of an inner and an outer part representing the two opposite poles of the quadrupole resonant mode. Due to the small separation of 300 µm, the capacitance of one coaxial segment amounts to $\sim 230\,\mathrm{pF}$. This increases the quadrupole capacitance C_{QP} by two orders of magnitude compared to simple rod electrodes and, thereby, lowers the resonance frequency of the quadrupole mode, $\omega_0^2 \propto C_{\mathrm{QP}}^{-1}$ (see Sec. 2.3.2). The coaxial electrode design was developed using finite element method (FEM) simulations, which are described in Sec. 4.4.1.

The positioning of the coaxial electrodes is shown in Fig. 4.5. The inner and outer electrodes of one coaxial segment are one-sidedly mounted into opposite walls of the monolithic housing and electron-beam welded from the outside. There, the weld follows

the circular contour of the electrodes, which ensures a proper thermal and superconducting electrical connection. The other side of the electrodes is held in position by sapphire insulators. In order to ensure precise alignment of the electrodes, tight mechanical tolerances are employed for positioning (see Fig. 4.5). Each side of the monolithic cavity housing supports two inner and two outer electrodes, where the four inner and the four outer electrodes are each arranged in an electric quadrupole configuration.

For larger optical access to the trap center, the hyperbolic electrode geometry of an ideal Paul trap is not convenient and was therefore modified. A blade-style electrode geometry was chosen for the outer electrodes, while the inner electrodes feature a circular cross section (see Fig. 4.4). The tapered outer electrodes feature an electrode tip radius of 0.9 mm and allow for optical access within a two-dimensional opening angle perpendicular to the trap axis of $\Omega_{2D} = 50.3°$. This is large compared to circular trap electrodes with minimized anharmonic contributions to the radial potentials (see Sec. 2.1.2), which are limited to $\Omega_{2D} = 25.4°$. The electrode geometry was optimized using electrostatic simulations of the radial trapping potentials to reduce higher-order anharmonic contributions. These are presented in Sec. 4.5.1.

4.2.3 DC electrodes

For axial confinement of ions, eight dc electrodes are embedded inside the quadrupole electrodes around the trap center, as can be seen in Fig. 4.3 and in more detail in Fig. 4.6. Their contour follows the tapered shape of the quadrupole electrodes. They are held in position using three sapphire rods of 1.5 mm diameter providing electrical insulation and proper thermal contact. The sapphire rods are hidden from the direct line of sight of the ions by choosing their length accordingly. Thereby, stray electric fields on the trap axis are avoided in case the insulators charge up, e.g. by incident ions or ultraviolet (UV) photons.

Mounting the dc electrodes directly into the quadrupole electrodes at a distance of $z_0 = 2.05$ mm from the trap center yields a strong axial confinement. In case of $^9Be^+$ ions, this allows for high axial secular frequencies of $\omega_z/2\pi \simeq 1$ MHz at moderate dc voltages around 25 V. The electrode geometry as well as its distance z_0 to the trap center were optimized using FEM simulations (see Sec. 4.5.1) to reduce anharmonic contributions to the electrostatic trapping potential. The geometric factor from Eq. (2.4) is determined by simulations and amounts to $\kappa \simeq 0.3379$.

The dc electrodes can be individually biased, which allows to minimize the excess micromotion originating from mismatching dc and rf nodes. Electric connection is provided using long niobium rods of 1.8 mm diameter (silver in Fig. 4.6), which are screwed into a M1.6 thread inside the dc electrode. They are guided out of the cavity inside a 3 mm hole in the quadrupole electrode. In order to ensure electric insulation, the rod is precisely positioned using polytetrafluoroethylene (PTFE) tubes mounted at the outer surface of the cavity housing. Additionally, a polyether ether ketone (PEEK) sleeve positioned along the middle of each rod acts as a spacer between rod and quadrupole electrode. To avoid cold welding between dc electrode and supply rod, the thread is greased with high-purity indium foil (99.999 %), which offers low outgassing rates com-

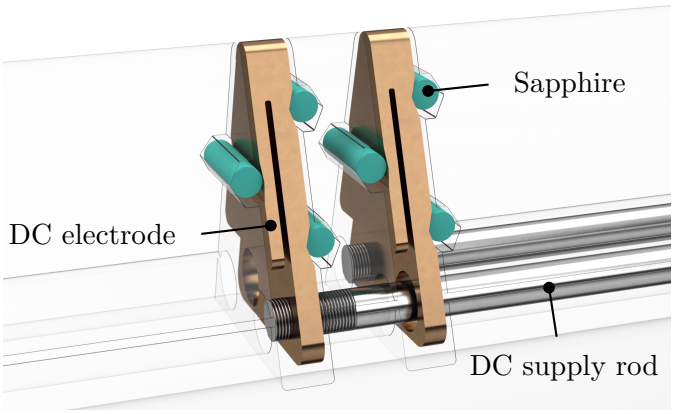

Figure 4.6: Detailed view of the dc electrodes. The electrodes (orange) are fixed in position using three sapphire rods (cyan) of 1.5 mm diameter. Electrical connection is provided by niobium rods (silver), which are screwed into the electrodes. The outer quadrupole electrode (light grey) is only indicated. A picture of two dc electrodes installed inside a quadrupole electrode is shown in Fig. A.1.

pared to other cryo-compatible vacuum greases. This is crucial in close proximity to the trap center to reach long storage times of HCIs.

Due to the large geometric capacitance between the dc electrode including the supply rod and the quadrupole electrode of about 15 pF, a sizable fraction of the rf voltage will be picked up by the dc electrode. This is intended, since a purely electrostatic potential of the dc electrodes would result in a drastic loss of HCIs during transit due to the reduced radial confinement at the dc electrode position. In order to determine the required rf potential of the dc electrodes to render these losses insignificant, ion-flight simulations were performed, which are presented in Sec. 4.5.2. These suggest equal rf potentials of dc and quadrupole electrodes for a maximized retrapping efficiency. In order to limit the outcoupled fraction of the em energy stored inside the cavity, the supply rods are connected to the external supply circuit using 66 MΩ resistors. This reduces the load to the cavity and leaves the dc electrodes at 100 % of the rf voltage amplitude of the quadrupole. A detailed description of the 4 K electronics is given in Sec. 3.2.2.

4.2.4 Mirror electrodes

For the injection and retrapping of slow HCIs from the transfer beamline, two mirror electrodes are mounted on both sides of the trap. The electrodes are mounted onto the monolithic housing using a sapphire ring, which grants electric insulation and proper thermalization with the cavity (see Fig. 4.3). The large distance between the two electrodes of 155 mm ensures that the complete incoming HCI bunch can enter the trap before the first mirror electrode is switched to a higher potential to close the trap for retrapping. Additionally, the field penetration of the mirror electrode potential into the

quadrupole structure was maximized by mounting it close to the trap electrodes. This increases the radial confinement at the turning point of the ions during reflection from the electrostatic mirror and, thereby, reduces ion loss. Ion-flight simulations for the retrapping of HCIs are shown in Sec. 4.5.2 for the optimized electrode geometry.

4.2.5 Radio-frequency coupling

Three different rf couplers are installed at the cavity. An overview of the couplers and their relative orientation is shown in Fig. 4.7.

Coupling to the resonant mode of the cavity is realized using one capacitive pickup, which couples to the electric field, and one inductive coil, that couples to the magnetic field. The latter is used for efficient incoupling of rf power by impedance matching the cavity to an external signal generator. As explained in Sec. 2.3.4, this can be achieved by adjusting the orientation of the coil with respect to the enclosed magnetic field vector of the resonant mode. Thereby, the enclosed area of the loop needs to be roughly matched to the quality factor of the cavity. The inductive coupler is fixed to a rotatable mount, which allows to continuously adjust the coil orientation, as can be seen in Fig. 4.7. While one end of the coil is connected to the external electronic circuit, the other is connected to the rf ground of the cavity via the rotatable mount.

Characterization and monitoring of the stored em energy inside the cavity is performed using the capacitive coupler. It is kept rather short and protrudes only 4.9 mm into the inner volume of the cavity. This results in weak coupling to the electric fields and, thereby, limits the fraction of em power drained from the cavity. The capacitive coupler will be used in the future to lock the frequency of the rf drive to the quadrupole resonance of the cavity using Pound locking [Lin+11; Pou46; Dre+83].

Additionally, a microwave antenna is installed, which is intended to drive the ground state hyperfine transition in $^9Be^+$ ions at 1250 MHz. This can be used to characterize the shielding of external ac magnetic field noise by measuring coherence times of Rabi flops [Leo+19]. The antenna is mounted under an oblique angle, i.e. not parallel to any of the three trap axes or the bias magnetic field, to ensure coupling to all polarization components of the transition (see Fig. 3.14). In order to minimize reflection of the incoupled rf power, the length of the $\lambda/4$ antenna needs to be matched to a quarter of the transition wavelength, $\lambda \simeq 24$ cm. However, due to capacitive coupling between antenna and cavity housing, this approach still results in a sensible fraction of the rf power being reflected at 1250 MHz. Thus, the antenna length was adjusted inside the cavity while simultaneously measuring the reflected power. For the commissioning experiments presented in Chapter 5, the microwave antenna was replaced with a second capacitive coupler identical to the first one, which allows for more flexibility during cavity characterization.

All rf couplers are made of niobium to suppress eddy current losses by oscillating em fields. The 2 mm thick rods are machined from the same niobium sample as the other parts of the cavity. They are mounted to the cavity using PTFE holders. In order to limit dielectric losses, the holders are retracted into the respective opening inside cavity housing and do not protrude into the inner volume. Connection to the external electronic circuit is provided by soldering the couplers into SMA connectors.

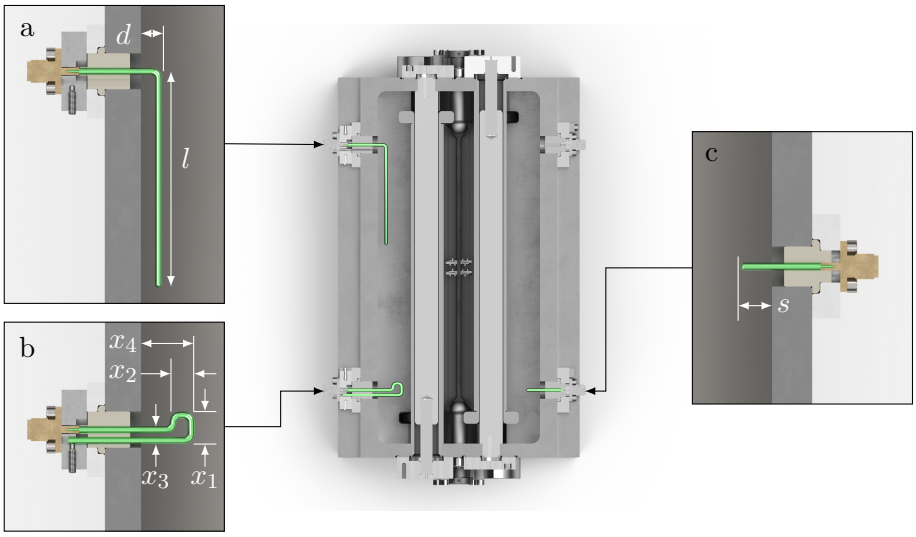

Figure 4.7: Horizontal section view of the rf cavity at the position of the upper coaxial electrodes. The detailed views show the rf couplers made of 2 mm thick niobium rods. (**a**) The microwave antenna is intended to drive the ground state hyperfine transition in $^9Be^+$. It has dimensions of $l = 57\,\mathrm{mm}$ and $d = 5.9\,\mathrm{mm}$ and is tilted $\sim 17°$ into the plane (not shown). (**b**) The inductive coupler used to drive the quadrupole mode has a coil geometry of $x_1 = 9\,\mathrm{mm}$, $x_2 = 7\,\mathrm{mm}$ and $x_3 = 5\,\mathrm{mm}$ and extends $x_4 = 14.9\,\mathrm{mm}$ into the cavity. (**c**) A short pickup, $s = 4.9\,\mathrm{mm}$, is used to couple capacitively to the electric field inside the cavity.

4.3 Cavity fabrication

The cavity described in this thesis was fabricated in the mechanical workshop at Max-Planck-Institut für Kernphysik (MPIK). The following chapter covers the material selection (Sec. 4.3.1), as well as the fabrication process including the surface preparation of the cavity (Sec. 4.3.2).

4.3.1 Material selection

The main requirements for the material of a superconducting cavity are a high critical temperature, T_c, and a high critical magnetic field, H_{sh}. Among all elemental superconductors, niobium offers the highest T_c and H_{sh} [Pad01]. It has thus been used for superconducting cavities already since 1967, replacing lead-plated copper cavities [Kne+13]. Alternative materials for the fabrication of cavities include composite superconductors, such as Nb_3Sn. It features an increased critical rf magnetic field, which is about twice as large as the one of niobium [Pad01]. Thus, these superconductors can potentially be used to reduce surface losses and reach higher em fields. However, further research

regarding the techniques for fabrication and surface preparation is required until they can potentially outperform niobium cavities [Kec+19].

One major limitation for the cavity performance regarding the highest achievable em fields is thermal breakdown of superconductivity caused by microscopic regions of high rf loss [Pad01]. Two complementary approaches for the fabrication of niobium cavities were developed over the years representing different measures to overcome thermal breakdown: copper cavities coated with thin films of niobium and cavities made of bulk or sheet niobium.

The first approach provides an improved stability against thermal breakdown of superconductivity due to the excellent thermal conductivity of copper. Furthermore, it offers the advantage of being cost-efficient, as only very little high-purity niobium material is needed. Different techniques for the coating of copper surfaces including electrolytic deposition [MS65], vapour deposition [Piz+16], ultra high vacuum (UHV) cathodic arc [Cat+07] and cylindrical magnetron sputtering [Orl+93] were reported. Alternatively, the second approach relies on the use of high-purity bulk niobium to achieve a reasonably high thermal conductivity at cryogenic temperatures. The performance of the cavity depends on the material purity as well as surface inclusions (see Sec. 2.4.2).

For the presented cavity geometry, it would have been challenging and costly to apply a homogeneous coating to all surfaces due to the unusual shape of the quadrupole electrode structure. Therefore, the cavity is made of high-purity bulk niobium. The material specifications are related to the requirements used at accelerator facilities. However, the design requirements are relaxed compared to state-of-the-art superconducting rf cavities [Sin+16]. Especially the designated highest electric fields of $6\,\mathrm{MVm}^{-1}$ as well as the quality factors of $Q_0 = 10^5 - 10^7$ are well below the values reported for the cavities of the European X-Ray Free-Electron Laser (EuXFEL) with $Q_0 > 10^{10}$ at gradients of $20\,\mathrm{MVm}^{-1}$ [Res+17]. These cavities are operated at 2 K and, therefore, require a high residual-resistance ratio (RRR) of about 300 to ensure a sufficiently high thermal conductivity. Here, the RRR serves as an indicator for the purity of the metal and is commonly defined as the ratio of the electrical resistivity ρ at 273 K compared to 4.2 K [Sch81]:

$$\mathrm{RRR} = \frac{\rho_{273\,\mathrm{K}}}{\rho_{4.2\,\mathrm{K}}} \quad . \tag{4.5}$$

Since the cavity presented here is operated at 4.2 K, the thermal conductivity of niobium is increased compared to operating temperatures of 2 K [KB96]. Additionally, due to the reduced highest fields, thermal breakdown of superconductivity should not pose a limitation. Therefore, the limits for the material impurities were partially weakened and the requirement for an RRR above 300 defined for the EuXFEL cavities [Sin+15] was rejected.

For the niobium material used for the fabrication of the rf cavity, the RRR was not specified by the supplier[1]. However, an upper limit for the RRR can be obtained using the dependence of the residual resistance on the atomic concentration of selected

[1] Companhia Brasileira de Metalurgia e Mineração (CBMM)

Table 4.1: Excerpt from the chemical analysis of the niobium ingot used for the fabrication of the cavity, as provided by the supplier. The material has a total purity $\Delta m/m > 99.86\,\%$. The measured dependence of the electrical resistivity on the atomic concentration, $\Delta\rho/\Delta c$, is taken from [Sch81].

Impurity atom	$\Delta\rho/\Delta c$ ($10^{-12}\,\Omega$m/ppm)	$\Delta m/m$ (ppm)	Impurity atom	$\Delta\rho/\Delta c$ ($10^{-12}\,\Omega$m/ppm)	$\Delta m/m$ (ppm)
N	5.2	18	W	0.4-1.1	5
O	4.5	4	Ta	0.25	1233
C	4.3	30	H	0.8	2
Ti	1.4	7	Mo	0.21	2
Hf	1.4	2	Ni	–	1
Zr	0.6-1.4	1	Fe	–	3

impurities in niobium. In general, the electrical resistivity of metals at low temperatures can be expressed as [Sch81]

$$\rho = \rho_{\mathrm{ph}}(T) + \rho_{\mathrm{im}} + \rho_{\mathrm{d}} + \rho_{\mathrm{s}} \quad . \tag{4.6}$$

It comprises contributions from scattering of electrons on lattice defects ρ_{d}, physical boundaries ρ_{s}, chemical impurities ρ_{im} and lattice excitations ρ_{ph}. The latter depends strongly on temperature and is typically negligible at cryogenic temperatures.

The impact of homogeneously distributed chemical impurities onto the resistivity ρ_{im} depends only their concentration c_i [Sch81]:

$$\rho_{\mathrm{im}} = \sum_i \frac{\Delta\rho}{\Delta c_i} c_i \quad . \tag{4.7}$$

The proportionality constants $\Delta\rho/\Delta c_i$ were determined in [Sch81] for high-purity niobium by intentionally contaminating the samples and measuring its electrical resistivity. They are listed in Tab. 4.1 together with the chemical analysis of the niobium ingot used for the fabrication of the cavity. The total effect of the impurities listed in Tab. 4.1 results in a residual resistivity of $5.7 \times 10^{-10}\,\Omega$m at 4.2 K, which corresponds to RRR < 267.

4.3.2 Fabrication and surface preparation

The machining of metallic surfaces causes plastic deformations and the inclusion of foreign materials. For niobium, this is often referred to as the damaged or dirty layer, which has to be removed to achieve a good performance as an rf superconductor [KR17]. Therefore, the main fabrication steps were performed using wire electrical discharge machining (EDM), which is non-intrusive and was performed at small material ablation rates with negligible heating of the niobium surface. The latter is crucial since niobium getters hydrogen, oxygen, and other gases when heated above 200 °C [Bau80].

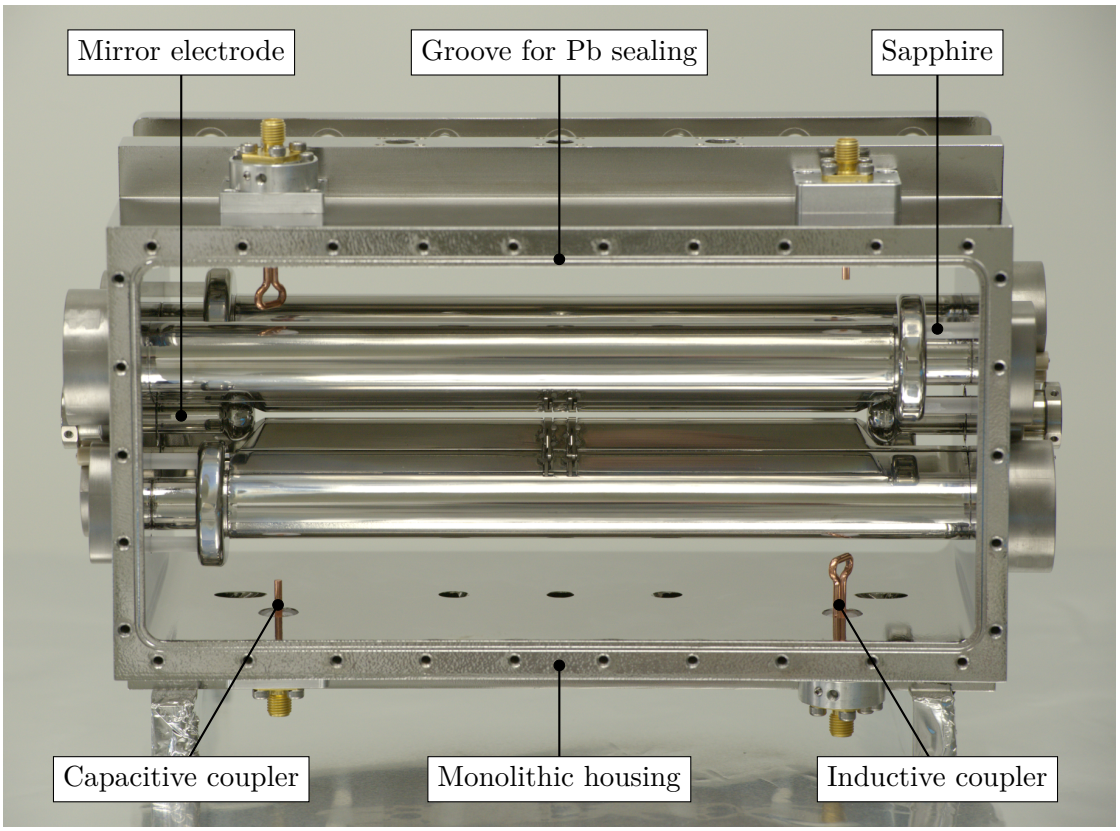

Figure 4.8: Picture of the electropolished and welded cavity (top view) with both lids removed from the housing. The rf couplers shown here are made of OFHC copper and were replaced with niobium couplers after the first commissioning measurements.

At the beginning of the fabrication process, all parts were cut from a single niobium ingot using wire EDM. Several steps of wire EDM followed with stepwise decreasing material-ablation rate approaching the final contour. Subsequently, all holes, fits and threads were milled.

After degreasing and cleaning, electropolishing (EP) was employed to remove the damaged surface layer. Its thickness depends on the details of the fabrication process and varies between 50 µm and 200 µm [KR17]. Due to the gentle fabrication process described above, only 50 µm were removed from all surfaces[2]. During the EP process, all fits and threads were covered using PTFE covers and protective varnish.

After EP, all parts were cleaned including several rounds of ultrasonic cleaning in destilled water (50 kΩ cm), isopropyl alcohol (99.9 % purity), ethanol (99.9 % purity) and deionized water certified with 18.2 MΩ cm and a total organic carbon content below

[2]The EP process was performed by the company Poligrat GmbH.

3 ppb. Subsequently, the parts were dried using pressurized nitrogen (99.999 % purity). For the transport into the clean room and the storage before being assembled, they were sealed in bags filled with nitrogen (99.999 % purity).

The cavity was assembled inside an ISO6 clean room. First, the dc electrodes are mounted inside the quadrupole electrodes. Subsequently, the coaxial segments are mounted inside the cavity housing, before being joined using electron-beam welding. Welding is chosen to ensure a pure superconducting connection between the coaxial electrodes and the cavity housing. This provides a small electrical and thermal contact resistance. Contamination of the inner cavity surface during welding is avoided by closing all access ports to the inner volume, except for a long and thin tube used for evacuation. Electron-beam welding was performed with a background pressure below 1.2×10^{-4} mbar. A total of 7 h exposure to clean room air between cleaning and welding of the cavity parts was was not exceeded.

After welding, the dc supply rods, the mirror electrodes as well as the rf antennas were installed and all three lids were sealed using lead wire. A picture of the fully assembled cavity before closing the lids can be seen in Fig. 4.8.

4.4 Simulating the cavity performance

This chapter covers simulations and estimates of the expected performance of the presented rf cavity. For the development of a cavity geometry satisfying the specifications formulated in Sec. 4.2, especially a quadrupole resonant mode with an eigenfrequency on the order of 10 MHz, simulations are required. These are discussed in Sec. 4.4.1, where the main focus is on the quadrupole resonant mode. Subsequently, possible limitations of the quality factor and performance of the cavity are analyzed in Sec. 4.4.2.

4.4.1 Simulations of the quadrupole resonant mode

The em eigenmodes of the presented cavity geometry were determined using FEM simulations. In general, this method allows to compute numerical approximations to partial differential equations for complex geometries and the associated boundary conditions. The details will not be discussed here, as these are described in many textbooks, e.g. [Zoh15]. The simulations described in this section are performed using the commercial COMSOL Multiphysics software [COM20a]. It can be expanded by the RF module [COM20b] to simulate rf properties of complex structures. In particular, this allows to perform an eigenfrequency and eigenmode analysis of the presented cavity geometry in full 3D vector mode.

At the start of the simulations, the CAD model of the rf cavity is imported and approximated using small tetrahedral elements, which make up the so-called mesh. The minimum and maximum size of the mesh elements can be specified by the user. Subsequently, an algorithm chooses the size of individual elements automatically to resolve narrow regions, e.g. the gap between the two coaxial electrodes. In the next step, the boundary conditions for the simulation are defined, e.g. material properties. Based on

this information, the resonance frequencies and the corresponding eigenmodes of the geometry are determined by solving the time-dependent wave equation. However, some combinations of material properties and boundary conditions can results in non-linear differential equations. This can be handled by linearizing the description around a given frequency. The computed eigenfrequencies consist of real and imaginary part, where the latter represents the damping of the harmonic oscillations (see Sec. 2.3.2). For the simulations presented here, the eigenfrequencies were determined with five significant digits and feature a zero imaginary component.

The quality of the simulations depends critically on the size of the mesh elements, since these only approximate the real geometry. For all rf applications, the maximum element size should be limited to a fraction of the wavelength of the em fields. In addition, the minimum element size needs to be substantially smaller than the smallest structures to resolve detailed regions of the geometry. Thus, the required computation power increases dramatically with the spatial dimensions of the simulation volume. Accordingly, the simulations were performed on the MPIK cluster with an available memory of 300 GB RAM. This allowed to refine the simulation mesh down to a minimum mesh size of 51 µm.

However, in order to allow for sufficient mesh refinement, the geometry had to be simplified. Therefore, elements of the geometry which are located at low field amplitudes or are expected to have a minor effect on the result, were not included. This applies for all threads located at the outer surface of the housing, the sapphire insulators, the rf couplers, and the protective lids around the weld joint of the inner electrodes.

The simulations are performed at room temperature, $T = 293.15\,\mathrm{K}$. All cavity parts are modelled with identical material properties. The electric conductivity was set to $\sigma = 5.7 \times 10^{12}\,\mathrm{Sm}^{-1}$, which represents the maximum value that could handled by COMSOL for the finest mesh size employed here. Additionally, the relative permittivity ϵ_r and relative permeability μ_r are both set to unity. The cavity is completely embedded in vacuum and enclosed by a perfectly conducting box to yield well-defined boundary conditions.

Eigenfrequencies and resonant modes

The simulations yield four resonant modes in the frequency range between 1 MHz and 100 MHz. An overview of the determined eigenfrequencies is given in Tab. 4.2 together with an error budget, which will be discussed in the next section.

The quadrupole mode of the cavity has a resonance frequency of 34.851 MHz, which is within the frequency range specified in Sec. 4.2. It will be used to radially confine ions similar to a linear Paul trap and represents the relevant eigenmode of the cavity. The quadrupole mode is well-separated from the other three resonances, which exhibit fundamentally different mode structures. Therefore, they will not be considered for the following discussion.

The relative amplitude of the electric field of the quadrupole mode is shown in Fig. 4.9(a,b). The highest field strengths are radially confined around the central electrode structure and decay quickly towards the cavity walls. The peak values are found

Table 4.2: Overview of the simulation results. The eigenfrequencies of the four resonant modes between 1 MHz and 100 MHz are shown together with estimates of the simulation uncertainty. The simulations yield five significant digits for the determined eigenfrequencies. The uncertainties from mesh and geometry are added quadratically to estimate the total uncertainty. For details see text.

Resonance frequency (MHz)	Mesh uncertainty (MHz)	Geo. uncertainty (MHz)	Tot. uncertainty (MHz)
34.851	0.009	0.002	0.009
58.613	0.034	0.104	0.109
58.651	0.036	0.102	0.108
70.372	0.051	0.231	0.237

in between the coaxial segments of each quadrupole electrode. This is expected due to the small gap of 300 µm, which yields a high capacitance and, thereby, a low resonance frequency of the complete geometry. The inner electrodes do not contribute to the electric field around the trap axis, which is determined by the shape of the outer electrodes and features a quadrupole structure.

Due to the high geometric capacitance between quadrupole and dc electrodes, they exhibit nearly identical rf potentials. Accordingly, the simulation shows nearly zero electric field between the quadrupole electrodes and dc supply rods or dc electrodes, respectively. Along the quadrupole structure, the electric field strength near the trap axis stays approximately constant, which corresponds to a homogeneous radial confinement (see Fig. 4.9(b)). A detailed analysis of the radial electric field structure is presented in Sec. 4.5.1.

The simulated magnetic fields are shown in Fig. 4.9(c,d). They are produced by alternating currents inside the cavity surface, which reverse the polarity of the quadrupole electrodes. Due to symmetry, the magnetic field vanishes around the trap axis and reaches sizable values around the electrode structure. This is in accordance with the simulated current density inside the cavity walls, which is shown in Fig. 4.10. The maximum current densities are located at the backside of the outer quadrupole electrodes and produce the highest magnetic fields. The simulations of the em fields show a limited leakage of em energy through the optical ports or the upper lid, as both the magnetic as well as the electric fields do not penetrate deep into the openings of the cavity housing (see Fig. 4.9(a,c)). However, as the imaginary part of the simulated eigenfrequencies determined with five significant digits is zero, the presented simulations do not allow to estimate the residual rf loss due to leakage.

The simulated electric current density inside the cavity walls is shown in Fig. 4.10. The currents connect the poles of the resonant mode, i.e. the inner and outer quadrupole electrodes, via the cavity housing. In the radial plane, the current density is more or less equally distributed between the four walls of the housing. This is not obvious, since the direct path over the central, monolithic housing naturally features less resistive

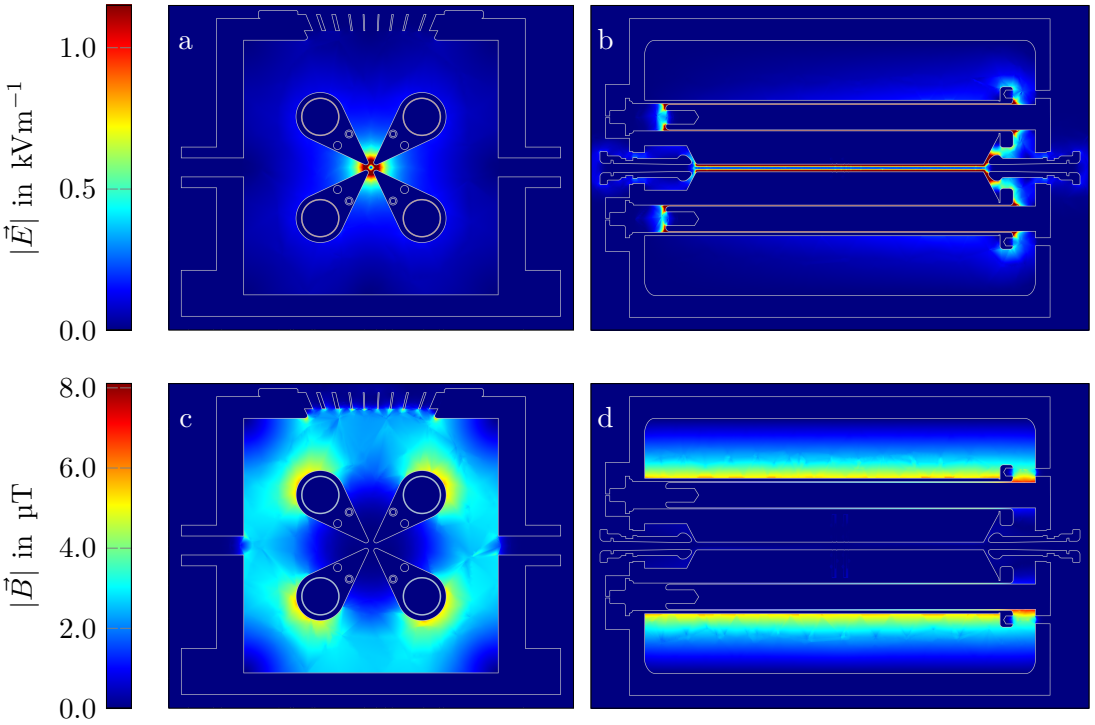

Figure 4.9: FEM simulations of the em field structure of the quadrupole mode obtained for a minimum mesh size of 51 µm. **Top:** The relative electric field strength is plotted in the radial plane at $z = 0$ (**a**) and in the (yz)-plane at $x = 0$ (**b**). The maximum field strength of $10\,\mathrm{kVm}^{-1}$ is cut off for better visibility of the fields around the symmetry axis of the quadrupole. **Bottom:** The relative magnetic field strength is plotted in the radial plane at $z = 0$ (**c**) and in the (yz)-plane at $x = 0$ (**d**). The cavity contour is indicated in all four plots.

losses compared to the connections via the upper and lower lid, which have to bridge two geometric boundaries. However, the currents reflect the symmetry of the electric and magnetic mode structure and, therefore, are symmetrically distributed around the cavity housing. In order to achieve low resistive losses for the currents flowing through the lids, these are connected to the monolithic housing using lead sealings, which become superconducting below 7.2 K (see Sec. 4.2.1).

In order to estimate the effect of thermal contraction during cooldown, the resonance frequency of the quadrupole mode was additionally simulated for a re-scaled cavity geometry. According to [Eki06], the thermal expansion integral for niobium amounts to $\Delta L/L = 0.143\,\%$ for the cooldown from room temperature to 4 K. The resonance frequency of the accordingly scaled cavity geometry was computed with a minimum mesh size of 200 µm. The simulation yields a modified resonance frequency of the quadrupole mode of 34.897 MHz, which is shifted by 50 kHz to higher frequencies compared to the room-temperature result for similar mesh size.

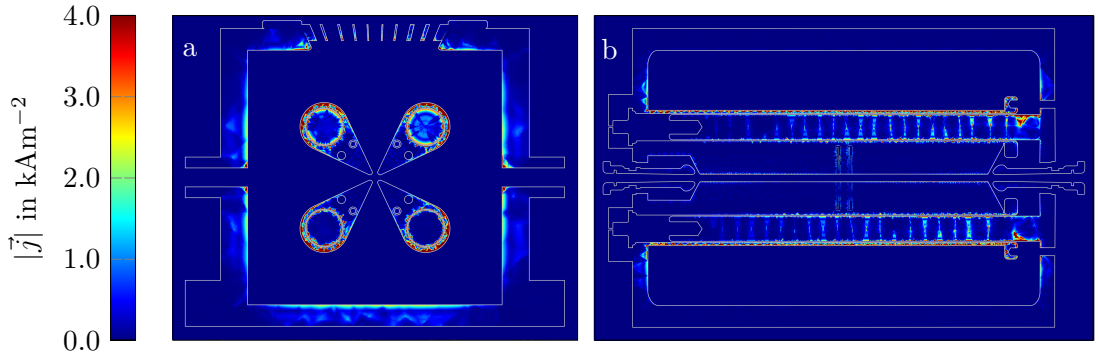

Figure 4.10: FEM simulation of the quadrupole mode current density inside the cavity surface obtained for a minimum mesh size of 51 µm. The relative current density is plotted in the radial plane at $z = 0$ (**a**) and in the (yz)-plane at $x = 0$ (**b**). The maximum values for the current density of 10^3 kAm^{-2} are cut off for better visibility of the currents inside the cavity walls. The cavity contour is indicated.

Simulation uncertainty

Several sources of uncertainty of the simulations have to be taken into account. An overview of the estimated uncertainties for the determined eigenfrequencies of the cavity is shown in Tab. 4.2.

A systematic uncertainty stems from the fact that the mesh is only approximating the real geometry. For the presented simulations, the mesh was refined down to a minimum element size of 51 µm, which is below the smallest features of the cavity geometry. The narrowest regions are given by the minimum separation between dc electrodes and quadrupole electrodes of 250 µm and the 300 µm gap between the coaxial electrode segments. Furthermore, the discretization of the real geometry by the mesh introduces an error, which depends on the element size. In order to estimate this uncertainty, the simulations were performed for different minimum mesh element sizes between 51 µm and 2.6 mm. The results for the four resonant modes are shown in Fig. 4.11.

One can see that the simulated eigenfrequencies of all resonant modes are converging to the final result for decreasing element size. This effect is most distinct for the quadrupole resonant mode, which is shown in detail in the right panel of Fig. 4.11. The simulation converges until no clear trend is observable for minimum element sizes below 200 µm. In this region, the simulations show fluctuations on the kHz level. In order to account for this, the values below and including 200 µm minimum element size are averaged to obtain the final simulation result. The largest deviation between any two eigenfrequencies in this mesh range is used to estimate the systematic uncertainty.

A similar behaviour can be observed for the other three resonant modes, although the convergence is less pronounced. The results show finite fluctuations on the level of tens of kHz. The corresponding uncertainty is estimated using the identical procedure

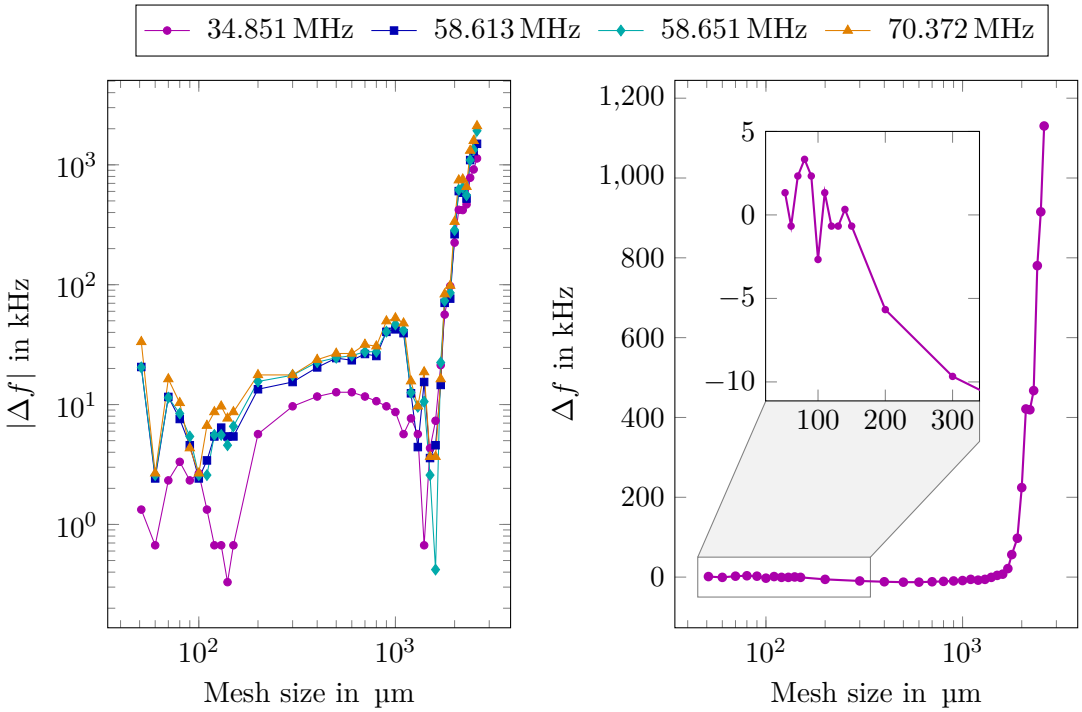

Figure 4.11: Simulation results for the eigenfrequencies of the four resonant modes between 1 MHz and 100 MHz. The difference Δf between the simulated eigenfrequency and the final simulation result, as listed in Tab. 4.2, is shown as a function of the minimum mesh size. A comparison of the four resonant modes (**left**) is shown together with a detailed view of the quadrupole mode simulations (**right**).

as for the quadrupole mode. The values are listed in Tab. 4.2, where the systematic uncertainties are denoted as mesh uncertainty.

The discussed convergence of the simulation results with refined mesh size does not rule out a systematic offset from the real eigenfrequencies. This can only be determined by comparison to a system with known or analytical solution. Since this is not available for the presented cavity geometry, this source of uncertainty cannot be excluded.

Another possible simulation uncertainty arises from the simplification of the real cavity geometry, which was necessary since the available memory for the simulations was limited. The corresponding effect on the final result was estimated by simulating the complete cavity geometry without any simplifications for a minimum mesh size of 0.8 mm, which could still be handled by the cluster. This yields resonance frequencies of 34.842 MHz, 58.484 MHz, 58.521 MHz and 70.110 MHz. The corresponding uncertainty is estimated by the difference between the simulation result obtained for the reduced geometry and the one of the complete geometry for identical mesh size. Here, the smallest deviation is found for the quadrupole resonant mode, since the simplifications

of the cavity geometry were chosen accordingly. The values are listed Tab. 4.2 and denoted as geometric uncertainty.

Finally, the influence of the linearization point on the simulation result was investigated. As described above, non-linearities of differential equations can be solved by linearizing the description around a given frequency. For the presented simulations, this frequency was set to 34.854 MHz, which corresponds to the simulation result of the quadrupole mode obtained for the minimum mesh size. Varying this linearization point between 30 MHz and 40 MHz resulted in unchanged eigenfrequencies of the four resonant modes. Thus, this effect can be neglected for the simulations presented here.

4.4.2 Cavity loss mechanisms

Several loss mechanism of superconducting rf cavities are distinguished in literature, which can fundamentally limit their performance. Many of them have been studied extensively over the past decades [CAS89; PHK98]. Among the most common ones are field emission and thermal breakdown, which manifest themselves only at high fields above $10\,\mathrm{MVm^{-1}}$ [Kno97]. Since the presented cavity is designed for electric fields below $6\,\mathrm{MVm^{-1}}$, both processes should be negligible. However, several loss mechanisms are known, which might be relevant even at low fields. These will be discussed in the following chapter based on [CAS89; Kno97; PHK98], together with an analysis of their potential impact on the presented cavity.

Flux trapping

This process describes the trapping of residual dc magnetic flux inside the cavity walls during cooldown through the superconducting phase transition at T_c. According to the Meissner-Ochsenfeld effect, the magnetic field should be expelled from the interior of the superconductor once it is cooled below its critical temperature (see Sec. 2.4.3). However, defects and impurities in the superconducting sample can lead to flux pinning and prevent the complete expulsion of magnetic field. Experimentally it was shown that this holds true even for high-purity niobium samples with RRR = 500, for which the complete magnetic flux up to an external field of 3 Oe was trapped [Val+92].

The trapped flux leads to the formation of normal-conducting regions, which carry a single flux quantum, $\phi_0 = hc/2\mathrm{e}$, each. In the presence of rf fields, these so-called fluxoids perform oscillations, which dissipate power. These losses correspond to a flux-dependent contribution to the surface resistance, R_Φ, which is theoretically described by [BS65; KHS65; GR03]

$$R_\Phi = R_\mathrm{n}\frac{H_\mathrm{ext}}{H_\mathrm{c2}} \quad , \tag{4.8}$$

where R_n is the surface resistance of the sample in the normal-conducting state, H_ext denotes the external magnetic field and H_c2 is the upper critical magnetic field of the superconductor. Experimental values for critical magnet fields of niobium are listed in Tab. 4.3.

Table 4.3: Measured critical magnetic fields of high-purity niobium with RRR = 1600(400) at 4.2 K. The data is taken from [FSS66].

Critical field	H_{c1}	H_c	H_{c2}
Exp. data (Oe)	1425	1598	2757

For the presented cavity with a resonance frequency of 34.52 MHz and RRR $\simeq$ 267, we obtain $R_n \simeq 278\,\mu\Omega$ using the expression from Eq. (2.67). Thus, already the earth magnetic field of $\sim 30\,\mu T$ increases the surface resistance by $R_\Phi \simeq 30\,n\Omega$. Additionally, we intend to apply a bias magnetic field along the direction of the cooling laser for future trapped ion experiments. With a typical field strength of $200\,\mu T$ in the center of the trap, the surface resistance is increased by $R_\Phi \simeq 202\,n\Omega$, if this bias field is applied during cooldown.

These values need to be compared to the surface resistance $R_{s,BCS}$ as predicted by the Bardeen–Cooper–Schrieffer (BCS) theory. A rough estimate for the BCS value can be obtained by comparison with results reported for niobium cavities operated at 1.3 GHz [Aun+00] using the frequency scaling from Eq. (2.69). The reported value of $800\,n\Omega$ at 4.2 K temperature translates to $R_{s,BCS} \simeq 1\,n\Omega$ for an operating frequency of 34.52 MHz. Thus, the flux-dependent contribution R_Φ to the surface resistance is substantially higher than the BCS value.

In order to reduce R_Φ, the cavity needs to be shielded from environmental magnetic fields during cooldown, e.g. using μ-metal. Additionally, the bias magnetic field for efficient laser cooling can be applied at temperatures below T_c to avoid flux trapping.

Adsorbed gases

The surface resistance can also be degraded by adsorbed gases on the cavity walls. Experimentally, a reduction of the highest achievable quality factor was observed in case the cavity was not completely evacuated before cooldown [Kne95]. However, a significant effect was only detected for vacuum levels above 10^{-4} mbar prior to cooldown. Here, the cooldown is typically started if the pressure inside the trap chamber, measured between the vacuum chamber and the 40 K heat shield, drops below 3×10^{-7} mbar. The corresponding pressure level inside the cavity at room temperature is about two orders of magnitude above this measured value (see Sec. 3.1.4). This corresponds to an intra-cavity vacuum well below 10^{-4} mbar before cooldown. Thus, this loss mechanism should be negligible for the experiments presented in this thesis.

Hydrogen contamination

Another cause for low-field rf losses of superconducting cavities is the contamination of niobium with hydrogen, which will be briefly discussed based on [Kno97; BRG12]. The accepted mechanism is the precipitation of dissolved hydrogen at temperatures between 100 K and 150 K. These hydrides are normal-conducting at cryogenic temperatures down

to 2 K and thus cause increased rf losses. This can reduce the quality factor by up to two orders of magnitude [Ant+91]. It is expected that the size of this effect depends on the atomic hydrogen concentration in the sample, the cooldown rate as well as the amount of interstitial impurities. The effect can be avoided altogether by vacuum annealing of the cavity at temperatures above 900 °C for several hours.

The hydrogen concentration in the niobium surface depends on the original purity of the sample. In addition, several processing steps, which are typically employed during the fabrication of rf cavities, can lead to an increased concentration. Contamination can occur during chemical polishing, especially at temperatures above 15 °C, and mechanical polishing in a solution which is not hydrogen-free [PHK98; Hig+01]. However, EP, which was applied here, should cause only a mild contamination of the processed niobium parts [BRG12].

The material used for the fabrication of the cavity exhibits a hydrogen concentration of $\Delta m/m = 2\,\mathrm{ppm}$ (see Tab. 4.1). This was previously identified as an upper limit resulting in the formation of significant amounts of hydrides. Additionally, the low-vibration cryostat, which is used to cool the cavity, takes several days for the complete cooldown (see Sec. 3.1.4). In particular, the cavity spends more than ten hours in the temperature range critical for the formation of precipitates. Considering that vacuum annealing of the cavity was not applied, hydrogen contamination represents a realistic source of rf loss for the presented cavity.

Multipacting

A loss mechanism typically present in rf cavities is multipacting (MP), which stands for multiple impact electron amplification [Par11; Pad15]. It describes a resonant process, in which a large number of electrons builds up in an avalanche within a small region of the cavity surface. Acceleration of the emitted charges absorbs power from the cavity and limits the achievable em field amplitudes, i.e. the fields inside the cavity do not increase with increasing input power. MP requires the trajectory of the emitted electrons to be synchronized with the rf fields and electron multiplication via secondary emission. The second condition is satisfied for a secondary emission coefficient larger than one. This is typically achieved for electron impact energies between 50 eV and 1000 eV, depending on the cleanliness of the surface. The initial ejection of an electron can be caused by cosmic rays, photoemission or field emission.

Two types of MP can are distinguished. One-point MP occurs when the electrons impact the cavity surface almost at the same place where they were emitted. Synchronization requires the time-of-flight (TOF) to be an integer multiple of the rf period. Since the trajectory depends strongly on the details of the field distribution, no analytical description is possible. The general scenario requires an electric field normal to the cavity surface, which accelerates the emitted electrons, and a magnetic field, that forces them on quasi-circular orbits.

A rough estimate can be made to evaluate the likeliness of MP to develop. In case of circular orbits, the resonant condition is satisfied for a magnetic field of [Par11]

$$B_0 = \frac{\omega_0 m_e}{en} \quad , \tag{4.9}$$

where n is the MP order, m_e and e are the mass and charge of the electron and ω_0 is the resonance frequency of the cavity. This yields a magnetic field of $B_0 \simeq 1.2\,\mathrm{mT}$ for the first order. Such high magnetic fields could be found at the backside of the quadrupole electrodes, where the highest magnetic field strengths are located (see Fig. 4.9). However, detailed simulations are required to determine if the energy gain is enough to cause secondary emission and therefore MP.

The second type of MP, which was also observed for quadrupole resonators [Kle17], is two-point MP. There, electrons travel between two opposite surfaces within half, or odd multiples of half an rf period. Potential locations are small gaps, in which the magnetic field vanishes. In addition, the gap width l should be much smaller than the rf wavelength, $l \ll \lambda_0$. This can be found between inner and outer coaxial electrodes, which are separated by $l = 300\,\mu\mathrm{m}$. Here, the electric field distribution is very homogeneous and can be approximated by two parallel plates. In good approximation, the electrons are emitted with zero kinetic energy. This yields an expression for the gap voltage V_g and the corresponding impact energy of the electrons E_imp [Par11]:

$$\begin{aligned} V_\mathrm{g} &= \frac{m_e(\omega_0 l)^2}{\pi e(2n+1)} \quad , \\ E_\mathrm{imp} &= \frac{2m_e(\omega_0 l)^2}{\pi^2(2n+1)^2} \quad . \end{aligned} \tag{4.10}$$

The gap voltage for the first order process ($n = 1$) of about 2.5 mV allows only for kinetic energies on the order of a few meV at impact. Since this is not sufficient for secondary electron emission, two-point MP is strongly suppressed for the presented cavity geometry.

Dielectric losses

Several electrical insulators are installed inside the cavity, which are used, for example, to position the quadrupole electrodes relative to the housing (see Sec. 4.2). These dielectric materials can cause significant rf loss, if they are located at high em field amplitudes of the resonant mode.

In general, the frequency-dependent rf loss inside a dielectric material is described by its loss tangent, $\tan\delta$, which is defined as [Poz12]

$$\tan\delta(\omega) = \frac{\omega\epsilon'' + \sigma}{\omega\epsilon'} \quad , \tag{4.11}$$

with the complex permittivity $\epsilon = \epsilon' - i\epsilon''$ and the electrical conductivity σ of the material. If some fraction the total em energy U of the cavity is stored inside a dielectric material, the quality factor of the resonator is limited to [EK02]

$$Q_\mathrm{de} = \frac{U}{U_\mathrm{de}} \frac{1}{\tan\delta} \quad , \tag{4.12}$$

Table 4.4: Dielectric rf loss $\tan\delta$ of sapphire, PTFE and PEEK.

Material	Frequency (GHz)	Temperature (K)	$\tan\delta$	Reference
Sapphire	$21.4 - 21.7$	15	$< 5.0 \times 10^{-8}$	[Kru+99]
Sapphire	9	4	7.0×10^{-10}	[BIB87]
PTFE	18.92	28	2.3×10^{-6}	[Jac+02]
PTFE	9.95	77	8.0×10^{-6}	[GK95]
PEEK	0.001	296	4.8×10^{-3}	[CGT20]

where U_{de} denotes the electric field energy stored inside the dielectric. In order to suppress these rf losses, the employed insulators were carefully selected according to their material-specific $\tan\delta$.

For the presented cavity, sapphire crystals are used to mount the trap electrodes. These dielectrics are located at high field amplitudes and can, therefore, significantly affect the performance of the cavity. Additionally, the dc supply rods are positioned inside the quadrupole electrodes using PEEK sleeves, which are mounted in the middle of the rods. Since the electric field between quadrupole electrode and dc rods is basically zero (see Fig. 4.9), the induced losses are expected to be negligible. In addition, the dc rods are fixed to the outside of the cavity housing using PTFE mounts, which are located at high field amplitudes and, thus, need to be taken into account. Finally, the rf couplers are mounted to the cavity using PTFE holders.

A rough estimate of the dielectric losses can be obtained using FEM simulations similar to the ones presented in Sec. 4.4.1. Thereby, the insulators were included into the simulation geometry, but modelled as vacuum to determine the relative em energy stored inside them. This yields a fractional stored energy of 8.6×10^{-6} and 8.2×10^{-4} for the PTFE and sapphire insulators, while the PEEK sleeves only contribute with 9.7×10^{-10}.

The rf losses of dielectric materials depend strongly on frequency as well as temperature. Experimental values for the involved materials are shown in Tab. 4.4. For crystals, the dielectric losses are expected to increase with frequency and temperature [GT86]. Although this does not directly apply for PTFE and PEEK, the listed values should correspond to an upper limit for the expected losses at 34.52 MHz and 4 K. Using the values from [Jac+02; BIB87], the quality factor of the cavity is limited to 5.0×10^{10} and 1.7×10^{12} by the losses of the PTFE and sapphire parts, respectively. The dielectric losses of PEEK correspond to an upper limit for the quality factor of 2.1×10^{11}. Therefore, the installed dielectric materials are expected to limit the cavity performance only at quality factors which are three orders of magnitude above the design value.

4.5 Simulating ion confinement inside the cavity

In addition to the performance as an rf cavity, the confinement of ions inside the electric potentials of the cavity puts further constraints on the electrode design. The cavity

geometry presented in this chapter was developed using various simulations of the trapping potentials. In order to ensure harmonic confinement of ions, simulations of the axial and radial trapping potentials were used to optimize the geometries of rf and dc electrodes (Sec. 4.5.1). Additionally, ion-flight simulations were performed to optimize the geometry of mirror electrode and dc supply to allow for efficient retrapping of HCIs (Sec. 4.5.2).

4.5.1 Trapping potentials

Deviations from the ideal electrode geometries result in higher-order contributions to the harmonic trapping potentials (see Sec. 2.1.2). In order to suppress these anharmonicities, the cavity geometry was optimized according to the specifications described in Sec. 4.2, using electrostatic FEM simulations of the axial and radial potentials. These are performed using the AC/DC module [COM20c] of the COMSOL Multiphysics software [COM20a].

The simulations are divided into several steps. First, the CAD model of the cavity is imported and approximated using tetrahedral mesh elements, as described in Sec. 4.4.1. Since the complete cavity geometry would have been too detailed to be solved with the given computation power, the geometry was simplified. Thus, insulators, inner coaxial electrodes, and dc supply rods are removed and the cavity housing is replaced by a closed cuboid shell coinciding with its inner walls. These modifications of the geometry are expected to have a negligible effect onto the simulation results regarding the region around the trap center, which is of interest here. Since the inner coaxial electrodes are enclosed by the outer quadrupole electrodes, they do not contribute to the potential around the trap center. The same holds true for the dc supply rods as well as the insulators, which are mounted at a large distance from the trap center, hidden inside the quadrupole electrodes. Additionally, the effect of the simplified cavity housing is suppressed, since the trap region is enclosed and shielded by the quadrupole structure (see Fig. 4.9).

In the second step, the cavity surfaces are modeled as perfect conductors and Dirichlet boundary conditions are applied. After all surfaces are assigned with an individual electrostatic voltage, the potential distribution inside the simulation volume is computed by solving Gauss' law.

In the following, the simulation results obtained for the minimum achievable mesh size within the given computation power of 300 GB RAM are discussed. These are intended to serve as an estimate for the anharmonic contributions to the axial and radial trapping potentials.

Axial confinement

For the simulation of the electrostatic potential used for axial confinement of ions, the geometry is meshed with a minimum element size of 10 µm. The housing and all electrodes were set to ground, while only the eight dc electrodes were supplied with a potential of

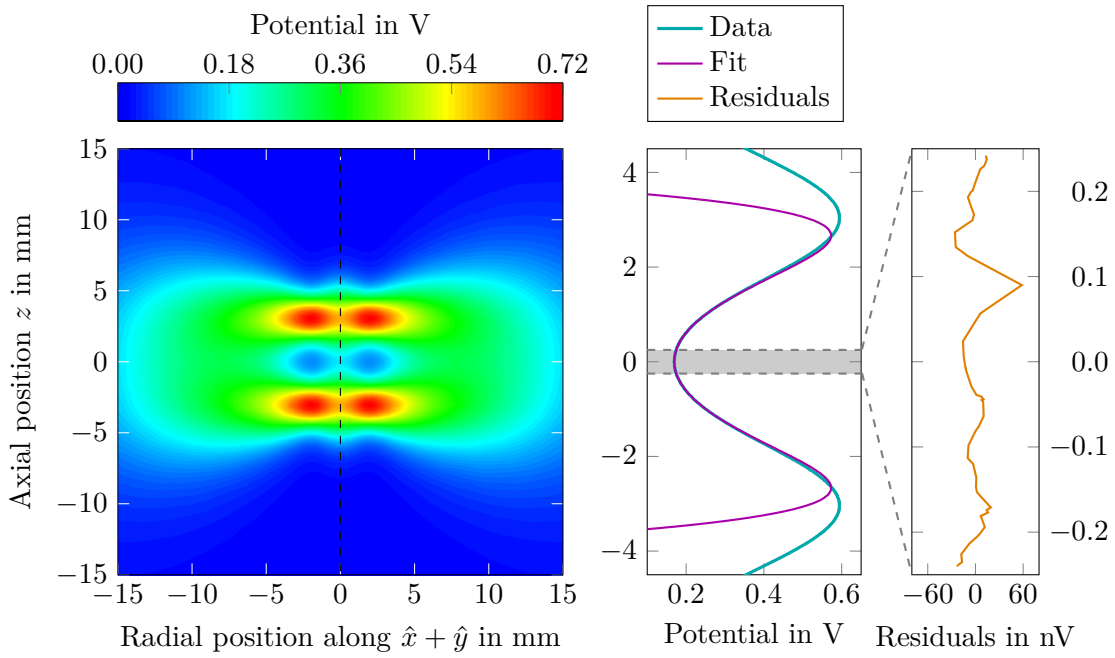

Figure 4.12: Simulation of the electrostatic potential around the trap center in the case of eight identical dc electrode potentials of 1.0 V. **Left:** The two-dimensional potential is plotted in the horizontal plane of the cavity spanned by the trap axis z (dashed line) and the direction $\hat{x}+\hat{y}$. **Middle:** The simulated potential along the trap axis is shown together with a sixth order polynomial fit to the data. The fit range of $\pm 0.25\,\mathrm{mm}$ is indicated by the gray region. **Right:** The residuals of the fit are plotted (note the different scale).

1 V. The simulation of the electrostatic potential around the center of the trap is shown in Fig. 4.12.

In order to evaluate the harmonicity of the axial potential, the simulated potential along the trap axis is plotted on the right side Fig. 4.12 with a polynomial fit to the data. As discussed in Sec. 2.1.2, the potential can be written as

$$\Phi(z) = C_0 + C_2 z^2 + C_4 z^4 + C_6 z^6 + ... \tag{4.13}$$

around its minimum. By fitting this model to the data, the expansion coefficients up to C_6 were determined for different fit ranges Δz. The results are summarized in Tab. 4.5. This can be used to calculate the corresponding maximum shift of the axial trap frequency resulting from the first two higher-order contributions, C_4 and C_6. Using the approximation $\Delta\omega_z/\omega_z \ll 1$, the resulting frequency shift from Eq. (2.12) can be expressed as

$$\frac{\Delta\omega_z}{\omega_z} = \frac{3}{4}\left(\frac{C_4}{C_2} + \frac{5}{4}\frac{C_6}{C_2}z^2\right)z^2 \quad . \tag{4.14}$$

Table 4.5: Coefficients of the axial trapping potential at the rf node for identical dc electrode potentials of 1.0 V. The parameters are determined by applying a polynomial fit (see Eq. (4.13)) to the simulation data from Fig. 4.12 with different fit ranges Δz around the potential minimum. The geometric factor of the linear Paul trap is determined using $\kappa = C_2 z_0^2$. The corresponding frequency shift $\Delta\omega_z/\omega_z$ (see Eq. (4.14)), caused by the listed anharmonicities, is given for the maximum displacement z within the fit range.

	$\Delta z = \pm 0.25\,\mathrm{mm}$	$\Delta z = \pm 0.5\,\mathrm{mm}$	$\Delta z = \pm 1.0\,\mathrm{mm}$
$C_2\,(\mathrm{V/mm^2})$	$8.04145(8) \times 10^{-2}$	$8.04134(2) \times 10^{-2}$	$8.04115(2) \times 10^{-2}$
$C_4\,(\mathrm{V/mm^4})$	$1.32(3) \times 10^{-3}$	$1.349(3) \times 10^{-3}$	$1.3592(7) \times 10^{-3}$
$C_6\,(\mathrm{V/mm^6})$	$-7(4) \times 10^{-4}$	$-8.56(7) \times 10^{-4}$	$-8.731(5) \times 10^{-4}$
κ	$3.37942(3) \times 10^{-1}$	$3.37937(1) \times 10^{-1}$	$3.37929(1) \times 10^{-1}$
$\Delta\omega_z/\omega_z$	$7.3(3) \times 10^{-4}$	$2.522(8) \times 10^{-3}$	$2.498(9) \times 10^{-3}$

The results are also listed in Tab. 4.5. As expected, anharmonic contributions to the potential become increasingly important at larger distances to the potential minimum. This is also reflected in the estimated frequency shifts for the different fit ranges. Closer to the trap center, the absolute contribution to the potential by higher-order terms is suppressed by z^4 and z^6, respectively. Thus, for typical Coulomb crystals used for the preparation of cold HCIs for spectroscopy, which feature an axial extent of about 200 µm [Sch17; Leo18], the maximum frequency shift is expected to be significantly smaller compared to the values listed in Tab. 4.5. A rough estimate for the corresponding frequency shift can be determined using the expansion coefficients obtained for the fit range of $\Delta z = \pm 0.25\,\mathrm{mm}$. This yields an upper limit for the expected frequency shift of $\Delta\omega_z/\omega_z = 1.22(3) \times 10^{-4}$ for the outermost ion at $z = 100\,\mu\mathrm{m}$ compared to the center ion at $z = 0$. For a single $^9\mathrm{Be}^+$ ion confined inside the cavity with a secular frequency of $\omega_z/2\pi = 1\,\mathrm{MHz}$, the residual motion with an amplitude of 120 nm at the Doppler temperature of 0.3 mK corresponds to a maximum frequency shift of $\Delta\omega_z/\omega_z = 1.77(5) \times 10^{-10}$.

In principle, it is possible suppress C_4 and C_6 by optimizing the distance between dc electrode and trap center (z_0) and adjusting the axial length of the electrodes. However, for the cavity presented in this thesis, additional requirements had to be considered. Most importantly, the axial distance of the dc electrodes, $2z_0 = 4.1\,\mathrm{mm}$, was kept small to allow for high secular frequencies on the order of 1 MHz at moderate dc voltages around 10 V. Thus, it was not possible to further minimize the anharmonic contributions to the axial potential within the constraints for mechanical stability of the mounting.

In order to further reduce these anharmonicities, correction electrodes need to be added to the trap geometry. The corresponding correction voltage is chosen such that the first higher-order contribution vanishes, $C_4 = 0$. In order to ensure that the axial trap frequency is not changed during the minimization of C_4, the correction electrodes should be positioned to yield $C_2^{\mathrm{corr}} = 0$. Furthermore, the electrode length should be

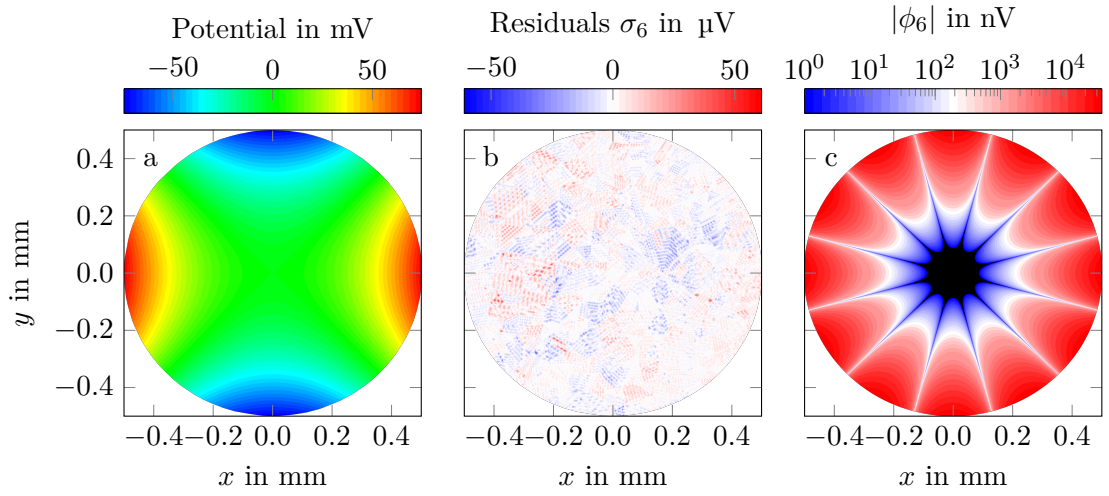

Figure 4.13: Electrostatic simulation of the radial potential around the trap axis at $z = 0$. Anharmonic contributions to the potential are estimated using polynomial fits to the data within a radial distance of $r \leq 0.5\,\mathrm{mm}$ to the trap axis. (**a**) The radial potential of the cavity is shown for quadrupole potentials of $\pm 1.0\,\mathrm{V}$. (**b**) The residuals σ_6 of the sixth order polynomial fit are shown. (**c**) Shown is the absolute value of the first anharmonic contribution ϕ_6 of the sixth order polynomial fit. Values below 1 nV are shown in black.

adjusted such that the ratio $C_4^{\mathrm{corr}}/C_6^{\mathrm{corr}}$ is identical to the ratio of the dc electrodes. This yields a very small contribution $C_6 \simeq 0$ for compensated $C_4 = 0$ term of the axial potential and results in an orthogonal and compensated trap [Ulm11; Stu12].

The presented design of the cavity does not include correction electrodes. However, the lids of the housing feature designated mounting ports, which can be used in the future to install additional electrodes above and below the trap axis. These allow to insert two electrodes each on the base and the lid of the housing, which can be used to compensate the C_4 and C_6 terms of the axial potential.

Radial confinement

In order to characterize the radial confinement inside the quadrupole potential of the cavity, electrostatic simulations were performed. The cavity geometry was meshed with a minimum mesh size of 47.5 µm. All conducting surfaces were placed on ground, except for the dc and the quadrupole electrodes, which were supplied with $\pm 1\,\mathrm{V}$. The resulting electrostatic potential in the $z = 0$ plane around the trap axis is shown in Fig. 4.13(a).

In order to estimate the deviation from the ideal quadrupole potential, a two-dimensional model is fitted to the data. For this, the potential perpendicular to the symmetry axis (z) of the quadrupole is expanded in a multipole series:

$$\Phi(x, y) = A_0 + \sum_n A_n \phi_n(x, y) \quad , \tag{4.15}$$

Table 4.6: Coefficients of the radial trapping potential at $z = 0$ for quadrupole potentials of $\pm 1.0\,\mathrm{V}$. The parameters are determined by fitting a polynomial of n^{th} order (see Eq. (4.15)) to the simulation data from Fig. 4.13. The fit range is restricted to a radial distance of $r \leq 0.5\,\mathrm{mm}$ to the trap axis.

Polynomial order	$A_2\,(\mathrm{V/mm^2})$	$A_6\,(\mathrm{V/mm^6})$	$A_{10}\,(\mathrm{V/mm^{10}})$
2^{nd}	$3.029136(5) \times 10^{-1}$		
6^{th}	$3.029161(2) \times 10^{-1}$	$2.2852(2) \times 10^{-3}$	
10^{th}	$3.029161(2) \times 10^{-1}$	$2.285(6) \times 10^{-3}$	$-1(1) \times 10^{-4}$

where the first three terms are given by [Den+15]

$$\begin{aligned}\phi_2 &= (x^2 - y^2) \quad , \\ \phi_6 &= (x^6 - 15x^4y^2 + 15x^2y^4 - y^6) \quad , \\ \phi_{10} &= (x^{10} - 45x^8y^2 + 210x^6y^4 - 210x^4y^6 + 45x^2y^8 - y^{10}) \quad . \end{aligned} \tag{4.16}$$

To evaluate the influence of the the lowest-order anharmonic contributions to the radial potential, ϕ_6 and ϕ_{10}, three different fits up to the second, sixth and tenth polynomial order were performed. The results are summarized in Tab. 4.6. One can see that the first anharmonicity, ϕ_6, contributes significantly to the radial potential and has to be considered for the analysis of the radial confinement. This is different for second order anharmonic contribution with expansion coefficient A_{10}, which can be neglected within the statistical error of the fit. Thus, the second order anharmonicity ϕ_{10} will be discarded in the following discussion.

The residuals σ_6, representing the difference of the sixth order polynomial fit to the simulated radial potential, are shown in Fig. 4.13(b). One can see that the coarse structure of the data is well-described by an ideal quadrupole potential extended by the first order anharmonic contribution, ϕ_6. Especially, no higher-order multipoles are visible, which is in agreement with the fit parameters from Tab. 4.6. The fine structure in the fit residuals σ_6 are suspected to result from the simulation mesh. Since only a section view through the three-dimensional FEM simulation volume is shown, the residual plot reflects the mesh structure around $z = 0$.

In order to estimate the relative contribution of anharmonic terms to the radial potential, the first order anharmonicity ϕ_6 of the sixth order polynomial fit from Tab. 4.6 is plotted in Fig. 4.13(c). The largest deviations from the ideal quadrupole potential are on the level of tens of µV and become negligible around the trap axis, where the ions are confined. Typical Coulomb crystals feature a radial extent of less than 200 µm. In this case, the outermost ions will experience a relative contribution of anharmonic terms to the radial potential of 7.5×10^{-7}. Therefore, the radial potential close to the trap axis can, in good approximation, be described as an ideal harmonic quadrupole potential.

4.5.2 Retrapping of highly charged ions

Sympathetic cooling of HCIs inside a linear Paul trap represents an import pre-requisite for the application of high-precision laser spectroscopy. It was for the first time demonstrated in [Sch+15a] utilizing a versatile approach based on the retrapping of slow HCIs and the subsequent multi-pass stopping inside a laser-cooled Coulomb crystal of $^9Be^+$ ions. In order to define the important parameters and time scales, the retrapping process will be briefly discussed in the following based on [Sch+15b; Sch17]. Additionally, ion-flight simulations were performed to optimize the geometries of mirror and dc electrodes and to determine experimental parameters allowing for efficient retrapping of HCIs.

Working principle

The injected HCIs are decelerated by the Coulomb interaction with pre-stored and laser-cooled $^9Be^+$ ions confined inside the Paul trap. An upper limit for the initial kinetic energy of the HCIs allowing for efficient retrapping and stopping inside the target Coulomb crystal can be estimated using the plasma frequency ω_p of the target. It defines the time scale for the interaction with the incoming HCIs and is given by [ZTR99]

$$\omega_\mathrm{p} = \sqrt{\frac{q_\mathrm{t}^2 n_\mathrm{t}}{\epsilon_0 m_\mathrm{t}}} \quad , \tag{4.17}$$

which depends on the mass m_t, charge q_t and number density n_t of the $^9Be^+$ target. The number density n_t can be calculated using the assumption that the interior of the Coulomb crystal is free of electric fields. This is, however, only valid at the position of the ions, where the repulsive Coulomb interaction between target ions and the confining force of the pseudopotential Ψ of the Paul trap exactly balance each other. Following this approximation, the total electric potential inside the crystal has to be constant: $\Phi_\mathrm{t} + \Psi = c$. This defines the electric potential of the target ions Φ_t inside the Coulomb crystal up to a constant. The target charge density ρ_t is then derived by solving the Poisson equation, $\epsilon_0 \Delta \Phi_\mathrm{t} = -\rho_\mathrm{t}$. Using the expression for the pseudopotential from Eq. (2.8) yields the number density of the target ions:

$$n_\mathrm{t} = \frac{\rho_\mathrm{t}}{q_\mathrm{t}} = \frac{\epsilon_0 m_\mathrm{t}}{q_\mathrm{t}^2}(\omega_x^2 + \omega_y^2 + \omega_z^2) \quad . \tag{4.18}$$

Typical trap frequencies of $(\omega_x, \omega_y, \omega_z)/2\pi = (1.56, 1.56, 0.90)\,\mathrm{MHz}$ result in densities of the $^9Be^+$ target on the order of $10^{15}\,\mathrm{m}^{-3}$. This is a factor of 50 higher compared to the value reported [Sch+15b], where Coulomb crystals with an axial extent of 2 mm were considered for retrapping. Here, we consider a target crystal with an equal number of ions and similar aspect ratio, which results in an axial length of the Coulomb crystal of 0.5 mm due to the increased trap frequencies. In order to guarantee efficient collective stopping of HCIs, the interaction time inside the target crystal for each transit needs to be on the order of the plasma response time [Sch+15b], $\tau_\mathrm{p} = \omega_\mathrm{p}^{-1} \simeq 66\,\mathrm{ns}$. This yields an upper limit for the kinetic energy of the incoming HCIs, e.g. $E_\mathrm{kin}^\mathrm{max} \simeq 12.6\,\mathrm{eV}$ in the case of $^{40}Ar^{13+}$.

The interaction of the injected HCIs with the laser-cooled $^9Be^+$ ions inside the Paul trap can be described by a frictional force acting on the HCIs during transit. In order to estimate the retarding force of the Coulomb crystal, the interaction is described in terms of the stopping power of the $^9Be^+$ plasma [Bus+06]:

$$\frac{\mathrm{d}E_{\mathrm{HCI}}}{\mathrm{d}s} = \frac{q_{\mathrm{HCI}}^2}{4\pi\epsilon_0 v_{\mathrm{HCI}}^2}\omega_{\mathrm{p}}^2\Lambda_c(E_{\mathrm{HCI}}) \quad . \tag{4.19}$$

This expression gives the energy loss of the projectile per travelled distance, which is derived from integrating the energy loss of a single Coulomb collision with impact parameter b over all possible impact parameters. Here, E_{HCI} denotes the initial kinetic energy of the incoming HCI with mass m_{HCI}, charge q_{HCI} and velocity v_{HCI}. The last term in Eq. (4.19) describes the so-called Coulomb logarithm, $\Lambda_c = \int_{b_{\min}}^{b_{\max}} \frac{db}{b}$. It can be expressed by [Bus+06]

$$\Lambda_c = \ln\left(\frac{\sqrt{128}\pi\epsilon_0 E_{\mathrm{HCI}}^{3/2}}{q_{\mathrm{HCI}} q_{\mathrm{t}} \sqrt{m_{\mathrm{HCI}}}\omega_{\mathrm{p}}}\right) \quad . \tag{4.20}$$

The required stopping length s of the target can be estimated by neglecting the energy dependence of Λ_c and assuming that the target does not undergo a phase transition, i.e. $\omega_{\mathrm{p}} \simeq$ constant. This modifies Eq. (4.19) to

$$\frac{\mathrm{d}}{\mathrm{d}s}E_{\mathrm{HCI}} = -\frac{f}{E_{\mathrm{HCI}}} \quad . \tag{4.21}$$

In the case of $^{40}Ar^{13+}$ projectile ions, the maximum kinetic energy derived above yields $f = 157\,\mathrm{meV^2\,\mu m^{-1}}$. The corresponding stopping length $s \simeq 500\,\mathrm{mm}$ is much longer than the largest Coulomb crystal that can be confined inside the trap. Therefore, multiple transits through the trap center are required to stop the ions. This is achieved using the retrapping scheme developed in [Sch+15b], which is schematically shown in Fig. 4.14.

The HCIs are extracted from the EBIT in bunches at high kinetic energies of $695\,\mathrm{V} \times q$ and decelerated to $130\,\mathrm{V} \times q$ before they reach the Paul trap. In order to ensure efficient ion transport, the last deceleration step is realized by the common trap bias of 130 V. Whenever an ion bunch arrives at the Paul trap, the first electrostatic mirror is pulsed down to the trap bias to allow the ion bunch to enter. In this process, the ions lose most of their remaining kinetic energy. Once the ion bunch passed this mirror, it is switched to 200 V and the HCIs are axially confined between the two electrostatic mirrors at both ends of the quadrupole. The ions are then successively reflected back and forth through the trap center, where they are slowed down and finally stopped by Coulomb interaction with laser-cooled $^9Be^+$ ions.

The comparison of the stopping length $s \simeq 500\,\mathrm{mm}$ with the crystal length of 0.5 mm yields a required number of reflections on the order of 10^3 to stop the injected HCIs. In order to ensure a high efficiency of the retrapping process with minimum ion loss, ion-flight simulations were performed.

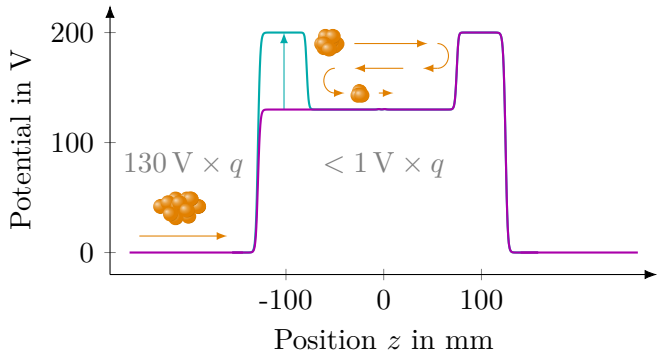

Figure 4.14: Schematic of the retrapping process. The simulated electric potential along the trap axis before the arrival of HCIs is shown in magenta. After the bunch of HCIs has entered the cavity, the first electrostatic mirror is switched to 200 V to close the trap (cyan line). The simulation parameters are given in Tab. 4.7.

Ion-flight simulations

Ion-flight simulations were carried out to determine the experimental parameters allowing for efficient retrapping of HCIs inside the cavity. The simulations are performed using the commercial SIMION software [SIM19]. It allows to solve partial differential equations using the finite difference method. At the beginning of the simulation, the trap geometry is approximated by a uniform mesh consisting of cubes. The electric potentials inside the simulation volume are obtained by solving the Laplace equation for each electrode individually. Subsequently, the electric fields are calculated as the potential gradient. For the simulations presented here, Dirichlet boundary conditions are applied. Each part of the geometry is set to an electrostatic potential and the cavity is enclosed by a grounded box, yielding well-defined boundary conditions. This approximates the real situation in the trap chamber to a high degree, since the cavity is completely surrounded by the cryogenic shields.

Based on the simulated electric fields, the trajectories of the charged particles are calculated stepwise. For each step, the ion parameters, e.g. velocity, electric field, and acceleration, are initialized. Subsequently, a forth-order Runge-Kutta algorithm with variable step size is used to propagate the ion one step further. In general, SIMION only allows to calculate quasi-static electric fields. In order to simulate ion trajectories in the time-dependent fields of the cavity, the temporal evolution of the rf potentials is divided into discrete steps. Hence, for each simulation step the ion experiences an adjusted static electric field, which approximates the time evolution of the rf potentials and is used to calculate the ion trajectory.

The simulation geometry includes the rf cavity and the 4 K electrostatic lenses. Due to the limited computational power, the housing of the cavity was replaced by a simplified geometry. In addition, the inner electrodes of the quadrupole were removed, since they do not modify the potentials along the trajectory of the ion (see Sec. 4.4.1). The simulation

Table 4.7: Parameters used for the simulation of the retrapping process. The cavity is operated with frequency Ω and rf amplitude V_{rf}. During injection of HCIs with mass m and charge q, the first mirror electrode potential is switched from the common trap bias, U_{bias}, to the mirror electrode voltage, U_{mirror}, with a time constant of τ_{mirror}. The dc electrodes are set to U^z_{dc} above the trap bias to mimic the axial confinement of $^9\mathrm{Be}^+$ ions.

Parameter	Value	Parameter	Value
q	$13\,e$	U_{bias}	130 V
m	40 u	U^z_{dc}	1 V
V_{AC}	400 V	U_{mirror}	200 V
$\Omega/2\pi$	34.46 MHz	τ_{mirror}	0.1 µs

grid has a limited resolution of $\mathrm{d}x = \mathrm{d}y = 0.2\,\mathrm{mm}$ and $\mathrm{d}z = 1.0\,\mathrm{mm}$. Therefore, the simulations are intended to give only a qualitative insight into the retrapping process using the cavity. The simulation parameters are summarized in Tab. 4.7.

The simulation sequence is very similar to the retrapping process shown in Fig. 4.14. At the beginning of the simulation, $t = 0$, the ion is located in the middle of the 4 K electrostatic lens with a certain radial distance r to the trap axis z. For each ion, the rf phase of the quadrupole potential is set randomly between zero and 2π. The complete trap assembly including the cavity housing is set to a dc bias of 130 V, while the 4 K electrostatic lenses are set to ground. In order to allow the ion to enter the trap, only the second mirror behind the trap is put on the mirror voltage of 200 V, while the first one is kept at the trap bias. After the ion has entered the trap, the first mirror electrode potential is switched to 200 V at $t = 6\,\mu\mathrm{s}$. The ion is then axially confined between the mirror electrodes and its TOF is registered every time it passes through the center of the trap. The simulation stops in case the ions hits a geometry boundary. This is repeated several times with only one single ion inside the cavity. Similar to the simulations performed in [Pie15], the retrapping efficiency is characterized by the fraction of ions left inside the trap after $t = 500\,\mu\mathrm{s}$.

Three different simulations are performed, which are shown in Fig. 4.15. First, the influence of the dc electrodes on the retrapping process was investigated. Since each quadrupole electrode is equipped with two dc electrodes, the radial ion confinement of the transiting ions strongly depends on the fraction of the rf voltage picked up by the dc electrodes. The simulations are shown in Fig. 4.15(a). The ions are injected parallel to the trap axis with a maximum distance of $r = 0.05\,\mathrm{mm}$. In case of purely static potentials on the dc electrodes, the retrapping efficiency drops drastically. With increasing rf voltage amplitude, the retrapping efficiency increases as well as the acceptance range in kinetic energy. This result is reflected in the dc electrode geometry presented in Sec. 4.2.3. The high capacitance between quadrupole electrode and dc electrode of 15 pF corresponds to a small impedance of about 300 Ω at the quadrupole resonance frequency. By connecting the dc supply rods to the external electronic circuit via a resistance of

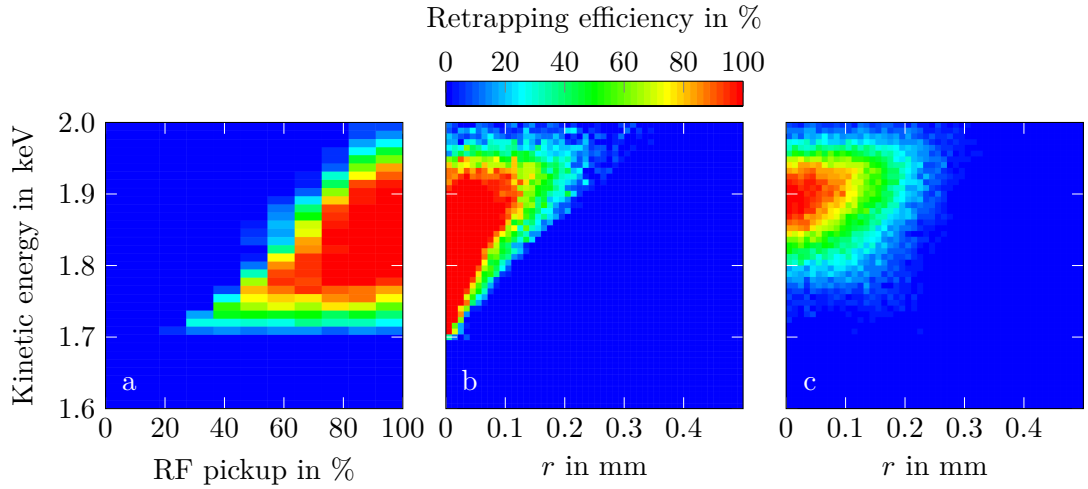

Figure 4.15: Ion-flight simulations of retrapping of HCIs inside the cavity. The colors indicate the retrapping efficiency, which corresponds to the percentage of ions confined for more than 500 µs inside the cavity. (**a**) The retrapping efficiency for injection parallel to the trap axis at a distance of $r < 0.05\,\mathrm{mm}$ is shown as a function of the fractional rf voltage on the dc electrodes and the initial kinetic energy. (**b**) The retrapping efficiency for injection parallel to the trap axis is shown as a function of the initial radial distance r and kinetic energy of the ions. The dc electrodes hold the full rf voltage. (**c**) The ions are injected with a random angle of up to 1° with respect to the trap axis. The retrapping efficiency is shown as a function of the initial radial position r and kinetic energy. The dc electrodes hold the full rf voltage.

66 MΩ (see Sec. 3.2.2), the dc electrodes are charged to the full rf potential present at the quadrupole electrodes. This is considered for the remaining two simulations, for which the dc electrodes are supplied with the full rf voltage.

In order to determine the HCI beam characteristics, which allow for efficient retrapping, the initial kinetic energy of the ions as well as their radial distance to the trap axis are varied. For injection parallel to the trap axis (Fig. 4.15(b)), a clear cut off energy around 1690 eV (130 V × 13 e) is visible at $r = 0$. This corresponds to the minimum kinetic energy required to overcome the potential barrier of the trap bias. For larger distances to the trap axis, the retrapping efficiency drops quickly and allows only ions with higher kinetic energies to be retrapped.

Finally, the influence of the injection angle with respect to the trap axis is investigated (Fig. 4.15(c)). To this end, the ions are injected with a random angle of up to 1° with respect to the trap axis. The angle was chosen according to geometric considerations. If the ions pass through all electrostatic lenses on both sides of the cavity, the angle of the ion beam with respect to the trap axis is already restricted to < 1°. The simulation shows that the total retrapping efficiency is reduced compared to the case of injection

parallel to the trap axis, but still allows for retrapping of a decent fraction of the injected ion bunch. This agrees qualitatively with the results obtained in [Pie15].

4.6 Application of image current detection techniques

Image current detection techniques are well established in Penning trap experiments to determine the eigenfrequencies of trapped ions, e.g. [Ulm11]. Due to the confinement in extremely stable, purely static magnetic and electric potentials, such measurements have reached relative accuracies on the level of $\Delta\nu/\nu \simeq 10^{-11}$ and below [Sch19].

In Paul traps the situation is different. Here, the rf fields for the radial confinement of ions constitute a noise source, which might exceed the amplitude of the induced image current at the frequency of the ion motion. However, due to the high quality factor Q_0 of the cavity developed in this thesis, the residual signal amplitude of the rf drive at the secular frequency of the ion is strongly suppressed (see Fig. 4.2). This might allow for the application of image current techniques, which is discussed in the following section based on [WD75; Ulm11; Stu12].

We consider the case of a single ion of mass m and charge q, which is confined inside the ion trap. The harmonic motion of the ion along the trap axis z with frequency ω_z induces an image current in the trap electrodes. It can be derived by modelling the electrodes as two infinitely extended plates. The induced image current is then given by

$$I_{\mathrm{ind}} = \frac{q}{D_{\mathrm{eff}}}\dot{z} \quad , \tag{4.22}$$

where D_{eff} denotes the effective distance between the trap electrodes, which are used for image current detection. It depends on the trap geometry and the electrode configuration used for readout. In order to reach sizable image currents, one set of four dc electrodes at identical axial distance to the trap center is read out together.

The effective distance D_{eff} can be determined using FEM simulations, similar to the one described in Sec. 4.5.1. To this end, a voltage of 1 V is applied to one set of dc electrodes, while the remaining parts of the cavity are set to ground. The axial electric field in the center of the trap determines the effective distance:

$$D_{\mathrm{eff}} = \frac{1\,\mathrm{V}}{E_z(z=0)} \simeq 11.74\,\mathrm{mm} \quad . \tag{4.23}$$

In order to measure the image current, the trap electrodes are connected to a detection system. A typical detection system consisting of a cryogenic resonator and amplifier is shown in Fig. 4.16 based on [Wei19]. It will be used for the following discussion.

The image current induces a voltage drop over the external LCR resonant circuit, which is given by

$$U_{\mathrm{ind}} = Z_{\mathrm{cav}} I_{\mathrm{ind}} \quad , \tag{4.24}$$

where Z_{cav} denotes the impedance of the cavity from Eq. (2.35). Due to the voltage

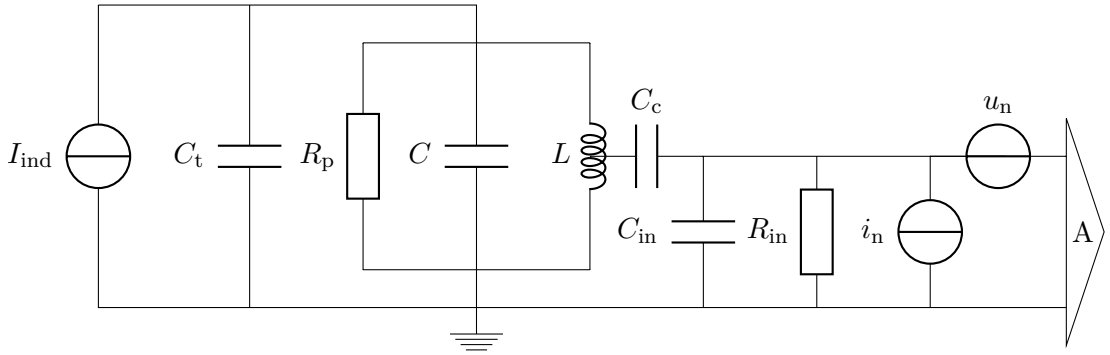

Figure 4.16: Equivalent circuit of ion and detection system consisting of an external resonator, which is modelled by an inductance L, capacitance C and resistance R_{p}, and a cryogenic amplifier. The ion motion induces an image current I_{ind} in the trap electrodes. The capacitance of the trap electrodes and the cable connecting it to the detection system are described by C_{t}. The cryogenic amplifier consists of an ideal amplifier A with input resistance and capacitance R_{in} and C_{in}, which is coupled to the LCR circuit using a coupling capacitance C_{c}. The electronic noise of the amplifier is modelled by a current source i_{n} and voltage source u_{n}. Modified from [Wei19].

drop over the electrodes, the ion motion in the trap is damped with the force

$$F_{\mathrm{ind}} = \frac{qU_{\mathrm{ind}}}{D_{\mathrm{eff}}} = Z_{\mathrm{cav}} \frac{q^2}{D_{\mathrm{eff}}^2} \dot{z} \quad . \tag{4.25}$$

This modifies the equation of motion, which is then given by

$$\ddot{z} + \frac{q^2 Z_{\mathrm{cav}}}{m D_{\mathrm{eff}}^2} \dot{z} + \omega_z^2 z = 0 \quad . \tag{4.26}$$

Therefore, the ion motion depends on the impedance of the external LCR circuit, Z_{cav}. The real part of the impedance leads to dissipation of axial kinetic energy until the ion is in thermal equilibrium with the detection circuit. The decay constant is given by

$$\tau = \frac{1}{\Re(\gamma)} = \frac{m D_{\mathrm{eff}}^2}{q^2 \Re(Z_{\mathrm{cav}})} \quad . \tag{4.27}$$

The imaginary part of the impedance shifts the axial frequency of the ion by [Nat93]

$$\Delta\omega_z \simeq \frac{2q^2 L Q_0^2}{m D_{\mathrm{eff}}^2} (\omega_z - \omega_0) \quad , \tag{4.28}$$

where ω_0, L and Q_0 denote the resonance frequency, inductance and quality factor of the external resonator, respectively. Here, the detuning of the axial frequency of the ion from the resonance frequency was assumed to be small, i.e. $\omega_z \simeq \omega_0$.

Two methods to determine the motional frequency of the ion based on this image current detection technique can be distinguished, which will be explained in the following.

4.6.1 Dip detection

The comparison of Eq. (4.26) with the differential equation for an LCR circuit, allows to model the ion interacting with the trap electrodes and detection system as a series LC circuit. The complete system of ion and detection system is thus described by two coupled resonant circuits with effective impedance Z_{dip}.

The measurable signal is given by the thermal Johnson-Nyquist noise [Joh28; Nyq28] of the equivalent circuit of resonator with ion. It depends on the electric resistance of the component and is given by

$$u_{\mathrm{dip}} = \sqrt{4k_{\mathrm{B}}T\Re(Z_{\mathrm{dip}})\Delta\nu} \quad , \tag{4.29}$$

where $\Delta\nu$ is the frequency bandwidth of the measurement and the real part of the effective impedance is described by

$$\Re(Z_{\mathrm{dip}}(\omega)) = R_{\mathrm{p}}\left[1 + \left(\frac{\omega}{\tau(\omega^2-\omega_z^2)} - Q_0\left(\frac{\omega}{\omega_0} - \frac{\omega_0}{\omega}\right)\right)^2\right]^{-1} \quad . \tag{4.30}$$

Here, R_{p} denotes the parallel resistance of the external resonator. If the ion is in resonance with the external resonator, $\omega_z = \omega_0$, the spectrum exhibits a dip at ω_0, which features a width of

$$\delta\omega_z = \frac{1}{\tau} = \frac{q^2\Re(Z_{\mathrm{cav}})}{mD_{\mathrm{eff}}^2} \quad . \tag{4.31}$$

In order to be able to detect this signal, the trap frequency ω_z and, thus, also the axial trapping potential need to be stable on the level of $\delta\omega_z/\omega_z$ for the duration of the measurement. Additionally, higher-order contributions to the trapping potential induce an energy-dependent shift of the axial frequency (see Eq. (4.14)). This limits the maximum oscillation amplitude of the ion to

$$z_{\mathrm{max}} = \sqrt{\frac{4}{3}\frac{C_2}{C_4}\frac{\delta\omega_z}{\omega_z}} \quad , \tag{4.32}$$

including only the first order anharmonic contribution C_4. For the presented trap geometry, this was estimated in Sec. 4.5.1. Due to the small oscillation amplitude of the ion, we will use the expansion coefficients C_2 and C_4 obtained for the smallest fit range $\Delta z = \pm 0.25\,\mathrm{mm}$.

The dip width $\delta\omega_z$ is directly proportional to the real part of the resonator impedance, $\Re(Z_{\mathrm{cav}})$, which is approximately equal to its parallel resistance R_{p} close to resonance. Therefore, R_{p} needs to be large enough to achieve reasonable dip widths. Typical tank resonators used for image current detection at Penning trap experiments [Ulm+09; Sch19] exhibit loaded quality factors around 5000 with resonance frequencies between 500 kHz and 740 kHz and parallel resistances R_{p} of several 10 MΩ. For the detection system described in [Wei19], even larger values of $R_{\mathrm{p}} \simeq 344\,\mathrm{M\Omega}$ were reported for a detection system with a loaded quality factor of 40000 at $\omega_0/2\pi \simeq 651\,\mathrm{kHz}$. Since

the resistive losses of the resonator increase approximately quadratically with frequency (see Eq. (2.69)), it seems feasible to achieve $R_\mathrm{p} = 100\,\mathrm{M\Omega}$ at a resonance frequency of 1 MHz. This will be considered for the following evaluation.

In the case of a single $^9\mathrm{Be}^+$ ion, Eq. (4.31) yields a dip width of $\delta\omega_z/2\pi \simeq 198\,\mathrm{mHz}$, which corresponds to a required stability of the axial frequency of $\delta\omega_z/\omega_z \simeq 2.0 \times 10^{-7}$ throughout the measurement. For the estimated anharmonic contribution C_4 to the axial potential, the maximum oscillation amplitude is given by $z_\mathrm{max} = 4.0\,\mu\mathrm{m}$. However, in order to detect the dip of the ion motion, the ion has to be in thermal equilibrium with the tank resonator, which is typically at 4 K temperature. This results in a thermal oscillation amplitude of the ion on the order of $z_\mathrm{th} \simeq 13.7\,\mu\mathrm{m}$. Therefore, it will be challenging to detect the dip signal, since the dip is smeared out due to the anharmonicity of the axial potential.

For a single $^{40}\mathrm{Ar}^{13+}$ ion confined inside the trap, the dip width for the same axial frequency is given by $\delta\omega_z/2\pi \simeq 7.5\,\mathrm{Hz}$, which corresponds to a required stability of axial frequency below $\delta\omega_z/\omega_z \simeq 7.5 \times 10^{-6}$. This yields a maximum oscillation amplitude of $z_\mathrm{max} \simeq 24.8\,\mu\mathrm{m}$ for the estimated anharmonicity of the trap. As the motional amplitude in thermal equilibrium with the resonator is on the order of $z_\mathrm{th} \simeq 6.5\,\mu\mathrm{m}$, this signal should be detectable.

In case the ion is cooled far below 4 K, e.g. by direct laser-cooling in the case of $^9\mathrm{Be}^+$, an additional damping term is added to left side of Eq. (4.26). Since the coupling to the resonator is typically much weaker than the coupling to the laser field, the ion motion is strongly damped, depending on the saturation intensity of the laser, and the dip amplitude decreases drastically [Kra17]. In order to increase the ion-resonator coupling, the effective distance between ion and electrode has to be reduced.

4.6.2 Peak detection

If the ion is not in thermal equilibrium with the tank circuit, i.e. for large oscillation amplitudes, the image current of the ion results in a signal peak on top of the noise spectrum of the detector. The detected signal depends on the cryogenic detection system and will be briefly discussed for the detection system shown in Fig. 4.16 based on [Ulm11; Wei19].

The quality of the detection system is quantified by the signal-to-noise ratio (SNR) of the peak signal. This is given by the ratio of the image voltage amplitude and the sum of all noise sources:

$$\mathrm{SNR} = \frac{I_\mathrm{ind}\kappa_c R_\mathrm{p}^* \sqrt{\tau_\mathrm{m}}}{\sqrt{4k_\mathrm{B}TR_\mathrm{p}^*\kappa_\mathrm{c}^2 + u_\mathrm{n}^2 + \left(i_\mathrm{n}R_\mathrm{p}^*\kappa_c^2\right)^2}} \quad , \tag{4.33}$$

where the coupling between resonator and amplifier is given by the coupling constant κ_c, R_p^* denotes the effective parallel resistance, $R_\mathrm{p}^* = (1/R_\mathrm{p} + \kappa_\mathrm{c}^2/R_\mathrm{in})^{-1}$, and the measurement time is given by τ_m. At typical experimental conditions, the current noise i_n can be neglected and the thermal noise dominates, $4k_\mathrm{B}TR_\mathrm{in} \gg u_\mathrm{n}$ [Ulm11]. The maximum

SNR for an optimized coupling constant κ_c is given by

$$\mathrm{SNR} = \frac{I_\mathrm{ind}\sqrt{R_\mathrm{p}\tau_\mathrm{m}}}{\sqrt{4k_\mathrm{B}T\left(1+\dfrac{u_\mathrm{n}}{k_\mathrm{B}TR_\mathrm{in}}\right)}} \quad , \tag{4.34}$$

where $\kappa_\mathrm{c}^2 R_\mathrm{p}/R_\mathrm{in} \ll 1$ was taken into account. This can be used to estimate a lower limit for the oscillation amplitude of the ion, which results in SNR $> 3\,\mathrm{dB}$. Neglecting the technical noise of the amplifier u_n compared to thermal noise at 4 K, this yields a minimum oscillation amplitude $\hat{z}_\mathrm{min}$ for a $^9\mathrm{Be}^+$ ion of

$$\hat{z}_\mathrm{min} = \frac{I_\mathrm{ind}D_\mathrm{eff}}{2\pi\nu_z q} \simeq 4.4\,\mu\mathrm{m} \quad , \tag{4.35}$$

using a measurement time of $\tau_\mathrm{m} = \delta\omega_z^{-1} \simeq 32\,\mathrm{s}$ (see Eq. (4.31)). This is smaller than the oscillation amplitude of the ion in thermal equilibrium with the detection system at 4 K. Thus, this detection scheme can in principle be used to detect the motion of a hot $^9\mathrm{Be}^+$ ion confined inside the cavity. The same holds true in case of an $^{40}\mathrm{Ar}^{13+}$ ion, for which the minimum motional amplitude is given by $z_\mathrm{min} \simeq 2.1\,\mu\mathrm{m}$.

5

CryPTEx-II: Commissioning and First Trapped Ions

This chapter covers the commissioning of the cryogenic Paul trap experiment CryPTEx-II with a focus on the novel superconducting ion trap. This includes both a detailed performance characterization as a radio-frequency (rf) cavity as well as the first experiments with trapped ions. The presented results constitute the proof-of-principle operation of the unique resonator ion trap combination developed within the scope of this work.

The description of the superconducting cavity follows selected results of the cavity prototype in Sec. 5.1, which was built to understand the main features of the cavity and test the fabrication process. In particular, the experimental scheme for impedance matching of the cavity to an external rf source was successfully implemented.

The characterization of the superconducting cavity starts with its performance as an rf resonator presented in Sec. 5.2. Here, the focus is on the electric quadrupole resonant mode of the cavity, especially its resonance frequency and the achieved quality factor. In addition, the cavity behaviour at high electromagnetic (em) field amplitudes, which are required for the strong confinement of ions at high secular frequencies, was investigated.

Besides the commissioning as an rf cavity, the confinement of ions inside the electric potentials of the cavity was investigated (see Sec. 5.3). Therefore, two complementary experiments were performed, which constitute the successful commissioning of the superconducting cavity as an rf ion trap. For future experiments, the cavity is designed to capture and retrap highly charged ions (HCIs) from the external ion source. In order

to characterize the injection performance and probe the quadrupole eigenmode of the cavity, the transmission of HCIs through the cavity was investigated.

Additionally, the first experiments with trapped ions were performed. By operating the cavity as an rf ion trap, the production, confinement, and laser-cooling of $^{9}Be^{+}$ ions was successfully implemented within this thesis.

5.1 The cavity prototype

Before the development of the superconducting cavity, a cavity prototype made of copper was built to investigate the main rf characteristics of the resonator. This allowed in particular to test the frequency of the quadrupole resonant mode, as predicted by finite element method (FEM) simulations. In addition, different experimental procedures for cavity characterization and impedance matching were implemented, which are crucial for the operation of the superconducting cavity. Selected results for the quadrupole resonant mode will be presented in Sec. 5.1.2.

Furthermore, the prototype was used to test and advance the fabrication of critical cavity parts as well as the mounting and positioning of the quadrupole electrodes relative to each other. Consequently, the prototype design differs from the final geometry of the superconducting cavity. The main design features will be briefly reviewed in Sec. 5.1.1 in order to compare the characterization results of prototype and superconducting cavity.

The cavity prototype was built within the scope of this work based on the design developed during the author's Master thesis [Sta15]. Therein, a detailed description of the prototype design and the corresponding FEM simulations of the quadrupole mode is presented. The commissioning experiments of the prototype presented here were performed in the framework of this thesis and partially within [Lie17].

5.1.1 Design

The cavity prototype was primarily built to investigate the rf characteristics of the resonator. Therefore, the design does not include mirror electrodes or direct current (dc) electrodes, which are only required in order to confine ions inside the cavity (see Sec. 4.2). However, the basic geometric structure of both resonators is very similar. The following discussion is focused on the main differences and their impact on the rf properties of the cavities.

Similar to the superconducting cavity, the coaxial quadrupole electrodes consist of an inner and outer electrode, representing the opposite poles of the resonant structure (see Sec. 4.1.2). The main differences are related to the positioning and mounting of the coaxial segments inside the cavity and relative to each other. At the prototype, the electrodes are mounted individually onto socket plates, which are screwed into the resonator housing. Electrical connection between the electrodes and socket plates, as well as between these plates and the housing is provided by solder joints. Since the electrodes on opposite sides of the housing are mounted on individual sockets, the relative alignment is expected to be much worse compared to the superconducting cavity, where

all electrodes are mounted to the monolithic tank. Positioning of the inner and outer electrodes is ensured by insulating spacers made of PEEK, which are positioned at the highest electric field amplitudes. This causes substantial rf loss inside the dielectrics (see Sec. 4.4.2) and lowers the breakdown voltage of the cavity.

These shortcomings were improved substantially for the superconducting cavity, which features suppressed dielectric losses due to low-loss insulators as well as an increased breakdown voltage. The latter is achieved by mounting the positioning insulators to the housing and decreasing the length of the coaxial segments, which increases the creeping distance between the cavity poles. These modifications result in a reduced coaxial capacitance of the superconducting cavity and, thereby, an increased resonance frequency of the quadrupole mode compared to the prototype [Sta15].

This effect is enhanced by the differing electrode geometry. At the prototype, the outer tapered electrodes feature a tip radius of $r_e = 2.1\,\mathrm{mm}$ and are placed at a radial distance of $r_0 = 2\,\mathrm{mm}$ to the trap axis. The corresponding ratio $r_e/r_0 = 1.05$ is much larger compared to $r_e/r_0 \approx 0.51$ for the superconducting cavity (see Sec. 4.2). This results in an increased quadrupole capacitance of the prototype and, therefore, further lowers its resonance frequency compared to the superconducting cavity.

Coupling to the resonant mode is realized using four rf couplers, two capacitive pickups and two inductive coils. They are are made of 1.5 mm thick oxygen-free high thermal conductivity (OFHC) copper rods and feature similar shapes as the couplers of the superconducting cavity (see Sec. 4.2.5). However, they protrude deeper into the cavity volume and are mounted closer to the quadrupole electrodes. Similar to the superconducting cavity, the inductive couplers are fixed to rotatable mounts. This is used to match the impedance of the cavity prototype to an external rf source, using the scheme described in Sec. 2.3.4.

The discussed differences of the cavity geometries are expected to have a minor effect on the rf properties of the resonator. However, the resonance frequency of the quadrupole mode is expected to be smaller for the prototype. In addition, since all electrically conducting parts of the prototype are made of OFHC copper (99.95 %), it is expected to feature increased resistive losses at cryogenic temperatures. This limits the achievable quality factor and thereby the highest em fields amplitudes inside the cavity due to heat-up. Still, the main results obtained for the prototype can be qualitatively compared and applied to the superconducting cavity.

5.1.2 Characterization of the cavity prototype

The prototype was built and characterized before the construction of the cryogenic setup of CryPTEx-II was completed. Therefore, the experimental setup employed for the characterization of the prototype is substantially different compared to the one of the superconducting cavity. In particular, the deviating external electronic circuit and its effect on the experimental results has to be taken into account for a direct comparison.

In order to evaluate the performance at cryogenic temperatures, the prototype was installed at the test bench of the cryogenic storage ring at Max-Planck-Institut für Kernphysik (MPIK). It features a closed-cycle cryocooler, which allowed to cool the pro-

totype to approximately 12 K. Since the cavity was directly mounted to the inner stage of the cold head, the induced vibrations prevented any sensible measurement while the cryocooler was operational. Thus, the cryogenic tests of the prototype were performed directly after the cooler was turned off. In order to account for the temperature increase over the course of the measurement, the nominal temperature is given by the average value. Its uncertainty represents the temperature difference between the start and the end of the measurement, which is much larger than the accuracy of the employed temperature sensors[1].

The cavity prototype features a single resonant mode between 1 Hz and 40 MHz. It was experimentally identified with the quadrupole resonant mode of the electric field by directly measuring the relative rf phase of the quadrupole electrodes during resonant excitation. The following performance characterization of the prototype is focused on this resonant mode. The measurements are performed using a vector network analyzer[2].

Quality factor and resonance frequency

In order to determine the quality factor and resonance frequency of the quadrupole mode, transmission spectra are recorded. The transmitted rf signal between two ports of the cavity is described by Eq. (2.44). Since the transmission is typically measured in decibel, the following model is used to describe the data:

$$\begin{aligned} |S_{21}| &= 10\log_{10}\left(\frac{4(Q_2Q_1)^{-1}}{Q^{-2}+\left(\frac{\omega}{\omega_0}-\frac{\omega_0}{\omega}\right)^2}\right)+10\log_{10}(\tilde{A}) \quad , \\ &= 10\log_{10}\left(\frac{1}{Q^{-2}+\left(\frac{\omega}{\omega_0}-\frac{\omega_0}{\omega}\right)^2}\right)+10\log_{10}(A) \quad . \end{aligned} \tag{5.1}$$

Here, Q and ω_0 denote the loaded quality factor and resonance frequency of the cavity, and $Q_{1,2}^{-1}$ represent the losses of the corresponding ports (see Sec. 2.3.3). Additionally, the losses of the external electronic circuit, e.g. transmission lines, and the gain of external rf amplifiers are taken into account by $\tilde{A}$. Since the losses of the two rf ports and the external circuit cannot be distinguished by fitting this model to the data, they are combined to $A = \tilde{A}(Q_2Q_1)^{-1}$.

Two typical transmission spectra recorded at room temperature and 15(1) K are shown in Fig. 5.1. Within the measurement uncertainty, given by the accuracy of the network analyzer, both measurements are well described by the model from Eq. (5.1). The fit results are listed in Tab. 5.1. Since the two measurements are performed using different experimental setups, not all results can be directly compared. While the effect on the quality factor should be rather small, the determined amplitudes A depend strongly on the external electronic circuit. In addition, the resonance frequency deter-

[1] model DT670 from from Lake Shore Cryotronics, Inc
[2] model Bode100 from OMICRON Lab

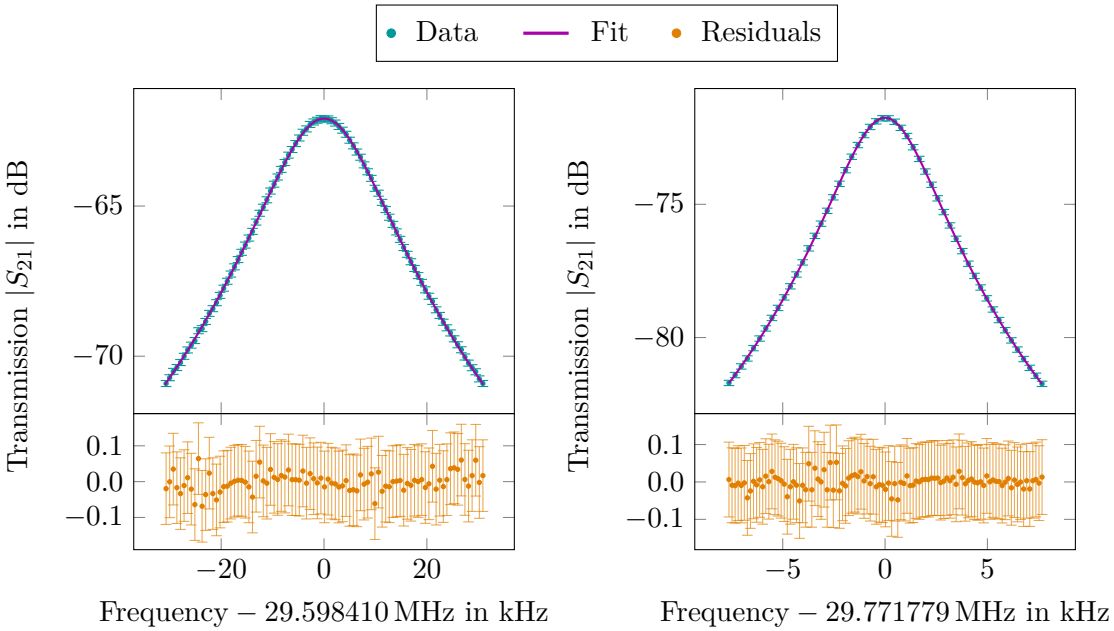

Figure 5.1: Transmission measurement of the cavity prototype at room temperature (**left**) and 15(1) K (**right**) using capacitive coupling at both ports. The measured data is fitted with the model from Eq. (5.1). The residuals are plotted below.

mination is affected by the temperature-dependent properties of the rf couplers and the external circuit. This will be discussed in Sec. 5.2 for the superconducting cavity.

Both measurements yield a resonance frequency of the quadrupole mode around 30 MHz. The results can be compared with the FEM simulations of the prototype performed in [Sta15], where a resonance frequency of 27.2(3) MHz was determined. The large deviation can be explained by the limited computation power of 128 GB available for the simulations, which restricted the mesh resolution to a minimum element size of 2.1 mm. Compared to the detailed simulations of the superconducting cavity presented in Sec. 4.4.1, the simulation result obtained at this large mesh size deviates by ~ 1 MHz

Table 5.1: Characteristics of the cavity prototype at room temperature and 15(1) K. The parameters are determined by fitting the model from Eq. (5.1) to the measured transmission spectra presented in Fig. 5.1. The parameter uncertainties denote the statistical uncertainty of the fit result.

Temperature (K)	Quality factor	Resonance frequency (MHz)	Amplitude A
300	$1.236(1) \times 10^3$	29.598410(7)	$1.2720(6) \times 10^{-6}$
15	$5.820(4) \times 10^3$	29.771779(2)	$8.881(3) \times 10^{-8}$

from the simulation result determined with a minimum element size of 51 µm. Thus, the experimental results are in reasonable agreement with the simulations.

After cooldown to 15(1) K, the resonance frequency is shifted by ~ 173 kHz towards higher frequencies. This is in qualitative agreement with the simulations of the superconducting cavity, which predict an increased resonance frequency after cooldown due to thermal contraction. However, a quantitative comparison is not meaningful since the cavity geometries differ significantly. A detailed discussion of the temperature dependence of the resonance frequency will be given in Sec. 5.2.2 for the superconducting cavity.

The measurements yield a loaded quality factor of 1236(1) at room temperature and 5820(4) at 15(1) K. This corresponds to a resonance linewidth, i.e. the width 3 dB below the maximum, of 23.94(2) kHz and 5.115(4) kHz, respectively. The observed increase of the loaded quality factor after cooldown is related to the temperature-dependent resistivity of the metal, as described by Eq. (4.6). Due to the freeze-out of lattice excitations at low temperatures, the surface resistance of the cavity is reduced. Although the prototype was never tested at temperatures below 12 K, measurements of the quality factor as a function of temperature indicate that the limit is already reached at 17 K. Thus, further reducing the temperature of the prototype will not significantly improve its performance.

The determined quality factor can be used to estimate the expected rf losses during operation as an rf ion trap. For strong radial confinement of $^9Be^+$ ions with secular frequencies on the order of 1 MHz, quadrupole voltage amplitude of $V_{rf} = 325$ V are required for the prototype geometry. Using the LCR model of a resonator (see Sec. 2.3.2), its resistive losses are characterized by the parallel resistance, $R_p = Q(\omega_0 C)^{-1}$. The capacitance of the prototype can be calculated using the formula presented in [Sta15] and amounts to ~ 994.7 pF. This yields a parallel resistance of $R_p = 31.28(2)\,\mathrm{k\Omega}$ at 15(1) K. The corresponding power dissipation for the required rf voltage can be estimated by

$$P_d = 2\frac{V_{rf}^2}{R_p} = 6.753(5)\,\mathrm{W} \quad . \tag{5.2}$$

For the cryogenic setup of CryPTEx-II, the available cooling power of the trap region is limited. Compared to the capacity map of the employed cryocooler [SHI19], the estimated heat load given in Eq. (5.2) would significantly increase the second stage pulse tube temperature to about $7 - 12$ K. The corresponding increase of the trap temperature would drastically reduce HCI storage times due to the deteriorated vacuum conditions inside the 4 K enclosure. Therefore, the prototype cannot be used for the planned experiments at CryPTEx-II.

Impedance matching

The cavity prototype was used to test the technique for impedance matching described in Sec. 2.3.4. In order to match the cavity to the impedance of an external rf drive,

$Z_\mathrm{s} = 50\,\Omega$, the coupling strength of the inductive coupler is adjusted. Close to resonance, the transformed input impedance of the cavity as seen by the external circuit is given by

$$R_\mathrm{in} = \frac{1}{2}\omega_0 N^2 A_\mathrm{c}^2 \frac{B_0^2}{U} Q_0 \cos^2\gamma \quad , \tag{5.3}$$

where the inductive coil is described by the number of windings N and the enclosed area A_c. The em fields of the cavity are described by the average magnetic flux enclosed by the coil, B_0, and the average em energy stored inside the cavity, U. For impedance matching, the coupling strength of the inductive coupler is adjusted by varying the angle γ between its surface normal and the local magnetic field vector.

It has to be noted that the relation from Eq. (5.3) neglects the effect of the external electronic circuit on the effective cavity impedance. Coaxial transmission lines as well as parasitic capacitances of the setup can potentially add a substantial reactive contribution to the total impedance. Therefore, impedance matching is typically achieved for $R_\mathrm{in}/\cos^2\gamma > 50\,\Omega$.

Nevertheless, Eq. (5.3) can be used to estimate the dimensions of the coil allowing for impedance matching. Since the value of B_0^2/U is independent of the employed em field amplitudes inside the cavity, it was determined using simulations similar to the ones described in Sec. 4.4.1. This yields an average magnetic flux inside the coil of approximately $B_0 = 5\,\mu\mathrm{T}$ with an average em energy of $U = 4.5\,\mathrm{nJ}$ stored inside the cavity. For high mechanical stability of the coupler, the number of windings is set to unity. Using the room temperature characteristics of the prototype determined in Sec. 5.1.2, the coil area for $R_\mathrm{in} = 100\,\Omega$ is given by

$$A_\mathrm{c} = \sqrt{\frac{2UR_\mathrm{in}}{\omega_0 B_0^2 Q_0 \cos^2\gamma}} \simeq \frac{4\,\mathrm{cm}^2}{\cos\gamma} \quad . \tag{5.4}$$

Since the effective area can always be reduced by decreasing γ, the first coil geometry was chosen slightly larger and features $A_\mathrm{c} \simeq 6 - 7\,\mathrm{cm}^2$.

Impedance matching of the prototype can be tested either by measuring the frequency-dependent impedance of the cavity, or by measuring the reflection from the impedance-matched port. Both measurements were performed at room temperature for the coil geometry described above. The coil orientation γ is estimated by the angle between its surface normal and the vertical axis and features a typical uncertainty of 10°.

The measurement of the cavity impedance is shown in the left panel of Fig. 5.2 for frequencies between 29.0448 MHz and 29.9255 MHz and three different coil orientations γ. As discussed in Sec. 2.3.4, the impedance of the cavity in the complex plane follows a circular evolution, where the real part of the impedance is maximized at resonance ω_0 and given by $R_\mathrm{in}/\cos^2\gamma$. The measurement performed with $\gamma = 0$ yields a transformed input resistance of $R_\mathrm{in} \simeq 600\,\Omega$.

The horizontal symmetry axis is shifted from the imaginary axis by the impedance of the inductive coupler, $\omega_0 L_\mathrm{c}$, with self inductance L_c. However, the offset of $128\,\Omega$ would correspond to an inductance of $0.7\,\mu\mathrm{H}$, which is nearly two orders of magnitude larger

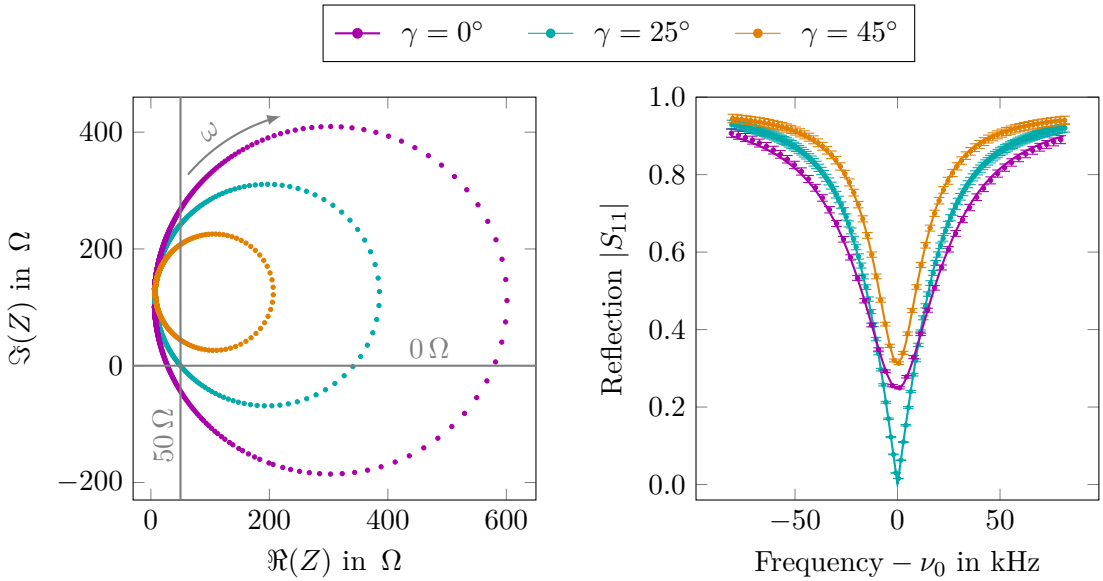

Figure 5.2: Impedance matching of the cavity prototype at room temperature using inductive coupling. The colours indicate different angles of the inductive coil with respect to the vertical axis. **Left:** The measured impedance of the cavity including the external electronic circuit is shown as a function of frequency around its resonance. The frequency increases by following the curves clockwise. The typical source impedance of 50 Ω is indicated by the intersection of the grey lines. **Right:** The corresponding reflection from the cavity is shown as a function of frequency. The measured data is fitted with the model from Eq. (5.5) (solid line).

than the expected value for the coil geometry on the order of 10 nH. Thus, the offset is most likely related to the external electronic circuit including the coaxial transmission lines.

Impedance matching is only achieved for a coil orientation of $\gamma = 25°$, for which the source impedance of 50 Ω is matched at a modified resonance frequency. This is indicated by the grey lines in the left plot of Fig. 5.2. The other two coil orientations feature an input resistance R_{in} which is either too large or too small to allow for impedance matching. This is confirmed by the measurement of the reflected power from the inductive port, shown in the right panel of Fig. 5.2. For perfect impedance matching, the reflected power vanishes at resonance. This is the case for $\gamma = 25°$, for which a minimum reflection of $-71.9(1)$ dB was measured. The other two coil orientations result in a sizable fraction of the rf power being reflected at resonance.

For a quantitative analysis, the coupling constant k of the inductive coupling can be determined using the theoretical description from Eq. (2.41). The reflection is measured

Table 5.2: Impedance matching of the cavity prototype at room temperature. The parameters are determined by fitting the model from Eq. (5.5) to the measured reflection spectra presented in Fig. 5.2. The parameter uncertainties denote the statistical uncertainty of the fit result.

Coil angle γ (deg)	Quality factor	Resonance frequency (MHz)	coupling k	Amplitude A
0	$1.1912(6) \times 10^3$	29.723803(8)	1.6867(7)	0.96794(5)
25	$1.179(1) \times 10^3$	29.7171527(3)	1.000(1)	0.9701(2)
45	$1.1838(4) \times 10^3$	29.712553(3)	0.5119(1)	0.96524(2)

in decibel and accordingly fitted with the model

$$|S_{11}| = 10\log_{10}\left(\frac{(k-1)^2 + Q_0^2\left(\frac{\omega}{\omega_0} - \frac{\omega_0}{\omega}\right)^2}{(k+1)^2 + Q_0^2\left(\frac{\omega}{\omega_0} - \frac{\omega_0}{\omega}\right)^2}\right) + 10\log_{10}(A) \quad , \tag{5.5}$$

where the scaling factor A accounts for the losses of the external electronic circuit. The fit results are presented in Tab. 5.2.

Within the measurement uncertainty, the coil orientation of $\gamma = 25°$ corresponds to perfect impedance matching with $k = 1.000(1)$. For the two other configurations, the coupling strength is either too high ($\gamma = 0°$, $k > 1$) or too small ($\gamma = 45°$, $k < 1$) to achieve impedance matching. As expected, the coil orientation with the smallest angle, i.e. the largest effective area $A_c \cos^2\gamma$, corresponds to the strongest coupling with the largest coupling constant.

Since the logarithm in Eq. (5.5) is not defined at resonance for $k = 1$, the fitting process for $\gamma = 25°$ was unstable and converged to two different results depending on the initial value of k. Therefore, the fitting process was performed for 1000 initial values of $k \in \{0.01, ..., 2.0\}$. The results listed in Tab. 5.2 represent the mean value of the obtained fit results. The uncertainties are given by the squared sum of the fit uncertainty and the standard deviation of the distribution.

The results are in good qualitative agreement with the theoretical description from Sec. 2.3.4. For a detailed quantitative comparison, e.g. including the exact frequency shift of the resonance as a function of coupling strength, the external electronic circuit has to be taken into account. Additionally, the comparably small quality factor of the cavity prototype required a large inductive coil to be mounted in between the quadrupole electrodes and the cavity walls. Due to the close proximity, the coil also couples capacitively to the cavity, where the coupling strength should also depend on the coil orientation. This modifies the load to the cavity represented by the coupler coil and might affect the determined quality factor.

In order to achieve impedance matching at cryogenic temperatures, the coil orientation corresponding to impedance matching at room temperature needs to be adjusted.

Following Eq. (5.3), the relation between the impedance-matched angles γ_{IM} at temperatures T_1 and T_2 is given by

$$\cos^2\gamma_{\mathrm{IM}}(T_2) = \cos^2\gamma_{\mathrm{IM}}(T_1)\frac{A_{\mathrm{c}}(T_1)\omega_0(T_1)Q_0(T_1)}{A_{\mathrm{c}}(T_2)\omega_0(T_2)Q_0(T_2)} \simeq \cos^2\gamma_{\mathrm{IM}}(T_1)\frac{Q_0(T_1)}{Q_0(T_2)} \quad . \tag{5.6}$$

The final result neglects changes of the coil cross section A_{c} due to thermal contraction or expansion as well as the temperature dependence of the resonance frequency. The latter is justified due to the measured change in resonance frequency listed in Tab. 5.1, which is below 1 % for a cooldown from room temperature to 15(1) K. Additionally, the thermal expansion integral $\Delta L/L$ for a complete cooldown from room temperature to 4 K is smaller than 1 % in the relevant cases of niobium or copper [Eki06]. Thus, the approximation of Eq. (5.6) should agree with the exact result on the level of a few percent.

Since the coil orientation can only be adjusted at room temperature, each attempt for impedance matching at low temperatures requires a separate cooldown and warmup. In addition, the influence of the external electronic circuit on the total impedance of the cavity, as shown in Fig. 5.2, is temperature dependent. Thus, it is challenging to precisely set the coupler orientation which corresponds to impedance matching at low temperatures. For the prototype, the minimum reflection achieved at 15(1) K amounts to −25.0(1) dB at resonance. This value can be further reduced by additional fine-tuning of the coupler orientation. The result is in reasonable agreement with the expectation for impedance matching at low temperatures, given the experimental challenges.

In conclusion, the employed scheme for impedance matching of the high-Q cavity to the external rf drive was successfully tested, both at room temperature and at cryogenic temperatures. Thus, it will also be implemented at the superconducting cavity.

5.2 Characterization of the superconducting cavity

The presented commissioning experiments of the novel superconducting cavity were performed after integrating it into the cryogenic setup of CryPTEx-II. As the cavity is designed to confine ions, the main focus is on the performance characterization of its electric quadrupole resonant mode. This is identified using the FEM simulation described in Sec. 4.4.1 to analyze the excitation spectrum of the cavity (see Sec. 5.2.1).

The performance characterization of the cavity includes the evaluation of its quality factor and resonance frequency at room temperature and during cooldown to 4 K (see Sec. 5.2.2). Here, a detailed study of the rf coupling to the cavity is conducted in order to evaluate the performance of the loaded cavity as well as the properties of the employed capacitive and inductive couplers (see Sec. 5.2.3). In addition, since the cavity is intended to confine ions at high secular frequencies, its behaviour at high rf amplitudes is investigated in Sec. 5.2.4. The characterization results are discussed in Sec. 5.2.5 together with potential limitations of the cavity performance.

A major part of the characterization is based on the analysis of transmission and reflection spectra. These are recorded with a vector network analyzer[3]. The measurement uncertainty for all recorded spectra is given by the instrument accuracy.

The first commissioning experiments were performed with rf couplers made of OFHC copper. These have nearly identical shapes as their niobium equivalents described in Sec. 4.2.5 and thus exhibit similar rf properties. However, a direct comparison of the obtained results has to account for material-specific effects, e.g. the power dissipation of the coupler itself. The measurements performed with the copper couplers are indicated.

5.2.1 Resonant modes

In order to identify the quadrupole resonant mode of the cavity, a broad excitation spectrum is recorded at room temperature, which is shown in Fig. 5.3. The spectrum features three isolated regions of increased transmission between 1 Hz and 100 MHz, which indicate the eigenfrequencies of the cavity. These can be compared to the simulated eigenfrequencies from Sec. 4.4.1, which are indicated by the magenta lines in Fig. 5.3.

Although the simulation results deviate from the measured resonances, they can definitely be assigned to the corresponding transmission peaks. The resonant mode around 34.4 MHz is identified as the electric quadrupole mode. It shows the smallest discrepancy between the simulation result and the measured resonance frequency. This could be related to the simplifications of the simulation geometry, which were chosen in order to minimize their effect on the quadrupole mode (see Sec. 4.4.1). The two distinct eigenfrequencies at 58.6(1) MHz and 58.7(1) MHz predicted by the simulations are not resolved in the measurement. It is suspected that the resonance linewidths are larger than their separation.

For a detailed comparison of the quadrupole mode frequencies of simulation and experiment, the transmission spectrum from Fig. 5.3 is fitted with the model from Eq. (5.1). This yields a resonance frequency of 34.3829(2) MHz, which deviates by 468.1 kHz from the simulation result. This discrepancy is much larger than the estimated simulation uncertainty of 9 kHz. Since the simulation is neglecting resistive and dielectric losses, the corresponding damping of the em fields inside the cavity might cause a shift of the resonance frequency in experiment. According to Sec. 2.3.2, the resonance frequency ω_d of the damped LCR circuit is given by $\omega_\mathrm{d}^2 = \omega_0^2 - \gamma^2$, with the damping constant $\gamma = \omega_0/2Q$. Thus, for the determined quality factor of $Q = 270(3)$ at room temperature, the correction contributes only at the level of $\omega_\mathrm{d}/\omega_0 \simeq 1 - 10^{-6}$. Therefore, this effect is smaller than the uncertainty of the fit result and cannot explain the deviation from the simulation. However, the simulation did not include the rf couplers as well as the external electronic circuit. These can cause a significant shift of the resonance frequency, e.g. due to the capacitance of the coaxial transmission lines or parasitic capacitances between coupler and rf ground.

[3] model ZVL3 from Rohde & Schwarz GmbH & Co. KG

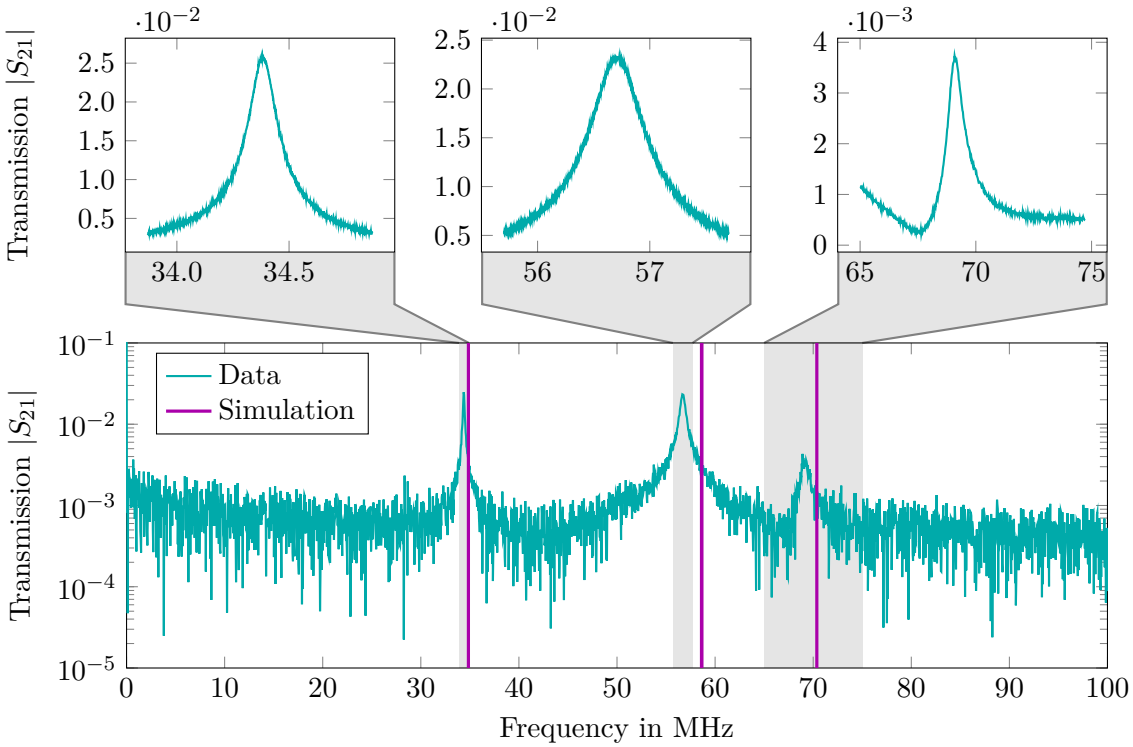

Figure 5.3: Excitation spectrum of the superconducting cavity between 1 Hz and 100 MHz recorded at room temperature. The transmission was measured using inductive coupling at port one and capacitive coupling at port two (cyan). The vertical lines (magenta) represent the simulated eigenfrequencies of the cavity (see Sec. 4.4.1). Detailed views of the resonances are shown in the panels above.

Both, the simulation as well as the measured transmission spectrum, indicate that the quadrupole resonance is well-separated from the other eigenmodes of the cavity. This allows to selectively couple to this mode and justifies its theoretical description as an isolated resonance. The following commissioning results of the superconducting cavity are completely focused on the quadrupole mode.

5.2.2 Cooldown of the cavity

In order to understand the behaviour of the superconducting cavity during the transition from the normal conducting to the superconducting state, the transmission is continuously measured during cooldown. Each recorded transmission spectrum is fitted with the model from Eq. (5.1) to determine the resonance frequency and quality factor of the cavity. The temperature at the position of the cavity is measured before and after each scan and the nominal temperature is given by the average of both measurements. The temperature uncertainty is estimated by the squared sum of the sensor accuracy and the

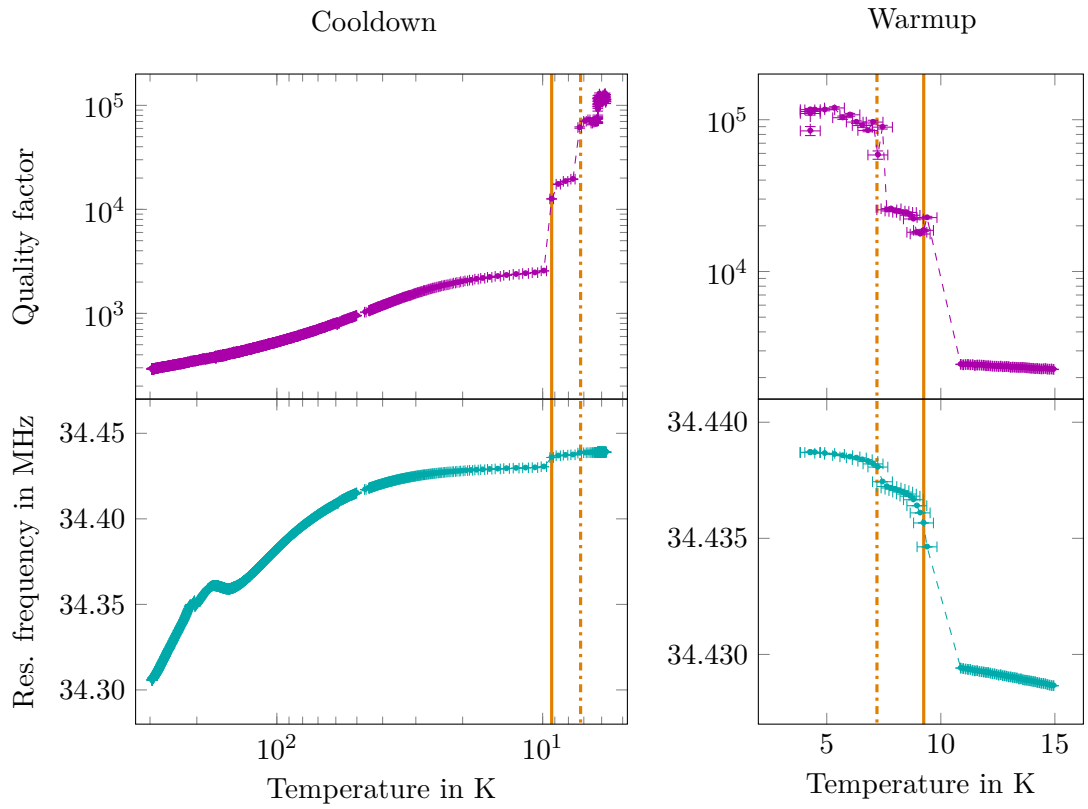

Figure 5.4: The quality factor and resonance frequency of the superconducting cavity as a function of temperature during cooldown (**left**) and warmup (**right**). The parameters are determined by fitting the model from equation Eq. (5.1) to the measured transmission spectra. The vertical lines indicate the critical temperatures of niobium ($T_c^{Nb} = 9.25\,K$, solid) and lead ($T_c^{Pb} = 7.2\,K$, dashed). The measurements are performed using capacitive couplers made of OFHC copper at both ports.

difference of the two measurements. A complete cooldown scan from room temperature to below 6 K is shown in the left panel of Fig. 5.4.

For temperatures above 10 K, the change of the quality factor is related to the temperature-dependent resistivity of the normal-conducting metal (see Eq. (4.6)). As the lattice excitation freeze out towards lower temperatures, the surface resistance of the cavity is reduced and the quality factor increases.

Below 10 K, the quality factor shows three distinct jumps. The first two are related to the drastic decrease of the resistive cavity losses below the critical temperatures of the involved superconductors. They coincide reasonably well with the critical temperatures of niobium, $T_c^{Nb} = 9.25\,K$ [Fis+05], and lead, $T_c^{Pb} = 7.2\,K$ [Fis+05], which are indicated in Fig. 5.4.

While the first observed discontinuity around T_c^{Nb} is expected, since most of the cavity parts are made of niobium, the extent of the second feature at T_c^{Pb} might be surprising. However, as shown by the FEM simulations presented in Sec. 4.4.1, the lids of the cavity housing, which are connected to the monolithic tank using lead sealings, contribute significantly to the oscillating rf currents inside the cavity walls. Thus, at temperatures $T_c^{Pb} < T < T_c^{Nb}$, the resistive losses of the normal-conducting lead sealings dominate the rf losses of the cavity and limit its quality factor.

A precise comparison of the temperatures related to the observed sudden increases of the quality factor and the indicated critical temperatures of the involved superconductors reveals that the temperature measurement is lagging. These small deviations can easily be explained by the short time-scale of the cooldown through both critical temperatures. The temperature range between 10 K and 6.9 K is bridged within approximately 4 min, while each transmission spectrum in this region takes approximately 40 s. Since the temperature sensor is constantly heated by thermal conduction through its electrical connections, it needs a finite time to thermalize with its surroundings. Therefore, it is expected to show a certain time delay to the actual temperature of the 4 K stage.

Below 7 K, the measurements shown another sudden increase in quality factor, which is caused by the measurement settings. For the short cooldown through the superconducting phase transitions, the measurement bandwidth was set to 100 Hz to allow for fast measurements. At temperatures below 7 K, this limits the measured linewidth of the resonance, which amounts to approximately 350 Hz at $Q = 10^5$. Thus, the measurement bandwidth was decreased to 10 Hz in order to resolve the narrow resonance at lower temperatures.

The resonance frequency as a function of temperature during cooldown can also be seen in the left panel of Fig. 5.4. The measurement shows two distinct jumps at T_c^{Nb} and T_c^{Pb}, where the latter is hardly visible due its small size. They are expected to result from the sudden increase of the quality factor at the corresponding temperatures. As discussed in Sec. 5.2.1, the suppression of the resistive losses of the cavity, indicated by the increase of the quality factor, should have a negligible effect on the free resonance frequency. However, the observed jumps of the quality factor can potentially cause a drastic change of the capacitive coupling strength and thereby shift the measured resonance frequency.

The overall increase of the resonance frequency during cooldown from room temperature to 6 K amounts to 133.1(1) kHz. This is substantially larger than the value predicted by the simulations presented in Sec. 4.4.1, which show an increase of 50 kHz after cooldown to 4 K due to thermal contraction. This deviation can be explained by the temperature dependence of the coupling strength, which affects the resonance frequency determination. In addition, the simulations do not include the external electronic circuit, which loads the cavity. Since the coaxial transmission lines connected to the rf couplers are directly thermalized to 4 K, this effect is expected to be temperature-dependent and could potentially cause an increased frequency shift during cooldown.

As a consistency check, an identical measurement of the cavity transmission is performed during warmup. The results are displayed in the right panel of Fig. 5.4. The

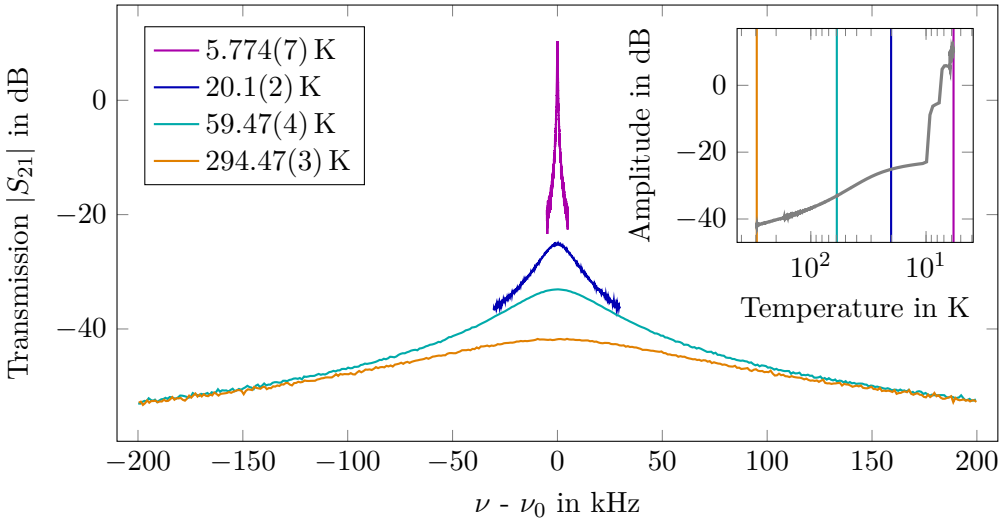

Figure 5.5: Transmission spectra of the superconducting cavity recorded at different temperatures using capacitive coupling at both ports. The data represents an excerpt of the cooldown measurement presented in Fig. 5.4. The inset shows the transmission amplitude at resonance as a function of temperature for the complete cooldown. The vertical lines mark the displayed transmission measurements.

measurements are taken after the cryocooler was turned off. Due to the large temperature gradients over the course of a single measurement below 10 K, the temperature uncertainty is estimated by the largest difference between any two consecutive measurements. Again, the evolution of the quality factor shows two distinct discontinuities at the critical temperatures of lead and niobium. The same can be observed for the resonance frequency. Compared to the cooldown measurement, the second jump at T_c^{Pb} is clearly visible due to the different frequency scale of the plot.

In order to show the drastic transformation of the transmission spectrum during cooldown, Fig. 5.5 shows selected resonance curves. These were recorded during the cooldown measurement shown in Fig. 5.4. With decreasing cavity temperature, the bandwidth of the resonance decreases while the transmission amplitude at resonance increases.

A second cooldown measurement of the cavity is shown in Fig. 5.6 for temperatures below 6 K. Both the determined quality factors as well as the resonance frequencies show fluctuations larger than the measurement uncertainties. While the quality factor is determined with a typical uncertainty below 10^4, the resonance frequency features an uncertainty on the level of a few Hz. Each measurement represents the average of 200 individual transmission scans and took more than one hour. Therefore, the temperature change of the second stage as well as the first stage (see Sec. 3.1.4) over the course of one measurement is significant. This can affect the external electronic circuit inside the cryogenic shields and thereby cause shifts of the measured resonance frequency. Ac-

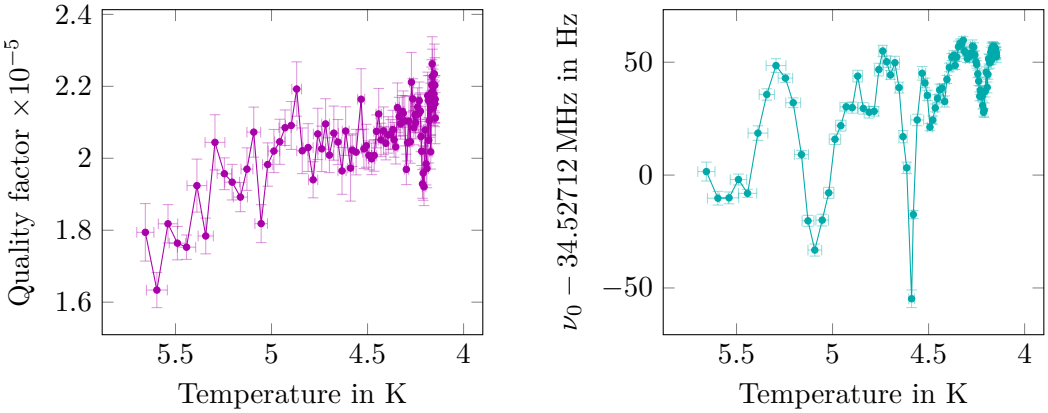

Figure 5.6: The quality factor (**left**) and resonance frequency (**right**) of the superconducting cavity as a function of temperature during cooldown. The parameters are determined by fitting the model from equation Eq. (5.1) to the measured transmission spectra. The measurements are performed using capacitive couplers made of niobium at both ports.

cordingly, most spectra showed mildly asymmetric lineshapes of the resonance, which also affects the quality factor determination. Nevertheless, the measurements consistently show quality factors around 2×10^5 below 5 K. A detailed analysis of the cavity transmission and reflection at 4 K will be given in the subsequent sections.

5.2.3 Cavity performance at low temperatures

As described in Sec. 2.3.3, an rf cavity can be characterized by measuring its transmission and reflection spectra. Thereby, it is in general not possible to determine the free, i.e. the uncoupled properties of the cavity, since the measurement itself is affecting the cavity performance. This is related to the influence of the external electronic circuit, which also depends on the coupling constant k of the employed rf couplers, and the supplied input power of the rf drive. While the former effect was already observed for the cavity prototype and the cooldown measurement, the latter will be discussed in detail in Sec. 5.2.4.

Capacitive coupling to the cavity

The capacitive couplers of the cavity are designed to couple very weakly ($k \ll 1$) to the electric fields of the resonant mode. Therefore, they present a minor load to the cavity and are expected to have a negligible effect on the determination of its quality factor Q. In order to determine the free parameters of the cavity, the input power is reduced as much as possible. The measurements are taken with supplied rf powers of −60 dBm and −40 dBm for the transmission and reflection scans, respectively. In order to provide the

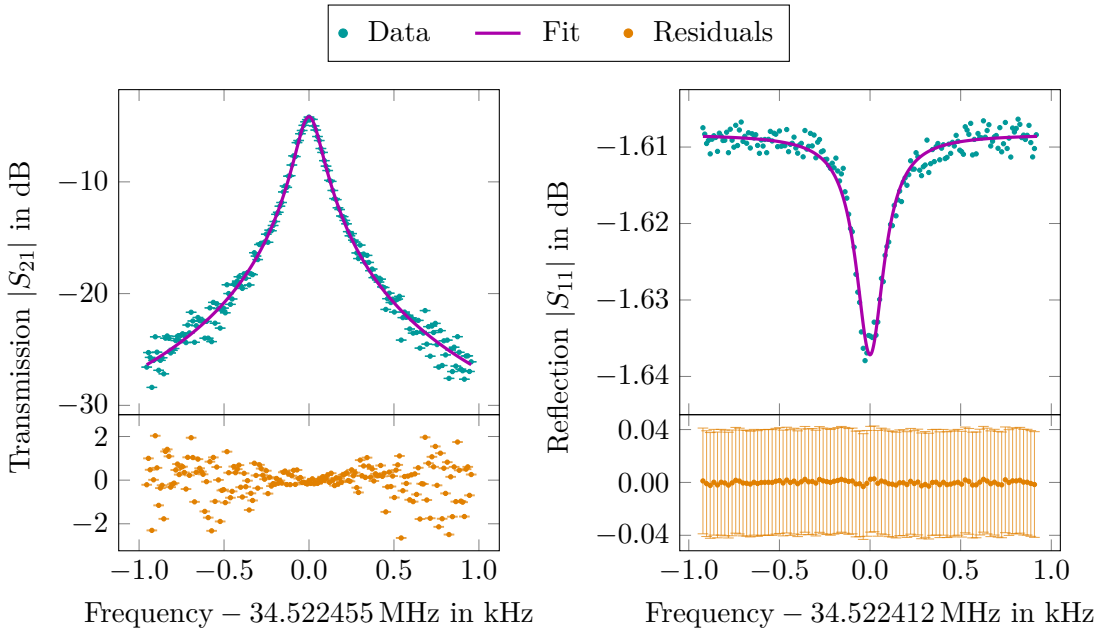

Figure 5.7: Characterization of the superconducting cavity using capacitive coupling at both ports. **Left:** The transmission measured at 4.26(1) K is shown as a function of frequency together with a fit to the data (model from Eq. (5.1)). The residuals are plotted below. **Right:** The reflection measured at 4.14(1) K is plotted as a function of frequency together with a fit to the data (model from Eq. (5.5)). For better visibility, the error bars are only shown for the residuals, which are plotted below.

network analyzer with a measurable signal, the transmitted power is typically amplified using two broadband amplifiers[4], which yields a total amplification around 48 dB.

The characterization measurements of the superconducting cavity using capacitive coupling are shown in Fig. 5.7. In order to determine the cavity characteristics, the transmission and reflection spectra are fitted with the models from Eq. (5.1) and Eq. (5.5), respectively. The results are listed in Tab. 5.3.

The transmission measurement shown in the left panel of Fig. 5.7 is well described by the fitted model, with the residuals scattered symmetrically around zero. However, the residuals increase towards lower signal amplitudes, i.e. for larger detuning from the resonance, and are significantly larger than the measurement uncertainty. This is suspected to result from strongly underestimated uncertainties, which are given by the instrument accuracy. Since this is only specified for a source power of 0 dBm down to a signal size of −40 dB, it does not cover the detected signals of the transmission measurement with absolute amplitudes between −65 dBm and −85 dBm.

[4]model ZFL-500LN-BNC+ from Mini-Circuits

Table 5.3: Characteristics of the superconducting cavity for capacitive coupling. The parameters are determined by fitting the model from Eq. (5.1) (transmission) and Eq. (5.5) (reflection) to the measured data presented in Fig. 5.7. The parameter uncertainties denote the statistical uncertainty of the fit result.

Measurement type	Quality factor	Resonance frequency (MHz)	coupling k	Amplitude A
Transmission	$2.32(8) \times 10^5$	34.522455(2)	-	$5.33(4) \times 10^{-6}$
Reflection	$1.83(5) \times 10^5$	34.522412(2)	0.00166(3)	$8.3097(1) \times 10^{-1}$

The reflection measurement is shown in the right panel of Fig. 5.7. Due to the weak coupling, only a small fraction of the supplied signal is fed into the cavity while most of it gets reflected. Therefore, the absorption dip at resonance is much smaller than the measurement uncertainty. Additionally, the input power had to be increased to $-40\,\mathrm{dBm}$ in order to achieve a reasonable signal-to-noise ratio (SNR). The data is rather well described by the fitted model, although the measurement shows comparably large fluctuations and asymmetric residuals on the wings of the resonance.

The transmission fit yields a loaded quality factor of $2.32(8) \times 10^5$, which corresponds to resonance linewidth of $149(5)\,\mathrm{Hz}$. As described in Sec. 2.3.3, the quality factor determined using a transmission measurement represents a lower limit for the unloaded quality factor of the cavity. However, since the capacitive coupling is so weak, $k < 0.002$ (see Tab. 5.3), the external losses introduced by the measurement are suppressed. Therefore, the determined quality factor also represents a good approximation for the unloaded quality factor of the cavity.

The quality factor determined by the reflection measurement is significantly lower compared to the result of the transmission scan. However, since the measurement was performed at much higher rf power, heating of the coupler and the external circuit cannot be neglected. This can cause the observed asymmetry of the lineshape and, thereby, affect the quality factor determination (see Sec. 5.2.4). In addition, the measurement features a small SNR and comparably large fluctuations of the data points around resonance. Therefore, the reflection measurement is only intended to give an estimate for the capacitive coupling constant. The determined value supports the expected weak coupling strength. This allows to use the capacitive coupler to monitor the status of the cavity during operation without influencing its performance.

The determined quality factor of $2.32(8) \times 10^5$ is within the specifications for the performance of the superconducting cavity given in Sec. 4.3.1. However, it is much smaller than typical values reported for state-of-the-art superconducting cavities used at accelerator facilities, e.g. [Res+17]. Possible limitations of the cavity performance and potential measures to improve it will be discussed in Sec. 5.2.5.

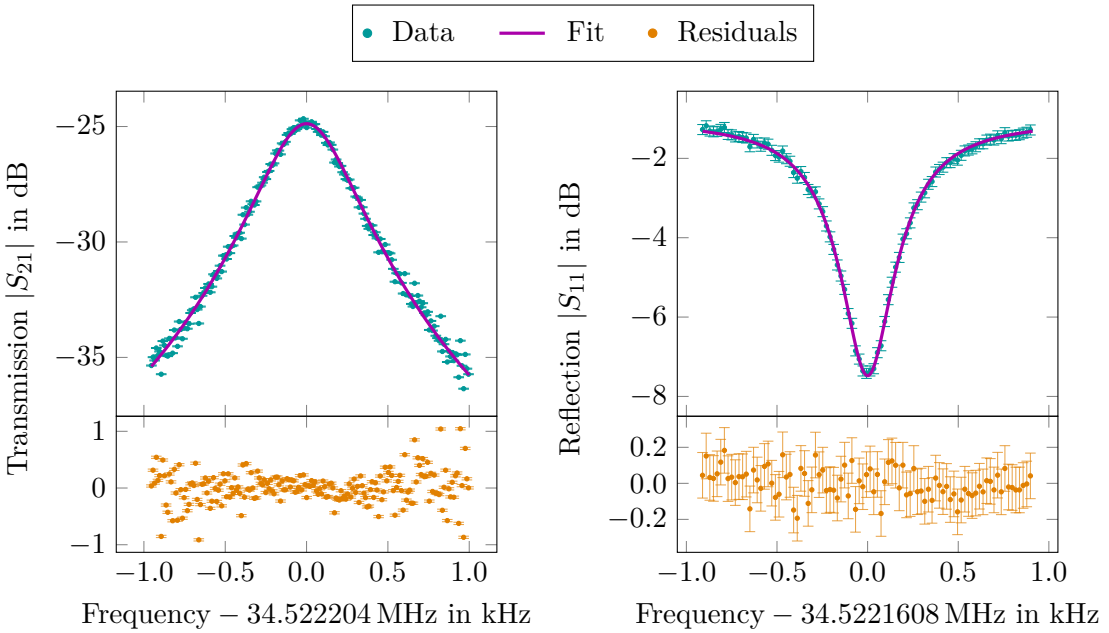

Figure 5.8: Characterization of the superconducting cavity using inductive coupling at port one and capacitive coupling at port two. **Left:** The transmission measured at 4.12(1) K is shown as a function of frequency together with a fit to the data (model from Eq. (5.1)). The residuals are plotted below. **Right:** The reflection measured at 4.12(1) K is plotted as a function of frequency together with a fit to the data (model from Eq. (5.5)). The residuals are shown below.

Inductive coupling to the cavity

The inductive coupler is designed to efficiently drive the cavity. For impedance matching, the experimental scheme introduced in Sec. 2.3.4 will be employed. This method was successfully implemented at the cavity prototype, as described in Sec. 5.1.2. Since the superconducting cavity was not yet characterized when the niobium rf couplers had been installed, it was not attempted to impedance-match the cavity. For the commissioning experiments presented here, the niobium coupler was installed in horizontal orientation, which corresponds to the maximum coupling strength.

The transmission and reflection measurements are performed at input powers of −80 dBm and −70 dBm, respectively. These are reduced compared to the characterization measurements using the capacitive coupling in order to suppress the asymmetry of the resonance lineshape induced by heating. This effect will be discussed in more detail in Sec. 5.2.4.

The transmission measurement is shown in the left panel of Fig. 5.8. Due to the increased coupling strength of the inductive coupler compared to the capacitive pickups, the measurement is performed without external amplification. The data is well described by the model from Eq. (5.1) and shows symmetrically scattered residuals. Similar to

Table 5.4: Characteristics of the superconducting cavity for inductive coupling. The parameters are determined by fitting the model from Eq. (5.1) (transmission) and Eq. (5.5) (reflection) to the measured data presented in Fig. 5.8. The parameter uncertainties denote the statistical uncertainty of the fit result.

Measurement type	Quality factor	Resonance frequency (MHz)	coupling k	Amplitude A
Transmission	$5.79(5) \times 10^4$	34.522204(2)	-	$1.969(8) \times 10^{-6}$
Reflection	$2.43(2) \times 10^5$	34.5221608(6)	2.820(9)	$8.88(1) \times 10^{-1}$

the capacitive characterization, the measurement uncertainty, given by the instrument accuracy, is substantially underestimated.

The reflection spectrum shown in the right panel of Fig. 5.8 exhibits a sizable absorption dip at resonance. This already indicates a strong coupling to the cavity. The data is well described by the fitted model from Eq. (5.5).

The fit results of both measurements are listed in Tab. 5.4. The resonance frequency in reflection is shifted to smaller values compared to the transmission measurement. The determined coupling constant of $k \simeq 2.8$ indicates over-critical coupling to the cavity, which was expected due to the coil orientation chosen to maximize its effective area.

The reflection measurement yields an unloaded quality factor of $Q_0 = 2.43(2) \times 10^5$. This result has to be compared to the loaded quality factor determined in transmission. According to Eq. (2.38), the loaded quality factor can be expressed by

$$Q^{-1} = Q_0^{-1} + \sum_n Q_n^{-1} \quad , \tag{5.7}$$

where the sum represents all external losses introduced to the systems. This includes the losses of the employed rf couplers. Using the definition of the coupling strength at port i, $k_i = Q_0/Q_i$, the unloaded quality factor can be approximated by

$$Q_0 \simeq Q \left(1 + \sum_n k_n\right) \quad , \tag{5.8}$$

neglecting further loss mechanisms. Since the inductive coupling strength is much larger than the capacitive one, the latter can neglected. This yields an unloaded quality factor of $Q_0 = 2.21(6) \times 10^5$, which is in reasonable agreement with the result from the reflection measurement considering the simplified description. In addition, both values agree with the result obtained with capacitive coupling and are thus also within the performance specification of the superconducting cavity (see Sec. 4.3.1). A detailed discussion of the cavity performance and its potential limitations will be provided in Sec. 5.2.5.

For impedance matching at cryogenic temperatures, the cavity needs to be impedance-matched at room temperature first. Even though this was not attempted during commissioning, the obtained characterization results can be used to estimate the input impedance of the cavity, which is described by Eq. (5.3). The FEM simulations presented

in Sec. 4.4.1 yield an average magnetic field amplitude inside the inductive coupling coil of $B_0 \simeq 3\,\mu\mathrm{T}$ with a total em energy stored inside the cavity of $U = 1.84\,\mathrm{nJ}$. Using the characterization results from Tab. 5.4, one finds a transformed input resistance of the inductively coupled cavity of $R_{\mathrm{in}}/\cos^2\gamma \simeq 58\,\Omega$. However, the real value can be slightly larger as the enclosed area of the coil might be increased due to fabrication tolerances. Eventually, the suitability of the coil for impedance matching depends on the external electronic setup and needs to be tested in experiment.

5.2.4 Power dissipation of the cavity

The rf power dissipation of the cavity during operation represents a heat load to the cryogenic system and leads to an increased trap temperature. This can limit the storage times of HCIs, since the residual gas pressure inside the cryogenic enclosure increases with the second stage temperature. Therefore, it is necessary to evaluate the cavity performance at high amplitudes of the intra-cavity em fields, which are required for the operation as an rf ion trap.

For the strong radial confinement of $^9\mathrm{Be}^+$ ions with secular frequencies around 1 MHz, the superconducting cavity requires quadrupole voltage amplitudes on the order of $V_{\mathrm{rf}} = 280\,\mathrm{V}$. The corresponding power dissipation can be estimated using the parallel resistance $R_{\mathrm{p}} = Q_0(\omega_0 C)^{-1}$ of the equivalent LCR circuit. The geometric capacitance of the superconducting cavity can be calculated using the formula presented in [Sta15] and amounts to $C \approx 928\,\mathrm{pF}$. This is slightly smaller compared to the capacitance of the prototype due to the design changes of the coaxial segments. Using the cavity parameters of the inductive reflection measurement listed in Tab. 5.4, one obtains a parallel resistance of $R_{\mathrm{p}} = 1.207(8)\,\mathrm{M}\Omega$. The corresponding losses can be calculated using Eq. (5.2), which yields a dissipated power of $129.9(8)\,\mathrm{mW}$ for an rf amplitude of $V_{\mathrm{rf}} = 280\,\mathrm{V}$.

Compared to the capacity map of the employed cyrocooler [SHI19], the estimated heat load would only cause a minor heat-up of the pulse tube and leave the trap at a temperature below 5 K. This is comparable to the trap temperatures reported for CryPTEx-PTB [Leo+19] and should therefore allow for reasonable storage times of HCIs. However, this rough estimate neglects the temperature-dependence of the surface resistance of the cavity, which is shown by the cooldown measurements (see Sec. 5.2.2). The resistive losses of the cavity, which are indicated by its quality factor, increase with temperature, which leads to an enhanced heat-up of the cold stage. In order to investigate this effect two measurements were performed, which will be discussed in the following.

In order to characterize the cavity performance at high input powers, its transmission and reflection is measured as a function of the input power supplied to the inductive coupler. The measurements are performed using the rf couplers made of OFHC copper and are shown in Fig. 5.9. Each spectrum represents the average of ten measurements, which were recorded in one series. The total measurement time at each input power amounts to 20 min.

Both measurements show a shift of the resonance towards lower frequencies with increasing input power. This shift is accompanied by an asymmetry of the resonance

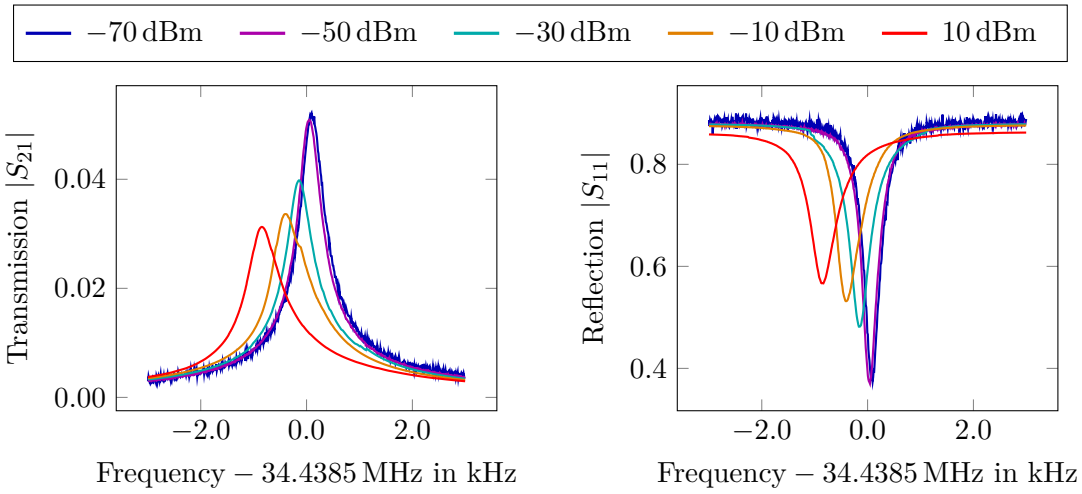

Figure 5.9: Transmission (**left**) and reflection (**right**) spectra of the superconducting cavity as a function of the input power applied to port one. The data was recorded at 4.29(1) K using inductive coupling at port one and capacitive coupling at port two. The measurements are performed using the rf couplers made of OFHC copper.

lineshape, which becomes more pronounced for higher rf powers. Additionally, the amplitude of the transmission peak as well as the amplitude of the reflection dip decreases as a function of power.

According to the measurements of the cavity cooldown and warmup (see Sec. 5.2.2), both the resonance frequency shift as well as the reduced quality factor indicate a rise of the cavity temperature. However, no significant increase above 10 mK was observed over the course of the complete measurement series. The measured frequency shifts on the order of kHz can be compared to the warmup measurement. This shows that an increase of the cavity temperature on the order of 1 K would be necessary in order to cause the observed shifts.

Another explanation could be a potential warmup of the rf coupler, which is used to drive the cavity. In contrast to the cavity, which features a frequency-dependent rf power acceptance, the rf coupler is constantly exposed to the applied rf signal and thus continuously dissipates power. This could increase the temperature of coupler and external electronic circuit, which causes a change of the coupling and the coupling constant k, thereby affecting the load to the cavity. Accordingly, the measured resonance frequency drifts, which could explain the observed frequency shift as well as the asymmetry of the lineshape due to the averaging. In addition, a modified coupling constant would also affect the fraction of the applied rf power which is coupled into the cavity. This could explain the reduced amplitudes of transmission peaks and reflection dips at high powers.

In order to investigate the steady-state power consumption of the cavity at high amplitudes of the stored em fields, the cavity was resonantly driven with an external rf

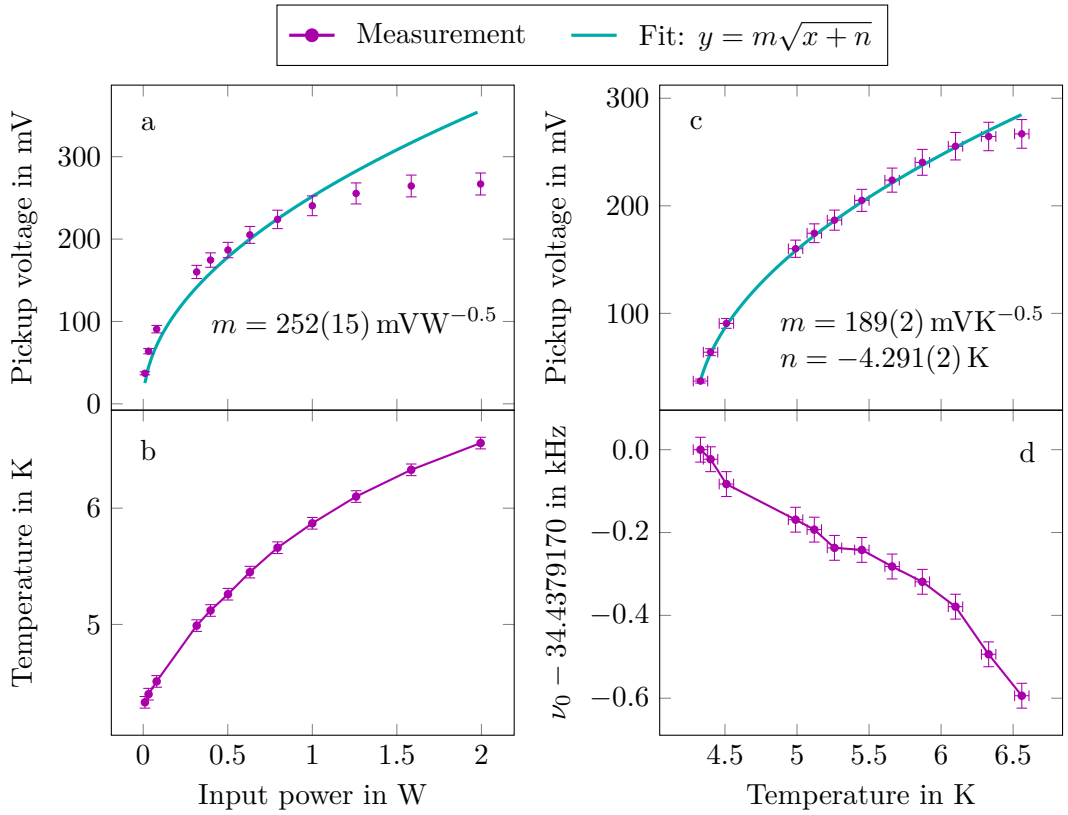

Figure 5.10: Characterization of the superconducting cavity for high rf powers supplied to the inductive coupler. The measurements are performed in steady state using the rf couplers made of OFHC copper. **Left:** The pickup voltage at the capacitive coupler (**a**) as well as the cavity temperature (**b**) are shown as a function of the supplied input power. **Right:** The pickup voltage (**c**) and resonance frequency (**d**) are plotted as a function of the cavity temperature, which depends on the supplied rf input power. The data in (**a**) and (**c**) are fitted with the given model, the fit results for the employed parameters are stated.

signal generator. The intra-cavity power is monitored using the capacitive coupler and parametrized by the measured pickup voltage. As the resonance frequency of the cavity depends on the supplied rf power, the frequency of the applied rf signal was precisely adjusted to the modified resonance frequency at a given input power. This is identified by the maximum of the measured pickup voltage, which is extremely sensitive to small frequency variations due to the narrow resonance linewidth on the order of 100 Hz. This procedure allows to determine the resonance frequency of the cavity, its temperature as well as the stored em energy as a function of the supplied input power. The results are shown in Fig. 5.10 for various input powers between 10 dBm and 33 dBm.

The measurements for a given input power are performed after the average pickup voltage at resonance stabilized and the remaining temperature change of the cavity was on the order of mK per minute. This corresponds in good approximation to steady-state operation of the cavity. The temperature uncertainty of 50 mK accounts for the finite temperature gradient as the measurement was taken. The uncertainty of the pickup voltage reflects the fluctuations of the measured signal, which are conservatively estimated to 5 %. Similarly, the frequency uncertainty of 30 Hz represents an upper limit for the observed tolerance of the applied signal, for which the pickup voltage remained unchanged.

As can be seen in the left panel of Fig. 5.10, both the stored em energy (a) as well as the cavity temperature (b) increase with input power. In steady state, the temperature of the cavity should increase linearly with its dissipated power, which is identical to the fraction of the supplied rf power that is coupled into the cavity. Neglecting the losses of the external electronic circuit, one might therefore expect a linear increase of temperature with input power. This is contradicted by the measurement, which shows that the relative increase of cavity temperature gets smaller at larger input powers.

A similar behaviour is shown by the measured pickup voltage (Fig. 5.10(a)). Ideally, it should increase with the square-root of the intra-cavity power. Thus, neglecting external losses, one might expect a similar dependence on the supplied rf power. However, the measurement deviates substantially from the fitted model, especially at high input powers.

Both observations can be explained by the same effect. Due to the strong temperature dependence of the quality factor, the coupling efficiency of the inductive as well as the capacitive coupler changes with the cavity temperature and thus with the supplied input power. The heat-up of the rf couplers can cause an additional change of the coupling constant, as discussed for the previous measurement, and thereby enhance this effect. Thus, the fraction of the supplied rf power, which is coupled into the cavity, varies with temperature. The same holds true for the outcoupled fraction of the intra-cavity power, which depends on the coupling efficiency of the capacitive pickup.

In order to investigate the latter, the pickup voltage is plotted as a function of the cavity temperature (Fig. 5.10(c)). Due to the linear increase of the temperature with the dissipated power in steady state, the pickup voltage should increase proportional to $\sqrt{T}$. The measurement shows the expected behaviour and the data is well described by the fitted model within the measurement uncertainty. However, the small deviations at high temperatures might hint towards a heat-up of the capacitive coupler, which is accompanied by a change in coupling efficiency and therefore modifies the outcoupled rf power.

Finally, the temperature dependence of the resonance frequency is shown in Fig. 5.10(d). The total frequency shift of approximately 600 Hz between 4.3 K and 6.6 K is consistent with the warmup measurement presented in Sec. 5.2.2. This temperature-dependent shift of the resonance frequency has to be considered for efficient coupling to the cavity at high rf powers. Since it took up to 15 min for the cavity to reach steady state after increasing the input power, it is cumbersome to manually adjust the frequency

of the rf drive after each adjustment to the input power. Therefore, the frequency of the rf supply will be locked to the resonance of the cavity using Pound locking [Pou46]. This will allow for highly stable operation, which is required for the confinement of ions.

The overall behaviour of the superconducting cavity at high em fields is well understood. However, the significant increase of cavity temperature at high intra-cavity powers is unexpected. This can potentially limit the performance of the cavity as an rf ion trap, which will be discussed in the next section.

5.2.5 Evaluation of the cavity performance

The characterization results of the superconducting cavity presented within this section have to be compared to the performance specification as given in Chapter 4. The two most important characteristics of the cavity are the resonance frequency of the electric quadrupole resonant mode and its quality factor.

The resonance frequency around 34.52 MHz meets the specified requirements and is additionally in reasonable agreement with the predicted eigenfrequency from FEM simulations. The unloaded quality factor of the cavity was determined by transmission and reflection measurements at low rf input powers. The obtained value around 2.3×10^5 is within the specified range of $10^5 < Q_0 < 10^7$. However, it is much smaller than typical values reported for state-of-the art superconducting cavities used at accelerator facilities, e.g. [Res+17].

Finally, the cavity was operated at high em field amplitudes to investigate its power dissipation. The observed performance is sufficient to operate the cavity as an rf ion trap. However, it was found that the cavity heats up significantly when supplied with high rf input powers above 0.5 W. This can eventually limit the achievable em field amplitudes inside the cavity and thereby the secular frequencies of trapped ions.

Possible limitations of the cavity performance were discussed in Sec. 4.4.2. The two most probable loss mechanisms are hydrogen contamination and flux trapping. Both mechanism increase the surface resistance of the cavity and can limit its performance even at low rf amplitudes. In order to investigate their impact on the presented cavity, additional measurements are required. The effect of trapped magnetic flux inside the cavity wall can be avoided by shielding the cavity from external magnetic fields during cooldown through the critical temperatures of niobium and lead, e.g. using µ-metal. In addition, hydrogen contamination of the cavity material can pose a serious limitation to the achievable quality factors, due to the slow cooldown and the high original hydrogen concentration of the cavity material (see Sec. 4.4.2). However, the effect could be avoided by vacuum annealing of the cavity at temperatures above 900 °C.

Furthermore, the quality factor can in principle be limited by multipacting (MP). The experimentally observable signature of this mechanism is a limitation of the achievable em field amplitudes inside the cavity, which cannot be overcome by increasing the input power. Additionally, the onset of MP is marked by a sudden drop of the measured quality factor at the threshold of the em field amplitude. Both effects are not visible in the presented characterization measurements, which excludes MP as a possible limitation of the cavity performance.

Other loss mechanism which are typically considered for superconducting cavities at accelerator facilities are expected to be negligible for the employed rf amplitudes. The two most common one are thermal breakdown and field emission. The latter is characterized by an exponential drop of the quality factor with increasing em field amplitudes inside the cavity [Kno97]. Although this effect was not studied in detail, the measured pickup voltage as a function of temperature is well-described by a square-root dependency and does not show an exponential behaviour (see Sec. 5.2.4). Thus, field emission should not be relevant for the presented results.

Thermal breakdown can be identified by a quench of the superconducting phase at high rf amplitudes due to microscopic regions of increased rf loss [Pad01]. Although this was not directly observed during operation of the cavity, it is possible that the cavity exhibits regions of increased surface resistance. Potential candidates are local defects or inclusions of the cavity material and microscopic particles on the cavity surface [Kno97]. The increased power dissipation of the corresponding regions can cause a heat-up of the surrounding cavity material, which again increases the cavity losses. Therefore, this could easily dominate the total rf power dissipation and therefore explain the heat-up of the cavity.

A similar effect could be caused by regions of the cavity, which are not well thermalized to 4 K. These could continuously heat up during operation, which increases their surface resistance. This could apply to the dc electrodes and their supply rods, as well as for the rf couplers. In principle, the electrodes are well-thermalized to the quadrupole electrodes by sapphire rods. However, the supply rods are only thermalized via the dc electrodes. Although the rf currents inside the rods are small (see Sec. 4.4.1), their potentially increased power dissipation could heat up the dc electrodes and increase the total rf loss of the cavity.

In addition, the rf couplers heat up if the cavity is supplied with high rf powers (see Sec. 5.2.4). This increases the resistive losses of the couplers and can potentially heat the surrounding cavity parts. The corresponding measurements were performed with rf couplers made of copper, which feature increased eddy current losses compared to the superconducting couplers made of niobium. However, if these are heated above their critical temperature, they feature similar losses. Both effects can be excluded by adding a proper thermalization of rf couplers and dc rods to the cavity setup.

In summary, the superconducting cavity was successfully commissioned and features an electric quadrupole mode satisfying the design requirements. This allows for the confinement of ions inside the novel resonator ion trap combination.

5.3 Ion confinement inside the superconducting cavity

The superconducting cavity is designed for efficient retrapping and capturing of injected HCIs. In order to test the injection performance of the cavity, it is operated as a quadrupole mass filter and the transmission efficiency of HCIs is measured as a function of the em field amplitudes inside the cavity (see Sec. 5.3.1). This allows to directly probe

its quadrupole eigenmode. The experiments are performed with highly charged argon ions, since $^{40}Ar^{13+}$ will serve as the first test case for laser spectroscopy at CryPTEx-II.

Additionally, experiments with trapped $^{9}Be^{+}$ ions were performed (see Sec. 5.3.2). These ions will be used in the future to sympathetically cool a broad range of HCIs, as described in Sec. 2.2.3. The confinement and laser cooling of $^{9}Be^{+}$ represent an important pre-requisite for the intended experiments at CryPTEx-II.

5.3.1 Operation as a quadrupole mass filter

The transmission measurements with HCIs are performed using the experimental setup described in Sec. 3.5. HCIs are produced inside the electron beam ion trap (EBIT), which is operated with an electron beam current of 9.5 mA at 1.15 keV beam energy. This is sufficient to produce argon ions in charge states up to $q = 16\,e$. After a breading time of about 100 ms inside the trap, the ions are ejected into the beamline with a kinetic energy of about 695 eV $\times\, q$. During transfer, the ion bunch separates according to the charge-to-mass ratio q/m of its constituents and is detected behind the cavity using a microchannel plate (MCP). This allows to identify individual charge states using the recorded time-of-flight (TOF) spectra. In order to detect q/m species with a low ion yield, the MCP signal is amplified using a fast pre-amplifier[5] and subsequently acquired with an oscilloscope. As the MCP is positioned around 30 cm behind the cavity, the measured transmission is possibly affected by a potential defocusing of the ion bunch leaving the quadrupole. This is not considered here.

For the presented experiments, the low-energy beamline is optimized for an efficient transfer of HCIs to the MCP behind the cavity. The beamline is operated with purely static electric potentials, i.e. the pulsed drift tubes were not used for deceleration or refocusing. The cavity is driven inductively with a constant frequency of 34.525625 MHz at various input rf powers between −10 dBm and 18 dBm. Due to the heat up at high input powers (see Sec. 5.2.4), measurements for a given rf input were performed only after the cavity temperature reached steady state.

Typical TOF spectra are shown in Fig. 5.11. The separated peaks correspond to Ar^{10+} to Ar^{16+} ions. The measured ion yield for a specific charge state at the MCP depends on the experimental parameters of the EBIT, which determine the charge-state distribution of the extracted ion bunch. Additionally, the beamline operated with fixed electrode voltages features a strong q/m dependence of the transmission efficiency. Furthermore, the MCP signal depends both on the charge of the detected ions as well as their kinetic energy, which itself depends on the charge of the ion. Therefore, the signal amplitudes of different q/m species within the TOF spectrum cannot be directly compared.

The ion yield for individual charge states depends strongly on the amplitude of the em fields inside the cavity, as can be seen in Fig. 5.11. For larger amplitudes, the transiting ions experience a stronger radial refocusing by the quadrupole, which increases the ion

[5] model VT120B from Ortec

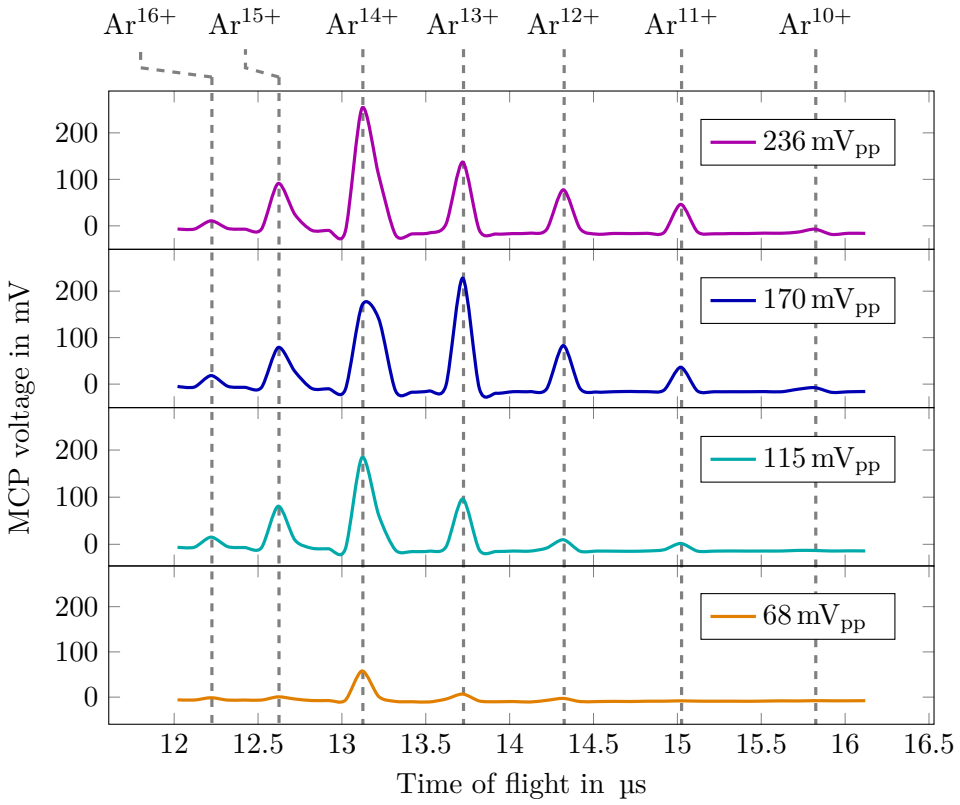

Figure 5.11: TOF spectra of highly charged argon ions measured behind the cavity using an MCP. The radial confinement strength inside the quadrupole is varied and quantified using the pickup voltage at the capacitive coupler, which is indicated in the plots. Each spectrum represents the average of 192 extraction cycles of the EBIT. The dashed lines mark the different argon charge states.

yield at the detector. Here, the fastest ions spend around 1 µs inside the quadrupole potential of the cavity, which corresponds to approximately 35 cycles of the rf field.

In order to investigate the dependence of the transmission efficiency on the intra-cavity rf power, the integral of each q/m peak is plotted as a function of the pickup voltage in Fig. 5.12. Different regions along the TOF axis are assigned to the corresponding charge states and the MCP signal within each region is integrated. Due to the large separation of neighbouring peaks, these regions do not overlap and the MCP counts can be unambiguously assigned to a specific q/m species. As the recorded TOF spectra show negative voltages for high ion yield (see Fig. 5.11), the integration is performed after baseline subtraction. This should also reduce the systematic offset of the determined integrals, which is introduced due to the random choice of the TOF boundaries for integration.

The transmission efficiency of each species increases with intra-cavity power until it saturates for most charge states above 160 $\mathrm{mV_{pp}}$ pickup voltage. Above this voltage,

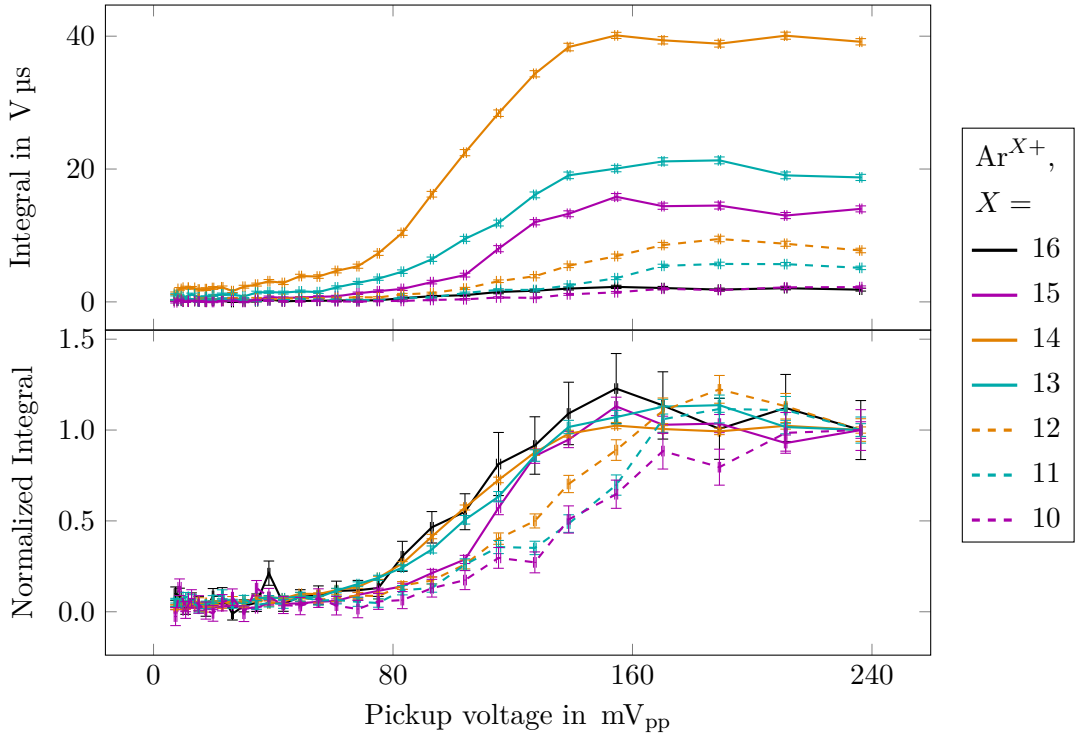

Figure 5.12: Transmission efficiency for different argon charge states as a function of the radial confinement strength inside the cavity, characterized by the pickup voltage at the capacitive coupler. **Top:** The area below the individual TOF peaks after baseline subtraction is plotted as a function of the measured pickup voltage at the capacitive coupler. Each data point represents the mean of 192 extraction measurements and the errorbars are the statistical uncertainty of the mean. **Bottom:** The same data is shown normalized to the value at maximum pickup voltage.

the measurement shows approximately constant ion yield for all species. Especially, no substantial reduction of transmission efficiency is observed at high rf amplitudes. This could have been related to unstable ion trajectories outside the stability region of the rf quadrupole and therefore used to calibrate the quadrupole potentials, similar to the measurements performed in [Sch+12]. However, this requires higher rf voltages and cannot be performed using the presented measurement.

The lower panel in Fig. 5.12 shows the relative ion yield of each charge state normalized to the TOF integral at the highest rf amplitude. It can be seen that the rf voltage, at which the transmission efficiency increases, differs significantly between the ions species. Here, the higher charge states show a significant increase in ion yield already at smaller voltages, while the lower charge states require stronger rf fields to be affected. This is expected due to the radial stability parameter of the quadrupole potential, which scales

as $q_r \propto V_{\mathrm{rf}} \times q$. Therefore, the observed gain in ion yield as a function of the rf voltage can be directly related to the influence of the electric quadrupole mode of the cavity.

The presented measurement represents the first successful operation of the cavity as a quadrupole mass filter. Furthermore, the ion injection, crucial for retrapping and future HCI experiments inside the Paul trap, was successfully implemented.

5.3.2 Trapped ion experiments

The first trapped-ion experiments at CryPTEx-II were performed using $^9\mathrm{Be}^+$ ions. The implementation of in-trap ion production, subsequent trapping and direct laser cooling represent the successful commissioning of the superconducting cavity operated as an rf ion trap.

The ions are produced inside the trap region, where the photoionization laser and the beryllium atomic beam are superimposed (see Fig. 3.15). Directly after production, the ions feature kinetic energies on the order of 140 meV for typical oven temperatures around 1250 K. Thus, they can be confined inside the potentials of the ion trap, which is continuously operational throughout the experimental sequence. The cavity is typically driven with rf input powers between 18 dBm and 22 dBm, while axial confinement is provided by electrostatic potentials around 1 V supplied to the dc electrodes.

Directly after production, the kinetic energy of the ions is reduced by Doppler cooling using the scheme described in Sec. 3.3.3. To this end, the trap region is continuously illuminated with cooling and repumper laser, while the photoionization laser is only unblocked for the loading of ions. During Doppler cooling, the dissipative scattering of photons at 313 nm allows to image the ions onto an electron multiplying charge-coupled device (EMCCD) camera using the cryogenic imaging system. An overview of some of the first ion ensembles confined inside the cavity is shown in Fig. 5.13.

The trapped ions arrange according to the equipotential surfaces of the pseudopotential. For the given hierarchy of secular frequencies, $\omega_z < \omega_x \approx \omega_y$, the ions typically form a spheroid (e.g. Fig. 5.13(h)). Its aspect ratio depends on the ratio ω_r/ω_z [HD02]. In the special case of $\omega_r/\omega_z > 0.73N^{0.86}$, where N denotes the number of trapped ions, the ions arrange in a one-dimensional configuration along the trap axis [Ste97] (see Fig. 5.13(a)-(d)). Here, the ion separation depends on the axial confinement strength. At the crossover from one to higher dimensions, when the radial confinement is not strong enough to force the ions onto the trap axis, they can arrange in a so-called zig-zag configuration (see Fig. 5.13(e)). In this case, the local potential minimum at the position of the ions along the trap axis becomes a saddle point due the small inter-ion distance [Ste97] and the ions are displaced from the trap axis.

At low kinetic energies, the ion ensemble develops spatially ordered structures and forms a so-called Coulomb crystal. The condition for Coulomb crystallization is typically given in terms of the plasma coupling parameter Γ_c, which relates the inter-particle potential energy to their kinetic energy [Dre15]:

$$\Gamma_\mathrm{c} \sim \frac{\text{Coulomb energy}}{\text{Kinetic energy}} \quad . \tag{5.9}$$

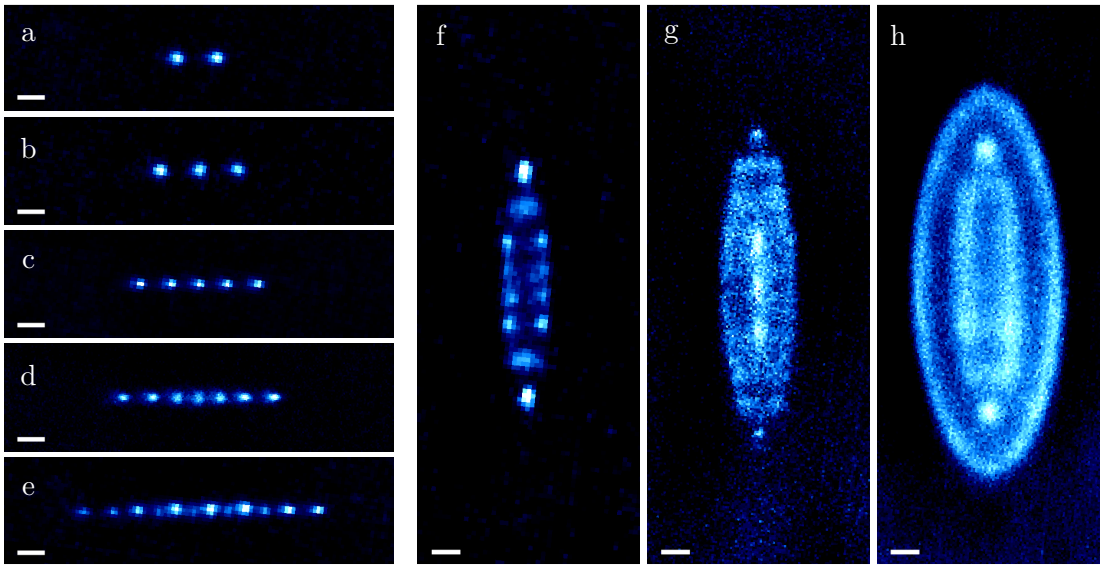

Figure 5.13: Images of various ion ensembles confined inside the superconducting cavity. These are taken with an EMCCD camera for typical exposure times around 10 s. The white bar indicates a length of 200 µm at the camera.

It was observed experimentally that Coulomb crystallization is achieved for $\Gamma_c \geq 175$ [Dre15]. The required ion temperature is given by $T < T_{cc} \sim 10\,\mathrm{mK}$ [Dre15], which is far above the Doppler temperature of $^9Be^+$.

Although no dedicated temperature measurement of the trapped ions was performed, the EMCCD images of three-dimensional ion ensembles allow to draw some conclusions. As can be seen in Fig. 5.13(f)-(h), the ions form distinctive shell structures. However, the shells themselves are not completely crystallized as not all ions can be resolved individually, which indicates ion temperatures around or slightly above T_{cc}. This could be related to heating by residual excess micromotion, which was not yet fully compensated for the presented measurements. Additionally, the experiments were performed without a bias magnetic field at the trap center. Thus, the quantization axis for laser cooling is given by the ambient magnetic field, which reduces the cooling efficiency. For the presented experiments, cooling and repumper laser are operated with typical powers on the order of 1 mW and 0.5 mW, respectively, which saturates the cooling transition. However, strong saturation causes an increase of the minimum achievable ion temperature using Doppler cooling (see Eq. (2.21)).

The loading of $^9Be^+$ ions was performed with typical photoionization laser powers of 1 mW and oven temperatures around 1250 K. Without systematic optimization of the loading process, loading rates of several ions per second are achieved. This allows to load small ion crystals up to 10 ions within a few seconds. For the loading of single ions, the photoionization laser is only unblocked for a small fraction of a second. Alternatively, the last frequency-doubling cavity of the laser can be operated in scan mode, which reduces

the average power substantially. Loading of single ions was achieved reliably for laser powers down to 80 µW. In case the loading rate is not sufficient to load large crystals of up to 1000 ions, it can be improved by increasing the overlap of photoionization laser and the atomic beryllium beam. Additionally, the oven temperature can be temporarily increased to enhance the atom flux.

The reproducibility of the loading process is sufficient for the planned experiments at CryPTEx-II. Using the pointing stabilization scheme discussed in Sec. 3.4, the overlap of photoionization laser and beryllium atomic beam was maintained after many days without readjusting the laser pointing inside the trap. Even after maintenance work at the laser setup in the ground floor laboratory, overlap was reestablished within minutes.

Stability of the trapping conditions

In order to investigate the stability of the ion confinement and the observed heating rates of trapped ions, a single ion was confined inside the trap without laser cooling. The observed storage times of 15.5 h and 16.25 h without ion loss are promising, especially since no longer storage times were probed. A very conservative upper limit of the corresponding motional heating rates $\dot{n}$ can be obtained by comparing the employed axial potential depth, $\Delta U < 0.5\,\mathrm{eV}$ (see Fig. 4.12), to the axial trap frequency ω_z. Assuming a purely harmonic confinement with $\omega_z/2\pi = 200\,\mathrm{kHz}$ and neglecting micromotion-induced heating at higher motional amplitudes, an upper limit is estimated to $\dot{n} < \Delta U/\hbar\omega_z < 10^4\,\mathrm{s}^{-1}$. This is far above the values reported for other cryogenic Paul trap experiments, e.g. $\dot{n} < 3\,\mathrm{s}^{-1}$ [Leo+19]. For the presented superconducting ion trap, even lower motional heating rates are expected, as discussed in Sec. 4.1. Such small heating rates are typically measured using sideband thermometry [Tur+00], where the excitation probability of red and blue sideband transitions is evaluated. This was not implemented here, since the Raman laser system required for sideband cooling was still being set up at the end of this thesis.

The lifetimes of trapped, laser-cooled $^9\mathrm{Be}^+$ is limited by chemical reactions with residual H_2 molecules resulting in the formation of BeH^+. The underlying reaction, $\mathrm{Be}^+ + \mathrm{H}_2 \rightarrow \mathrm{BeH}^+ + \mathrm{H}$, is endothermic for beryllium ions in the ground state [RG83]. Therefore, only ions in an excited state, e.g. the $^2\mathrm{P}_{3/2}$ state used for Doppler cooling, can react to form BeH^+ ions. The production rate of BeH^+ thus depends on the population probability of the excited state and thereby on the saturation parameter $s = I/I_\mathrm{s}$ of the employed Doppler cooling transition. This can be used to estimate the residual gas pressure inside the trap region by measuring the lifetime of laser-cooled $^9\mathrm{Be}^+$ ions. In [Saw+15], a pressure of 5×10^{-11} mbar was estimated from a $^9\mathrm{Be}^+$ lifetime of 2.2 h using large ion clouds continuously excited with $s = 0.3$.

At CryPTEx-II, no hydride formation was directly observed during experiments with laser-cooled $^9\mathrm{Be}^+$ ions. However, this can be related to the short experimental cycles ($\sim$ 1h) during trap optimization. In order to further investigate this effect, a dedicated measurement of a single $^9\mathrm{Be}^+$ ion confined inside the trap was performed over 12.5 h. The employed laser power of 2.5(1) mW with an $1/\mathrm{e}^2$ beam diameter of 340 µm at the position of the ion indicates strong saturation given the theoretical value for the satu-

ration intensity of $I_s = 765\,\mathrm{W m^{-2}}$ (see Sec. 2.2.1). However, regularly taken pictures with the EMCCD camera indicate that the beam pointing of the cooling laser drifts over the course of the measurement. In order to account for the resulting variation of the saturation parameter, a conservative lower limit is estimated by $s > 1$.

Although the measurement performed here with one single ion is not statistically meaningful, compared to the reaction rates reported in [Saw+15] the measurement hints towards pressures below 5×10^{-11} mbar. In the future, experiments with trapped HCIs will allow to put a more restrictive limit on the residual gas pressure inside the trap via the observed rates of charge-exchange reactions with neutral background gas (see e.g. [Sch17]).

Estimation of the ion temperature

The temperature of the trapped ions can be estimated using the method of spatial thermometry [Neu+80; Bla+86; Knü+12; Raj+16]. As described in Sec. 2.2.1, a single ion confined inside the pseudopotential of the Paul trap can be described by three uncoupled harmonic oscillators. For sufficiently strong radial confinement, the ions arrange in a one-dimensional configuration along the trap axis and the motion in the radial directions can be neglected. The following discussion is therefore reduced to the axial direction.

Assuming that the stochastic motion of the laser cooled ion caused by the random nature of photon absorption and emission processes is ergodic, one can assign a temperature to a single ion. The time-averaged thermal motion of the ion around its equilibrium position is described by a Gaussian function. For the given experimental parameters, i.e. small secular frequencies compared to the linewidth of the cooling transition ($\omega_u \ll \Gamma$), the standard deviation of the spatial distribution along the trap axis z is given by [Knü+12]

$$\Delta z_{\mathrm{th}} \approx \sqrt{\frac{k_{\mathrm{B}} T}{m \omega_z^2}} \quad , \tag{5.10}$$

where k_{B} denotes the Boltzmann constant. The thermal ion motion can be analyzed using EMCCD images. In order to determine Δz_{th} from a Gaussian fit to the measured intensity distribution, the secular frequency of the ion as well as the magnification of the imaging system needs to be known.

Since no measurement of the secular frequencies was performed, the axial frequency ω_z can only be determined using the theoretical expression from Eq. (2.9):

$$\omega_z = \sqrt{\frac{2q\kappa U_{\mathrm{dc}}^z}{m z_0^2}} \quad . \tag{5.11}$$

However, the exact voltages U_{dc}^z present at the dc electrodes are not known. These can differ significantly from the supplied voltages, e.g. due to contact potentials. For the following calculation, this systematic effect will be neglected and we assume that the

supplied dc voltages are identical to the real voltages at the trap electrodes. Thus, the determined values are only intended to give a rough estimate.

For the presented measurements, the dc electrodes are supplied with a mean voltage of 0.94(0.17) V, where the uncertainty denotes the largest deviation between any two applied potentials. Using the geometric factor κ determined with FEM simulations in Sec. 4.5.1, Eq. (5.11) yields an axial frequency of $\omega_z/2\pi = 203(18)$ kHz.

The magnification of the imaging system can be determined by comparing the measured axial distance of two ions confined along the trap axis with the theoretical expectation. This will be performed in the following using the two-ion crystal presented in Fig. 5.13(a). The positions of the two ions are determined by fitting two-dimensional Gaussian functions to the intensity distribution. This yields an ion distance at the camera of $d_{\mathrm{CCD}} = [\Delta x^2 + \Delta y^2]^{1/2} = 296(20)$ µm.

The theoretical equilibrium positions of the ions can be calculated by considering the potential energy of the system [Jam98]. Neglecting the radial motion, the total potential energy of the two-ion string is given by

$$V = \sum_{i=1}^{2} \frac{1}{2} m\omega_z^2 z_i^2 + \frac{q^2}{4\pi\epsilon_0 |z_1 - z_2|} - \sum_{i=1}^{2} F_{z,i}^{\mathrm{cl}} z_i \quad , \tag{5.12}$$

where $z_i(t)$ denotes the position of the i-th ion and ϵ_0 is the vacuum permittivity. The first two terms describe the potential energy of the ions inside the axial pseudopotential of the trap and their repulsive Coulomb interaction. Additionally, the light force exerted onto the ions by the cooling laser is represented by $F_{z,i}^{\mathrm{cl}}$, which denotes the projection of the light force onto the trap axis.

For the following calculation, we assume that the ions are sufficiently cold, such that the position of the i-th ion can be expressed as $z_i(t) \approx z_{i,0} + l_i(t)$, where $z_{0,i}$ is the equilibrium position and $l_i(t)$ is a small displacement. This is realized experimentally by the application of laser cooling. The equilibrium positions can be determined by solving the equation [Jam98]

$$\left.\frac{\partial V}{\partial z_i}\right|_{z_i = z_{i,0}} = 0 \quad . \tag{5.13}$$

In case of two ions, this yields two conditions, one for $z_{1,0}$ and one for $z_{2,0}$. Taking the difference of the two equations results in

$$m\omega_z^2 (z_{1,0} - z_{2,0}) - \frac{q^2}{2\pi\epsilon_0 (z_{1,0} - z_{2,0})^2} + \Delta F_z^{\mathrm{cl}} = 0 \quad , \tag{5.14}$$

where $\Delta F_z^{\mathrm{cl}} = F_{z,2}^{\mathrm{cl}} - F_{z,1}^{\mathrm{cl}}$ accounts for the difference in light force onto both ions. An upper limit for ΔF_z^{cl} can be estimated assuming resonant excitation of the ions. The measurement was performed with a cooling laser power of 2.5 mW and a $1/e^2$ beam diameter of 310 µm at the position of the ions. Using Eq. (2.19), this yields a maximum force of $F_0 \approx 1.2 \times 10^{-19}$ N. As the laser force onto the ion is proportional to the number

of scattered photons, the differential light force can be estimated by comparing the area of the fitted Gaussian distributions A_i of the two ions in Fig. 5.13(a):

$$\Delta F_z^{\mathrm{cl}} = F_0 \left(1 - \frac{A_1}{A_2}\right) \quad . \tag{5.15}$$

The fit yields an asymmetry of $A_1/A_2 = 0.99(22)$, which affects the determined inter-ion distance only at the level of 0.01 µm and is therefore negligible. However, the large fit uncertainty is reflected in the total uncertainty of the ion separation. Solving Eq. (5.14) yields a theoretical inter-ion distance of $d_{\mathrm{theo}} = 26.7(2.2)\,\mu\mathrm{m}$. In comparison with the distance of the two ions determined from the EMCCD image, d_{CCD}, this yields the magnification of the imaging system:

$$M = \frac{d_{\mathrm{CCD}}}{d_{\mathrm{theo}}} = 11.1(1.2) \quad . \tag{5.16}$$

As discussed [War19], the magnification of the imaging system can be adjusted between 7.8 and 20 by varying the vertical position of the 40 K asphere (see Sec. 3.2.3). For the first trapped ion experiments presented here, the positioning was geared towards a medium magnification in order to be less sensitive for a potential misalignment of the imaging system with respect to the trap center. Therefore, the determined magnification agrees reasonably well with the expectation, especially as the vertical position of the asphere cannot be measured directly.

This result can be used to determine the temperature of a single ion confined inside the cavity employing the identical experimental parameters as for the two-ion crystal. The EMCCD image is shown in Fig. 5.14 together with the projection of the spatial intensity distribution onto both camera axes. In order to account for the relative angle of the camera with respect to the trap axis, a two-dimensional Gaussian function is fitted to the data. This yields a standard deviation of $\sigma_{x'} = 27.7(6)\,\mu\mathrm{m}$ and $\sigma_{y'} = 41.7(9)\,\mu\mathrm{m}$ at the camera, where x' and y' denote the axes of the rotated coordinate system. The values agree reasonably well with the one-dimensional fits shown in Fig. 5.14.

For the determination of the axial ion temperature, only the spatial width along the trap axis, $\sigma_{y'}$, is considered to describe the thermal motion of the ion by $\Delta z_{\mathrm{th}} = \sigma_{y'}/M$. Besides the thermal motion, the widths of the spatial distribution $\sigma_{x',y'}$ at the camera contain additional contributions from the point-spread function of the imaging system as well as the axial micromotion of the ion [Knü+12]. Both are not precisely known and thus neglected in the presented calculation, which accordingly overestimates the ion temperature. Using Eq. (5.10), the ion temperature can be estimated to

$$T \approx \frac{\Delta z_{\mathrm{th}}^2 m \omega_z^2}{k_{\mathrm{B}}} = 25(5)\,\mathrm{mK} \quad . \tag{5.17}$$

Given that this estimate is based on various assumptions, it agrees well with the previous discussion of Coulomb crystallization of three-dimensional ion ensembles, which indicated ion temperatures around or slightly above $T_{\mathrm{cc}} \sim 10\,\mathrm{mK}$.

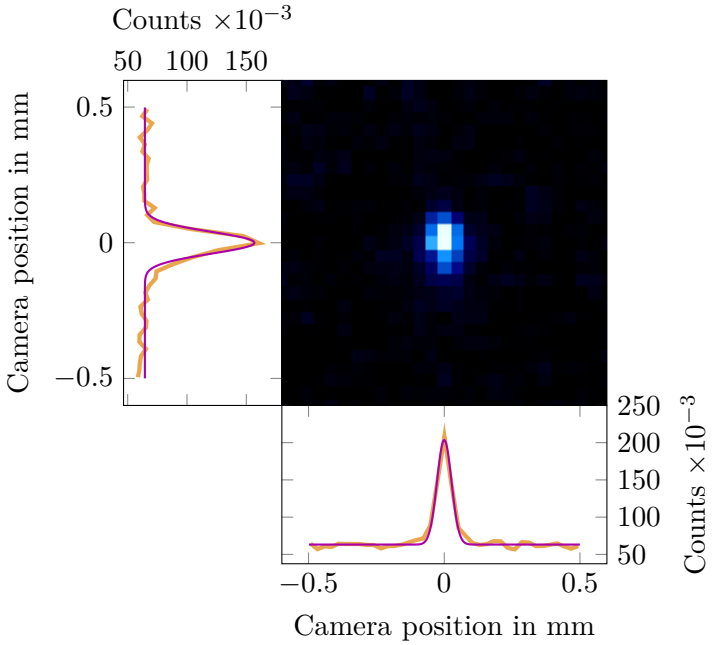

Figure 5.14: EMCCD image of a single $^9Be^+$ ion confined inside the cavity, taken with 20 s exposure time. The intensity distribution is projected onto both camera axes, $\tilde{x}$ (bottom) and $\tilde{y}$ (left). Fitting a Gaussian function (magenta) to the projected data (orange) yields standard deviations of $\sigma_{\tilde{x}} = 26.6(7)\,\mu m$ and $\sigma_{\tilde{y}} = 40(2)\,\mu m$.

The determined ion temperature is far above the Doppler limit of $T_D \sim 0.3\,mK$ (see Eq. (2.21)), which can be reached for small laser intensities ($s \ll 1$) and a detuning of $\delta = \Gamma/2$ from the cooling transition. As no frequency scan of the cooling transition was performed, the employed laser detuning could differ substantially from the optimum value, which would increase the lowest reachable temperature. In addition, the employed laser intensity strongly saturates the cooling transition ($s \approx 87$) and thereby increases T_D. Furthermore, no bias magnetic field was applied at the trap, such that the quantization axis for laser cooling was defined by the ambient magnetic field, which can reduce the cooling efficiency.

The presented result corresponds only to a conservative upper limit for the ion temperature. Especially the point-spread function of the imaging system [War19] is expected to contribute substantially to the measured width of the spatial intensity distribution. Therefore, the result is very promising and concludes the commissioning of CryPTEx-II.

6

Summary and Outlook

Within this thesis, the technical development and commissioning experiments of the new cryogenic Paul trap experiment (CryPTEx)-II were presented. The distinct feature of the new apparatus is the superconducting ion trap, which represents a unique combination of a radio-frequency (rf) cavity and a Paul trap. The successful confinement of ions constitutes the proof-of-principle operation of this novel ion trap. In addition, the performed experiments show the functional interaction of all main parts of the experimental apparatus, including the source and transfer beamline for highly charged ions (HCIs), the beryllium oven, as well as the ultraviolet (UV) laser systems for photoionization of beryllium and laser cooling of $^{9}Be^{+}$. This forms the basis for the next steps towards high-precision spectroscopy of cold HCIs at CryPTEx-II.

The cryogenic setup

The cryogenic setup of CryPTEx-II comprises the low-vibration cryogenic supply and the cryogenic trap chamber. The former was developed in collaboration with the Physikalisch-Technische Bundesanstalt (PTB), where the twin setup is located [Mic+19].

The presented apparatus was successfully set up and commissioned during this thesis. The trap environment reaches steady state temperatures around 69.5 K at the first stage and 4.15 K at the second stage. This is in agreement with the defined specifications and allows operating the superconducting ion trap far below its critical temperature. In comparison to the achieved trap temperature at the PTB setup of 4.6 K, this should correspond to suitably low residual gas pressures which ensure long HCI storage times

on the order of several 10 min. However, this remains to be verified experimentally, once the first HCIs are trapped at CryPTEx-II.

The flexible copper links mounted to the first temperature stage represent the thermal bottleneck of the cryogenic setup and will be upgraded to larger cross sections in the future. The enhanced thermal conductance will accelerate the cooldown of the apparatus from room temperature, which takes about one week for the current setup. In addition, this will lower the steady-state temperatures of the cryogenic shields around the ion trap and thereby improve the vacuum conditions inside the trap.

One major design goal of the cryogenic supply is the decoupling of external vibrations from the ion trap, especially the residual vibrations relative to the optical table. This was not characterized during the presented commissioning experiments and remains to be measured in the future. However, the results from the twin setup at PTB should be comparable [Leo18; Mic+19], where vibration amplitudes below 20 nm in the horizontal plane were measured between 1 Hz and 100 Hz using an interferometric setup.

The superconducting cavity

The superconducting ion trap of CryPTEx-II represents a unique combination of an rf cavity and a linear Paul trap and thus features design elements from both fields. Axial ion confinement is accomplished by eight direct current (dc) electrodes, which allows for a precise minimization of contributions to excess micromotion resulting from mismatched rf and dc nodes. Radially, ions are confined in the standing fields of the electric quadrupole resonant mode of the cavity, using four pairs of coaxial electrodes. The cavity housing features several optical ports which provide access to the trap center for various lasers, atom and ion sources, as well as for the imaging of fluorescence photons from trapped ions. Different rf couplers are installed at the cavity for resonant excitation of the quadrupole mode, as well as to monitor the intra-cavity fields. Additionally, a microwave antenna allows for resonant coupling to the ground state hyperfine transition in $^9Be^+$. This can be used for the trap characterization in the future, which is discussed below.

The superconducting ion trap was developed using various simulations. These were employed to optimize and adjust the cavity geometry according to the design specification for ion confinement and future experiments with HCIs. Detailed finite element method (FEM) simulations of the resonant modes of the cavity were performed to guarantee a moderate resonance frequency of the electric quadrupole mode. For harmonic confinement of ions, the axial and radial trapping potentials were analyzed using electrostatic simulations. For typical Coulomb crystals with a radial extent of less than 200 µm, these show a relative contribution of anharmonic terms to the radial trapping potential below 7.5×10^{-7} up to the tenth order. Due to mechanical constraints for the dc electrodes, the axial potential exhibits larger relative anharmonic contributions on the level of 10^{-4} for crystal lengths of 200 µm, including anharmonicities up to the sixth order. This can be improved in the future by adding correction electrodes to the setup at the designated mounting positions. Furthermore, ion-flight simulations were used to

optimize the electrode geometries as well as electronic connections to the dc electrodes to ensure efficient retrapping of HCIs inside the cavity. Finally, the feasibility of the application of image current detection techniques to detect the motional state of an ion confined inside the rf cavity was investigated. This might be possible due to the reduced rf noise inside the high-Q cavity.

The performance characterization of the rf cavity was focused on the electric quadrupole mode. This features a resonance frequency around 34.52 MHz, which is in good agreement with the performed simulations and meets the design requirements. The quality factor and resonance frequency of the cavity were studied in detail during cooldown and warmup in order to investigate possible rf loss mechanisms. The strong influence of the lead sealings employed at the cavity lids on the intra-cavity losses could be understood using FEM simulations of the electric current density inside the cavity walls. These show a homogeneous distribution of the oscillating currents between the monolithic tank and the lids, which emphasizes the need to ensure a low temperature of all cavity parts to achieve a high quality factor.

In addition, detailed measurements of the transmission and reflection characteristics of the cavity were performed for strong and weak coupling. The determined quality factor around $Q_0 = 2.3 \times 10^5$ at 4.1 K is much larger compared the values around 10^3 reported for other Paul trap experiments, see e.g. [Siv+12; Joh+16; Bra+16; Leo+19].

Finally, the behaviour of the cavity at high electromagnetic (em) field amplitudes, which are required for the strong confinement of ions at high secular frequencies, was studied. A significant heat-up of the cavity, especially at rf input powers above 0.5 W, is observed which is accompanied by a substantial shift of its resonance frequency on the order of 600 Hz for a temperature increase of 2.3 K. Although this can potentially limit the achievable rf amplitudes, it did not affect the operation of the cavity as an rf ion trap.

The presented measurements represent the successful commissioning of the cavity and provide a detailed understanding of its rf properties. The future plans for the cavity include the following:

Limitation of the Q value: A better understanding of the current limitations of the quality factor as well as the corresponding heat up of the cavity at high rf amplitudes is needed. As discussed in Sec. 5.2.5, three effects have to be considered for the presented cavity. First, hydrogen contamination can seriously limit the cavity performance due to enhanced precipitation of dissolved hydrogen between 100 K and 150 K during cooldown. The effect can be avoided by applying vacuum annealing to the whole cavity at temperatures above 900 °C. Due to the much lower melting points of the contained indium foil and lead sealings, this requires the partial deconstruction of the cavity and is therefore not the first target for investigation.

The second potential limitation is given by trapped magnetic flux inside the cavity walls. This can be tested by warming up the cavity above the critical temperature of niobium and applying an external magnetic field before cooling down to 4 K, again. Measuring the quality factor as a function of the applied magnetic field,

similar to the measurements performed in [Ulm+09], allows identifying potential limitations due to external magnetic fields.
And finally, insufficient thermalization of distinct cavity parts can cause a local heat up of the cavity, which increases the total power consumption and thereby heats the complete setup. Thus, additional connections for thermalization will be mounted to the cavity parts which are expected to be more susceptible for rf heating, in particular the rf couplers and the dc supply rods.

Impedance matching: In order to efficiently drive the cavity, it needs to be impedance-matched to the external electronic circuit. This can be achieved using the scheme which was already successfully applied to the cavity prototype.

Stabilization of the rf potential: In order to stabilize the rf potential inside the cavity, variations of the coupling efficiency, e.g. due to temperature changes of the external electronic circuit as well as the cavity itself, need to be compensated. To this end, the external rf drive will be locked to the resonance of the quadrupole mode using Pound locking [Pou46; Lin+11]. In addition, residual amplitude fluctuations of the intra-cavity em fields could be detected and stabilized using the capacitive pickup.

Image current: Finally, a proof-of-principle experiment towards image current detection of trapped ions could be conducted. The calculations performed during this work indicate that the application of these techniques is indeed within reach even with the simulated anharmonicities of the trap. However, this requires the previous determination of the trap frequencies in order to design the cryogenic detection system.

Ion trap operation

The HCI measurements performed in the framework of this thesis represent the first direct test of the rf quadrupole potential of the cavity. By tuning the intra-cavity rf amplitude, the transmission efficiency of the injected highly charged argon ions was varied. In principle, this can be used to map out the radial stability diagram of the Paul trap using the method applied in [Sch+12]. However, the rf amplitudes applied here were not sufficiently high.

The successful implementation of ion injection into the rf ion trap represents an important pre-requisite for the retrapping and stopping of HCIs inside the Paul trap. As the mirror electrodes were not supplied with defined electric potentials during the commissioning run, retrapping was not attempted. However, the observed acceptance of the cavity is sufficient for the planned experiments, where only single HCIs need to be retrapped inside the Paul trap.

The presented experiments with trapped $^{9}Be^{+}$ ions consist of the successful implementation of ion production by photoionization, trapping and Doppler cooling. The production and loading of $^{9}Be^{+}$ ions was shown to work reliably and with the expected

ion yield. Although no dedicated measurement of the ion temperature was performed, the observed onset of Coulomb crystallization hints towards ion temperatures on the level 10 mK. This is in agreement with the estimate based on the measured spatial distribution of a single ion confined inside the cavity, yielding a conservative upper limit for the ion temperature of 25(5) mK. The underlying calculation neglects broadening due to excess micromotion and the point-spread function of the imaging system, since both are not precisely known. Especially the latter is expected to be accountable for a substantial fraction of the measured spatial distribution on the EMCCD camera. Accordingly, the actual ion temperature is expected to be significantly smaller than the estimated value.

The superconducting ion trap was designed to provide extremely low motional heating rates of trapped ions. In this respect, the observed ion storage times of more than 16 h without laser cooling are promising, especially since no in-depth compensation of excess micromotion had been performed. In order to estimate the expected heating rates, the presented ion trap setup can be compared to other Paul trap experiments.

Motional heating rates above superconducting electrode surfaces have been measured in [Wan+10] for microfabricated sapphire structures coated with Nb and NbN. The measurements at 6 K below the critical temperatures show heating rates of a single $^{88}Sr^+$ ion down to $\dot{n} = 2.1(3)\,s^{-1}$, comparable with the lowest values obtained for normal conducting traps of the same design tested with the same setup. They concluded that the remaining heating rate is predominantly caused by anomalous heating of the ion located 100 µm above the trap. Due to the strong inverse scaling with the effective electrode-ion distance d_{eff}, between d_{eff}^{-2} and d_{eff}^{-4} depending on the nature of the noise source [Sed+18a], this heating mechanism should be several orders of magnitude smaller for the presented cavity with an electrode-ion distance of 1.75 mm. However, as pointed out in [Bro+15], other sources of electric-field noise remain basically unchanged when the trap electrodes become superconducting.

This includes heating by technical noise from the rf trap drive. For the presented setup, this mechanism is strongly suppressed due to the large quality factor of the cavity around 2×10^5. For typical secular frequencies of $\omega/2\pi \sim 1$ MHz, rf noise at the motional sidebands of the quadrupole frequency is suppressed by more than 80 dB compared to the quadrupole excitation rendering this heating mechanism negligible. In addition, external em field noise is suppressed by the highly conductive cryogenic copper shields enclosing the trap region, as reported for the PTB setup [Leo+19], where a suppression of ac magnetic field noise of $30 - 40$ dB was measured between 60 Hz and 1 kHz. The shielding is further enhanced at CryPTEx-II by the superconducting cavity walls, according to the Meissner-Ochsenfeld effect [MO33]. Finally, technical noise from the dc supply as well as Johnson-Nyquist noise in the cabling is reduced at the trap electrodes due to the 4 K filter electronics. The employed filter design is based on [Leo+19], where heating rates below $\dot{n} = 2.5\,s^{-1}$ (limited by rf noise) were measured for a single $^9Be^+$ ion trapped at an electrode-ion distance of 0.9 mm. For identical noise of the dc electronics, a similar voltage noise is expected at the dc electrodes of the presented trap. This translates into a reduced electric-field noise at the position of the ions due to the larger electrode-ion distance.

In summary, the ion trap setup developed in the course of this thesis allows for efficient suppression of typical sources of electric-field noise and should therefore feature strongly reduced motional heating rates of trapped ions compared to other cryogenic Paul trap experiments. The actual heating rates at CryPTEx-II will be measured in the near future as part of a detailed trap characterization. This requires several modifications of the experimental setup complementing the cryogenic ion trap:

Stabilization of the laser pointing: During the commissioning run, laser intensity and pointing were stabilized using the stabilization system set up during this thesis and [Bog19]. While this allowed for reliable operation of the experiment over many days without major readjustment, small drifts on short time scales of $10 - 30\,\mathrm{min}$ were observed. This can be improved by delivering the lasers to the trap center using short UV fibres [Col+14; Mar+17] mounted onto the optical ports of the vacuum chamber [Leo18]. Thereby, the remaining variation of the laser pointing at the fibre coupler is reduced to a variation of the laser intensity at the position of the ion, which can be corrected in real time by monitoring the laser power, e.g. behind the trap center.

Raman lasers: Currently, a Raman laser system for resolved sideband cooling of $^9\mathrm{Be}^+$ ions using the scheme described in [Leo18] is being set up. This will allow for the preparation of ions in the motional ground state.

After the implementation of these upgrades to the setup, the trapping conditions inside the superconducting ion trap will be investigated. The main trap characteristics to be evaluated are:

Trap frequencies: For the application of coherent operations to the trapped ions, e.g. ground state cooling, an exact knowledge of the secular frequencies is required. These can be measured using parametric excitations of the ion motion, where the pseudopotential of the trap is modulated with twice the motional frequency [Win+98b; Sed+18b]. As this might not be applicable for the radial modes due to the high quality factor of the cavity, which averages the induced amplitude modulation, a similar measurement can be performed by modulating the intensity of the cooling laser. Since the radial secular frequencies depend on the rf voltage amplitude of the quadrupole electrodes, this measurement additionally allows for calibration of the rf potentials inside the cavity.

Excess micromotion: Excess micromotion represents one of the main contributions to the trap-induced motional shifts. Thus, it needs to be measured and minimized using the methods described in [Kel+15; Ber+98], e.g. measuring the strength of micromotion-induced sidebands of the cooling transition or using the photon-correlation method to measure the photon-scattering rate as a function of the rf phase.

Motional heating rates: The expected motional heating rates on the order of a few quanta per second for a single $^{9}Be^{+}$ ion can be measured using sideband thermometry [Tur+00], which requires the ion to be prepared in its motional ground state. Subsequently, the lasers are turned off and the ion can heat freely for a defined period after which the final ground state population is determined by evaluating the asymmetry of red and blue sidebands. This method can only be implemented after the setup of the Raman laser system.
An alternative method for the measurement of heating rates is Doppler recooling [Eps+07], where the ion temperature is determined after an extended period without the application of laser cooling. Despite the appealing simplicity of this method, the measurement of low heating rates requires extremely long delay times in combination with extended periods of averaging [Eps+07]. This demands a high stability of the experimental parameters.

Magnetic-field stability: Magnetic-field noise at the trap center can limit the achievable coherence times during the manipulation of trapped ions with lasers or microwave fields. The shielding of external magnetic fields can be characterized using a single $^{9}Be^{+}$ ion by driving the ground state hyperfine transition $^{2}S_{1/2}(F = 2) \rightarrow {}^{2}S_{1/2}(F = 2)$ between two magnetic field sensitive substates and measuring coherence times as well as frequency stability, see [Leo+19]. As reported for the PTB setup [Leo+19], the thick cryogenic copper shields enclosing the trap region are efficiently shielding high-frequency magnetic field noise. At CryPTEx-II, both the shielding efficiency as well as the noise suppression should be significantly enhanced by the superconducting cavity walls.

Towards spectroscopy of highly charged ions

The recent demonstration of QLS with HCIs [Mic+20] opens up the potential of HCIs for the numerous applications in fundamental physics or frequency metrology [Koz+18]. This requires the preparation of a two-ion crystal, consisting of one $^{9}Be^{+}$ ion and one HCI, in its motional ground state. To this end, the next step at CryPTEx-II is the sympathetic cooling of HCIs inside the Paul trap by implantation into a Doppler cooled $^{9}Be^{+}$ Coulomb crystal. This was already successfully implemented at predecessor experiment using highly charged argon ions and allowed reaching HCI temperatures around 10 mK [Sch+15b; Sch17]. Subsequently, resolved sideband cooling can be applied to further reduce ion temperatures and finally reach the motional ground state.

The first spectroscopy experiment will be performed using the $2p\,{}^{2}P_{1/2} \rightarrow {}^{2}P_{3/2}$ transition in $^{40}Ar^{13+}$, which represents the best-known optical transition in HCIs [Egl+19; Mic+20]. This will serve as a proof-of-principle experiment which allows to gain a better understanding of the ion trap setup and test possible systematic effects.

Finally, the CryPTEx-II experiment will be moved from its current location to a ground floor laser laboratory to be combined with the XUV frequency comb located at MPIK [Nau+17; Nau20]. The apparatus was setup and commissioned parallel to this

work within [Nau20] and [Oel21]. The long-term goal is to perform direct frequency comb spectroscopy of cold HCIs. Recently, high harmonics up to the 35^{th} order of the fundamental wave at 1035 nm were produced with sufficiently high intensities for spectroscopy. The versatility of both, the frequency comb as a broadband light source as well as the CryPTEx-II experiment, where the method for the production and cooling of HCIs can be easily adapted to different species, makes the combination of the two setups an excellent experiment to study a wide range of atomic systems.

A

Appendix: Lab Pictures

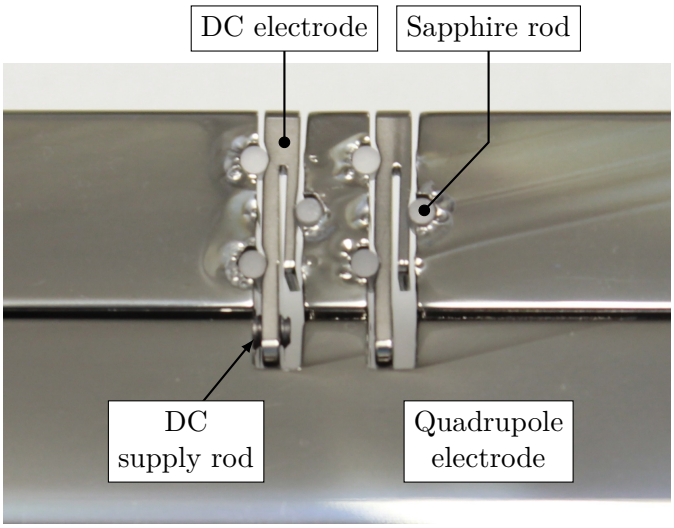

Figure A.1: Picture of a quadrupole electrode equipped with two direct current (dc) electrodes and one dc supply rod, taken before installation inside the monolithic cavity housing. The deformations of the quadrupole electrode around the sapphire rods are a result of the electropolishing process. They are far away from the trap center and hidden from the line of sight of the ions.

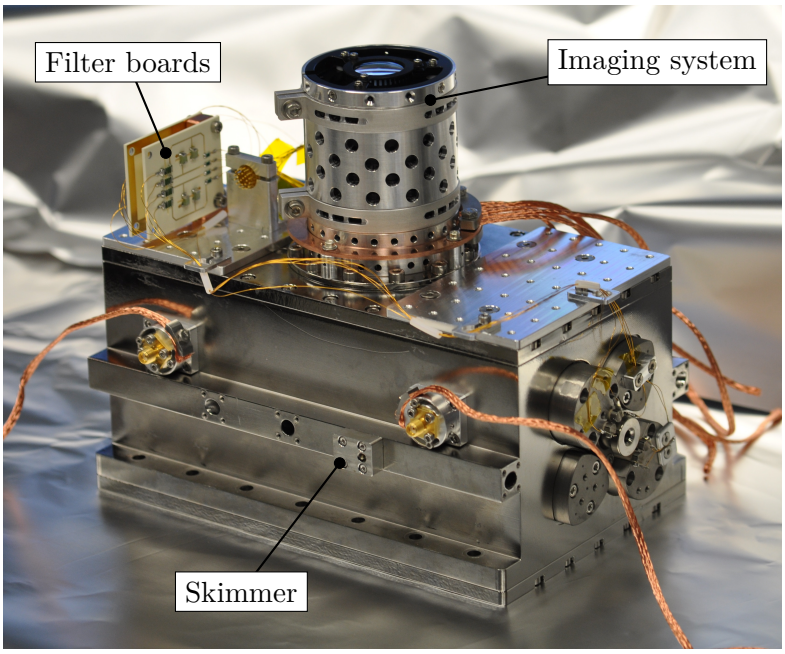

Figure A.2: Picture of the radio-frequency (rf) cavity with imaging system, dc wiring, dc filter boards and skimmer for the beryllium beam. The copper braids are used to thermalize the rf couplers and the imaging system to $4\,\mathrm{K}$.

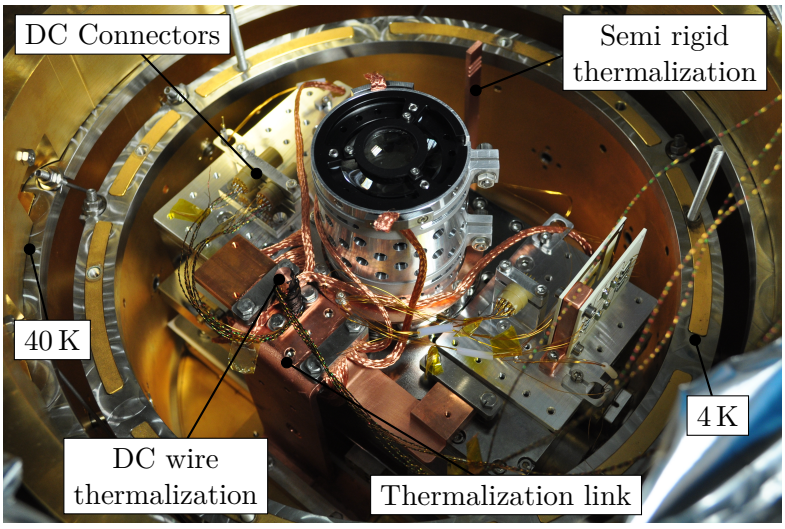

Figure A.3: Picture of the rf cavity mounted inside the $4\,\mathrm{K}$ cryogenic enclosure. Imaging system, dc wires and rf couplers are thermalized using a massive copper link connecting the $4\,\mathrm{K}$ stage and the upper cavity lid.

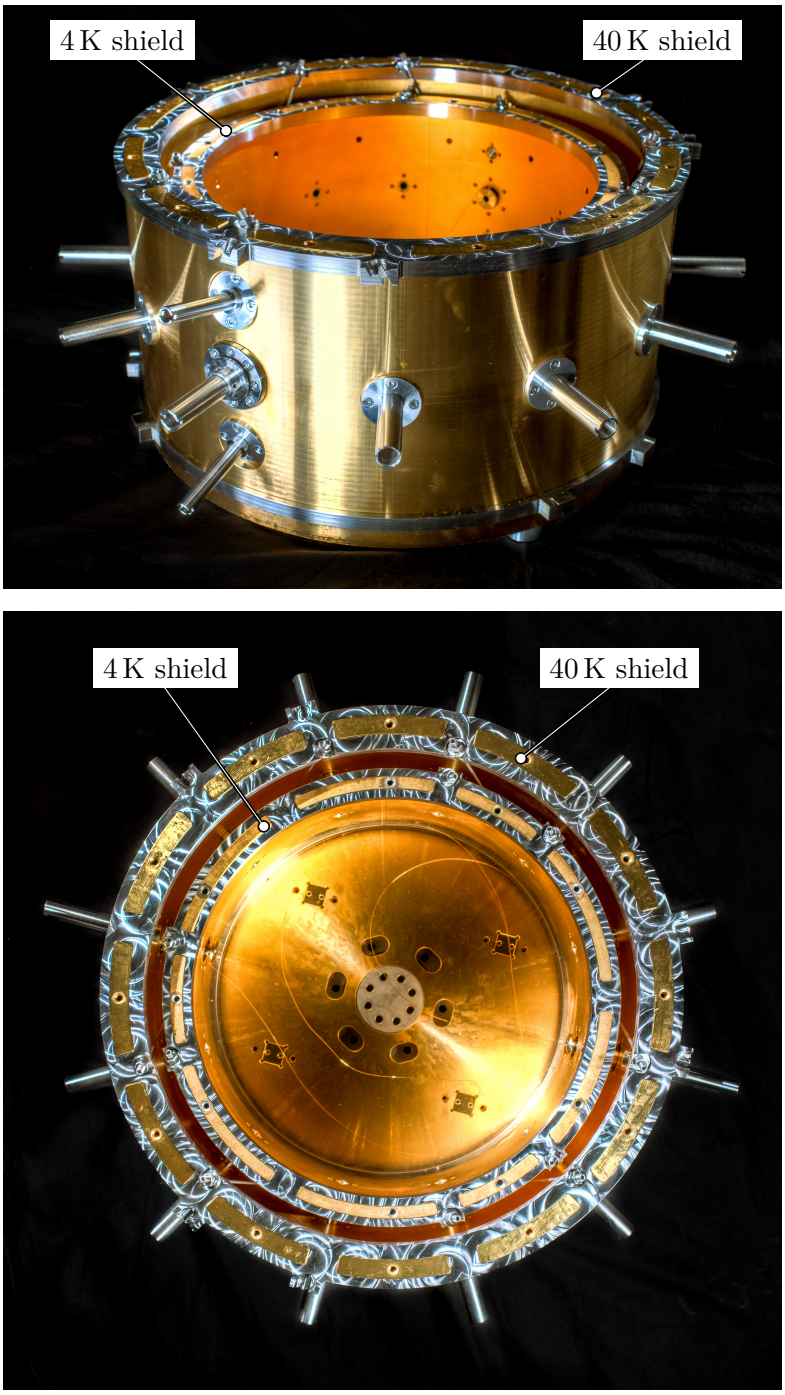

Figure A.4: Pictures of the cryogenic shields around the rf ion trap.

Publications by Julian Stark

1. J. Stark et al. "An ultralow-noise superconducting radio-frequency ion trap for frequency metrology with highly charged ions", *In preparation* (2020).

2. P. Micke et al. "Closed-cycle, low-vibration 4 K cryostat for ion traps and other applications". *Review of Scientific Instruments* **90** (2019), 065104. DOI: 10.1063/1.5088593.

   Note: cited as [Mic+19].

3. J. Nauta et al. "Towards precision measurements on highly charged ions using a high harmonic generation frequency comb". *Nuclear Instruments and Methods in Physics Research Section B: Beam Interactions with Materials and Atoms* **408** (2017), 285–288. DOI: 10.1016/j.nimb.2017.04.077.

   Note: cited as [Nau+17].

4. T. M. Baumann et al. "Contributions of dielectronic, trielectronic, and metastable channels to the resonant intershell recombination of highly charged silicon ions". *Physical Review A* **90** (2014), 052704. DOI: 10.1103/PhysRevA.90.052704.

Bibliography

[Abe+06] R. Abela et al. *XFEL: The European X-Ray Free-Electron Laser - Technical Design Report*. DESY, 2006, 1–646. DOI: 10.3204/DESY_06-097 (cited on page 10).

[Ade+14] P. a. R. Ade et al. "Planck 2013 results. XVI. Cosmological parameters". *Astronomy & Astrophysics* **571** (2014), A16. DOI: 10.1051/0004-6361/201321591 (cited on page 1).

[Ado+13] C. Adolphsen et al. "The International Linear Collider Technical Design Report - Volume 3.I: Accelerator R&D in the Technical Design Phase". *arXiv:1306.6353 [physics.acc-ph]* (2013). URL: http://arxiv.org/abs/1306.6353 (cited on page 10).

[AL05] A. Agarwal and J. Lang. *Foundations of analog and digital electronic circuits*. Elsevier, 2005 (cited on page 26).

[Alc+93] C. Alcock et al. "Possible gravitational microlensing of a star in the Large Magellanic Cloud". *Nature* **365** (1993), 621–623. DOI: 10.1038/365621a0 (cited on page 1).

[Ant+91] C. Antoine et al. "The role of atomic hydrogen in Q-degradation of niobium superconducting rf cavities: analytical point of view". *Proc. of 5th Workshop on RF Superconductivity, DESY, Hamburg, Germany*. 1991, 616–634 (cited on page 99).

[Aub+93] E. Aubourg et al. "Evidence for gravitational microlensing by dark objects in the Galactic halo". *Nature* **365** (1993), 623–625. DOI: 10.1038/365623a0 (cited on page 1).

[Aun+00] B. Aune et al. "Superconducting TESLA cavities". *Physical Review Special Topics - Accelerators and Beams* **3** (2000), 092001. DOI: 10.1103/PhysRevSTAB.3.092001 (cited on pages 37, 98).

[Bau80] W. Bauer. "Fabrication of niobium cavities". *Proc. 1st Workshop RF Supercond., M. Kuntze, ed., Karlsruhe*. 1980, 271 (cited on page 89).

[BCS57a] J. Bardeen, L. N. Cooper, and J. R. Schrieffer. "Microscopic Theory of Superconductivity". *Physical Review* **106** (1957), 162–164. DOI: 10.1103/PhysRev.106.162 (cited on page 35).

[BCS57b] J. Bardeen, L. N. Cooper, and J. R. Schrieffer. "Theory of Superconductivity". *Physical Review* **108** (1957), 1175–1204. DOI: 10.1103/PhysRev.108.1175 (cited on pages 34, 35).

[BDF10] J. C. Berengut, V. A. Dzuba, and V. V. Flambaum. "Enhanced Laboratory Sensitivity to Variation of the Fine-Structure Constant using Highly Charged Ions". *Physical Review Letters* **105** (2010), 120801. DOI: 10.1103/PhysRevLett.105.120801 (cited on pages 3, 7).

[Bek+19] H. Bekker et al. "Detection of the 5p – 4f orbital crossing and its optical clock transition in Pr^{9+}". *Nature Communications* **10** (2019), 1–7. DOI: 10.1038/s41467-019-13406-9 (cited on page 3).

[Ber+11] J. C. Berengut, V. A. Dzuba, V. V. Flambaum, and A. Ong. "Electron-Hole Transitions in Multiply Charged Ions for Precision Laser Spectroscopy and Searching for Variations in α". *Physical Review Letters* **106** (2011), 210802. DOI: 10.1103/PhysRevLett.106.210802 (cited on pages 2, 6).

[Ber+12a] J. C. Berengut, V. A. Dzuba, V. V. Flambaum, and A. Ong. "Highly charged ions with $E1$, $M1$, and $E2$ transitions within laser range". *Physical Review A* **86** (2012), 022517. DOI: 10.1103/PhysRevA.86.022517 (cited on pages 2, 3, 7).

[Ber+12b] J. C. Berengut, V. A. Dzuba, V. V. Flambaum, and A. Ong. "Optical Transitions in Highly Charged Californium Ions with High Sensitivity to Variation of the Fine-Structure Constant". *Physical Review Letters* **109** (2012), 070802. DOI: 10.1103/PhysRevLett.109.070802 (cited on pages 2, 6).

[Ber+18] J. C. Berengut et al. "Probing New Long-Range Interactions by Isotope Shift Spectroscopy". *Physical Review Letters* **120** (2018), 091801. DOI: 10.1103/PhysRevLett.120.091801 (cited on page 5).

[Ber+98] D. J. Berkeland et al. "Minimization of ion micromotion in a Paul trap". *Journal of Applied Physics* **83** (1998), 5025–5033. DOI: 10.1063/1.367318 (cited on pages 9, 16, 158).

[BIB87] V. B. Braginsky, V. S. Ilchenko, and K. S. Bagdassarov. "Experimental observation of fundamental microwave absorption in high-quality dielectric crystals". *Physics Letters A* **120** (1987), 300–305. DOI: 10.1016/0375-9601(87)90676-1 (cited on page 101).

[Bla+86] R. Blatt, P. Zoller, G. Holzmüller, and I. Siemers. "Brownian motion of a parametric oscillator: A model for ion confinement in radio frequency traps". *Zeitschrift für Physik D Atoms, Molecules and Clusters* **4** (1986), 121–126. DOI: 10.1007/BF01437349 (cited on page 149).

[Bog19] S. Bogen. "Frequenz-, Leistungs- und Positionsstabilisierung von UV-Lasersystemen für Frequenzmetrologie mit hochgeladenen Ionen". Master's thesis. Ruprecht-Karls-Universität Heidelberg, 2019. URL: http://hdl.handle.net/21.11116/0000-0005-1733-8 (cited on pages 62, 63, 70, 71, 158).

[Bra+16] M. F. Brandl, P. Schindler, T. Monz, and R. Blatt. "Cryogenic resonator design for trapped ion experiments in Paul traps". *Applied Physics B* **122** (2016), 157. DOI: 10.1007/s00340-016-6430-z (cited on pages 10, 155).

[Bre+19] S. M. Brewer et al. "Al Quantum-Logic Clock with a Systematic Uncertainty below 10^{-18}". *Physical Review Letters* **123** (2019), 033201. DOI: 10.1103/PhysRevLett.123.033201 (cited on pages 2, 8).

[BRG12] F. Barkov, A. Romanenko, and A. Grassellino. "Direct observation of hydrides formation in cavity-grade niobium". *Physical Review Special Topics - Accelerators and Beams* **15** (2012), 122001. DOI: 10.1103/PhysRevSTAB.15.122001 (cited on pages 98, 99).

[Bro+15] M. Brownnutt, M. Kumph, P. Rabl, and R. Blatt. "Ion-trap measurements of electric-field noise near surfaces". *Reviews of Modern Physics* **87** (2015), 1419–1482. DOI: 10.1103/RevModPhys.87.1419 (cited on pages 9, 76, 77, 157).

[BS03] H. F. Beyer and V. P. Shevelko. *Introduction to the physics of highly charged ions*. Institute of Physics Publishing, 2003. DOI: 10.1201/9781420034097 (cited on page 4).

[BS65] J. Bardeen and M. J. Stephen. "Theory of the Motion of Vortices in Superconductors". *Physical Review* **140** (1965), A1197–A1207. DOI: 10.1103/PhysRev.140.A1197 (cited on page 97).

[Bus+06] M. Bussmann et al. "Stopping highly charged ions in a laser-cooled one component plasma of Mg^{24+} ions". *International Journal of Mass Spectrometry* **251** (2006), 179–189. DOI: 10.1016/j.ijms.2006.01.042 (cited on page 108).

[Cas12] F. Caspers. "RF engineering basic concepts: S-parameters". *arXiv preprint arXiv:1201.2346* (2012) (cited on page 27).

[CAS89] *CAS CERN Accelerator School: Superconductivity in particle accelerators*. European Organization for Nuclear Research (CERN), 1989. DOI: 10.5170/CERN-1989-004 (cited on pages 33, 97).

[Cat+07] L. Catani et al. "Nb coating of copper cavities by UHV cathodic arc". *Proceedings of 13th International Conference on RF Superconductivity (SRF 2007), Peking Univ., Beijing, China*. 2007 (cited on page 88).

[CGT20] CG.TEC Injection. *Dielectric properties of PEEK^{TM} Polymer*. URL: https://www.cgtec.eu/wp-content/uploads/dielectric-properties-450G-GL30-vs-T-and-f-e.pdf (visited on Mar. 20, 2020) (cited on page 101).

[Cio15] G. Ciovati. "AC/RF Superconductivity" (2015). DOI: 10.5170/CERN-2014-005.57 (cited on pages 25, 37).

[Col+14] Y. Colombe et al. "Single-mode optical fiber for high-power, low-loss UV transmission". *Optics Express* **22** (2014), 19783–19793. DOI: 10.1364/OE.22.019783 (cited on pages 70, 158).

[COM20a] Comsol Multiphysics GmbH. *COMSOL Multiphysics 5.4. Reference Manual.* URL: https://doc.comsol.com/5.4/docserver/#!/com.comsol.help.comsol/helpdesk/helpdesk.html (visited on Mar. 11, 2020) (cited on pages 91, 102).

[COM20b] Comsol Multiphysics GmbH. *COMSOL Multiphysics 5.4. RF Module User's Guide.* URL: https://doc.comsol.com/5.4/docserver/#!/com.comsol.help.comsol/helpdesk/helpdesk.html (visited on Mar. 11, 2020) (cited on page 91).

[COM20c] Comsol Multiphysics GmbH. *COMSOL Multiphysics 5.4. AC/DC Module User's Guide.* URL: https://doc.comsol.com/5.4/docserver/#!/com.comsol.help.comsol/helpdesk/helpdesk.html (visited on Mar. 11, 2020) (cited on page 102).

[Cre+96] J. R. Crespo López-Urrutia, P. Beiersdorfer, D. W. Savin, and K. Widmann. "Direct Observation of the Spontaneous Emission of the Hyperfine Transition $F = 4$ to $F = 3$ in Ground State Hydrogenlike $^{165}Ho^{66+}$ in an Electron Beam Ion Trap". *Phys. Rev. Lett.* **77** (1996), 826–829. DOI: 10.1103/PhysRevLett.77.826 (cited on page 5).

[DDF12a] A. Derevianko, V. A. Dzuba, and V. V. Flambaum. "Highly Charged Ions as a Basis of Optical Atomic Clockwork of Exceptional Accuracy". *Physical Review Letters* **109** (2012), 180801. DOI: 10.1103/PhysRevLett.109.180801 (cited on pages 2, 7).

[DDF12b] V. A. Dzuba, A. Derevianko, and V. V. Flambaum. "High-precision atomic clocks with highly charged ions: Nuclear-spin-zero f^{12}-shell ions". *Physical Review A* **86** (2012), 054501. DOI: 10.1103/PhysRevA.86.054501 (cited on page 7).

[DDF12c] V. A. Dzuba, A. Derevianko, and V. V. Flambaum. "Ion clock and search for the variation of the fine-structure constant using optical transitions in Nd^{13+} and Sm^{15+}". *Physical Review A* **86** (2012), 054502. DOI: 10.1103/PhysRevA.86.054502 (cited on pages 2, 7).

[Deh90] H. Dehmelt. "Experiments with an isolated subatomic particle at rest". *Reviews of Modern Physics* **62** (1990), 525–530. DOI: 10.1103/RevModPhys.62.525 (cited on page 2).

[Den+15] K. Deng et al. "Design of blade-shaped-electrode linear ion traps with reduced anharmonic contributions". *Journal of Applied Physics* **118** (2015), 113106. DOI: 10.1063/1.4931420 (cited on pages 19, 106).

[Des+06] L. Deslauriers et al. "Scaling and Suppression of Anomalous Heating in Ion Traps". *Physical Review Letters* **97** (2006), 103007. DOI: 10.1103/PhysRevLett.97.103007 (cited on page 77).

[DFM03] V. A. Dzuba, V. V. Flambaum, and M. V. Marchenko. "Relativistic effects in Sr, Dy, Yb II, and Yb III and search for variation of the fine-structure constant". *Physical Review A* **68** (2003), 022506. DOI: 10.1103/PhysRevA.68.022506 (cited on page 6).

[Dit00] F.-M. Dittes. "The decay of quantum systems with a small number of open channels". *Physics Reports* **339** (2000), 215–316. DOI: 10.1016/S0370-1573(00)00065-X (cited on page 27).

[DK03] M. Dine and A. Kusenko. "Origin of the matter-antimatter asymmetry". *Reviews of Modern Physics* **76** (2003), 1–30. DOI: 10.1103/RevModPhys.76.1 (cited on page 1).

[Dob19] S. Dobrodey. "Charge-exchange studies of bare and hydrogen-like low-Z ions in the X-ray and extreme-ultraviolet ranges inside an electron beam ion trap". PhD thesis. Ruprecht-Karls-Universität Heidelberg, 2019. DOI: DOI:10.17617/2.3181746 (cited on page 73).

[DP14] A. Derevianko and M. Pospelov. "Hunting for topological dark matter with atomic clocks". *Nature Physics* **10** (2014), 933–936. DOI: 10.1038/nphys3137 (cited on page 6).

[Dra+03] I. Draganić et al. "High Precision Wavelength Measurements of QED-Sensitive Forbidden Transitions in Highly Charged Argon Ions". *Physical Review Letters* **91** (2003), 183001. DOI: 10.1103/PhysRevLett.91.183001 (cited on page 4).

[Dre+83] R. W. P. Drever et al. "Laser phase and frequency stabilization using an optical resonator". *Applied Physics B* **31** (1983), 97–105. DOI: 10.1007/BF00702605 (cited on page 86).

[Dre15] M. Drewsen. "Ion Coulomb crystals". *Physica B: Condensed Matter* **460** (2015), 105–113. DOI: 10.1016/j.physb.2014.11.050 (cited on pages 146, 147).

[Dru00] P. Drude. "Zur Elektronentheorie der Metalle". *Annalen der Physik* **306** (1900), 566–613. DOI: 10.1002/andp.19003060312 (cited on page 36).

[DSW08] T. Dent, S. Stern, and C. Wetterich. "Unifying cosmological and recent time variations of fundamental couplings". *Physical Review D* **78** (2008), 103518. DOI: 10.1103/PhysRevD.78.103518 (cited on page 6).

[Ear48] S. Earnshaw. "On the Nature of the Molecular Forces which Regulate the Constitution of the Luminiferous Ether". *Transactions of the Cambridge Philosophical Society* **7** (1848), 97 (cited on page 14).

[Ebe13] S. Eberle. "Photoionization of the Beryllium atom". Master's thesis. Ruprecht-Karls-Universität Heidelberg, 2013. URL: http://hdl.handle.net/11858/00-001M-0000-0014-C595-D (cited on page 67).

[Egl+19] A. Egl et al. "Application of the Continuous Stern-Gerlach Effect for Laser Spectroscopy of the $^{40}Ar^{13+}$ Fine Structure in a Penning Trap". *Physical Review Letters* **123** (2019), 123001. DOI: 10.1103/PhysRevLett.123.123001 (cited on pages 4, 62, 159).

[EK02] V. N. Egorov and M. V. Kashchenko. "The Measurement of Small Dielectric Losses in a Cavity Resonator". *Measurement Techniques* **45** (2002), 93–101. DOI: 10.1023/A:1015124018896 (cited on page 100).

[Eki06] J. Ekin. *Experimental Techniques for Low-Temperature Measurements: Cryostat Design, Material Properties and Superconductor Critical-Current Testing*. Oxford University Press, 2006. DOI: 10.1093/acprof:oso/9780198570547.001.0001 (cited on pages 47–50, 58, 63, 80, 94, 126).

[Eps+07] R. J. Epstein et al. "Simplified motional heating rate measurements of trapped ions". *Phys. Rev. A* **76** (2007), 033411. DOI: 10.1103/PhysRevA.76.033411 (cited on page 159).

[FG79] S. M. Faber and J. S. Gallagher. "Masses and Mass-To-Light Ratios of Galaxies". *Annual Review of Astronomy and Astrophysics* **17** (1979), 135–187. DOI: 10.1146/annurev.aa.17.090179.001031 (cited on page 1).

[Fis+05] C. Fischer et al. "Superconductors". *Springer Handbook of Condensed Matter and Materials Data*. Ed. by W. Martienssen and H. Warlimont. Springer, 2005, 695–754. DOI: 10.1007/3-540-30437-1_10 (cited on pages 33, 52, 81, 129).

[Fli65] R. B. Flippen. "The radial velocity of magnetic field penetration in type II superconductors". *Physics Letters* **17** (1965), 193–194. DOI: 10.1016/0031-9163(65)90476-2 (cited on page 38).

[Foo05] C. J. Foot. *Atomic Physics*. Oxford University Press, 2005 (cited on page 21).

[FSS66] D. K. Finnemore, T. F. Stromberg, and C. A. Swenson. "Superconducting Properties of High-Purity Niobium". *Physical Review* **149** (1966), 231–243. DOI: 10.1103/PhysRev.149.231 (cited on page 98).

[GC34] C. Gorter and H. Casimir. "On supraconductivity I". *Physica 1* 306 (1934). DOI: 10.1007/978-94-015-2998-3_1 (cited on page 35).

[Geb+15] F. Gebert et al. "Precision Isotope Shift Measurements in Calcium Ions Using Quantum Logic Detection Schemes". *Physical Review Letters* **115** (2015), 053003. DOI: 10.1103/PhysRevLett.115.053003 (cited on page 5).

[Gho95] P. Ghosh. *Ion traps*. Clarendon Press, 1995 (cited on page 13).

[Gil01] J. D. Gillaspy. "Highly charged ions". *Journal of Physics B: Atomic, Molecular and Optical Physics* **34** (2001), R93–R130. DOI: 10.1088/0953-4075/34/19/201 (cited on page 5).

[Gil05] P. Gill. "Optical frequency standards". *Metrologia* **42** (2005), S125–S137. DOI: 10.1088/0026-1394/42/3/S13 (cited on page 2).

[GK95] R. G. Geyer and J. Krupka. "Microwave dielectric properties of anisotropic materials at cryogenic temperatures". *IEEE Transactions on Instrumentation and Measurement* **44** (1995), 329–331. DOI: 10.1109/19.377844 (cited on page 101).

[God+14] R. M. Godun et al. "Frequency Ratio of Two Optical Clock Transitions in $^{171}Yb^{+}$ and Constraints on the Time Variation of Fundamental Constants". *Physical Review Letters* **113** (2014), 210801. DOI: 10.1103/PhysRevLett.113.210801 (cited on page 6).

[Goh+05] C. Gohle et al. "A frequency comb in the extreme ultraviolet". *Nature* **436** (2005), 234–237. DOI: 10.1038/nature03851 (cited on page 8).

[GR03] J. I. Gittleman and B. Rosenblum. "The Pinning Potential and High-Frequency Studies of Type-II Superconductors". *Journal of Applied Physics* **39** (2003), 2617. DOI: 10.1063/1.1656632 (cited on page 97).

[Gri86] M. Grieser. "Entwicklung eines neuartigen 7-Spaltresonators für die Beschleunigung schwerer Ionen". PhD thesis. Ruprecht-Karls-Universität Heidelberg, 1986 (cited on page 30).

[Gru+01] L. Gruber et al. "Evidence for Highly Charged Ion Coulomb Crystallization in Multicomponent Strongly Coupled Plasmas". *Physical Review Letters* **86** (2001), 636–639. DOI: 10.1103/PhysRevLett.86.636 (cited on page 4).

[GT86] V. L. Gurevich and A. K. Tagantsev. "Intrinsic dielectric loss in crystals: low temperatures". *Sov. Phys. JETP* **64** (1986), 142 (cited on page 101).

[Gur12] A. Gurevich. "Superconducting Radio-Frequency Fundamentals for Particle Accelerators". *Reviews of Accelerator Science and Technology* **5** (2012), 119–146. DOI: 10.1142/S1793626812300058 (cited on page 37).

[HD02] L. Hornekær and M. Drewsen. "Formation process of large ion Coulomb crystals in linear Paul traps". *Physical Review A* **66** (2002), 013412. DOI: 10.1103/PhysRevA.66.013412 (cited on page 146).

[Hig+01] T. Higuchi et al. "Hydrogen Q-disease and electropolishing". *10th Workshop on RF Superconductivity*. 2001 (cited on page 99).

[Hun+14] N. Huntemann et al. "Improved Limit on a Temporal Variation of m_p/m_e from Comparisons of Yb^{+} and Cs Atomic Clocks". *Physical Review Letters* **113** (2014), 210802. DOI: 10.1103/PhysRevLett.113.210802 (cited on pages 2, 6).

[Hun+16] N. Huntemann et al. "Single-Ion Atomic Clock with 3×10^{-18} Systematic Uncertainty". *Physical Review Letters* **116** (2016), 063001. DOI: 10.1103/PhysRevLett.116.063001 (cited on pages 2, 8).

[Ind19] P. Indelicato. "QED tests with highly charged ions". *Journal of Physics B: Atomic, Molecular and Optical Physics* **52** (2019), 232001. DOI: 10.1088/1361-6455/ab42c9 (cited on page 5).

[Jac+02] M. Jacob, J. Mazierska, K. Leong, and J. Krupka. "Microwave Properties of Low Loss Polymers at Cryogenic Temperatures". *IEEE Transactions on Microwave Theory and Techniques* **50** (2002), 474–480. DOI: 10.1109/22.982226 (cited on page 101).

[Jac07] J. D. Jackson. "Electrodynamics". *The Optics Encyclopedia*. John Wiley & Sons, 2007. DOI: 10.1002/9783527600441.oe014 (cited on pages 25, 33, 34).

[Jam98] D. F. V. James. "Quantum dynamics of cold trapped ions with application to quantum computation". *Applied Physics B* **66** (1998), 181–190. DOI: 10.1007/s003400050373 (cited on page 150).

[Joh+16] K. G. Johnson et al. "Active stabilization of ion trap radiofrequency potentials". *Review of Scientific Instruments* **87** (2016), 053110. DOI: 10.1063/1.4948734 (cited on pages 10, 155).

[Joh28] J. B. Johnson. "Thermal Agitation of Electricity in Conductors". *Physical Review* **32** (1928), 97–109. DOI: 10.1103/PhysRev.32.97 (cited on pages 59, 77, 114).

[Joh61] V. J. Johnson. *A compendium of the properties of materials at low temperature (PHASE I-II) (Wright Air Development Division, Air Research and Development Command, United States Air Force, Wright-Patterson Air Force Base, Ohio)*. 1961 (cited on pages 49, 51).

[Jon+05] R. J. Jones, K. D. Moll, M. J. Thorpe, and J. Ye. "Phase-Coherent Frequency Combs in the Vacuum Ultraviolet via High-Harmonic Generation inside a Femtosecond Enhancement Cavity". *Physical Review Letters* **94** (2005), 193201. DOI: 10.1103/PhysRevLett.94.193201 (cited on page 8).

[KB61] G. Kirchhoff and R. Bunsen. "Chemische Analyse durch Spectralbeobachtungen". *Annalen der Physik* **189** (1861), 337–381. DOI: 10.1002/andp.18611890702 (cited on page 2).

[KB96] F. Koechlin and B. Bonin. "Parametrization of the niobium thermal conductivity in the superconducting state". *Superconductor Science and Technology* **9** (1996), 453–460. DOI: 10.1088/0953-2048/9/6/003 (cited on page 88).

[Kec+19] S. Keckert et al. "Critical fields of Nb_3Sn prepared for superconducting cavities". *Superconductor Science and Technology* **32** (2019), 075004. DOI: 10.1088/1361-6668/ab119e (cited on page 88).

[Kel+15] J. Keller, H. L. Partner, T. Burgermeister, and T. E. Mehlstäubler. "Precise determination of micromotion for trapped-ion optical clocks". *Journal of Applied Physics* **118** (2015), 104501. DOI: 10.1063/1.4930037 (cited on pages 9, 16, 158).

[Kel+19] J. Keller et al. "Controlling systematic frequency uncertainties at the 10^{-19} level in linear Coulomb crystals". *Physical Review A* **99** (2019), 013405. DOI: 10.1103/PhysRevA.99.013405 (cited on page 2).

[Kel15] J. Keller. "Spectroscopic characterization of ion motion for an optical clock based on Coulomb crystals". PhD thesis. Gottfried Wilhelm Leibniz Universität Hannover, 2015 (cited on page 9).

[Ker99] A. Kerr. "Surface impedance of superconductors and normal conductors in EM simulators". *MMA Memo* **21** (1999), 1–17 (cited on page 36).

[KHS65] Y. B. Kim, C. F. Hempstead, and A. R. Strnad. "Flux-Flow Resistance in Type-II Superconductors". *Physical Review* **139** (1965), A1163–A1172. DOI: 10.1103/PhysRev.139.A1163 (cited on page 97).

[Kin63] W. H. King. "Comments on the Article "Peculiarities of the Isotope Shift in the Samarium Spectrum"". *Journal of the Optical Society of America* **53** (1963), 638–639. DOI: 10.1364/JOSA.53.000638. (Visited on May 1, 2020) (cited on page 5).

[Kla+94] I. Klaft et al. "Precision Laser Spectroscopy of the Ground State Hyperfine Splitting of Hydrogenlike $^{209}Bi^{82+}$". *Phys. Rev. Lett.* **73** (1994), 2425–2427. DOI: 10.1103/PhysRevLett.73.2425 (cited on page 5).

[Kle17] R. Kleindienst. "Radio frequency characterization of superconductors for particle accelerators". PhD thesis. Universität Siegen, 2017. URL: https://dspace.ub.uni-siegen.de/handle/ubsi/1329 (cited on pages 33, 100).

[Kne+13] P. Kneisel et al. "The Rise of Ingot Niobium as a Material for Superconducting Radiofrequency Accelerating Cavities". *arXiv:1304.1722 [physics.acc-ph]* (2013). URL: http://arxiv.org/abs/1304.1722 (cited on page 87).

[Kne95] P. Kneisel. "Effect of cavity vacuum on performance of superconducting niobium cavities". *Proc. of the 1995 Workshop on RF Superconductivity*. 1995 (cited on page 98).

[Kno97] J. Knobloch. "Advanced Thermometry Studies of Superconducting Radio-Frequency Cavities". PhD thesis. Cornell University, 1997. URL: https://search.proquest.com/docview/304346080?accountid=105321 (cited on pages 33, 37, 97, 98, 142).

[Knü+12] S. Knünz et al. "Sub-millikelvin spatial thermometry of a single Doppler-cooled ion in a Paul trap". *Physical Review A* **85** (2012), 023427. DOI: 10.1103/PhysRevA.85.023427 (cited on pages 149, 151).

[Koz+18] M. G. Kozlov, M. S. Safronova, J. R. Crespo López-Urrutia, and P. O. Schmidt. "Highly charged ions: Optical clocks and applications in fundamental physics". *Reviews of Modern Physics* **90** (2018), 045005. DOI: 10.1103/RevModPhys.90.045005 (cited on pages 2–8, 24, 159).

[KR17] M. P. Kelly and T. Reid. "Surface processing for bulk niobium superconducting radio frequency cavities". *Superconductor Science and Technology* **30** (2017), 043001. DOI: 10.1088/1361-6668/aa569a (cited on pages 89, 90).

[Kra+19] A. E. Kramida, Y. Ralchenko, J. Reader, and N. A. Team. NIST Atomic Spectra Database (ver. 5.7.1), [Online]. URL: https://physics.nist.gov/asd (visited on Feb. 23, 2020) (cited on pages 20, 66–68).

[Kra05] A. E. Kramida. "Critical Compilation of Wavelengths and Energy Levels of Singly Ionized Beryllium (Be II)". *Physica Scripta* **72** (2005), 309. DOI: 10.1238/Physica.Regular.072a00309 (cited on page 68).

[Kra17] S. Kraemer. "Towards Laser Cooling of Beryllium Ions at the Alphatrap Experiment". Master's thesis. Ruprecht-Karls-Universität Heidelberg, 2017. URL: http://hdl.handle.net/11858/00-001M-0000-002E-5729-1 (cited on page 115).

[Kru+99] J. Krupka et al. "Complex permittivity of some ultralow loss dielectric crystals at cryogenic temperatures". *Measurement Science and Technology* **10** (1999), 387–392. DOI: 10.1088/0957-0233/10/5/308 (cited on page 101).

[Küh21] S. Kühn. PhD thesis, to be submitted. Ruprecht-Karls-Universität Heidelberg, 2021 (cited on pages 39, 72).

[Lau05] N. M. Laurendeau. *Statistical Thermodynamics: Fundamentals and Applications*. 2005. DOI: 10.1017/CBO9780511815928 (cited on pages 65, 66).

[Lee+13] N. Leefer et al. "New Limits on Variation of the Fine-Structure Constant Using Atomic Dysprosium". *Physical Review Letters* **111** (2013), 060801. DOI: 10.1103/PhysRevLett.111.060801 (cited on page 6).

[Lei+03] D. Leibfried, R. Blatt, C. Monroe, and D. Wineland. "Quantum dynamics of single trapped ions". *Reviews of Modern Physics* **75** (2003), 281–324. DOI: 10.1103/RevModPhys.75.281 (cited on pages 19, 20, 22).

[Leo+16] T. Leopold et al. "A tunable low-drift laser stabilized to an atomic reference". *Applied Physics B* **122** (2016), 236. DOI: 10.1007/s00340-016-6511-z (cited on page 39).

[Leo+19] T. Leopold et al. "A cryogenic radio-frequency ion trap for quantum logic spectroscopy of highly charged ions". *Review of Scientific Instruments* **90** (2019), 073201. DOI: 10.1063/1.5100594 (cited on pages 4, 9, 10, 17, 40, 56, 57, 59, 86, 137, 148, 155, 157, 159).

[Leo18] T. Leopold. "A cryogenic ion trap system for quantum logic spectroscopy of highly charged ions". PhD thesis. Gottfried Wilhelm Leibniz Universität Hannover, 2018 (cited on pages 3, 24, 55, 69, 104, 154, 158).

[Lie17] D. Liebert. "Optimierung eines kryogenischen monolithischen Hochfrequenzresonators für eine Paul-Falle". Bachelor's thesis. Ruprecht-Karls-Universität Heidelberg, 2017. URL: http://hdl.handle.net/21.11116/0000-0005-81E5-6 (cited on page 118).

[Lin+11] T. Lindström, J. Burnett, M. Oxborrow, and A. Y. Tzalenchuk. "Pound-locking for characterization of superconducting microresonators". *Review of Scientific Instruments* **82** (2011), 104706. DOI: 10.1063/1.3648134 (cited on pages 86, 156).

[LL35] F. London and H. London. "The electromagnetic equations of the supraconductor". *Proceedings of the Royal Society of London. Series A - Mathematical and Physical Sciences* **149** (1935), 71–88. DOI: 10.1098/rspa.1935.0048 (cited on pages 33, 34).

[Lo+14] H.-Y. Lo et al. "All-solid-state continuous-wave laser systems for ionization, cooling and quantum state manipulation of beryllium ions". *Applied Physics B* **114** (2014), 17–25. DOI: 10.1007/s00340-013-5605-0 (cited on page 67).

[Lud+15] A. D. Ludlow et al. "Optical atomic clocks". *Reviews of Modern Physics* **87** (2015), 637–701. DOI: 10.1103/RevModPhys.87.637 (cited on pages 2, 8).

[Mäc+11] V. Mäckel et al. "Laser Spectroscopy on Forbidden Transitions in Trapped Highly Charged Ar^{13+} Ions". *Physical Review Letters* **107** (2011), 143002. DOI: 10.1103/PhysRevLett.107.143002 (cited on pages 4, 62).

[Mai60] T. H. Maiman. "Stimulated Optical Radiation in Ruby". *Nature* **187** (1960), 493–494. DOI: 10.1038/187493a0 (cited on page 2).

[Mar+17] C. D. Marciniak, H. B. Ball, A. T.-H. Hung, and M. J. Biercuk. "Towards fully commercial, UV-compatible fiber patch cords". *Optics Express* **25** (2017), 15643–15661. DOI: 10.1364/OE.25.015643 (cited on pages 70, 158).

[MDP48] C. G. Montgomery, R. H. Dicke, and E. M. Purcell. *Principles of microwave circuits*. New York: McGraw-Hill Book Co., 1948 (cited on page 26).

[Meg+19] E. Megidish, J. Broz, N. Greene, and H. Häffner. "Improved Test of Local Lorentz Invariance from a Deterministic Preparation of Entangled States". *Physical Review Letters* **122** (2019), 123605. DOI: 10.1103/PhysRevLett.122.123605 (cited on page 2).

[Mic+18] P. Micke et al. "The Heidelberg compact electron beam ion traps". *Review of Scientific Instruments* **89** (2018), 063109. DOI: 10.1063/1.5026961 (cited on pages 39, 72).

[Mic+19] P. Micke et al. "Closed-cycle, low-vibration 4 K cryostat for ion traps and other applications". *Review of Scientific Instruments* **90** (2019), 065104. DOI: 10.1063/1.5088593 (cited on pages 40, 41, 51, 52, 55, 153, 154, 165).

[Mic+20] P. Micke et al. "Coherent laser spectroscopy of highly charged ions using quantum logic". *Nature* **578** (2020), 60–65. DOI: 10.1038/s41586-020-1959-8 (cited on pages 5, 9, 41, 62, 159).

[Mic20] P. Micke. "Quantum Logic Spectroscopy of Highly Charged Ions". PhD thesis. Gottfried Wilhelm Leibniz Universität Hannover, 2020 (cited on pages 4, 7, 9, 39, 72–74).

[MLR02] E. D. Marquardt, J. P. Le, and R. Radebaugh. "Cryogenic Material Properties Database". *Cryocoolers 11*. Ed. by R. G. Ross. Boston, MA: Springer US, 2002, 681–687. DOI: 10.1007/0-306-47112-4_84 (cited on page 51).

[MO33] W. Meissner and R. Ochsenfeld. "Ein neuer Effekt bei Eintritt der Supraleitfähigkeit". *Naturwissenschaften* **21** (1933), 787–788. DOI: 10.1007/BF01504252 (cited on pages 33, 37, 157).

[Mon+95] C. Monroe et al. "Resolved-Sideband Raman Cooling of a Bound Atom to the 3D Zero-Point Energy". *Physical Review Letters* **75** (1995), 4011–4014. DOI: 10.1103/PhysRevLett.75.4011 (cited on page 68).

[Moo87] F. Moon. *Chaotic vibrations: an introduction for applied scientists and engineers*. New Zork: John Wiley & Sons, 1987 (cited on page 18).

[MS65] G. W. Mellors and S. Senderoff. "Electrodeposition of Coherent Deposits of Refractory Metals: I. Niobium". *Journal of The Electrochemical Society* **112** (1965), 266–272. DOI: 10.1149/1.2423521 (cited on page 88).

[MS67] J. Matricon and D. Saint-James. "Superheating fields in superconductors". *Physics Letters A* **24** (1967), 241–242. DOI: 10.1016/0375-9601(67)90412-4 (cited on page 38).

[MSM11] P. Mandal, G. Sikler, and M. Mukherjee. "Simulation study and analysis of a compact einzel lens-deflector for low energy ion beam". *Journal of Instrumentation* **6** (2011), P02004–P02004. DOI: 10.1088/1748-0221/6/02/P02004 (cited on page 73).

[Nat93] V. Natarajan. "Penning Trap Mass Spectroscopy at 0.1 Ppb". PhD thesis. Massachusetts Institute of Technology, 1993 (cited on page 113).

[Nau+17] J. Nauta et al. "Towards precision measurements on highly charged ions using a high harmonic generation frequency comb". *Nuclear Instruments and Methods in Physics Research Section B: Beam Interactions with Materials and Atoms* **408** (2017), 285–288. DOI: 10.1016/j.nimb.2017.04.077 (cited on pages 8, 39, 159, 165).

[Nau20] J. Nauta. PhD thesis, to be submitted. Ruprecht-Karls-Universität Heidelberg, 2020 (cited on pages 8, 39, 159, 160).

[Neu+78] W. Neuhauser, M. Hohenstatt, P. Toschek, and H. Dehmelt. "Optical-Sideband Cooling of Visible Atom Cloud Confined in Parabolic Well". *Physical Review Letters* **41** (1978), 233–236. DOI: 10.1103/PhysRevLett.41.233 (cited on page 2).

[Neu+80] W. Neuhauser, M. Hohenstatt, P. E. Toschek, and H. Dehmelt. "Localized visible Ba^+ mono-ion oscillator". *Phys. Rev. A* **22** (1980), 1137–1140. DOI: 10.1103/PhysRevA.22.1137 (cited on page 149).

[Nyq28] H. Nyquist. "Thermal Agitation of Electric Charge in Conductors". *Physical Review* **32** (1928), 110–113. DOI: 10.1103/PhysRev.32.110 (cited on pages 59, 77, 114).

[Oel21] J.-H. Oelmann. PhD thesis, to be submitted. Ruprecht-Karls-Universität Heidelberg, 2021 (cited on pages 8, 39, 160).

[Orl+93] G. Orlandi, C. Benvenuti, S. Calatroni, and F. Scalambrin. "Expected dependence of Nb-coated RF cavity performance on the characteristics of niobium". *Proc. Of 6th workshop on RF Superconductivity, CEBAF, USA*. 1993, 718 (cited on page 88).

[Ort+06] R. S. Orts et al. "Exploring Relativistic Many-Body Recoil Effects in Highly Charged Ions". *Physical Review Letters* **97** (2006), 103002. DOI: 10.1103/PhysRevLett.97.103002 (cited on page 5).

[Pad01] H. Padamsee. "The science and technology of superconducting cavities for accelerators". *Superconductor Science and Technology* **14** (2001), R28–R51. DOI: 10.1088/0953-2048/14/4/202 (cited on pages 38, 87, 88, 142).

[Pad15] H. Padamsee. "Design Topics for Superconducting RF Cavities and Ancillaries". *arXiv:1501.07129 [physics.acc-ph]* (2015), 141–169. DOI: 10.5170/CERN-2014-005.141 (cited on page 99).

[Pad17] H. Padamsee. "50 years of success for SRF accelerators - a review". *Superconductor Science and Technology* **30** (2017), 053003. DOI: 10.1088/1361-6668/aa6376 (cited on pages 9, 10).

[Pag+18] G. Pagano et al. "Cryogenic trapped-ion system for large scale quantum simulation". *Quantum Science and Technology* **4** (2018), 014004. DOI: 10.1088/2058-9565/aae0fe (cited on page 40).

[Par11] R. F. Parodi. "Multipacting". *arXiv:1112.2176 [physics.acc-ph]* (2011). URL: http://arxiv.org/abs/1112.2176 (cited on pages 99, 100).

[Par14] V. Parma. "Cryostat Design". *arXiv:1501.07154 [physics.acc-ph]* (2014). DOI: 10.5170/CERN-2014-005.353 (cited on page 48).

[PB53] A. B. Pippard and W. L. Bragg. "An experimental and theoretical study of the relation between magnetic field and current in a superconductor". *Proceedings of the Royal Society of London. Series A. Mathematical and Physical Sciences* **216** (1953), 547–568. DOI: 10.1098/rspa.1953.0040 (cited on pages 34, 35).

[PCE16] A. Papoulia, B. G. Carlsson, and J. Ekman. "Effect of realistic nuclear charge distributions on isotope shifts and progress towards the extraction of higher-order nuclear radial moments". *Physical Review A* **94** (2016), 042502. DOI: 10.1103/PhysRevA.94.042502 (cited on page 5).

[Ped+10] J. Pedregosa, C. Champenois, M. Houssin, and M. Knoop. "Anharmonic contributions in real RF linear quadrupole traps". *International Journal of Mass Spectrometry* **290** (2010), 100–105. DOI: 10.1016/j.ijms.2009.12.009 (cited on page 19).

[PHK98] H. Padamsee, T. Hays, and J. Knobloch. *RF superconductivity for accelerators*. Wiley series in beam physics and accelerator technology. New York, NY: Wiley, 1998 (cited on pages 25, 33, 97, 99).

[Pie15] B. Piest. "Injektion, Speicherung und Abbildung hochgeladener Argon-Ionen in der kryogenen Paul-Falle CryPTEx". Master's thesis. Ruprecht-Karls-Universität Heidelberg, 2015. URL: http://hdl.handle.net/11858/00-001M-0000-0027-A7E4-3 (cited on pages 110, 112).

[Pip47] A. B. Pippard. "The Surface Impedance of Superconductors and Normal Metals at High Frequencies. II. The Anomalous Skin Effect in Normal Metals". *Proceedings of the Royal Society of London. Series A, Mathematical and Physical Sciences* **191** (1947), 385–399 (cited on page 36).

[Piz+16] P. Pizzol et al. "CVD Deposition of Nb Based Materials for SRF Cavities". *Proc. of International Particle Accelerator Conference 2016, Busan, Korea*. 2016, 2241–2244. DOI: doi:10.18429/JACoW-IPAC2016-WEPMB056 (cited on page 88).

[Pou46] R. V. Pound. "Electronic Frequency Stabilization of Microwave Oscillators". *Review of Scientific Instruments* **17** (1946), 490–505. DOI: 10.1063/1.1770414 (cited on pages 86, 141, 156).

[Poz12] D. M. Pozar. *Microwave Engineering*. Fourth Edition, John Wiley & Sons, Inc, 2012 (cited on pages 30, 100).

[PR03] P. J. E. Peebles and B. Ratra. "The cosmological constant and dark energy". *Reviews of Modern Physics* **75** (2003), 559–606. DOI: 10.1103/RevModPhys.75.559 (cited on page 1).

[Pru+15] T. Pruttivarasin et al. "Michelson–Morley analogue for electrons using trapped ions to test Lorentz symmetry". *Nature* **517** (2015), 592–595. DOI: 10.1038/nature14091 (cited on page 2).

[PS53] W. Paul and H. Steinwedel. "Notizen: Ein neues Massenspektrometer ohne Magnetfeld". *Zeitschrift für Naturforschung A* **8** (1953), 448–450. DOI: 10.1515/zna-1953-0710 (cited on page 2).

[Qui+08] W. Quint, D. L. Moskovkhin, V. M. Shabaev, and M. Vogel. "Laser-microwave double-resonance technique for g-factor measurements in highly charged ions". *Physical Review A* **78** (2008), 032517. DOI: 10.1103/PhysRevA.78.032517 (cited on page 4).

[QV14] W. Quint and M. Vogel. *Fundamental Physics in Particle Traps*. Springer, 2014. DOI: 10.1007/978-3-642-45201-7 (cited on pages 3, 5).

[Raj+16] V. Rajagopal, J. P. Marler, M. G. Kokish, and B. C. Odom. "Trapped Ion Chain Thermometry and Mass Spectrometry through Imaging". *European Journal of Mass Spectrometry* **22** (2016), 1–7. DOI: 10.1255/ejms.1408 (cited on page 149).

[Res+17] D. Reschke et al. "Performance in the vertical test of the 832 nine-cell 1.3 GHz cavities for the European X-ray Free Electron Laser". *Physical Review Accelerators and Beams* **20** (2017), 042004. DOI: 10.1103/PhysRevAccelBeams.20.042004 (cited on pages 10, 33, 88, 134, 141).

[Reu+96] A. J. Reuben et al. "Ion trajectories in exactly determined quadrupole fields". *International Journal of Mass Spectrometry and Ion Processes* **154** (1996), 43–59. DOI: 10.1016/0168-1176(96)04374-1 (cited on page 19).

[RG83] M. Raimondi and J. Gerratt. "Spin coupled VB description of the potential energy surfaces for the reaction $Be^+ + H_2 \rightarrow BeH^+ + H$". *The Journal of Chemical Physics* **79** (1983), 4339–4345. DOI: 10.1063/1.446315 (cited on page 148).

[Ros+08] T. Rosenband et al. "Frequency Ratio of Al^+ and Hg^+ Single-Ion Optical Clocks; Metrology at the 17th Decimal Place". *Science* **319** (2008), 1808–1812. DOI: 10.1126/science.1154622 (cited on pages 2, 6).

[Ros19] M. K. Rosner. "Production and preparation of highly charged ions for re-trapping in ultra-cold environments". Master's thesis. Ruprecht-Karls-Universität Heidelberg, 2019. URL: http://hdl.handle.net/21.11116/0000-0005-5B37-8 (cited on pages 39, 72, 74).

[RS95] K. J. Ross and B. Sonntag. "High temperature metal atom beam sources". *Review of Scientific Instruments* **66** (1995), 4409–4433. DOI: 10.1063/1.1145337 (cited on page 66).

[San+19] C. Sanner et al. "Optical clock comparison for Lorentz symmetry testing". *Nature* **567** (2019), 204–208. DOI: 10.1038/s41586-019-0972-2 (cited on page 2).

[Saw+15] B. C. Sawyer, J. G. Bohnet, J. W. Britton, and J. J. Bollinger. "Reversing hydride-ion formation in quantum-information experiments with Be^+". *Physical Review A* **91** (2015), 011401. DOI: 10.1103/PhysRevA.91.011401 (cited on pages 148, 149).

[Sch+12] M. Schwarz et al. "Cryogenic linear Paul trap for cold highly charged ion experiments". *Review of Scientific Instruments* **83** (2012), 083115. DOI: 10.1063/1.4742770 (cited on pages 40, 56, 57, 145, 156).

[Sch+15a] L. Schmöger et al. "Coulomb crystallization of highly charged ions". *Science* **347** (2015), 1233–1236. DOI: 10.1126/science.aaa2960 (cited on pages 4, 107).

[Sch+15b] L. Schmöger et al. "Deceleration, precooling, and multi-pass stopping of highly charged ions in Be^+ Coulomb crystals". *Review of Scientific Instruments* **86** (2015), 103111. DOI: 10.1063/1.4934245 (cited on pages 74, 80, 107, 108, 159).

[Sch+20] R. X. Schüssler et al. "Detection of metastable electronic states by Penning trap mass spectrometry". *Nature* **581** (2020), 42–46. DOI: 10.1038/s41586-020-2221-0 (cited on pages 4, 8).

[Sch07] S. Schiller. "Hydrogenlike Highly Charged Ions for Tests of the Time Independence of Fundamental Constants". *Physical Review Letters* **98** (2007), 180801. DOI: 10.1103/PhysRevLett.98.180801 (cited on pages 2, 6, 7).

[Sch12] M. Schwarz. "Lasermanipulation von rotationsgekühlten Molekülionen in einer neuen kryogenen Paul-Falle". PhD thesis. Ruprecht-Karls-Universität Heidelberg, 2012. DOI: DOI:10.11588/heidok.00013535 (cited on page 57).

[Sch17] L. Schmöger. "Kalte hochgeladene Ionen für Frequenzmetrologie". PhD thesis. Ruprecht-Karls-Universität Heidelberg, 2017. DOI: DOI:10.11588/heidok.00023214 (cited on pages 18, 24, 55, 57, 64, 66, 67, 69, 72, 104, 107, 149, 159).

[Sch19] R. X. Schüssler. "First High-Precision Mass Measurements at PENTATRAP on highly charged Xe and Re ions". PhD thesis. Ruprecht-Karls-Universität Heidelberg, 2019. DOI: 10.17617/2.3183485 (cited on pages 112, 114).

[Sch81] K. K. Schulze. "Preparation and Characterization of Ultra-High-Purity Niobium". *JOM* **33** (1981), 33–41. DOI: 10.1007/BF03354422 (cited on pages 88, 89).

[SDR92] N. J. Simon, E. S. Drexler, and R. P. Reed. *Properties of Copper and Copper Alloys at Cryogenic Temperatures*. NIST Monograph No. 177 (U.S. Government Printing Offce, Washington), 1992 (cited on page 49).

[Sed+18a] J. A. Sedlacek et al. "Distance scaling of electric-field noise in a surface-electrode ion trap". *Physical Review A* **97** (2018), 020302. DOI: 10.1103/PhysRevA.97.020302 (cited on page 157).

[Sed+18b] J. A. Sedlacek et al. "Method for determination of technical noise contributions to ion motional heating". *Journal of Applied Physics* **124** (2018), 214904. DOI: 10.1063/1.5045326 (cited on page 158).

[SHI19] SHI Cryogenics Group. *SRP-082B2 Cold Head Capacity Map*. 2019. URL: http://www.shicryogenics.com/wp-content/uploads/2019/08/RP-082B2_Capacity_Map.pdf (visited on Feb. 27, 2020) (cited on pages 47, 53, 122, 137).

[SIM19] SIMION. *SIMION User Manual*. URL: https://simion.com/info/manual.html (visited on Mar. 11, 2020) (cited on page 109).

[Sin+15] W. Singer et al. "Superconducting cavity material for the European XFEL". *Superconductor Science and Technology* **28** (2015), 085014. DOI: 10.1088/0953-2048/28/8/085014 (cited on page 88).

[Sin+16] W. Singer et al. "Production of superconducting 1.3-GHz cavities for the European X-ray Free Electron Laser". *Physical Review Accelerators and Beams* **19** (2016), 092001. DOI: 10.1103/PhysRevAccelBeams.19.092001 (cited on page 88).

[Siv+12] J. D. Siverns, L. R. Simkins, S. Weidt, and W. K. Hensinger. "On the application of radio frequency voltages to ion traps via helical resonators". *Applied Physics B* **107** (2012), 921–934. DOI: 10.1007/s00340-011-4837-0 (cited on pages 10, 155).

[Sla46] J. C. Slater. "Microwave Electronics". *Reviews of Modern Physics* **18** (1946), 441–512. DOI: 10.1103/RevModPhys.18.441 (cited on page 30).

[Sor+07] R. Soria Orts et al. "Zeeman splitting and g factor of the $1s^2\,2s^2\,2p\ {}^2P_{3/2}$ and ${}^2P_{1/2}$ levels in Ar^{13+}". *Physical Review A* **76** (2007), 052501. DOI: 10.1103/PhysRevA.76.052501 (cited on page 4).

[Spi18] L. J. Spieß. "Setup of a vibration-suppressed cryogenic system for a RF ion trap with minimum micromotion". Master's thesis. Ruprecht-Karls-Universität Heidelberg, 2018. URL: http://hdl.handle.net/21.11116/0000-0002-5FE1-6 (cited on page 51).

[Sta15] J. Stark. "Design ultrastabiler Hochfrequenzfelder für die Langzeitspeicherung hochgeladener Ionen". Master's thesis. Ruprecht-Karls-Universität Heidelberg, 2015. URL: http://hdl.handle.net/11858/00-001M-0000-0027-7986-8 (cited on pages 118, 119, 121, 122, 137).

[Ste86] S. Stenholm. "The semiclassical theory of laser cooling". *Reviews of Modern Physics* **58** (1986), 699–739. DOI: 10.1103/RevModPhys.58.699 (cited on page 22).

[Ste97] A. Steane. "The ion trap quantum information processor". *Applied Physics B* **64** (1997), 623–643. DOI: 10.1007/s003400050225 (cited on page 146).

[Stu12] S. Sturm. "The g-factor of the electron bound in $^{28}Si^{13+}$: The most stringent test of bound-state quantum electrodynamics". PhD thesis. Johannes-Gutenberg Universität Mainz, 2012. URL: http://hdl.handle.net/11858/00-001M-0000-0010-1AD9-C (cited on pages 105, 112).

[TCD10] J. Tuttle, E. Canavan, and M. DiPirro. "Thermal and electrical conductivity measurements of CDA 510 phosphor bronze". *AIP Conference Proceedings* **1219** (2010), 55–62. DOI: 10.1063/1.3402333 (cited on page 51).

[Tin96] M. Tinkham. *Introduction to superconductivity*. 2nd ed. Mac-Graw-Hill Inc, 1996 (cited on pages 33, 34, 36–38).

[Tur+00] Q. A. Turchette et al. "Heating of trapped ions from the quantum ground state". *Physical Review A* **61** (2000), 063418. DOI: 10.1103/PhysRevA.61.063418 (cited on pages 148, 159).

[TV70] J. P. Turneaure and N. T. Viet. "Superconducting Nb TM010 mode electron-beam welded cavities". *Applied Physics Letters* **16** (1970), 333–335. DOI: 10.1063/1.1653215 (cited on page 10).

[Ulm+09] S. Ulmer et al. "The quality factor of a superconducting rf resonator in a magnetic field". *Review of Scientific Instruments* **80** (2009), 123302. DOI: 10.1063/1.3271537 (cited on pages 30, 114, 156).

[Ulm11] S. Ulmer. "First Observation of Spin Flips with a single Proton stored in a cryogenic Penning trap". PhD thesis. Ruprecht-Karls-Universität Heidelberg, 2011. DOI: DOI:10.11588/heidok.00012306 (cited on pages 18, 105, 112, 115).

[Uza11] J.-P. Uzan. "Varying Constants, Gravitation and Cosmology". *Living Reviews in Relativity* **14** (2011), 2. DOI: 10.12942/lrr-2011-2 (cited on page 6).

[Val+92] C. Vallet et al. "Flux trapping in superconducting cavities". *Proc. of the European Particle Accelerator Conference EPAC'92*. 1992, 1295 (cited on page 97).

[Vog+19] M. Vogel et al. "Electron Magnetic Moment in Highly Charged Ions: The ARTEMIS Experiment". *Annalen der Physik* **531** (2019), 1800211. DOI: 10.1002/andp.201800211 (cited on page 4).

[Wan+10] S. X. Wang et al. "Superconducting microfabricated ion traps". *Applied Physics Letters* **97** (2010), 244102. DOI: 10.1063/1.3526733 (cited on page 157).

[War19] C. Warnecke. "Imaging of Coulomb crystals in a cryogenic Paul trap experiment". Master's thesis. Ruprecht-Karls-Universität Heidelberg, 2019. URL: http://hdl.handle.net/21.11116/0000-0004-F47D-D (cited on pages 60, 61, 151, 152).

[War20] C. Warnecke. *Private communication*. 2020 (cited on pages 61, 62).

[WD75] D. J. Wineland and H. G. Dehmelt. "Principles of the stored ion calorimeter". *Journal of Applied Physics* **46** (1975), 919–930. DOI: 10.1063/1.321602 (cited on pages 18, 112).

[Wei19] A. Weigel. "Detection Electronics Design and First Observation of Bound-Electron Spin Transitions at the ALPHATRAP g-Factor Experiment". PhD thesis. Ruprecht-Karls-Universität Heidelberg, 2019. DOI: 10.17617/2.3150015 (cited on pages 112–115).

[Wet03] C. Wetterich. "Probing quintessence with time variation of couplings". *Journal of Cosmology and Astroparticle Physics* **2003** (2003), 002. DOI: 10.1088/1475-7516/2003/10/002 (cited on page 6).

[WI79] D. J. Wineland and W. M. Itano. "Laser cooling of atoms". *Physical Review A* **20** (1979), 1521–1540. DOI: 10.1103/PhysRevA.20.1521 (cited on pages 2, 22).

[Wil+11] A. C. Wilson et al. "A 750-mW, continuous-wave, solid-state laser source at 313 nm for cooling and manipulating trapped $^{9}Be^{+}$ ions". *Applied Physics B* **105** (2011), 741–748. DOI: 10.1007/s00340-011-4771-1 (cited on page 69).

[Win+03] D. J. Wineland et al. "Quantum information processing with trapped ions". *Philosophical Transactions of the Royal Society of London. Series A: Mathematical, Physical and Engineering Sciences* **361** (2003), 1349–1361. DOI: 10.1098/rsta.2003.1205 (cited on page 24).

[Win+98a] D. J. Wineland et al. "Experimental Issues in Coherent Quantum-State Manipulation of Trapped Atomic Ions". *Journal of Research of the National Institute of Standards and Technology* **103** (1998), 259–328. DOI: 10.6028/jres.103.019 (cited on pages 13, 22, 69).

[Win+98b] D. J. Wineland et al. "Experimental Primer on the Trapped Ion Quantum Computer". *Fortschritte der Physik* **46** (1998), 363–390. DOI: 10.1002/(SICI)1521-3978(199806)46:4/5<363::AID-PROP363>3.0.CO;2-4 (cited on page 158).

[YTD14] V. I. Yudin, A. V. Taichenachev, and A. Derevianko. "Magnetic-Dipole Transitions in Highly Charged Ions as a Basis of Ultraprecise Optical Clocks". *Physical Review Letters* **113** (2014), 233003. DOI: 10.1103/PhysRevLett.113.233003 (cited on page 7).

[Yu+18] Y. Yu et al. "Motional-ground-state cooling outside the Lamb-Dicke regime". *Physical Review A* **97** (2018), 063423. DOI: 10.1103/PhysRevA.97.063423 (cited on page 24).

[Zoh15] T. I. Zohdi. *A Finite Element Primer for Beginners: The Basics*. SpringerBriefs in Applied Sciences and Technology. Springer, 2015. DOI: 10.1007/978-3-319-09036-8 (cited on page 91).

[ZTR99] G. Zwicknagel, C. Toepffer, and P.-G. Reinhard. "Stopping of heavy ions in plasmas at strong coupling". *Physics Reports* **309** (1999), 117–208. DOI: 10.1016/S0370-1573(98)00056-8 (cited on page 107).

Acknowledgements

Ich möchte die Gelegenheit nutzen, mich bei einigen Menschen zu bedanken, die mich während meiner Promotionszeit begleitet und unterstützt haben.

Lieber José. Vielen Dank für dein großes Vertrauen, das du mir all die Jahre über entgegengebracht hast. Ich habe es sehr genossen an diesem spannenden und einzigartigen Projekt zu arbeiten. Und wenn es einmal nicht ganz nach Plan lief, standest du mir stets mit Rat und Tat (auch zu später Stunde im Labor) zur Seite. Deine Begeisterung für Physik und vieles darüber hinaus ist unglaublich ansteckend. Ich konnte viel von dir lernen und bin dankbar für die tollen Erfahrungen, die ich im Rahmen der Promotion machen durfte. Deiner Unterstützung und einem offenen Ohr für jegliche Belange konnte ich mir immer sicher sein. Vielen Dank für die letzten Jahre!

Vielen Dank an Wolfgang Quint für die Übernahme der Aufgabe des Zweitgutachters.

Liebe EBIT-Gruppe. Ich möchte mich bei euch allen sehr herzlich für die wunderbare Zeit bedanken. Ohne die lustigen Mittagessen, die erfrischenden Eispausen egal ob Sommer oder Winter, oder die streng verordneten Stammtische wären die letzten Jahre nicht annähernd so schön und unterhaltsam gewesen. Ich bin sehr dankbar für den durchgehend großen Zusammenhalt in der Gruppe und die vielen helfenden Hände, wann immer sie benötigt wurden. Danke für all die schönen Erfahrungen, die ich mit vielen von euch teile, sei es beim Pub-Quiz, beim Laser-Tag, beim Joggen am Königsstuhl, zu Besuch auf einer bestimmten Insel oder die Erweiterung meines musikalischen Horizonts im Labor. Es macht einfach unglaublich Spaß mit euch! Ganz besonders möchte ich mich bei den aktuellen und ehemaligen Mitgliedern des CryPTEx-Experiments bedanken. Vielen Dank Andrea, Christian, Dieter, Elwin, Karl, Lisa, Lukas, Maria, Sandra, Shaolong und Steffen. Egal ob bei der Pflege der UV-Laser, der Bändigung hochgeladener Plasmen oder beim Anziehen und Lockern zahlloser Schrauben: Ohne eure Leidenschaft und unermüdliche Arbeit wäre das Projekt heute nicht auf diesem Stand. Dankeschön.

Weiter haben Kollegen aus der Gruppe von Piet Schmidt aus Braunschweig wertvolle Beiträge zum Projekt geleistet und mich auch über diese Entfernung stets wunderbar unterstützt. Vielen Dank an Lukas, Peter, Piet, Steven und Tobias für die zahlreichen

Tipps und die schöne gemeinsame Zeit im Labor oder auf den jährlichen Retreats!

Darüber hinaus habe ich während meiner Promotion große Unterstützung in verschiedenster Hinsicht aus der Abteilung von Klaus Blaum erfahren. Dafür möchte ich mich sehr herzlich bedanken.

Für die tolle Zusammenarbeit bei der Planung und Fertigung dieses großen Projekts bin ich dem Konstruktionsbüro und der Feinmechanikwerkstatt des MPIK sehr dankbar. Ganz besonders bedanken möchte ich mich bei Frank Müller und Thorsten Spranz für die vielen guten Ideen, die Geduld mit "uns Physikern" und die unkomplizierte und pragmatische Art Probleme zu lösen. Darüber hinaus möchte ich mich ausdrücklich bei Rainer Heldner und Florian Säubert bedanken, die mit unglaublicher Ausdauer, Geschick und Hingabe einen großen Anteil an der Realisierung des Projekts haben. Dies gilt ebenso für Bettina Mörk und Yannick Steinhauser aus der Konstruktion, die vieles Erträumte erst ermöglicht haben. Ihnen/Euch allen gilt mein herzlicher Dank für die fantastische Zusammenarbeit.

Ebenso möchte ich Christian Kaiser und seinem Team für die tatkräftige Hilfe und zuverlässige Unterstützung im Labor danken.

Für die vielen anregenden Diskussionen und das wertvolle Wissen zur Hochfrequenztechnik bedanke ich mich bei Thomas Busch, Oliver Koschorreck, Sven Sturm, Andreas Weigel und Peter Werle.

Für das Korrekturlesen des Manuskripts und hilfreiche Kommentare: Herzlichen Dank an Christian, Elwin, Jan-Hendrik, Peter, Rima, Steffen, Stepan und Sven.

Ein besonderer Dank gilt meiner Familie und meinen Freunden, die mir stets ein großer Rückhalt waren und mir in der ganzen Zeit viel Verständnis und auch Geduld entgegenbrachten. Ganz besonders danken möchte ich meinen Eltern, Rosa und Dieter. Vielen Dank, dass ihr immer für mich da seid und mich so fantastisch unterstützt!

Liebe Rima. Ich bin dankbar, dich in meinem Leben zu haben, für deine wunderbare Liebe und bedingungslose Unterstützung. Depenew ist für dich und wird für immer mit dieser Arbeit verbunden sein!